Advanced Methods for Characterizing Battery Interfaces: Towards a Comprehensive Understanding of Interfacial Evolution in Modern Batteries

Israel Temprano, Javier Carrasco, Matthieu Bugnet, Ivan T. Lucas, Jigang Zhou, Robert Weatherup, Christopher O'Keefe, Zachary Ruff, Jiahui Xu, Nicolas Folastre, et al.

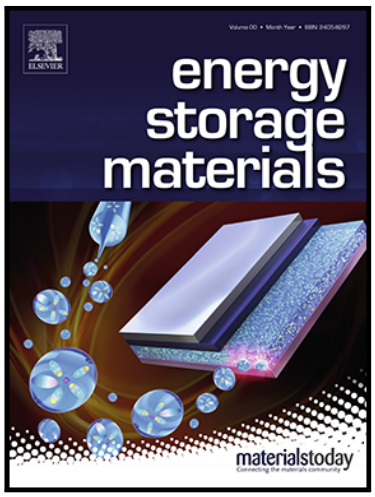

Advanced Methods for Characterizing Battery Interfaces: Towards a Comprehensive Understanding of Interfacial Evolution in Modern Batteries

Israel Temprano , Javier Carrasco , Matthieu Bugnet , Ivan T. Lucas , Jigang Zhou , Robert S. Weatherup , Christopher A. O'Keefe , Zachary Ruff , Jiahui Xu , Nicolas Folastre , Jian Wang , Antonin Gajan , Arnaud Demortière

PII: S2405-8297(24)00620-2
DOI: https://doi.org/10.1016/j.ensm.2024.103794
Reference: ENSM 103794

To appear in: *Energy Storage Materials*

Received date: 29 February 2024
Revised date: 25 August 2024
Accepted date: 13 September 2024

Please cite this article as: Israel Temprano , Javier Carrasco , Matthieu Bugnet , Ivan T. Lucas , Jigang Zhou , Robert S. Weatherup , Christopher A. O'Keefe , Zachary Ruff , Jiahui Xu , Nicolas Folastre , Jian Wang , Antonin Gajan , Arnaud Demortière , Advanced Methods for Characterizing Battery Interfaces: Towards a Comprehensive Understanding of Interfacial Evolution in Modern Batteries, *Energy Storage Materials* (2024), doi: https://doi.org/10.1016/j.ensm.2024.103794

Advanced Methods for Characterizing Battery Interfaces: Towards a Comprehensive Understanding of Interfacial Evolution in Modern Batteries

Israel Temprano[1,2,3,*], Javier Carrasco[5,6], Matthieu Bugnet[7], Ivan T. Lucas[8], Jigang Zhou[9], Robert S. Weatherup[10], Christopher A. O'Keefe[1], Zachary Ruff[1], Jiahui Xu[4], Nicolas Folastre[4], Jian Wang[9], Antonin Gajan[8,11], Arnaud Demortière[3,4,*]

[1]Yusuf Hamied Chemistry Department, University of Cambridge, CB2 1EW, Cambridge, UK

[2]CICA - Interdisciplinary Center for Chemistry and Biology, University of A Coruña, 15071, A Coruña, Spain

[3]ALISTORE-European Research Institute, FR CNRS 3104, 80039 Amiens Cedex, France

[4]Laboratoire de Réactivité et Chimie des Solides (LRCS), CNRS-UPJV UMR 7314, Hub de l'Energie, rue Baudelocque, 80039 Amiens Cedex, France

[5]Centre for Cooperative Research on Alternative Energies (CIC energiGUNE), Basque Research and Technology Alliance (BRTA), 01510 Vitoria-Gasteiz, Spain

[6]IKERBASQUE, Basque Foundation for Science, 48009 Bilbao, Spain

[7]CNRS, INSA Lyon, Université Claude Bernard Lyon 1, MATEIS, UMR5510, 69621 Villeurbanne Cedex, France

[8]Sorbonne Université, CNRS, LISE, F-75005 Paris, France / Nantes Université, CNRS, IMN, F-44322 Nantes, France

[9]Canadian Light Source Inc., University of Saskatchewan, Canada

[10]University of Oxford, UK

[11]SAFT Corporate Research, 33074 Bordeaux, France

[*]**Corresponding Authors**

Israel Temprano: it251@cam.ac.uk

Arnaud Demortière: arnaud.demortiere@cnrs.fr

Abstract

Batteries are complex systems operating far from equilibrium, relying on intricate reactions at interfaces for performance. Understanding and optimizing these interfaces is crucial, but challenges arise due to the diverse factors influencing their development, making comprehensive characterization essential despite experimental difficulties. Recent advancements in characterization tools offer new opportunities to explore interfacial evolution, particularly in the solid electrolyte interphase (SEI).

In this perspective article, leading experts in physical-chemical characterization techniques for electrochemical systems discuss the current state-of-the-art and emerging

approaches to study interfaces and their evolution in batteries. The focus here is on the capabilities, technical challenges, limitations, and requirements that these techniques must meet to advance our understanding of battery interfacial evolution. The emphasis is placed on techniques that enable probing interfaces under realistic conditions, close to commercial battery systems, and on the integration of multiple approaches within a single measurement (multimodal) to minimise variable effects.

This article focuses on the most promising techniques for characterizing all phases relevant to interfacial processes, as well as their integration with correlative analyses and computational modelling. We discuss solid phase characterization with X-ray spectroscopies and microscopies (XPS, XAS, STXM, X-PEEM & XCT), Raman spectroscopies (SERS, TERS & SHINERS), solid-state NMR and electron microscopies and spectroscopies (STEM, EDSX, EELS & 4D-STEM). The liquid phase characterization is discussed in terms of solution NMR spectroscopy, TEM and optical spectroscopies, while the gas phase can be characterized using OEMS, Pressure monitoring and GCMS. Computational modelling and simulation (DFT, ReaxFF & MLIP) are also discussed

Keywords

Advanced characterization techniques, Battery Characterizations, Interfacial Evolution, correlative analyses, computational modelling

1. INTRODUCTION

Batteries are dynamic systems, with active electrode materials and electrolytes in non-equilibrium during device operation. Their performances are ultimately linked to the extent and nature of reactions that result from interfacial instability [1-11]. Owing to the redox potentials of commonly used electrode materials, electrochemical energy storage systems currently operate beyond the thermodynamic stability window of liquid electrolytes [12-16]. In particular, the outcome of the electrochemical reactions occurring between the electrolyte and the electrode surfaces in Li-ion batteries (LIBs) upon initial polarisation creates solid barriers, e.g., the solid electrolyte interphase SEI) and the cathode electrolyte interphase (CEI) [2-4,17]. It is now well established that the long-term performance of LIBs depends critically on the nature of the reactions that ensues from this instability, as these barriers somewhat protect the electrolyte from further degradation [1,6,8,18].

Reactions leading to the formation and evolution of interfaces in batteries can have a number of sources in the solid (active materials, binders, current collectors, conducting carbon additives) and liquid phases (solvents, salts, additives), and generate products that can be in the solid, liquid or gas phases [1,2,4]. They contain a broad range of chemical constituents, containing light elements like Li or Na, as well as their heterogeneous distribution in layers not thicker than a few tens of nanometres. The contribution of individual processes to the formation and evolution of interfaces varies severely depending on a number of factors, such as cell chemistry, electrode/electrolyte combination, cycling protocol, etc.

The looming challenge to increase battery performance and lifespan will require a complete description (and then control) of interfacial processes over multiple length and time scales, including their initial formation, and evolution over the entire battery lifetime [6,19]. Special attention to evolution must be paid, as complex dynamical phenomena occur after SEI/CEI initial formation [18,20-22]. Constant (re)formation of interphase at the positive and negative electrodes and potential crosstalk effects between the two interfaces, depend on external stimuli such as temperature, charging conditions or on mechanical constraints associated with electrode expansion/contraction [3,19,23,24].

Considering the layered nature of the SEI, the possibility to investigate the composition with an excellent spatial and energy resolution would permit a clearer understanding of its chemistry. In general, the future development of batteries for a wide variety of applications, for which safety and efficiency will become the overriding factors, will require designing and employing multimodal and *operando* characterization techniques, coupled with modelling/simulation approaches capable of identifying these highly complex and interrelated processes [1,18-20,22-29]. Abundant data exist in the literature permitting the compilation of large databases in order to construct SEI/CEI models. However, only the combination of high-fidelity data gleaned from various characterisation techniques, coupled with advances in correlative analyses applied to commonly accepted *ex situ*, *in situ* and *operando* protocols, will provide a better understanding of the SEI/CEI and thus opportunities for major breakthroughs in the field of LIB [3,30,31]. Furthermore, the complex nature of interfacial reactions in modern batteries makes critical to characterise all phases to fully understand the evolution of their interfaces [1,3,19].

The daunting task of developing a comprehensive understanding of interface formation and evolution in modern batteries has stimulated the formation of major collaborative initiatives, such as the Faraday Institution and ALISTORE-ERI to gather complementary strengths, expertise and perspectives [9]. However, to date, researchers still overwhelmingly rely on an array of data/information to build a posteriori a coherent picture regarding battery interfaces, where the investigative power of all techniques is largely hampered by their inherent limitations [1,5,18,23-25,27,31]. The ultimate goal of interfacial analysis is the ability to perform correlative experiments providing information on the structural and chemical properties of evolving materials at different scales using complementary techniques. Significant work is still needed to design adequate electrochemical cells for each characterisation technique and to develop an efficient methodology allowing a correlative approach both for setting up transversal experiments and for coding an appropriate analytical algorithm based on statistical and artificial intelligence (AI) methods [30].

In consequence, investigation of battery interfaces is an intensely researched topic, and as such it has been covered in many, highly interesting, review articles already [19,23-29,31-34]. In this article, we focus on the technical characteristics of the most advanced methods that could provide information of processes influencing the formation and evolution of battery interfaces. We describe in detail the aspects of each method that influences the data that it can provide, as well as how to overcome current instrumental limitations. We pay particular attention to approaches that can provide information of all phases, in operando, and as close to commercially relevant conditions as possible. The

refinement of formation protocols will play a critical role in the coming years, as they must cover cell assembly, with large deviations naturally existing between cell formats (cylindrical, pouch, coin, etc.) owing, for example, to different electrolyte volume/mass of active material ratio and the relative weight of non-active components. A key challenge in this field that we discuss at depth, is designing cells and sample holders that can provide an accurate and consistent electrochemical behaviour while allowing spectroscopy techniques capable of looking at embedded interfaces in their working environment.

This article highlights emerging approaches, and especially the requirements and directions these approaches need to meet, to study battery interfaces and their evolution, being chemistry-agnostic. This review focuses on the most promising techniques for characterising all phases relevant to interfacial processes in batteries. Solid phase characterization techniques include X-ray spectroscopy, nuclear magnetic resonance, and various microscopy techniques. Liquid phase characterization involves the use of spectroscopic techniques such as NMR, infrared and Raman spectroscopy, ion-coupled plasma, and X-ray fluorescence spectroscopy. Gas phase characterization techniques, such as electrochemical mass spectrometry, pressure monitoring systems, and gas chromatography-mass spectrometry, provide valuable insights into the gas evolution during interfacial processes. Finally, computational modelling and simulation, particularly density functional theory, reactive force fields, and techniques borrowed from network science and machine learning, offer powerful tools for understanding complex interface systems. We put a strong emphasis on *in situ* and *operando* techniques and the need to integrate multiple approaches, ideally within a single measurement (multimodal) to control parameters as much as possible. Overcoming current instrumental limitations in *operando* characterization techniques would provide answers to some of the following central open questions: how does the SEI form and evolve during cycling? What is it made of? How do the solvated lithium ions escape from the solvation shell and pass through the SEI layer? How to control and rationally design the key features of the SEI layer such as ion conductivity, structure, density, and thickness?

2. SOLID PHASE CHARACTERIZATION

2.1. INTRODUCTION

Chemical and morphological changes to electrode surfaces are typically the starting point for understanding the interfacial reactions between the electrolyte and the electrodes. Under chemical and electrochemical stresses, the electrode surface will show evidence of mechanical stress (cracking), compositional changes (due to oxygen loss and ion dissolution) and contain insoluble degradation products from oxidation and reduction reactions at the electrodes (SEI and CEI).

X-Ray spectroscopy techniques such as X-ray photoemission (XPS), X-Ray fluorescence (XRF) and X-Ray absorption (XAS) spectroscopy all have energy dependent penetration depths and therefore are powerful techniques for selectively probing solid-electrode interfaces. Although nuclear magnetic resonance (NMR) spectroscopy is bulk sensitive, NMR also can be very useful for understanding chemical changes if they occur in sufficient concentrations, only involving elements occurring at the surface or by using more

specialised pulse sequences and excitation approaches to selectively enhance surface signals. Scanning probes and enhanced Raman spectroscopies are of course fundamentally surface sensitive techniques, so they also are of particular interest for measuring changes at electrode surfaces.

Electron, X-Ray, optical and scanning-probe microscopies are all commonly used techniques for understanding the physical nature of electrode interfaces, revealing 2D, 3D and 4D morphological and sometimes chemical information. Using a combination of the techniques, the electrode can be probed at different length-scales in order to gain a more complete understanding of interfacial evolution during cell operation.

2.2. X-RAY SPECTROSCOPIES

X-ray spectroscopies can provide powerful element-specific chemical information, by exciting core electrons into unoccupied orbitals or the continuum, with the energies of these transitions typically falling in the X-ray range (>50 eV). This provides a powerful means of probing electronic structure by measuring the absorption of X-rays associated with these transitions, or the emission of electrons and photons arising from the subsequent relaxation. The relatively long attenuation lengths of X-rays, do not in themselves lead to a high degree of interface sensitivity [35], rather, interface sensitivity can be achieved by the detection of ejected electrons. The escape depths of these electrons correlate closely with their inelastic mean free path (λ), which increases monotonically for electrons with >50 eV kinetic energy from ~5 Å, extending beyond 100 nm for 10 keV electrons [36].

This gives rise to two main interface-sensitive X-ray spectroscopy methods: 1) XPS (including Auger-Meitner emission spectroscopy: AES) where the energy of electrons emitted to the continuum is measured for a fixed X-ray excitation energy. 2) soft X-ray absorption spectroscopy (XAS) in electron yield (EY) mode, where the incident X-ray energy is scanned over an absorption edge whilst measuring the quantity of emitted electrons. We do not consider hard (>2 keV) XAS herein, as higher kinetic energy electrons are produced, decreasing the interface-sensitivity.

The availability of high-intensity, fixed energy (characteristic) X-ray sources means lab-based XPS systems are widely accessible. Nevertheless, the tuneable X-ray energy of synchrotron sources provides greater versatility to perform non-destructive depth-profiles, and avoid overlap between XPS and AES features. A continuously tuneable X-ray source is essential for XAS, and thus measurements are typically performed at synchrotron facilities. Lab-based XAS systems are now commercially available for energies >2 keV [37], however for the soft X-ray range the low fluxes achievable limits measurements to transmission mode, which is bulk sensitive and typically involves challenging preparation to produce samples of only a few hundred nm thick [38].

2.2.1. XPS & SOFT XAS: *EX SITU* CHARACTERIZATION

XPS and soft XAS measurements have become widely used in battery research over the last 3 decades, with several hundred articles published annually that mention both batteries and photoelectron spectroscopy [27]. These methods are typically performed under vacuum conditions due to the relatively short distances over which soft X-rays and

electrons are scattered when gas molecules are present. The interfaces in assembled batteries by their very nature are buried between the electrode and electrolyte, whose thicknesses are well beyond the probing depths of either technique. The well-established approach to apply these methods in battery research has thus been to measure devices *ex situ* following disassembly. This typically involves cell disassembly in a glovebox environment, rinsing of the electrodes with a solvent to remove non-volatile electrolyte components, drying, and then transferring to the measurement system using a sealed inert-transfer environment. A study may involve measuring multiple electrodes prepared in this way, and then comparing the spectra collected. Changes to the electrode surfaces and interphases formed by electrolyte decomposition can thus be detected and the different species observed, depending on electrode materials, electrolyte formulation, cycling conditions, or other pertinent variables. Through careful sample preparation and measurement chemical changes resulting from degradation processes including SEI thickening, reduced surface layer formation, and transition metal dissolution can be identified and connected with electrochemical cycling data [39]. As already noted, the ability to tune the excitation energy of the X-ray source can be valuable in changing the probing depth in XPS, particularly if relatively thick interphases are formed.

Despite the many insights available from these *ex situ* measurements, there are also many drawbacks, such as the ambiguity introduced by removing interfaces from the electrochemical environment, meaning intermediate species may be lost, reactions may occur with residual contaminants (particularly trace H_2O, CO_2, and O_2 in glovebox environments), and labile components may be removed through rinsing of the electrodes [40]. Furthermore, mechanistic studies are rendered impractical due to the large number of samples required and the inherent sample variation that can obscure the behaviour being probed. Finally, these studies cannot capture the interface in its real operating state - under electrochemical polarization, where the interfacial chemistry may be radically different. There is thus a strong motivation to move towards *in situ* or *operando* X-ray spectroscopy measurements of batteries, distinguished here on the basis of whether the measurements are performed under electrochemical control.

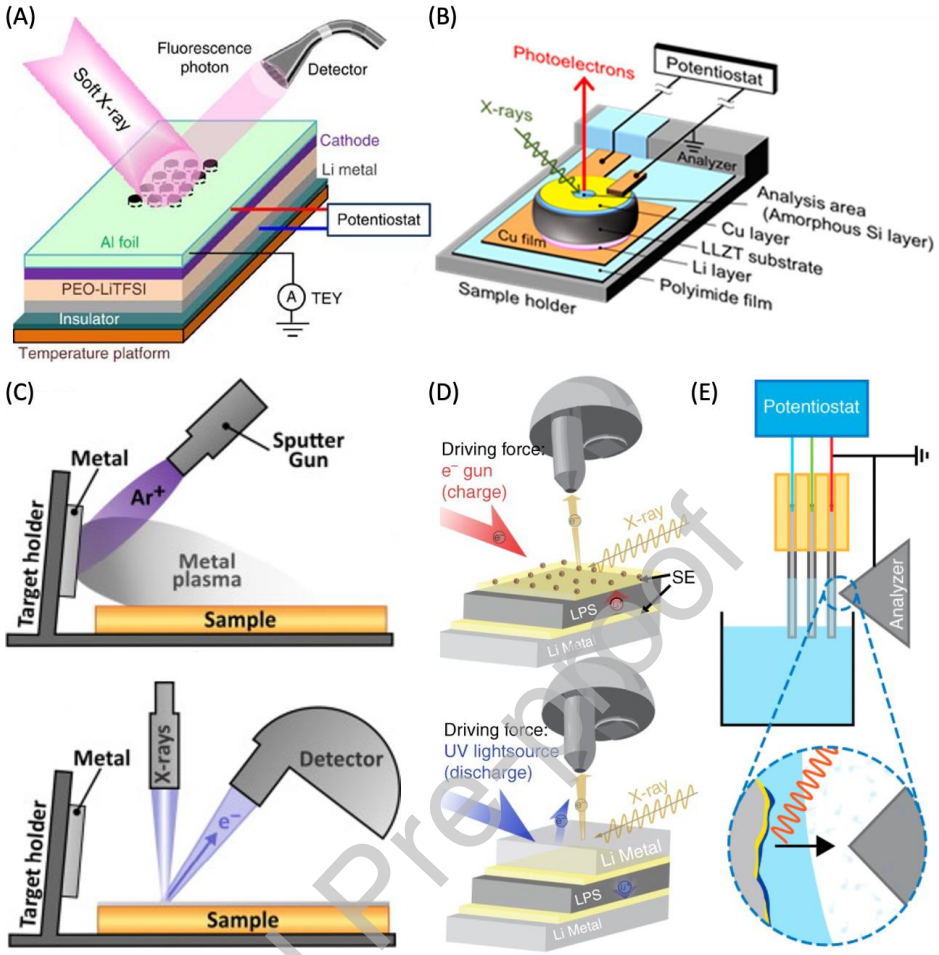

Figure 2.2.1. Open cell measurement geometries for XPS and XAS of battery interfaces a) Solid polymer electrolyte battery cell, where perforations in the Al current collector allow access to the reverse side of the cathode for XAS during electrochemical cycling [41]; b) Solid electrolyte cell for studying lithiation of sputtered Si electrode with XPS [42]; c) *In situ* sputter-deposition onto solid electrolytes for studying SEI evolution [43]; d) Virtual electrode approach on solid electrolytes for plating (top) and stripping (bottom) Li metal driving by an electron flood gun or UV light source [44]; e) Dip and pull method where electrode-electrolyte interfaces are probed using ambient pressure XPS through a meniscus formed by dipping and carefully withdrawing an electrode from a beaker of electrolyte [45].

2.2.2. XPS & SOFT XAS: *IN SITU* & *OPERANDO* APPROACHES

A key challenge in performing *operando* measurements is collecting the low-energy electrons that give rise to interface sensitivity, while maintaining the electrochemical environment needed to give realistic battery cycling. Approaches to achieve this can be broadly classed into open cell geometries (Figure 2.2.1), in which the electrochemical environment is exposed to the analysis chamber, and enclosed electrochemical cells where the electrochemical environment is sealed against the vacuum of the analysis chamber with an X-ray/electron transparent window or membrane (Figure 2.2.2). Hybrid approaches have also recently emerged, where partially permeable membranes are

employed, but their main application to date has been in electrocatalysis where ion-selective membranes are often inherent to the application being investigated [46].

2.2.2.1. OPEN CELLS WITH SOLID ELECTROLYTES

From the perspective of maintaining the vacuum environment typically required for soft X-ray measurements, the use of non-volatile solid-state electrolytes is often the most straightforward solution, with numerous such systems explored (Figure 2.2.1 a-d). Liu et al. demonstrated an early version of this approach using a polymer electrolyte, and composite cathode, where laser-drilled holes in the aluminium current collector allowed X-rays to access the cathode material to perform fluorescent yield (FY) mode XAS [8]. This approach also lends itself to XPS and TEY-XAS [47],[14] however the use of relatively thick electrodes mainly provides access to the electrode rather than the interface between electrode and electrolyte. Furthermore, the relatively large hole sizes used (>50 μm) in the study of Liu et al. give rise to inhomogeneous charging of the cathode, with regions close to the current collector becoming fully charged, whilst those at the centre of the hole show no change in transition metal oxidation state. This highlights the importance of achieving good in-plane electrical conductivity in the electrodes studied.

More recently the deposition of model thin-film silicon electrodes on top of garnet-type solid electrolytes has been used for *operando* XPS studies in a lab-based instrument, as shown in Figure 2.2.1 b [42],[9]. Whilst this allowed the state of lithiation of the electrode to be tracked during electrochemical cycling, the electrode thickness again does not allow the interface with the electrolyte to be observed. Much thinner electrodes approaching λ are required, and in this direction alkali metal thin films have primarily been investigated due to the interest in coupling these with solid electrolytes to achieve high energy densities, and perhaps also in part due to the anomalously large λ in these metals [36]. Wenzel et al introduced an approach based on sputter-deposition, through mounting a Li metal piece adjacent to the sample to be measured and using the sputter gun present in many XPS systems to sputter the Li onto the sample (see Figure 2.2.1 c) [43]. However, more recent studies have questioned the relevance of this approach since the highly energetic Li atoms produced by sputtering can induce significant physical damage to the surface under study. Alternatively, Li evaporation can be preferable, since the kinetic energy of the arriving Li is around two orders of magnitude lower [48]. However, this often requires a dedicated Li evaporator that can be a challenge to interface with an existing XPS system. An alternative approach introduced by Wood et al. uses the electron flood guns, typically used for charge neutralisation in XPS systems, in order to supply electrons to the exposed surface of a solid electrolyte, thereby drawing Li from a grounded Li electrode on the opposing side [44]. This so-called “virtual electrode” approach allows Li plating at a controlled rate whilst observing chemical changes at the electrode-electrolyte interface with XPS. It has been successfully applied to reveal the role of Li plating current density on the nature of the SEI formed on Li_6PS_5Cl pellets [49], as well as to investigate the SEI formed as a result of Na plating on NaSICON electrolytes [50]. Furthermore, using a UV-lamp (also commonly present to allow ultraviolet photoelectron spectroscopy) has been shown to drive the reaction in the opposite direction by increasing photoemission at the surface so that Li stripping can also be observed (see 2.2.1d) [44]. This can potentially give important insights into the interfacial reactions between alkali metal anodes and solid electrolytes but hasn’t yet been adapted to the

study of other electrode materials, where pre-deposition of suitable thin films would likely be necessary. Given the typically larger ionisation cross-sections of low-energy electrons/UV light compared to X-rays, the virtual electrode approach can also induce ionisation of residual gas phase contaminants and surface species, and thus the influence on the interface chemistry must be carefully considered when interpreting these measurements [48].

2.2.2.2. OPEN CELLS WITH LIQUID ELECTROLYTES

Given the commercial relevance of liquid electrolyte batteries, extending *operando* approaches to liquids is highly sought-after. Various attempts have been made with non-volatile liquid electrolytes such as ionic liquids (ILs) as they can be used directly in XPS instruments without compromising the vacuum, but their relevance to battery studies is limited due to their relatively high cost [51,52]. Furthermore, for X-ray spectroscopy studies ILs have also been shown to be susceptible to radiolysis, which may mask the interfacial chemistry being investigated [53].

Ambient pressure (AP)XPS, based on differentially pumped electron analyser and lens systems, has become an established technique for probing interfaces at pressures in the mbar-range [54]. This allows extension to more volatile electrolytes, although significant attenuation of the photoelectron signal at vapour pressures above a few mbar still limits which electrolytes can be practically measured. In order to access the electrode-electrolyte interface, photoelectrons must escape through the electrolyte on top of the electrode, meaning a liquid film with thickness comparable to or below λ must be stabilised. The dip and pull method has been introduced which forms a meniscus of 10-20 nm in thickness by dipping and carefully withdrawing an electrode from a beaker of electrolyte (see Figure 2.2.1 e) [55]. To measure the electrode-electrolyte interface, higher energy X-ray excitation (3-4 kV) is needed to increase λ so that sufficient photoelectrons can escape through the meniscus [45,56]. Through this approach Yu et al. observed instabilities in diglyme solvent and TFSI electrolyte species at a Mg electrode surface, providing insight into the stability of the Mg-electrolyte interface. Several variants of this approach with droplets or a similar dip and pull methodology have attempted to use lower energy X-ray excitation to measure the interface, but it has generally proved challenging to observe the interface, since the electrolyte overlayer dominates [56-58].

2.2.2.3. ENCLOSED CELL APPROACHES

Enclosed cell approaches, where the electrolyte is sealed behind a X-ray and/or electron transparent window, can avoid the signal attenuation issues posed by high-volatility electrolytes as well as changes in electrolyte concentration during measurement associated with continuous solvent evaporation [59]. However, this requires window materials that can sustain the pressure difference between the sealed cell and the vacuum of the analysis chamber, that are chemically stable in the electrochemical environment, and that remain sufficiently transparent for XAS/XPS measurements to be performed. For XAS, only X-ray transparency is required and therefore silicon nitride-based windows of up to a few hundred nm in thickness supported on silicon frames have been widely employed. Figure 2.2.2 a, shows such a cell where a small electrolyte volume is contained behind a window sealed against the cell using a polymer O-ring. These have been

extensively used for performing bulk-sensitive FY-mode XAS of liquids electrolytes and electrodes under electrochemical control [60]. This includes investigations of Mg plating and Mg insertion into cathode materials, as well as their extension to various beyond Li-ion technologies such as Na-ion, K-ion, Ca-ion, and Zn-ion batteries [61].

The information depth of FY-XAS (a hundred nm to a few microns depending on the energy) often makes it difficult to distinguish interfacial reactions from other processes occurring in the electrode or electrolyte bulk. Transmission mode XAS is similarly bulk sensitive, and so to get around this issue the formation of bubbles by *in situ* radiolysis/heating with the X-ray beam has been proposed [32]. However, this approach shares many of the drawbacks of *ex situ* measurements, with the production of radicals and/or exposure to elevated temperatures likely to significantly alter the chemical state of the interfaces being observed, and further cycling after bubble formation not demonstrated. *Operando* TEY mode measurements are therefore desirable to obtain interface-specific information with the electrolyte still present. However, when measuring under electrochemical control, separating the TEY current from the much larger Faradaic current is far from straightforward. An approach to overcoming this limitation is to modulate the X-ray beam, such that the TEY current is also modulated and can be extracted using lock-in techniques [62]. Figure 2.2.2 b shows an example of a cell from a recent report where this approach was demonstrated for a Li-ion battery to reveal the evolution of the SEI that forms on thin-film silicon anodes and the impact of additives to the electrolyte [63]. This allowed the potentials at which different SEI species such as LiF and organic components are formed to be determined, with the interface-sensitivity highlighted by the disappearance of electrolyte species as the SEI forms. Although this technique has only recently been introduced to the study of battery systems, it can potentially be applied to study a variety of thin film electrode materials in the future to enhance understanding of the interfacial reactions occurring.

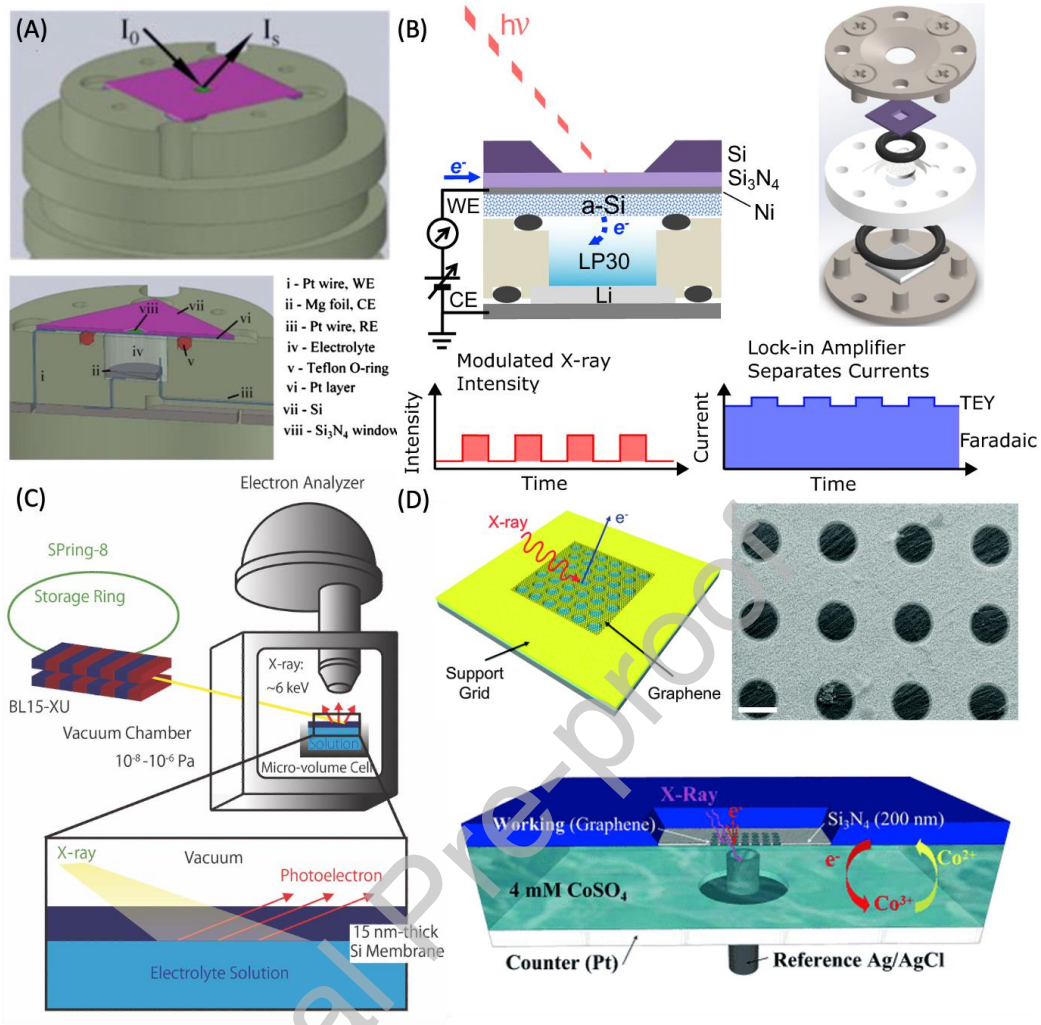

Figure 2.2.2. Enclosed electrochemical cells for XPS and XAS of battery interfaces. a) XAS cell sealed with ~100 nm SiN_x membrane, used primarily for FY measurements [60]; b) TEY-XAS cell and lock-in approach for separating faradaic and TEY currents, used to study SEI formation on a-Si [63]; c) Silicon membrane approach for studying solid-liquid interfaces with XPS using ~6kV X-ray excitation [64]; d) Graphene Membrane approach for studying the solid-liquid interfaces with XPS, so far demonstrated with aqueous electrolytes [65,66].

For *operando* XPS in enclosed cell geometries, much thinner windows, transparent to photoelectrons as well as X-rays, are needed. Masuda et al. demonstrated this concept in 2013 using 15-nm thick silicon membranes and an incident X-ray energy of ~6 keV (see Figure 2.2.2 c) [64]. This results in photoelectrons with λ ~10 nm, meaning that ~20% of the photoelectrons emitted at the solid/liquid interface are expected to pass through the membrane for collection by the electron analyser. More recently the same group reported measurements in a lab-based XPS system using 5-nm thick silicon nitride membranes, and a much lower energy Al Kα source [42].

Extending this further, 2D materials such as graphene represent the ultimate limit in terms of thin window material [67]. Indeed Kolmakov et al. showed that graphene oxide could be used to cap micron-sized holes in silicon oxide membranes to allow *in situ* XPS

[68]. A microfocussed X-ray source at a synchrotron beamline was required in this case, but this has since been extended to work with more typical X-ray spot sizes of ~100 μm by using arrays of holes covered with graphene, (see Figure 2.2.2 d) [66,69]. Although electrochemical reactions have been studied using this approach, the studies to date have focussed on aqueous systems not directly related to batteries [66,70]. Given that graphite can intercalate alkali-ions (e.g. Li-, K-ions), the stability of graphene membranes for alkali-ion battery studies is not yet clear, which may explain the lack of battery studies so far using the graphene membrane approach.

2.2.3. FUTURE PERSPECTIVE

Much progress has been made recently in developing *in situ* and *operando* approaches for performing X-ray spectroscopy of interfaces relevant to batteries, each with its own associated advantages and drawbacks. Proof-of-concept studies have shown that several of these approaches can reveal new mechanistic insights into the reactions occurring at electrode-electrolyte interfaces. Even so, these approaches have yet to reach full maturity and typically require a high degree of expertise and further adaptation of the technique to perform a particular investigation. These barriers to entry will undoubtedly reduce as the community using these techniques continues to grow. Although a variety of techniques is available, the trade-offs associated with each will likely mean that the development of the different methods will continue in parallel. Some methods promise detailed mechanistic insight but require significant changes to the electrode materials or electrochemical environment being studied, compared to well-established cell formats. Indeed, it seems likely that future studies may make use of several methods to address a particular research question, connecting those that use the most realistic materials and cell design to those that provide the most detailed mechanistic insight.

2.3. X-RAY SPECTROMICROSCOPIES

Synchrotron-based soft X-ray spectromicroscopies, specifically scanning transmission X-ray microscopy (STXM), and X-ray photoemission electron microscopy (X-PEEM), elegantly integrate X-ray microscopy and X-ray absorption spectroscopy, providing nanoscale high resolution chemical imaging and spectroscopy for a wide range of applications in many fields [71], particularly in the fast growing battery research [72]. In this section, first the fundamental aspects of STXM and X-PEEM, including principle and instrumentation, will be briefly introduced. Then, selected applications of STXM and X-PEEM in battery reach focusing on investigating electrode interfaces and surfaces will be illustrated in detail. Finally, perspectives on the future developments of STXM and X-PEEM to better understand battery electrode interfaces and surfaces, especially *in situ/operando* approaches and new opportunities available with next-generation diffraction-limited synchrotron sources (DLSR), will be discussed.

2.3.1. SCANNING TRANSMISSION X-RAY MICROSCOPY

2.3.1.1. X-RAY SPECTROMICROSCOPIES

Synchrotron-based soft X-ray spectromicroscopies, specifically scanning transmission X-ray microscopy (STXM), and the X-ray photoemission electron microscopy (X-PEEM),

elegantly integrate X-ray microscopy and X-ray absorption spectroscopy, providing nanoscale high resolution chemical imaging and spectroscopy for a wide range of applications in many fields [71], particularly in the fast growing battery research [72]. Over the past two decades, interferometer-controlled soft X-ray STXMs have been implemented at a number of synchrotron facilities through in-house development or commercial solutions, and the principle, instrumentation, experimental methods, and applications of STXM have been reviewed in the literature [73-80]. These STXMs are primarily used for conventional transmission-based X-ray spectromicroscopy measurements, with a few state-of-the-art instruments dedicated for high-resolution 2D and 3D chemical imaging. As for X-PEEM, there are a number of commercial instruments operating on synchrotron facilities around the world, either being used as a dedicated instrument for X-ray imaging and spectroscopy or integrated with low-energy electron microscopy (LEEM) for extended applications [73]. Using synchrotron radiation, X-PEEM has demonstrated to be a very powerful tool in delivering nanoscale chemical imaging and X-ray absorption and photoelectron spectroscopy in surface characterization of materials [73].

2.3.2. BATTERY INTERFACIAL PHENOMENA STUDIED BY STXM

2.3.2.1. MULTIMODAL STXM

A multimodal STXM integrates detection modes of transmission, XRF, TEY, and ptychography all together or at least two of them. In battery research, transmission is used to obtain sample bulk information for thin samples, semi-transparent to soft X-rays [81-87], which are typically prepared using focused ion beam milling (FIB) or ultramicrotomy coupled with resin embedding for electrodes or solid-electrolyte/electrode interfaces [88]; XRF is applied to obtain sample bulk or subsurface information for semi-transparent to non-transparent thick samples of electrodes and assemblies in their original format with a better detection sensitivity than transmission [89,90]; TEY is utilized to obtain sample surface information with sample thickness requirement and detection sensitivity similar to XRF [89]; ptychography is implemented to achieve much higher spatial resolution than the conventional STXM and acquire both X-ray absorption and phase contrast images [85,91-94].

These capabilities enable chemical imaging of critical interface structures in advanced batteries including CEI, SEI, and their interplays with active and non-active components in composite battery electrodes, all of which are crucial in determining ionic and electronic transportation within battery electrodes. Correlative imaging of those interfaces, especially in a practical battery electrode, is the key to a deeper understanding of the thermodynamic and kinetic properties of electrodes, such as phase separation within and among active particles in batteries. They are the core scientific foundations for the rational design of high-performance and long-life batteries, but it faces great challenges.

STXM with a combination of spectroscopy and multimodal imaging has been recognized as a powerful tool to integrate surface phenomena with the bulk phase separation in batteries. Shown in Figure 2.3.1 a-f the Ni oxidation state in $Li_{1-x}Ni_{0.5}Mn_{1.5}O_4$ (LNMO) within a composite electrode after long-term slow reduction in air has been mapped by

STXM [82]. The unexpected distinct variations in phase separation among and within individual battery particles have been experimentally correlated to the interface structures. The overall morphology of the electrode thin-section is displayed in Figure 2.3.1 a. Three regions (red boxes) were selected to obtain Ni oxidation state mapping and XANES (2.3.2b). The morphology maps of the three regions are displayed in Figure 2.3.1 c. Large particles with well-defined shapes and smaller ones that are plate-like shapes can be identified. Figure 2.3.1 d shows the corresponding chemical maps of the phase separation in each region. They were obtained by fitting the Ni L-edge STXM data by reference spectra in Figure 2.3.1 e, which were previously extracted via principle component analysis (PCA). Clearly top two regions, close to the separator, are mixtures of all the three phases, which contrast with that in the bottom region, where a more uniform Ni^{3+}-like phase dominates. Interestingly, in the top regions, large particles with a dominant Ni^{4+}-like phase always have a shell with a Ni^{2+}-like phase. While the reduction phase, Ni^{3+}-like-phase-dominated large particles, doesn't have such a protection shell. This suggests that the Ni^{2+}-like phase is related to the interface structure such as CEI, as being confirmed by more Ni^{2+} in a large particle (Figure 2.3.1 f).

X-ray scattering based ptychography can improve the spatial resolution in STXM to 5.6 nm as shown in Figure 2.3.1 g-h for a novel PH_3 treated, high-Ni, and Li-rich cathode (PLNR) thin section [91]. The conventional STXM absorption image with a spatial resolution of 37.3 nm cannot resolve PLNR primary particles within the micrometer-sized secondary particles. However, STXM-ptychography, at both amplitude-contrast mode (Figure 2.3.1 g) and phase-contrast mode (Figure 2.3.1 h), provides unprecedented high spatial resolution (7.8 and 5.5 nm, respectively) and can unambiguously resolve individual primary cathode crystalline particles, as well as phase-sensitive organic materials like PVDF and carbon black, demonstrating huge advantages in high resolution chemical imaging of electrode assemblies. Such high-quality elemental/chemical maps allow detailed chemical analysis at local regions of interest to reveal F incorporation into the cathode material lattice and formation of CEI. Furthermore, photon energy can also be scanned to enable 2D spectro-ptychography and 3D spectro-ptycho-tomography to deeply understand the chemical and structural information within electrode interfaces, particularly in solid-electrolyte based lithium batteries [88].

The complexity of the interplays of surface morphology, chemistry and local electric conductivity of LNMO particles has been thoroughly investigated by STXM with a combination of transmission, XRF, and TEY modes [89]. Figure 2.3.1 k shows STXM-XRF imaging of pristine LNFMO particles, in which Fe/Ni rich hot spots at the crystal edges and random facet inhomogeneity, such as Mn rich (111) facets, are clearly visualized.[89] The Mn L_3-edge XRF-XANES (Figure 2.3.1 l) shows the (111) facet is dominated by Mn^{4+}, while the (100) facet has a major contribution from Mn^{3+}, as suggested by the enhanced spectral intensity around 642 eV and lower energies. This implies a Ni/Mn disordered phase with oxygen vacancies that are compensated by Mn reduction in the surface. Figure 2.3.1 m shows the STXM-TEY imaging of a well-shaped single particle. The TEY-XANES (Figure 2.3.1 n) confirms the facet surface (dark regions) is dominated by stoichiometric Mn^{4+}, while there is a Mn^{3+}/Mn^{4+} mixture at the bright crystal edges, suggesting a Ni/Mn disordered phase in the edge surface. Recently, XRF-STXM has been employed to investigate graphite anode SEI for chemical composition, spatial heterogeneity, and location dependence, as well as its strong correlation with conductive additives/binders,

using XRF-based spectromicroscopy covering key elements such as C, O, and F [90].

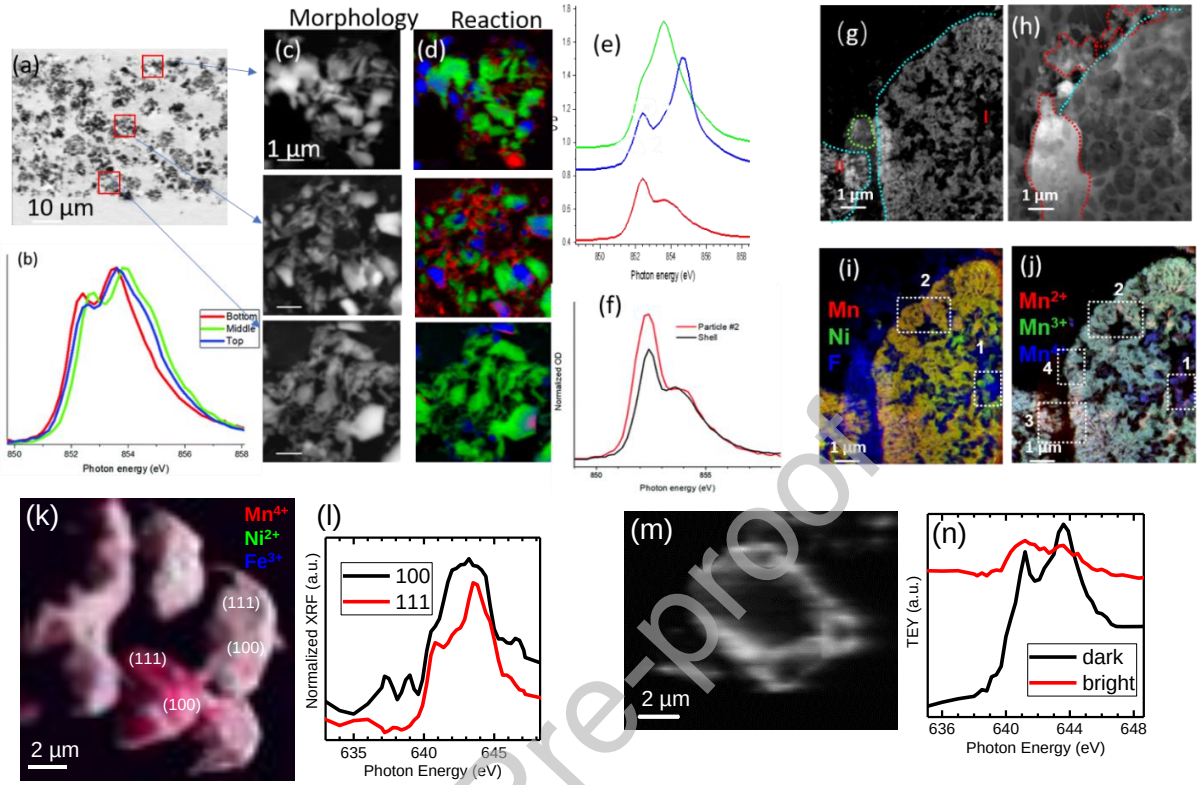

Figure 2.3.1. a) Morphology mapping of the self-discharged fully delithiated LNMO electrode thin-section; b) Ni L-edge XANES; c) morphology; d) chemical map (Ni^{2+}-like shown as red, Ni^{3+}-like shown as green and Ni^{4+}-like shown as blue) of the top, middle and bottom selected regions of the LNMO electrode in a) by SVD fitting of the Ni L_3-edge STXM image stack, using the internal fitting references displayed in e); f) Ni^{2+} L-edge comparison. Adapted from the literature with permission [82]; g) Ptychography amplitude (optical density) image, and h) ptychography phase image of a cycled P-treated High-Ni Li-rich cathode thin section obtained at the O K-edge; i) elemental distribution mapping by ptychography amplitude mode at the Mn L-edge, Ni L-edge and F K-edge, and j) Mn oxidation state mapping by ptychography amplitude mode at the Mn L-edge. Adapted from the literature with permission [91]; k) Chemical map of the pristine $LiNi_{0.33}Fe_{0.33}Mn_{1.33}O_4$ (LNFMO) cathode crystals, red: Mn^{4+}, green: Ni^{2+}, blue: Fe^{3+}; l) Mn L-edge XANES from the adjacent (111) and (100) facets; m) TEY-STXM morphologic imaging of a well-shaped LNFMO single crystal; n) Mn L-edge TEY-XANES from dark and bright regions on the crystal in m). Adapted from the literature with permission [95].

2.3.2.2. IN SITU STXM

The multimodal STXM measurements of battery materials, typically *ex situ*, have shown powerful capabilities in elucidating the chemical, electronic, and morphological structures of CEI, SEI, and interfaces among active and non-active components in electrodes. However, sample preparation and measurement environments could introduce artefacts or inaccurate characterization of battery samples. Therefore, the best

approach and the ultimate goal are to conduct *in situ* / *operando* measurements of battery materials or real batteries. Here, we show a few examples which have been performed on several STXM facilities.

Figure 2.3.2 a-b shows a thick *in situ* electrochemical cell that houses a $LiFePO_4$ working electrode, organic liquid electrolyte ($LiClO_4$ salt dissolved in ethylene carbonate (EC) and dimethyl carbonate (DMC)), and a lithium foil counter electrode [96]. Galvanostatic charge and discharge cycles of the $LiFePO_4$ particles in the electrochemical cell at a rate of 0.2 C have been successful and yield the expected $LiFePO_4$ plateau voltage, Figure 2.3.2 c. This in-house developed *in situ* electrochemical setup for STXM utilized XRF detection to overcome sample/device thickness restrictions for transmission detection. The work identified two types of $LiFePO_4$ particles which showed different Li intercalating behaviour and mechanism. The difference is essentially related to the surface properties and inhomogeneities of the particles, presumably resulted from different synthesis procedures and CEI properties, as visualized in Figure 2.3.2 c. Another worth-noting in-house developed 3-electrode *in situ* electrochemistry cell has been used for real-time STXM studies under both static (sealed, electrolyte non-flow) and continuous flow conditions [97]. An improved version of this setup, also coupled with the higher spatial-resolution ptychography, has recently been demonstrated [98]. Following some fundamental electrochemical works, such as Cu deposition/stripping, application of this device for battery research is being actively pursued.

Through adoption of advanced *in situ* devices, typically adapted from commercially available *in situ* electron microscopy devices, STXM has been applied in *operando* battery studies in which the interface phenomena can be inferred from battery particles bulk kinetics [99,100]. The pioneering *in situ* STXM electrochemistry work is shown in Figure 2.3.2 d-e [99]. A major innovation of this setup is to only place the half-cell ($LiFePO_4$/Au working electrode) in a sandwiched Si_3N_4 stack inside STXM chamber under vacuum, and leaves the Li foil counter/reference electrode in a syringe outside of the chamber with ionic and electric connection, Figure 2.3.2 d. This simplified half-cell configuration allows operando STXM transmission detection of single particles upon charging and discharging, Figure 2.3.2 e. The work showed the kinetics and uniformity of ion insertion reactions at the solid-liquid interface control the lithiation pathway at the sub-particle length scale [99]. Newer versions of the *in situ* electromechanical setup from Hummingbird Scientific and other vendors allow for continuous electrolyte flow down to sub-micrometre electrolyte thickness, reduced STXM working distance and weight load, multiple electrodes for full electrochemical needs, and advanced sealing technology with a leak-checking apparatus. More detailed chemical imaging and spectroscopy analysis during in situ/operando electrochemical operation could provide abundant information, such as solid-liquid interfacial chemistry, lithiation/delithiation mechanisms, phase evolution, and conductivity heterogeneity.

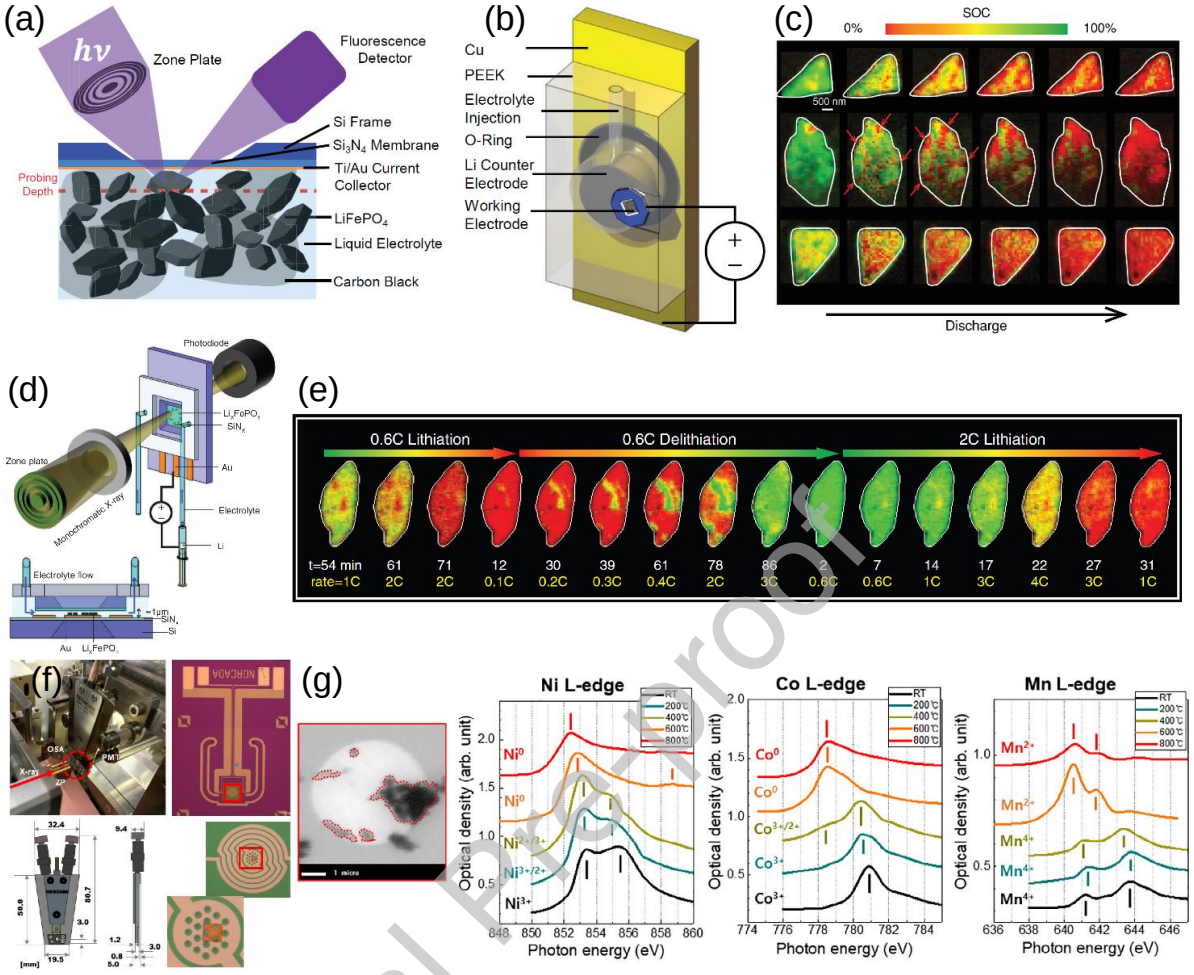

Figure 2.3.2. *In situ* STXM of lithium-ion battery and battery materials. a) Schematic of *in situ* XRF-STXM of a thick $LiFePO_4$ working electrode enclosed in liquid electrolyte and the geometry of the X-ray beam and the XRF detector; b) schematic of the electrochemical cell containing a $LiFePO_4$ working electrode, a Li counter electrode, and organic liquid electrolyte in a PEEK housing; c) state of charge (SOC) maps of three representative $LiFePO_4$ platelet particles as the electrode discharges at a rate of 0.2 C imaged with a 100 nm step size; adapted from literature with permission [96]. d) Schematic of *in situ* STXM of a thin electrochemical cell; the $LiFePO_4$/Au working electrode is placed in the sandwiched Si_3N_4 stack, and the Li foil counter/reference electrode is placed in a syringe outside of the chamber, connected ionically via the electrolyte tube and electronically via a potentiostat; the inset shows a cross-sectional view of the cell; e) operando Li composition frames of a single particle over multiple lithiation and delithiation cycles; adapted from literature with permission [99]. f) An *in situ* heating setup for STXM with dimensions of the heating holder (Norcada Inc.) and the heating microchip; adapted from literature with permission [101]; g) *in situ* STXM heating of Ni-rich NCM cathode materials at RT, 200, 400, 600, and 800 °C with acquisition of Ni, Co, and Mn L_3-edge spectra directly from the particles; adapted from literature with permission [102].

Figure 2.3.2 f shows *in situ* sample heating device in STXM, available at several synchrotron facilities [101-103]. The device is comprised of a TEM-based microelectromechanical system (MEMS) nanoreactor, housed in a custom-designed STXM

sample holder [101]. Figure 2.3.2 f also shows the nanoreactor microchip, which is functionalized with a microheater fabricated on an electron-transparent window with resistive heating up to 1100 ^{o}C and temperature measurement. Figure 2.3.2 g presents *in situ* heating of $Li_xNi_{0.88}Co_{0.08}Mn_{0.04}O_2$ (Ni-rich NCM) primary particles investigated by STXM XANES spectroscopy at the Ni, Co, and Mn L_3-edge from room temperature up to 800^{o}C. Reduction of Ni, Co and Mn upon heating along with strong changes in density distribution was clearly demonstrated *in situ*, which provided insight to the thermal runaway effect of cathode materials or assemblies.

2.3.2. BATTERY INTERFACIAL PHENOMENA STUDIED BY X-PEEM

Given the shallow penetration depth of soft X-rays, STXM operated in transmission mode requires advanced sample preparation techniques, such as FIB or ultramicrotomy, both of which may introduce sample damage or artefacts. To solve this problem, full-field view X-PEEM has been applied in investigating battery electrode interfaces including electrolyte additives in the formation of CEI, [69] ion and electron exchange among active particles [104]. Here we focus on its application in revealing the complex interfaces in overlithiated $LiCoO_2$ (LCO) composite electrodes [105], and *in situ* X-PEEM during electrode heating to investigate the surface/interface evolution during the LCO electrode thermal runaway [106].

Over-lithiation [107] can occur in LIB packs which will cause significant battery degradation, thus giving rise to severe safety issues. Therefore, it is necessary to understand the working mechanism of the electrode material in the over-discharge state for better battery tolerance. The capability in spatially resolving the interactions between components from the surface to the core in degraded porous composite Li-rich cathodes, especially correlating chemistry and electronic structure, is challenging but critical in better understanding of its complex degradation mechanism for rational developments.

As shown in Figure 2.3.3 a-i the surface phase heterogeneity and its correlation with the conductive carbon additive and the PVDF binder of the over-lithiated $LiCoO_2$ electrode was obtained by X-PEEM at the F, O K-edges and Co L-edge. Strikingly the mapping difference at O and Co hints a possible 3D heterogeneities in overlithiated LCO interface [106].

Figure 2.3.3 j-m present *in situ* X-PEEM of a LCO cathode under heating up to 210 ^{o}C in vacuum. The Co L-edge X-PEEM XANES spectroscopy and chemical imaging before and after heating show that Co reduction occurred on the LCO surface and the spatial variation of Co reduction was likely related to the CEI and additive materials, revealing some insightful information of the thermal runaway effect [107]. In addition to CEI investigations, X-PEEM has also been successfully applied in revealing the SEI heterogeneities in Si based anodes [86,108]. Finally, a correlative analysis of battery interfaces/surfaces has been performed through a combination of STXM and X-PEEM, highlighting the unique capabilities of each technique [105].

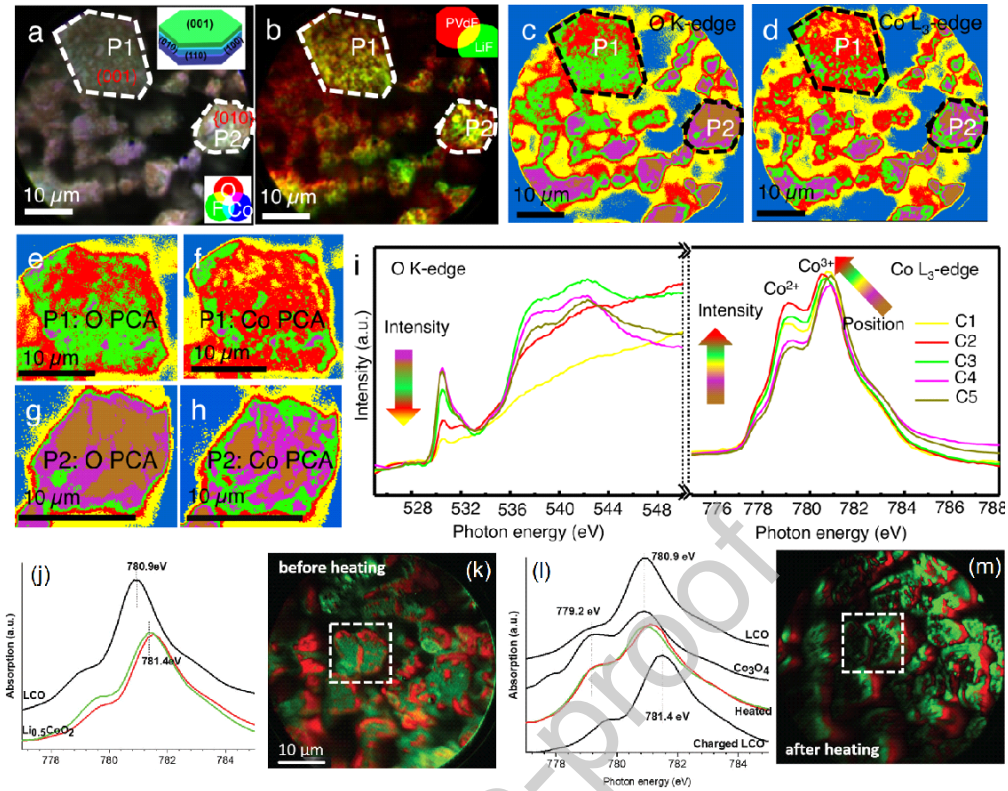

Figure 2.3.3. a) X-PEEM elemental composite mapping; b) chemical distribution of the F-containing compounds (PVDF and LiF); c) O K-edge PCA and d) Co L_3-edge PCA analysis of the D-0.0 V discharged LCO electrode; the magnified P1 (e, f) and P2 (g, h) regions in c) and d); i) O K-edge and Co L_3-edge XANES spectra extracted at various color regions from c) and d), with permission from Springer Nature [106]; j) Co L_3-edge XANES and k) phase distribution map of distinct phases in charged LCO; l) and m) for heated LCO by *in situ* X-PEEM. Adapted from the literature with permission [107].

2.3.3. FUTURE PERSPECTIVE

Synchrotron STXM has demonstrated powerful and versatile capabilities in characterizing battery materials and assemblies with a heterogeneous nature through high spatial-resolution, high chemical-sensitivity, highly quantitative, and non-destructive X-ray microscopy and spectroscopy, under *ex situ* or *in situ* conditions. With the forthcoming 4th generation diffraction-limited synchrotron radiation (DLSR) sources, which have superb beam coherence and brilliance, STXM-ptychography will be a dominant technique and have the full potential to achieve X-ray wavelength-limited high spatial resolution (i.e., 1 - 3 nm) at the soft X-ray energy range in 2D and 3D chemical imaging. Furthermore, beam flux and brilliance gain will largely extend beamline photon energy range together with new beamline optics and monochromator, thus drastically improving XRF and TEY detection sensitivity. The efforts toward the next-generation STXM will ensure the powerfulness, suitability, and uniqueness of the technique in understanding battery interfaces and electrode chemistry evolution under relevant conditions.

Synchrotron X-PEEM will also constantly improve to gain flux on sample, spatial resolution, and multifunctional capabilities including XPS imaging/spectroscopy and *in situ*, for battery research. Likewise, X-PEEM will also benefit significantly from a DLSR synchrotron source in the future. Specifically, the substantially increased beam flux and brilliance will significantly increase the yield of photoelectrons and secondary electrons, making X-PEEM have a much stronger signal to noise ratio for detection, particularly for the energy-filtered mode, i.e., XPS-PEEM. In addition, better quality and full coherence of the DLSR beam will further improve energy resolution of the monochromatic beam, in general, producing better controlled photoemission and resulting in much improved spatial resolution. Therefore, the overall performance, efficiency, and functionalities of X-PEEM will be largely improved on DLSR, making it an even more powerful tool in understanding battery electrode surface and interface chemistry and evolution, particularly advantageous for solid-state batteries.

2.4. X-RAY COMPUTED TOMOGRAPHY

The X-ray micro–Computed Tomography (microCT) technique is often highlighted for its capability to analyse extensive volumes, enabling comprehensive visualisation from the electrode and cell level up to the entire battery pack. Conversely, Transmission X-ray Microscopy (TXM) involves directing a precisely focused X-ray beam at a specimen, with subsequent measurement of the transmitted X-ray energies and intensities based on their position. TXM is distinguished by its high penetration power, facilitating the analysis of internal material structures. Notably, this technique achieves a spatial resolution below 50 nanometers, thereby granting access to nano-scale properties with a high degree of reliability. The application of TXM CT is contingent on a delicate balance between spatial resolution and probed volume. For instance, in achieving representativeness of an entire structure, one must carefully navigate the trade-off between obtaining suitable resolution and ensuring the analysis covers sufficiently large volumes, *i.e.* representativeness. Most TXM CT experiments rely on attenuation contrast, a phenomenon that increases with the density of materials or the atomic number of elements involved. This reliance underscores the importance of understanding the materials' composition, as it directly influences the efficacy and accuracy of the imaging results.

2.4.1. XCT EXPERIMENTAL APPROACH

The microCT technique employs parallel X-ray beams which pass through the rotating object at right angles and are subsequently captured by the X-ray detector. Subsequently, a collection of 2D cross-sectional image projections from various angles are acquired, which serve as the basis for 3D reconstruction, as depicted in Figure 2.4.1 a. This technology primarily relies on attenuation, which is related to the density and the composition of the physical objects and is inversely proportional to the contrast of the resulting image. The X-ray can be generated using either a lab based XCT instrument or synchrotron sources. Notably, synchrotron radiation as an X-ray source boasts superior brightness, surpassing several energy levels, providing a high coherent beam, and offering enhanced collimation. The X-ray energy used in XCT ranges from low energy (from 8 to 25 keV) to high energy (from 80 to 120 keV), varying depending on the sample thickness and objectives of the analysis, as well as the nature of the materials being studied. This

facilitates the discernment of subtle internal structural changes, thereby streamlining the reconstruction process.

These two main modes offer specific field of views and spatial resolution characteristics. For spatial resolution, it is needed at least 2 voxels to distinguish a feature in the image, so spatial resolution is 20 nm in an example of one voxel size of 10 nm. MicroCT usually has a typical field of view ranging from 1 mm to 1 cm with the spatial resolution generally in the range of 0.3 µm to 5 µm. MicroCT is well-suited for the imaging of larger objects where the measurement of internal structures and compositions of objects with dimensions ranging from millimetres to centimetres is required. NanoCT achieved a minimum resolution of approximately 25 nm, further advancing to 14.6 nm with the application of X-ray ptychography technique [109], usually ranging from 25 nm to 120 nm. The field of view of NanoCT spans 30 µm to 100 µm, making it significantly smaller than in microCT. It employs a convergent beam configuration, wherein the X-ray beam is focused and converges to a point, enabling the capture of high-resolution images. NanoCT is employed to examine intricate details and characteristics within a sample. It holds particular significance in the fields of materials science where the imaging and analysis of nanoscale structures and materials are essential. These technologies allow for *in situ*, *ex situ*, and *operando* experiments. In instances where electrode samples surpass the field of view, pre-treatment becomes imperative; commonly achieved through milling with a focused ion beam or laser. Notably, *operando* experiments utilise optimised coin cells featuring transparent windows made of low-absorption materials such as polyether ketone, polyimide, glassy carbon, and beryllium [110]. Some sample holders and setups used in the experiments are demonstrated in Figure 2.4.1 b-d. The total acquisition time hinges on variables such as the number of images and exposure time for acquiring an image, which is X-ray source and resolution related and spans from tens of seconds to several hours. This intricate interplay of factors underscores the dynamic nature of XCT experiments and their versatility in probing the internal intricacies of diverse materials.

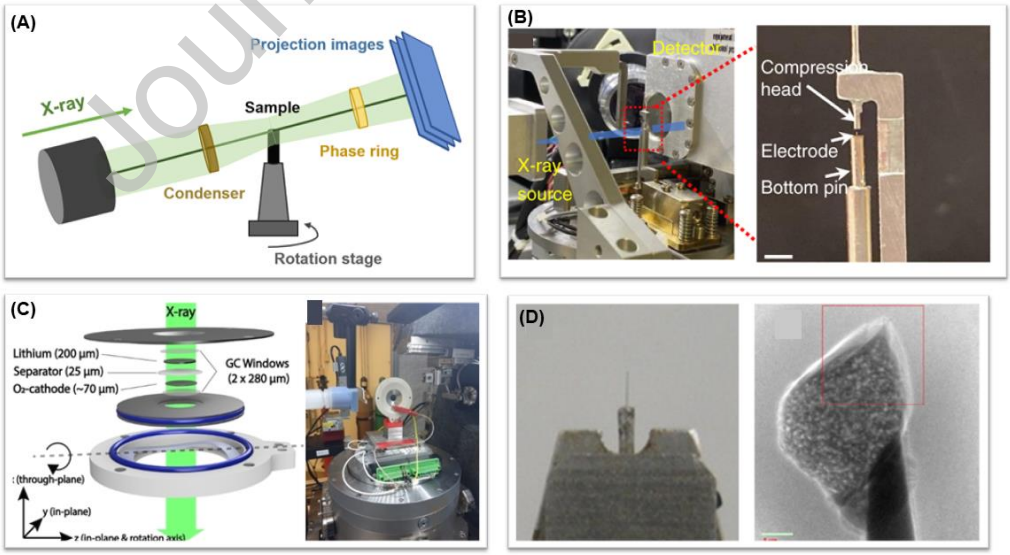

Figure 2.4.1: a) Schematic diagram of the X-ray CT principle; b) left: experimental setup for the X-ray nano-CT; right: magnified image showing the details of the alignment.[111]; c) left: a sketch of the cell for *operando* experiment; right: image of the cell seated and connected to the rotation stage [110]; d) left: A SOFC sample inserted in X-ray sample holder; right: X-ray transmission micrograph of the sample [112].

Typical data processing generally goes through image filtering, reconstruction, noise reduction, segmentation, and analysis. Image filtering is frequently the first step in reconstruction to address motion artefacts induced by movement, tilt, or volume changes in the active material during the measurement. The 3D reconstruction is usually conducted by a filtered back projection algorithm, which is available via commercial software. To visualise the electrode microstructure, a key strategy involves leveraging the disparities in absorbance among different phases. This principle enables the differentiation of distinct phases within the sample. A straightforward yet effective method for this purpose is the application of a simple threshold segmentation method based on the well-separated grey values histogram peaks to discern between the high absorption phase, typically associated with the active material, and the low absorption phase, encompassing components such as conductive carbon, pores, polymer binders, or non-evaporated electrolyte residues. The subsequent step involves the utilisation of image processing software for volume-based 3D microstructure visualisation and analysis. This software essentially allows for a comprehensive exploration of the intricacies within the reconstructed volume, facilitating a detailed understanding of the distribution and characteristics of different components.

2.4.2. BATTERY INTERFACIAL PHENOMENA STUDIED BY XCT

The microstructure datasets can be used to investigate and quantitatively study electrode properties such as porosity, tortuosity, specific reaction area, anisotropy, and homogeneity. Such work has been used on materials like graphite [113-115], $LiNi_xMn_yCo_{1-x-y}O_2$ (NMC) [114,116,117], $LiFePO_4$ (LFP) [118], and $LiCoO_2$ (LCO) [114,119] for lab-prepared and commercial lithium-ion batteries (LIBs), and electrodes like $(La_{0.7}Sr_{0.3})_{0.9}MnO_{3\pm\delta}$(LSM) and yttria-stabilized zirconia (YSZ) [112,120,121] for solid oxide fuel cells (SOFC), even under different temperatures, as shown in Figure 2.4.2 a-b. Microstructure extraction by using XCT and analysis has also been applied for polymer electrolyte membrane fuel cells (PEMFCs) [122], redox flow batteries (RFB) [123], and all solid state batteries (ASSBs) [124,125], as shown in Figure 2.4.2 c-e.

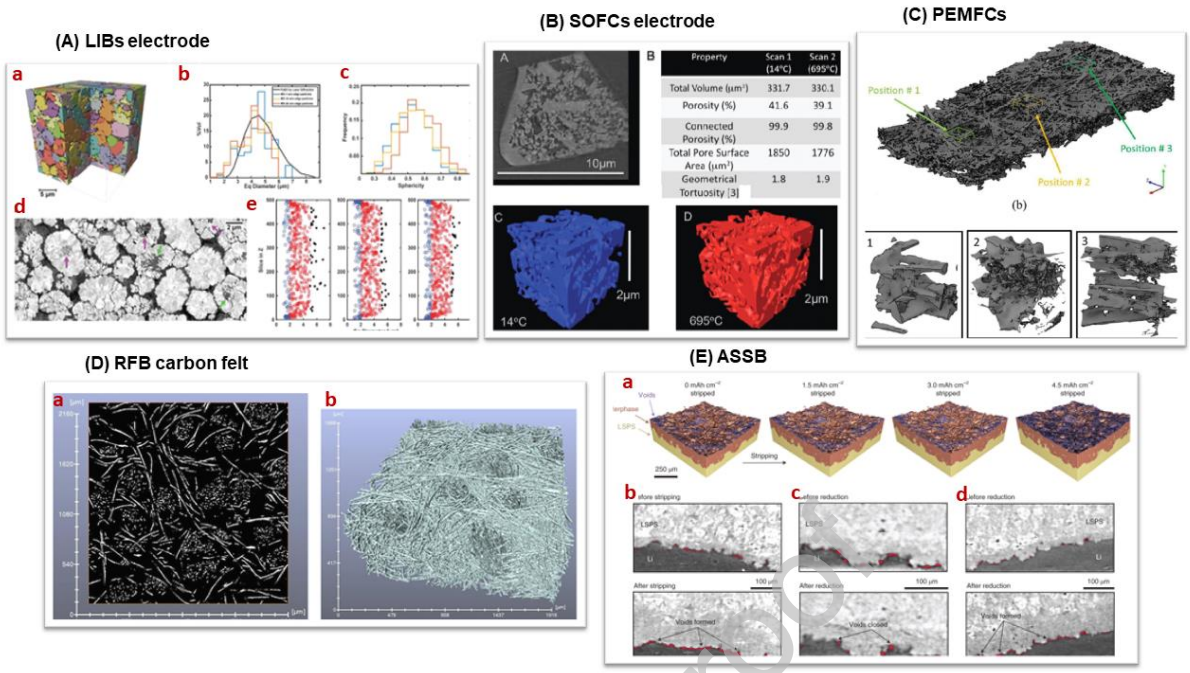

Figure 2.4.2: a) Morphology of the NMC phase in electrode (a) 3D volume with individual particles labelled; (b) Particle size distribution in the volume; (c) distribution of sphericity of NMC; (d) cross-section of the sample; (e) Spatial repartition of the NMC particles in the three samples in the direction normal to the current collector [126]; b) (a) Individual tomogram from the high temperature tomography sequence; (b) Material properties for full tomography data; (c) 3D rendering of selected region of interest from low temperature scan; (d) 3D rendering of same region of interest at high temperature [127]; c) 3D rendered image from XCT of gas diffusion layer. Locations 1, 2 and 3 were selected for water breakthrough predictions [122]; d) (a) Binary image of carbon felt from XCT data and (b) reconstructed 3D carbon felt model [123]; e) (a) Three-dimensional segmented renderings of the Li/LSPS interface at different times during stripping at 1 mA cm^{-2}. The renderings show the voids (purple), the interphase (red) and LSPS (yellow). 2D cross-sectional images of the Li/LSPS interface before (top) and after (bottom) (b) stripping at 1 mA cm^{-2}; (c) reduction at 4 mA cm^{-2}; (d) reduction at 1 mA cm^{-2} [128].

XCT allows for the tracking of the electrode size, shape, and network morphology changes like active material cracking and irreversible deformation due to mechanical factors during or after the manufacturing process [129]. Also, the (de)lithiation, volume expansion and the growth of passivation films in cycling [130-134] can be explored, such as the formation of solid electrolyte interphase (SEI) deposits [135], and silicon anode degradation [136].

The realistic geometries of the electrode can be extracted and are used for 3D manufacturing simulation to predict electrode microstructure [137,138], or liquid infiltration [122,139] and electrochemical simulations to forecast the distribution of the physical and electrochemical properties in the electrode [118,129,140]. The XCT can also be applied on all solid state batteries (ASSB) to monitor the lithium dendrite growth and separator rupture during the manufacturing and battery cycling [128].

XCT techniques is used on solid phases and the main challenges currently facing in resolving low absorbing phases and physical objects smaller than the minimum resolution size, as well as post-processing of large data sets. Due to the nano features and the similarity in attenuation contrast between void and light elements such as carbon, there is a limitation in capture and segmentation. The XCT coupled with Zernike phase contrast has been reported to better image the separate phases for LCO [136] and some light active material such as Li_2O_2 in Li–O_2 batteries [141]. Some other technologies such as holographic [126] and virtual design [142] are used in conjunction to extract the carbon and polymer phases. The technique of combining separate scans of high-attenuating active material and low-attenuating carbon and binder is reported to reconstruct the 3D electrode including microstructural heterogeneities at the nanoscale [111]. Machine learning and deep learning approaches have been developed in this field for post-treat the dataset to help improve the segmentation for different phases to obtain more accurate 3D structures [143] and labelling the individual particles to quantify and classify the flaws and microstructural evolution in uncycled and cycled electrode [144,145]. It has also been reported that machine learning can help with imaging and tracking phase interfaces in massive amounts of data [146].

2.4.3. FUTURE PERSPECTIVE

While the current state of technological development has enabled XCT technology to exhibit commendable performance in the analysis of solid materials, particularly in the context of batteries, there remains untapped potential for further enhancement. A critical area for improvement lies in refining the resolution and expanding the field of view, a pursuit that promises to augment our ability to scrutinise composite materials with both nano and micron features through nano-CT. Also, reducing the artefacts generated during experiments is paramount. Efforts to minimise these artefacts not only alleviate the complexities associated with data post-processing but also contribute to improving the accuracy of results. In addition, the development of more efficient and accurate data processing algorithms stands out as a key enabler for advancing XCT technique in the realm of solid materials. The development of sophisticated algorithms is poised to streamline the data analysis process, leading to enhanced insights into material structures and properties. This, in turn, will fortify the capabilities of XCT technology, allowing it to unravel the intricacies of solid materials more effectively, including those integral to the functioning of batteries.

2.5. RAMAN SPECTROSCOPY AND SIGNAL ENHANCEMENT TECHNIQUE

Infrared vibrational spectroscopy (Attenuated Total Reflectance ATR Fourier Transform Infrared spectroscopy ATR-FTIR and its surface-enhanced declination ATR-SEIRAS) has been long use to characterize battery materials [147]. Recent developments such as IR fiber evanescent wave spectroscopy FEWS [148] and also second-order nonlinear optics (vibrational sum-frequency generation: SFG) [147,149] represent interesting research directions. However, the lack of spatial information (no coupling with optical microscopy under operando conditions) and the technical constraints related to the spectro-cell design (e.g. strong IR absorption of LIB baseline electrolytes, difficult optical coupling for SFG) are severe bottlenecks for the development of these techniques.

Among benchtop spectroscopies, the emergence of Raman spectroscopy for *in situ* characterizations in the last two decades, especially when coupled to optical microscopy (Raman microscopy: *μRaman*), is spectacular. Raman spectroscopy first described in 1928 by Raman and Krishnan [150], relies on the elastic (Rayleigh) and inelastic (Stokes and Anti-Stokes) scattering of light upon illumination of a sample with a monochromatic excitation source (ultraviolet, visible or infrared laser sources). As a vibrational spectroscopy, its spectral signatures are indicative of oxidation state, chemical environment, crystal phase and solvation effects, while the Stokes/Anti-Stokes signal ratio is indicative of local temperature. The non-invasive sampling process, the possibility to work in aqueous solutions (weak scattering signal of water), the relatively high temporal (collection time ~ 1 s on dispersive Raman spectrometers equipped with CCD detectors) and the spatial resolution of surface chemical mapping (depth and lateral resolution diffraction limited ~ 1 μm) explain this burst of interest among the material science community. The ease in characterizing solvent mixtures, or anode and cathode materials in contact with carbonate organic electrolytes has made Raman extremely popular in the energy storage community [151]. Raman spectroscopy however shows two major limitations:

- It is intrinsically not sensitive (about one Raman photon per ten million incident photons), as the Raman effect seems to have the lowest effective cross-section among optical spectroscopies (i.e. the efficiency of the scattering process for a specific incident energy and a given normal mode of vibration, expressed in cm^2). The lack of sensitivity can be compensated by the energy of excitation source, within the limit of the material stability under irradiation (beam-induced damages). Thin interfacial layers like the SEI in LIBs, which are made of materials with low cross section for Raman scattering, are not detectable by standard μRaman.
- Competing background fluorescence signals can obscure the Raman signatures (e.g. the strong fluorescence of Li-ion battery electrolytes). The choice of Raman probe (excitation wavelength, λexc, of the laser source) is therefore critical. For example, the use of infrared or near-infrared Raman probes generally minimizes the fluorescence signal, but also results in a lower intensity of the Raman signal as compared to visible excitation (the intensity of the scattered light scales with $1/\lambda exc4$).

The introduction of Surface Enhanced Raman Spectroscopy (SERS) in the early 70's [152], which circumvented the poor sensitivity of Raman spectroscopy and brought the detection threshold of Raman spectroscopy down to the molecular level, constitutes a major breakthrough. This review covers the application of enhanced Raman spectroscopies for the *in situ/operando* characterization of interfacial processes taking place in operating batteries, mostly LIBs, as studies on Li-metal [153,154] and Li-air [155-157] batteries are scarce and as SERS studies on Na-ion are yet to be published.

2.5.1. SURFACE ENHANCED RAMAN SPECTROSCOPY

2.5.1.1. EXPERIMENTAL APPROACHES

SERS exploits the signal enhancement properties of roughened metal substrates or single metal nano-objects, in solution (colloids) or on the surface of a substrate illuminated by (visible) light sources of any analyte in close proximity (~ 20 nm). Although the phenomena behind Raman signal enhancement are still debated within the community, it is accepted that the different contributions involved in the amplification process can be grouped into two categories: electromagnetic effects (localized surface plasmon resonance LSPR with enhancement factor EF ~ 10^5-10^9) and chemical effects (e.g. charge transfer between the analyte and the metal EF ~ 10^3). Gold, silver and copper, are known materials with LSPR in the visible and are therefore ideal for SERS applications. The development of operando characterization of the battery interface through SERS face several challenges:

- The difficulty in SERS to extract the signal from an interface/interphase, especially under in situ conditions, given the strong signal contribution from both the electrode material and the electrolyte (superposition of the amplified signal: near-field / SERS signal and of the non-amplified signals: far-field or µRaman signal)
- The importance of achieving the plasmon resonance conditions (of the SERS platform) at the selected Raman probe, i.e. the one that provides the highest Raman to fluorescence signal ratio for a given system under study. The plasmon resonance can be tuned, as it depends on the size, shape and composition of the metallic nanostructures, on the nature of the surrounding medium [158],[159] and also on the occurrence of optical coupling between individual nanostructures known as plasmonic junctions or "hot spots". At these special coupling points, the Raman scattering enhancement factor can be increased by several orders of magnitude [160].
- The rapid degradation of the SERS activity of silver and copper platforms when exposed to ambient conditions (formation of silver sulfide, copper oxide surface layers) [161].
- The difficult spectral interpretation (activation of forbidden Raman modes [162] upon direct interaction between the SERS platform and the analyte, light-induced electron transfer [163], photo-thermal reactions…).

Using SERS-active electrode materials (gold or silver), or thin films of electrode materials deposited on SERS-active substrates, thin interfacial layers such as SEI made of low cross section materials, which are usually not detectable by µRaman, could be studied *in situ/operando*.

2.5.1.2. BATTERY INTERFACIAL PHENOMENA STUDIED BY SERS

Two *ex situ* studies from Huang's group on SERS-active Ag surfaces (nanoscale roughening of Ag foil upon lithium, λ_{exc} = 514 & 633 nm) cycled down to at 0.0 V vs Li/Li^+ revealed the presence of Li_2CO_3 and LiOH in 1 M $LiPF_6$ EC/DEC [164], while alkyl carbonates $ROCO_2Li$ were identified in 1 M $LiClO_4$ PC/DMC [165]. An *in situ* study by Mozhzhukhina et al. [166] then revealed compositional variations at the interface (Li_2CO_3 at ~1.8 V vs Li/Li^+) between a polarized roughened gold electrode (potentiostatic steps 3.0 to 0.5 V) and a LIB electrolyte (LP40 EC/DEC 1M $LiPF_6$). They also observed a potential-dependent growth of the EC/Li^+ peaks during negative polarization of the gold electrode, which they explained by the charging of the electric double-layer and

accumulation of Li^+ and solvating EC at the SERS substrate surface (see Figure 2.5.4 g). These studies, which demonstrated the possibility of extracting the chemical signature of an SEI by SERS, are however of limited impact due to the limited applicability of gold [167] and silver materials to LIB technology.

The formation of a CEI on positive composite NMC electrodes ($LiNi_{0.33}Co_{0.33}Mn_{0.33}O_2$) decorated with gold nanoparticles and polarized between 3 and 4.5 V versus lithium was studied by Chen et al. [168] in 2020. The authors were able to highlight a fluctuation/dynamic intensity of the Raman signal at the interface, which was interpreted by the formation and dissolution of species on the electrode surface upon cycling (Figure 2.5.4 d). The exact nature of the compounds formed (polymer chains containing ester and ether groups) was not revealed. The authors extended their conclusion by demonstrating that no variation in interfacial composition could be observed in "classical" micro-Raman on the undecorated electrodes. Another strategy, developed by Piernas-Muñoz in 2021, [169] consisted of the electrodeposition of gold on the electrode material (silicon anode) revealing that after cycling in 1.2 M $LiPF_6$ EC/EMC (3/7), SEI components such as Li_xSiO_y, Li_2CO_3, alkyl carbonates and olefins or organophosphate-based compounds were present. The use of bare gold nanoparticles in those two studies is open to criticism as the observed processes probed are those taking place on the surface of the gold objects (in electrical contact with the electrode) rather than those at play on the surface of the NMC or silicon material.

SERS electrode coated with the active material - An elegant approach developed by Ha et al. [170] in 2020 consisted in using a SERS active roughened copper mesh onto which a ~ 30 nm silicon thin film had been deposited (see Figure 2.5.4 f). These measurements, carried out *in situ* using a 633 nm Raman probe, allowed the authors to conclude that alkyl carboxylates and lithium propionate were formed on the silicon surface. If the range of material studiable by SERS can be extended beyond Au, Ag and Cu through this expedient, only thin layers of active material can be studied without compromising the enhancement process of the underlying SERS active electrodes. SHINERS, described hereafter, circumvents this limitation.

2.5.2. TIP ENHANCED RAMAN SPECTROSCOPY

The association of scanning probe microscopy techniques (SPM: Atomic Force Microscopy AFM and Scanning Tunnelling Microscopy STM) with signal enhancement processes (SERS-active SPM probes) laid the foundation for the introduction of Tip-Enhanced Raman Spectroscopy (TERS). The strong signal enhancement at the tip-sample junction in TERS allows chemical analysis and composition imaging far below the diffraction limit of optical microscopies, down to a few nanometers (*nanoRaman*). The difficult optical coupling of the nanoprobe and of the excitation source (laser) in liquids (distortion of the optical path at the air/liquid interface), and control of the atmosphere has however restrained the application of TERS to only *ex situ* characterizations of battery materials[171,172], although some groups are actively working on *in situ* implementations (Harvestore European project IREC, Spain). Note that similar optical coupling and nano-resolved composition imaging can be achieved with IR spectroscopy (scattering in s-NSOM [173] or photothermal sample expansion in AFM-IR [174]). IR signal absorption of most solvents and difficult optical coupling in liquid has also limited

the use of nanoIR to *ex situ* diagnoses of energy materials (e.g. phase distribution in Li_xFePO_4 micron-size crystals [175], SEI composition imaging [176,177].

2.5.3. SHELL-ISOLATED NANOPARTICLE ENHANCED RAMAN SPECTROSCOPY

2.5.3.1. EXPERIMENTAL APPROACHES

The SHINERS technique introduced in 2010 (Tian's group, Xiamen [178]), a declination of SERS which uses plasmonic nanoparticles as signal amplifier deposited on any substrate (Shell-isolated nanoparticles: SHINs) has broadened the range of studiable electrode materials beyond gold, silver and copper. The specificity of SHINERS, among SERS-active platforms, lays in the (electro)chemical inertia of the SHINs thanks to the thin shell (~5 nm thick oxide shell: Al_2O_3, SiO_2, TiO_2 but also MnO_2, ZrO_2, carbon and polymer layers, see Figure 2.5.1 e) surrounding the plasmonic material core (reactive metal ~ 50 nm diameter), limiting the chemical interference of the chemical probe with the studied system (electro-chemical reactivity of the metal core, direct metal-molecule interaction activating Raman forbidden modes).

Note that SHINERS, similarly to SERS, relies on a near-field interaction between the plasmonic amplifiers and the compounds at their immediate vicinity providing a submicron depth resolution (~ 20 nm due to the exponential decay of the enhancement with the distance to the particles, see Figure 2.5.1 f). However, lateral resolution is still diffraction limited (to ~ 1 µm) when using confocal microscopes.

Although already largely employed for *in situ* measurements in catalysis [178], the implementation of SHINERS on energy materials is still limited to a handful of research groups worldwide. SHINERS has been so far implemented on Li-air battery materials [157] and on LIB materials (e.g. silicon [179] and tin and gold [180] and $Zn_{0.9}Fe_{0.1}O$ [181] negative electrodes, layered (Li-rich [182], NMC [183-185]) and spinel (LNMO [186]) materials for positive electrode, organic cathode LIB [187]) and on Li-S batteries [188].

The extreme sensitivity of SHINERS was demonstrated through the extraction of the interfacial compositions and their dynamics under *in situ* and *operando* conditions. *In situ* implementation of SHINERS on energy materials has also brought up new challenges as (a) LIB-electrolyte strong fluorescence excitation with non-suitable SHINERS probes, (b) possible interference of the probe with the studied system (photo-thermal damages), (c) alteration of interfacial properties in spectro-cell filled with large volume of electrolyte (see Figures 2.5.3 d & e) (d) the possible metal-oxide shell instability in aged $LiPF_6$ based electrolyte and (e) the lack of Raman reference spectra of the SEI constitutive components to interpret the chemical signatures. All of these can be invoked as possible weak points in some of the most recent studies found in the literature.

2.5.3.2. BATTERY INTERFACIAL PHENOMENA STUDIED BY SHINERS

While the analytical potential of the SHINERS method has been exploited in many fields, notably in catalysis [189,190], to extract the composition of electrode/electrolyte interfaces under *in situ / operando* conditions, very few studies have been conducted on battery materials in operation, even less on LIBs. Only five studies related to the composition of passive layers formed in LIB conditions have been published so far. The

first "SEI" studies were reported as early as 2014 by Hwang 's group [179], then by Hardwick's group [181] in 2019 and Lucas's group [180] in 2021, while "CEI" studies were first published in 2014 by Hwang 's group [182] and then in 2020 by Tian's group [183] and then in 2023 by Baghernejad's group [185].

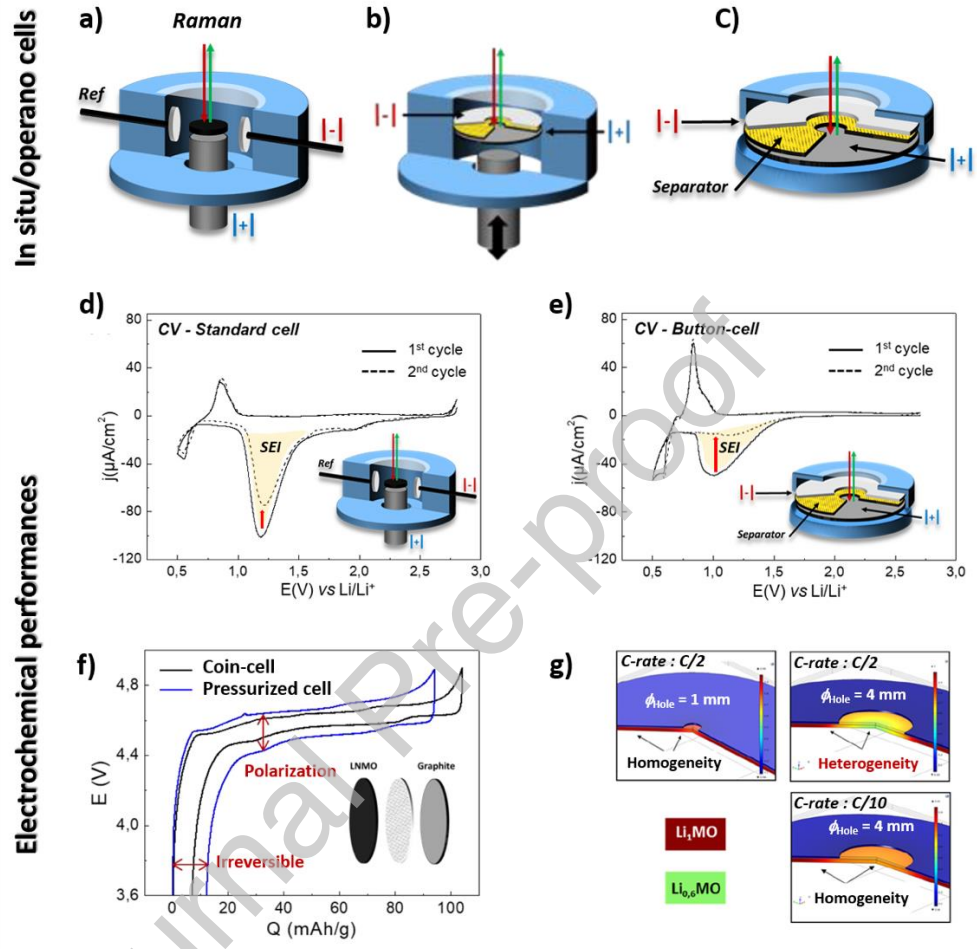

Figure 2.5.3. Different designs of custom-made *in situ / operando* Raman spectro-electrochemical half-cells with quartz windows: a) beaker cell with large volume of electrolyte (Li metal counter and reference electrode) ; b) pressurized cell with two possible configurations (not represented) enabling to observed the bottom electrode through holes in top electrode and separator (or the back of the top electrode through a metal mesh used as electrical contact – not represented) ; c) coin-cell like spectro-cell. Spectro-electrochemical cell performances: d) & e) Electrochemical response (2 successive CVs at 1 mV/s) of a tin electrode (vs lithium) in contact with large (beaker cell) and small volume (coin-cell) of LIB electrolyte (1.2 M $LiPF_6$ EC/EMC 30/70 (v/v) respectively, passivation of the electrode is achieved after one CV cycle in coin-cell ; f) C/10 cycling (second cycle 187 µA/cm^2 between 3.5 and 4.9 V) of composite positive LNMO / graphite assemblies in coin-cell and pressurized cells filled with LIB electrolyte (1.2 M $LiPF_6$ EC/EMC=30/70 (v/v)) ; g) lithiation distribution in positive electrode (LMO) as a function of the c-rate and of hole size in the graphite counter-electrode (Numerical simulations - Comsol Mutiphysics). Figures (a), (c) and (d) adapted with permission from [180]. Figures (b), (f) and (g) [186].

One recurrent question concerns the effectiveness of the thin shell protection against electron transfer to the metal core (via tunnelling effect for instance) and its stability/reactivity. Beside microscopic observations confirming the homogeneous coverage of metal particles, different tests have been proposed and commonly used in the community to assess the electrochemical inertia of SHINs (oxidation of SHINs at a glassy carbon electrode in acidic medium) and the presence of discontinuities (pinhole) in the protective oxide layer (surface contamination upon contact with pyridine) as described in Figure 2.5.1 g and h. If the stability of the oxide shell in aged LIB electrolyte (generation of HF in $LiPF_6$ based electrolyte, or direct lithiation of SiO_x compounds in the particle shell) can indeed be questioned, Gajan et al. [180] have evidenced different SEI responses on tin and gold electrodes in carbonate-based electrolyte, confirming that the gold core of $Au@SiO_2$ SHINs was not exposed nor that the silica shell had reacted. This is further supported by post-mortem microscopy analyses of cycled electrodes, showing the SHINs not covered with foreign material but "floating" on the SEI.

Most *operando* studies, i.e. microscopies, spectroscopies, gravimetry, are carried out in simple 2 or 3 electrode cells with quartz windows whose design is dictated by the constraints of the analytical techniques. Different cell designs were employed in SHINERS studies applied to LIBs, a "beaker cell" with large volume of electrolyte (see Figure 2.5.3 a & b), pressurized cells (using a piston or a spring or a combination of the two) or coin-cells with minimal volumes of electrolyte. Within these two latter configurations, the analyses can be made on the back side of the electrode positioned right below the window (a metal mesh used as electrode electrical contact is usually sandwiched between the window and the electrode) or at the surface of the bottom electrode providing that both separator and top electrodes are pierced.

Possible air contamination, non-optimized distribution of current lines (counter and reference electrodes positioning) and large volumes of electrolyte within such cell designs may impact the reliability of the analysis. This is particularly true for high-energy storage systems like LIBs in which the "filming" properties of the electrodes (passive layer formation: SEI, CEI) critically depends on both the volume and quality of the electrolyte (moisture and oxygen free) as evidenced on Figure 2.5.3 d & e depicting the electrochemical behavior of a tin foil electrode in two home-made spectro-electrochemical cells filled with, respectively, 1 mL and 60 µL of an EC-EMC-$LiPF_6$ electrolyte mixture. Tin anode passivation in larger volume cells is delayed (partial SEI dissolution) while surface passivation is achieved after the first cyclic voltammetry (CV) cycle in the small volume cell. Depending on the cell design, high current densities can be associated with large ohmic drops (contact and electrolyte ohmic resistance) as illustrated in Figure 2.5.3 f & g. Lithiation distribution on positive electrodes (LMO) can be highly inhomogeneous in *operando* cells depending on the C-rate and for the specific case of coin-cell like spectro-cells, on the hole-size in the counter-electrode.

Similarly to electron and X-ray microscopies/spectroscopies, the irradiance of the system under study with highly energetic visible photons in Raman (i.e. the dose) can induce damages, through direct or indirect effects. Photo-thermal degradation of the electrolyte can generate side products which the chemical signatures can be misinterpreted with those of the SEI. This was evidenced by Gajan et al. in 2021, who monitored the influence

of laser irradiation (785 nm Raman probe at different laser power exposure time) on the electrolyte degradation in close vicinity of the SHINs. [180]

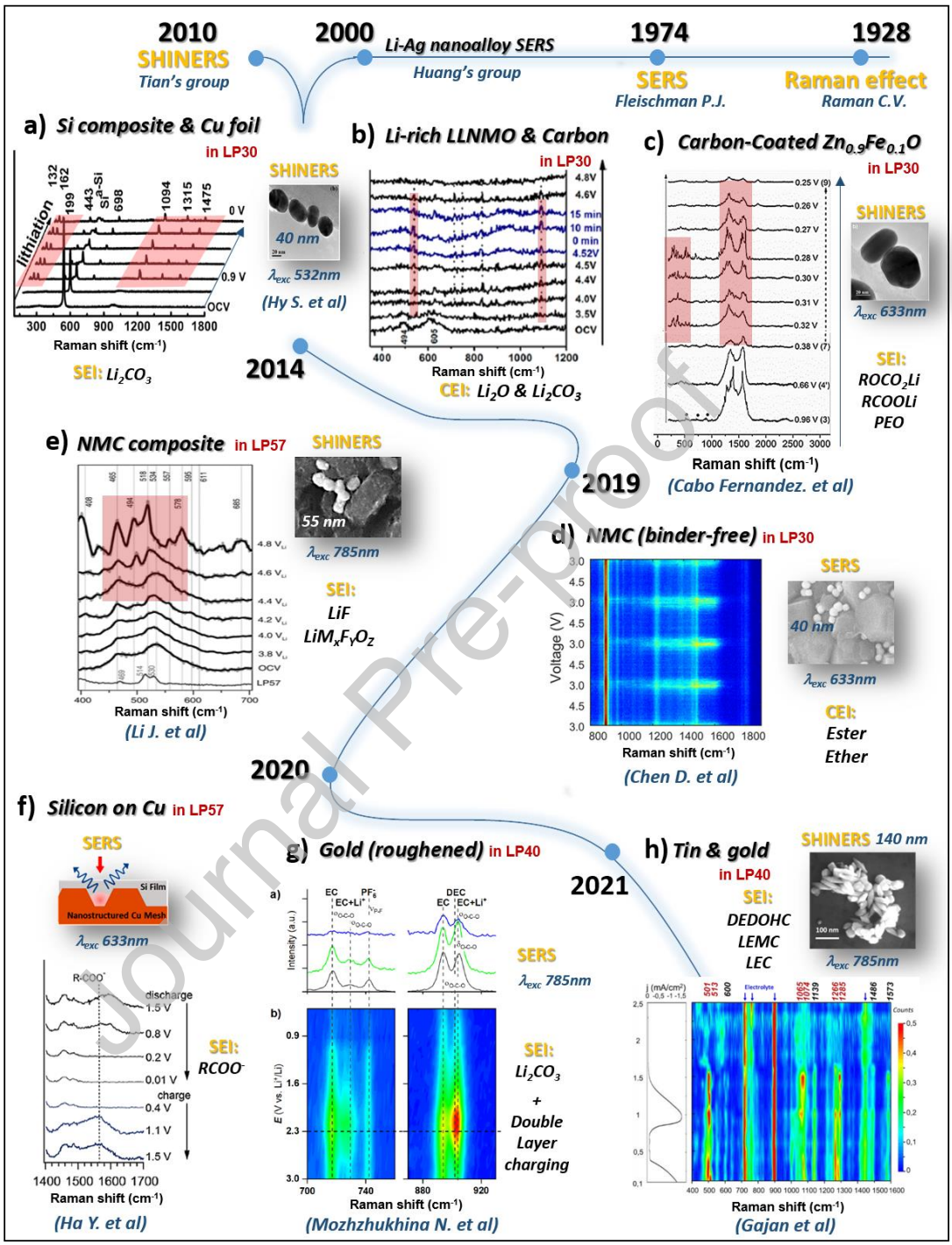

Figure 2.5.4. SERS & SHINERS *in situ / operando* characterization of interfacial processes in LIBs: a) SHINERS study ($Au@SiO_2$ nanospheres) on silicon/C composite negative electrode [179]; b) SHINERS study ($Au@SiO_2$ nanospheres) on Li-rich composite positive electrode [182]; c) SHINERS study ($Au@SiO_2$ nanospheres) on $Zn_{0.9}Fe_{0.1}O$ negative electrode [181]; d) SERS study (gold nanocubes) on ($LiNi_{1/3}Mn_{1/3}Co_{1/3}O_2$) (NMC 111) [168]; e) SHINERS study ($Au@SiO_2$ nanospheres) on ($LiNi_{0.8}Mn_{0.1}Co_{0.1}O_2$) NMC811 and

NMC111 composite (Carbon - PVdF) électrodes [183]; f) SERS study on copper-coated silicon thin film electrodes [170]; g) SERS study on roughened gold electrodes [166]; h) SHINERS study (Au@SiO_2 nanobipyramids) on tin foil and gold thin film electrodes [180]. Electrolyte compositions: LP30 (1M $LiPF_6$ in EC/DMC in a weight ratio of 1:1), LP 40 (1M $LiPF_6$ in EC/DEC in 1:1), LP57 (1 M $LiPF_6$ in EC/EMC a weight ratio of 3:7).

Strong modification of the Raman electrolyte signature (EC DEC $LiPF_6$) was observed at higher laser power (≈ 2 mW/μm^2) at exposure time as short as 1 second. This problem can be mitigated by using a scanning photon beam (similar to a scanning TEM), which allows the photon dose per unit area to be significantly reduced while maintaining high levels of Raman signals, leaving the electrolyte signature intact, even after prolonged exposure to laser power in the milliwatt range. Note that the combined effect of irradiance and potential on SHIN decorated electrodes can be also detrimental, as evidenced by Gajan et al. on high-voltage cathode material where fluctuation of spectral signatures above 4.6 V were indicative of damages [186].

2.5.3.3. INTERFACIAL COMPOSITION STUDIED BY SHINERS

The first study reported by Hwang's group [179] was carried out on a composite silicon electrode and also on a copper foil (lithium counter electrode, 1 M $LiPF_6$ electrolyte in EC/DEC 50/50 (v/v), half-cell 2032 coin cell-type battery spectro-cell) decorated with spherical Au@SiO_2 SHINs of an average diameter of 40 nm using a Raman probe at 532 nm. In particular, the authors report, under *in situ* conditions, the formation of lithium carbonates (Li_2CO_3, 1091 cm^{-1}) upon polarization of the silicon electrode at 0.05 V versus Li/Li^+ (Figure 2.5.4 a). Using an electrolyte containing 2% vinylene carbonate (VC), the authors observed an extra peak at 1000 cm^{-1} that they interpreted as the signature of polymerization products of VC (R-O and C-C stretching modes of semi-carbonates). The absence of fluorescence background in the spectra and the absence of a carbon signature (10% by mass, bands expected at 1350 and 1580 cm^{-1}) although recorded with at 532 nm Raman probe (significant auto-fluorescence of LIB electrolytes expected at this wavelength) [180], together with the dominating Raman signature of the Li_2CO_3 signal as early as 0.9 V vs. Li/Li^+ during the first silicon charge, seem however surprising. Although lithium carbonate was reported by IR spectroscopy by Nie et al. [191] on silicon after 20 cycles carried out at a C/5 regime, its detection at the end of a single cycle could reflect contamination of the system during the measurement (oxygen, water). Moreover, no information is provided on the delicate implementation of SHINERS on porous composite electrodes (difficulty of detecting plasmonic amplifiers "buried" in the porosity of the electrode).

Note that Hwang's group published concomitantly with their first report of the SEI on Si, a SHINERS study on positive electrodes [182] made of Li-rich layered materials describing also the interfacial signatures of composite mesocarbon microbead (MCMB) negative electrode (carbon and PVdF) in contact with EC/DEC 1 $LiPF_6$ electrolyte. Together with the evolution of the D and G band of disordered graphite during Li insertion and extraction, they reported the formation of Li_2CO_3 (MCMB/ Li_2MnO_3 and MCMB full cells/$Li_{1.2}Ni_{0.2}Mn_{0.6}O_2$ and of LiOH above 4V and 4.8 V (end of the charge), respectively.

The following "SEI'' study [181] carried out in 2019 on a Fe-doped ZnO electrode ($Zn_{0.9}Fe_{0.1}O$) coated with carbon and then decorated with 50 nm diameter SHINs (633 nm Raman probe) revealed under *in situ* conditions the formation of polyethylene oxide (PEO) and lithium alkyls of the types $ROCO_2Li$, RCOOLi, ROLi and $(CH_2OCO_2Li)_2$ upon reduction of the electrolyte between 2.7 and 0.0 V vs Li/Li^+ (see Figure 2.5.4 c). The experimental conditions associated with the data presented in this article seem to be more conducive to the detection of a change in the composition of the electrode/electrolyte interface (exciter at 633 nm and image of the SHINs deposits on the surface of the electrodes in particular) than in the previously cited article.

Gajan et al. in 2021 proposed a SHINERS study [180] of pure tin (foil) and gold (thin film) negative electrodes in contact with various electrolyte compositions (EC-DEC, EC-EMC PC 1M $LiPF_6$), using large bipyramidal $Au@SiO_2$ SHINs and a scanning 785 nm Raman probe to minimize damages to the electrolyte (see Figure 2.5.4 h). They evidenced the formation of lithium ethylene monocarbonate (LEMC) and an interfacial instability associated with the generation of electrolyte soluble compounds (diethyl 2,5-dioxahexanedicarboxylate DEDOHC). The formation of this latter compound, specific to tin (catalytic decomposition of DEC on tin oxides) is responsible for the large irreversible capacity of electrodes. Gajan et al. also showed that the DEDOHC signature is absent in DEC-free electrolyte (PC 1M $LiPF_6$ electrolyte), resulting in better passivation ability of the electrode.[180,186] They also reported in this study an extinction of the SHINERS signal at the end of the first cycle of the tin electrode in EC-EMC based electrolyte, which they attributed to the possible burial of the SHINs within a thick SEI layer, emphasizing the analytical limitation of the SHINERS technique. Finally, they confirmed the possibility to extract SEI layer Raman signature on a composite carbon electrode (amorphous carbon and PVdF binder) in contact with EC-DEC, EC-EMC based electrolytes with or without fluorine-based additives (LiF_2PO_2). They evidenced the formation of LEMC, Li_2CO_3 in the three electrolyte compositions and a strong background increase in EC-EMC which is cancelled out when using LiF_2PO_2 additives.

The first study on a composite Li-rich layer materials $xLi_2MnO_3{\cdot}(1-x)LiMn_{0.5}Ni_{0.5}O_2$ (LLNMO in half-cell vs lithium and full cell vs MCMB) was reported by Hwang's group [182] back in 2014. Despite the low signal- to- noise ratios of the produced spectra, they reported the formation of Li_2O at potentials greater than 4.4 V versus Li/Li^+ on $Li_{1.2}Ni_{0.2}Mn_{0.6}O_2$ and Li_2MnO_3, while it proved absent on $LiNi_{0.5}Mn_{0.5}O_2$, illustrating the critical role of the material composition on the chemistry of the interface upon cycling. They also reported the formation of Li_2CO_3 on the three materials below 4.4 V and its degradation at the end of the charge (4.8 V). For all composite electrodes, the signature of carbon is visible in all spectra, but that of the active material extracted at the open circuit voltage (and at 3.5 V) is no longer observed throughout cycling, even at high laser power (10 mW).

In 2020, Li et al. [183] used 55 nm diameter $Au@SiO_2$ SHINs and a near-infrared Raman probe (785 nm) to study the oxidation mechanisms of a LIB electrolyte (LP57, 1 M $LiPF_6$ in 3:7 EC/EMC) at composite electrodes composed of layer material (lithium-nickel-manganese-cobalt-oxide NMC 111 and 811) polarized at 4.8 V vs Li/ Li^+ (Figure 2.5.4 d). Changes in the Raman signature around 500 cm^{-1} starting from 4.6 V were interpreted as the gradual appearance of lithium fluoride (LiF at 406 cm^{-1}) and lithium nickel

(oxy)fluoride ($LiNi_xF_yO_z$ at 575 cm^{-1}). Despite the "non-characteristic" Raman signature of LiF, this assignment was supported by a post-mortem XPS studies. The authors also ran a comparative SHINERS study on amorphous carbon electrodes in LP57 but did not reveal any dynamics of surface composition in the [400-1000 cm^{-1}] energy range, despite the very high values of potential explored (up to 5.2 V vs Li/ Li^+). The association of small SHIN particles and 785 nm probe may not, however, provide the highest sensitivity conditions especially through LIB electrolyte.

Gajan et al. [186] studied interfacial processes on pure high-voltage spinel material LNMO ($LiNi_{0.5}Mn_{1.5}O_4$ thin film on copper) in contact with an EC-EMC 1.2 M $LiPF_6$ electrolyte (half-cell vs Li/Li^+), using 140 nm bipyramidal gold@SiO_2 SHINs and a scanning 785 nm Raman probe. Despite the use of scanning probes at relatively low power (0.9 mW), they could observe fluctuations of the electrolyte signature at a potential as high as 4.6 V, which could result from the synergetic effect of electrolyte electro-oxidation and photo-thermal damage. They also reported a damping of the active material signature (503, 641 cm^{-1} for LNMO and 540 cm^{-1} for LMO) starting from 4.5 V up to 5 V vs Li/Li^+, concomitant with the apparition of two large bands between 1128 and 1264 cm^{-1} and 1463 and 1626 cm^{-1}. These bands fade below 4.5 V then disappear below 4 V down to 3 V; the process repeats itself cycle after cycle, suggesting that the interfacial layer, i.e. the CEI, forms and dissolves at each cycle. The two bands could not be clearly assigned to any reaction products resulting from the electrolyte oxidation (lithium oxalate, formic acid, PEO, glyoxal $C_2H_2O_2$, glycoaldehydes $C_2H_4O_2$ or $OHCH_3CH_3CO_3CO$, CO_2 gas, etc.) or from the dissolution of the LNMO material (manganese acetate or oxalates). An additional experiment run on amorphous carbon under the same polarization condition revealed a similar interfacial behavior, with two large Raman bands centered on 1150 and 1550 cm^{-1} appearing at 4.5 V and totally absent at 3 V, suggesting that it is not material dependent. This strong instability of the CEI, which contrasts with that of the SEI, raised the question of the very nature of the CEI (solid, semi-solid) still under debate in the community.

2.5.4. FUTURE PERSPECTIVE

In the end, a limited number of studies has been published on the characterization of lithium-ion interfaces by surface sensitive techniques such as confocal Raman microscopy (μRaman) combined with SERS platforms, including its most versatile declination, SHINERS. Since its introduction in 2010, considerable progress has been made on the implementation of *in situ/operando* SHINERS for LIBs, benefiting from the experience developed in the electrocatalysis field for which much more efforts have been engaged so far. Dynamics of composition of the negative and positive interfaces upon cycling can now be extracted under conditions close to the "real" battery systems, drawing much interest in the analytical community.

Still, the slow "booming" of SERS/SHINERS analysis applied to LIBs, limited to a handful of research groups worldwide, can be explained by the combined difficulties to (i) design efficient and (electro)chemically inert and stable Raman signal nanoamplifiers while limiting photo-thermal damages, (ii) to design sealed and SERS/μRaman compatible spectro-electrochemical cells with performances as close as possible to real LIB systems, (iii) to work within thick layers of organic electrolyte which shows strong auto-fluorescence signals and (iv) to interrogate irregular interfaces (porous composite

electrode) whose not only composition, but also structure, evolve upon cycling. As this field is relatively new, Raman reference spectra associated to potential suspected SEI/CEI components beyond classical inorganic lithium salts are also crucially missing, the assignment of Raman bands of the SEI compounds being usually based on signatures extracted from FTIR studies or from DFT calculations.

Despite SHINERS having already reached a satisfying level of development and allowing the successful extraction of SEI, CEI chemical signatures under *operando* conditions, fundamental studies aiming at understanding how SHINs aggregates interact with their environment, especially in the case of evolving interfaces including the deposition of foreign material at the electrode surface are needed. The recently introduced depth-sensitive plasmon-enhanced Raman spectroscopy (DS-PERS20) [192], which combines SHINERS with SERS, may help to resolve the depth composition of multilayer SEI structures. SHIN particles other than Au@SiO_2, whose stability in the aged LIB electrolyte (with non-negligible HF contents) has yet to be proven, need to be developed for the characterization of ageing processes.

New designs for *operando* SERS experiments enabling the characterization of various interfaces, including electrode/polymer or gel electrolyte, in conditions even closer to real systems than spectro-coin-cells can be, remain to be proposed. The coupling of optical fibers and SERS platforms, for instance, could be developed in a similar way to the recently proposed IR fiber evanescent wave spectroscopy [148]. Considering the intensity fluctuations inherent to SERS, the tools of stochastic optical reconstruction microscopy (STORM) could be used to produce super-resolution SERS imaging, in alternative to cumbersome hyphenated imaging techniques like TERS.

Finally, SHINERS coupled with other techniques may open new diagnosis avenues, as proposed recently by P. Unwin and L. Hardwick through the association of scanning electrochemical cell microscopy (SECCM) and SHINERS for the combinatorial screening of the SEI formation [193] which could allow the fast screening of new candidate battery materials and accelerate the optimization of SEI formation protocols.

2.6. SOLID-STATE NUCLEAR MAGNETIC RESONANCE SPECTROSCOPY

Nuclear magnetic resonance (NMR) spectroscopy is an invaluable tool for chemists and materials scientists, providing detailed information on chemical composition, molecular connectivities, dynamics and kinetics. NMR has been routinely applied to the study of battery materials to obtain a detailed picture of how these complex systems change during electrochemical cycling. This is perhaps unsurprising as many of the chemical elements that are present in battery materials have NMR-active nuclides (e.g., $^{6/7}$Li, ^{23}Na, ^{25}Mg, ^{39}K, ^{1}H, ^{13}C, ^{17}O).

NMR is also a nuclide-specific technique, meaning that in a spectrum, only signals for species containing that given nuclide will be observed, thus providing a means for separating signals from different components of a battery cell. The widespread use of NMR for materials characterization can be explained by the extreme sensitivity of the internal NMR interactions to the local environment of a given nucleus. While in-depth review and discussion of the origin of these NMR interactions and their influence on

spectra is beyond the scope of this paper, a brief summary is given below, and the reader is referred to many excellent sources in the literature [194-198].

The chemical shift is perhaps the most familiar NMR interaction to chemists as each distinct chemical environment results in a unique resonant frequency. The differences in resonance frequency are caused by perturbations of the local magnetic field experienced by the nucleus due to surrounding electron density. Nuclei with spin $I > ½$ (e.g., ^{7}Li, ^{23}Na, $I = 3/2$) possess a nuclear quadrupole moment which can interact with surrounding electric field gradients resulting from surrounding electronic and nuclear charges. The magnitude of this quadrupolar interaction depends on the degree of symmetry about the nucleus and, therefore, provides information on bonding geometries. The dipolar interaction is a through-space magnetic coupling of nuclei. The strength of this interaction is inversely proportional to the cube of the distance between nuclei, rendering it a useful tool for probing distances of a few Å. *J*-coupling is the through-bond coupling mechanism between nuclei, which results in the characteristic splitting of signals into multiplet patterns in NMR spectra. *J*-coupling is particularly useful for determining connectivities in molecules, greatly assisting in spectral assignment.

Finally, of particular interest for the study of battery materials, is the paramagnetic interaction which is the coupling of nuclei to unpaired electrons. This interaction can occur through space (dipolar) or through bond (Fermi contact) and often results in the shifting of signals by hundreds or thousands of ppm. These NMR interactions can be exploited to obtain a wealth of information about a chemical system. Multi-dimensional NMR experiments are also available and are capable of determining atomic connectivity, spatial proximity, internuclear distance, diffusion coefficients, amongst other parameters.

2.6.1. EXPERIMENTAL APPROACHES

One important point to note is that these NMR interactions are anisotropic (i.e., orientation dependent) where the observed frequencies in the spectra are dependent upon the orientation of the molecule/crystallite with respect to the external applied magnetic field. For solid, polycrystalline samples, every orientation of the crystallite with respect to the magnetic field is possible, and each distinct crystallite gives rise to a unique frequency shift. This means that the signal intensity in solid-state NMR (SSNMR) spectra is spread over a range of several kHz to MHz resulting in low signal-to-noise ratios. Resolution can be increased in SSNMR spectra by exploiting the orientation-dependence of the NMR interactions. To first order, the NMR interactions have a $3\cos^2\theta$-1 orientation dependence, where θ is the angle between the external applied magnetic field and the largest component of the tensor describing the interaction. Rapidly spinning the sample at the magic angle (54.74°) with respect to the external magnetic field averages the anisotropic parts of the interaction. If the spinning speed is sufficiently high in relation to the magnitude of the interaction, very high-resolution spectra with well-resolved signals can be achieved. Samples for magic angle spinning (MAS) NMR experiments are powders or material scraped from electrodes, they are finely ground and packed into ZrO_2 rotors. Commercially available rotors range in outer diameters from 7 mm down to 0.7 mm and can achieve maximum spinning speeds of 4 and 111 kHz, respectively. The rotor is then placed inside a solenoid coil located in the stator of the probe, which is oriented at the magic angle, and the probe is loaded into the magnet from the bottom.

The study of interfaces with SSNMR proves to be more challenging as they are often only a few nanometers thick, and the NMR signal intensity is very weak as compared to other types of spectroscopies (this is due to the small population differences between Zeeman energy states). SSNMR is also generally a bulk technique, so the entire sample is observed, sometimes resulting in overlapping signals from the bulk material and species at the interface. The study of interfaces is further complicated by the anisotropic NMR interactions which spread the already low signal intensity over a large frequency range. Since the resolution of individual signals requires the use of MAS, the application of *in situ* or *operando* NMR to the study of interphases is somewhat limited (the physical connections of the cell to the external battery cycler preclude spinning the sample at several kHz). Nonetheless, there are several reports of the characterization of interphases using SSNMR available in the literature.

2.6.2. BATTERY INTERFACIAL PHENOMENA STUDIED BY SSNMR

The solid-electrolyte interphase (SEI) that forms from deposition of electrolyte decomposition products on the anode is often more amenable to SSNMR investigations as it is typically thicker than the interphase formed on the cathode, and the anode materials typically do not contain many paramagnetic species which can broaden the NMR signal. Silicon is a promising anode material due to its high specific capacity; however, the extreme volume expansion upon lithiation leads to cracking of the SEI and exposure of fresh surfaces for further electrolyte degradation reactions. Michan et al. completed a series of studies to determine the composition and conditions under which the SEI on Si anodes formed [199-202]. The use of ^{13}C-labeled electrolytes greatly increased the signal intensity from the organic SEI components and permitted the use of two-dimensional NMR experiments (including ^{13}C-^{13}C correlation experiments) to unambiguously assign the signals observed for the SEI components (Figure 2.6.1 a-c). ^{1}H SSNMR spectra acquired as a function of voltage showed that a significant amount of SEI is formed during the low voltage, long lithiation plateau at 150 mV while ^{13}C NMR spectra indicated that the major decomposition product of ethylene carbonate in the SEI was polyethylene oxide (PEO)-like polymers. It was also found that in the first cycle, inorganic components such as LiF and other Li salts are the principal constituents of the SEI; however, once the lithiation capacity drops below 50% of its initial value, significant amounts of organic SEI components were detected. A reaction mechanism for the reduction of fluoroethylene carbonate (FEC) and vinylene carbonate (VC), two common electrolyte additives, was also determined using data from SSNMR experiments. It was found that FEC reduction results in the formation of LiF and VC, which further reacts to form poly-VC polymers.

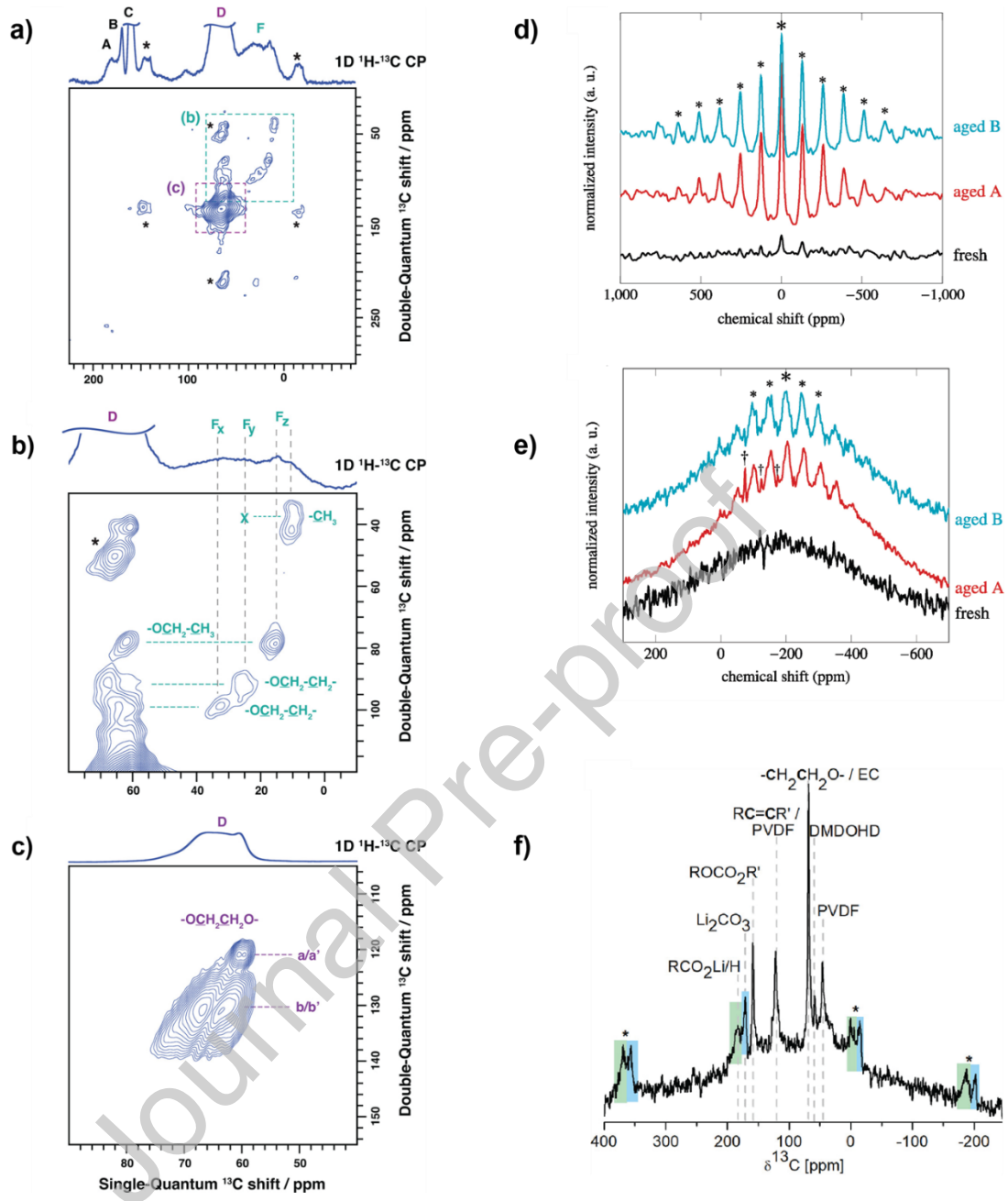

Figure 2.6.1. ^{13}C single-quantum/double-quantum (SQ/DQ) homonuclear correlation experiment performed with the ^{1}H-^{13}C cross-polarization *J*-based INADEQUATE pulse sequence of a Si anode extracted from a Li/Si cell with ^{13}C-labelled EC in the electrolyte. a) Entire spectrum; b) and c) zoomed in regions. Dashed lines are used to show correlations between signals which means those chemical groups are directly bonded to each other; d) ^{7}Li and e) ^{19}F SSNMR spectra of aged $LiFePO_4$ electrodes extracted from cells. * are used to indicate signals corresponding to LiF and † indicate signals originating from $LiPF_6$; f) ^{13}C direct excitation spectrum of an NMC811 cathode after 50 cycles. * denote spinning sidebands. Parts a), b) and c) are reproduced from Ref [203] with permission. Parts d) and e) are reproduced from Ref [204] with permission. Part f) is adapted from Ref [205] with permission.

By comparison, studies of the cathode-electrolyte interphase (CEI) using SSNMR are less available in the literature. This is likely due to many cathode materials containing a high number of paramagnetic metal ions which leads to broadening of the signals corresponding to CEI components. Castaing et al. used SSNMR to quantify the amount of CEI components formed on a $LiFePO_4$ electrode after cycling [204]. ^{7}Li and ^{19}F spectra of samples containing a known amount of LiF were used as calibration standard. The cathodes from the cycled cells were found to also contain LiF, but it only accounted for 13% of the total electrode mass gain suggesting that either other Li salts or organic species were also present in the CEI (Figure 2.6.1 d-e). Unfortunately, the small ^{7}Li chemical shift range (approximately 2 ppm) and the broadening of the signals due to paramagnetic ions, made the identification of other Li-containing compounds challenging. Hestenes et al. used SSNMR to investigate the CEI that forms on NMC811.[205] They showed that it was possible to obtained relatively high resolution SSNMR spectra for this cathode material in the charged state where most of the paramagnetic Ni^{2+}/Ni^{3+} ions have been oxidized to diamagnetic Ni^{4+}; this was verified by measuring ^{1}H spin-lattice relaxation times for CEI components which were found to be two orders of magnitude larger when the cathode was in the charged state as compared to the discharged state. The ^{13}C SSNMR spectrum of a NMC811 cathode cycled 50 times showed signals corresponding to several organic and inorganic electrolyte degradation compounds. Signals were observed corresponding to Li_2CO_3, RCO_2Li, and PEO-like polymer species (Figure 2.6.1 e).

2.6.3. FUTURE PERSPECTIVE

SSNMR provides a wealth of information on the chemical composition of interphases in batteries; however, it is inherently a bulk technique and signals from other components of the cell/electrode can overlap with those of the species in the interphase. Surface-sensitive measurement modes can circumvent this limitation. Dynamic nuclear polarization (DNP)-enhanced SSNMR is a technique in which spin polarization from a source of unpaired electrons (e.g., a radical in solution, paramagnetic ions, or conduction electrons) is transferred to the nuclei of interest. The much larger spin polarization of electrons means that drastic signal enhancements are possible, resulting in significantly decreased experimental times. Furthermore, since the transfer of spin polarization occurs over relatively short distances, DNP-enhanced SSNMR can be used to selectively probe surface and/or interphases.

To follow up the studies by Michan et al.,[199-202] Jin et al. used DNP-enhanced SSNMR to study the SEI formed on silicon anodes and the effect of using FEC as an additive.[206,207] Electrodes were collected from cycled cells and mixed with a solution of TEKpol in 1,1,2,2-tetrachloroethane as the source of unpaired electrons. They found that the addition of FEC resulted in the formation of highly branched, cross-linked, insoluble polymeric species in the SEI. In contrast, in the absence of FEC, soluble, unbranched PEO-like polymers were formed. DNP-enhanced SSNMR allowed for 2D ^{13}C-^{13}C correlation experiments to identify the molecular fragments in the polymeric SEI (Figure 2.6.2 a) and for the observation of Si-C bonds formed at the Si anode surface. Haber et al. used DNP-enhanced SSNMR to characterize the structure of a $Li_xSi_yO_z$ coating applied to Fe-doped TiO_2.[208] Through a combination of endogenous (i.e., the Fe dopant as the source of unpaired electrons) and exogenous (the use of a TEKpol radical solution),

the inner and outer structure of the coating was determined (Figure 2.6.2 b). Hope et al. used Overhauser DNP (i.e., conduction electrons acting as the polarization source) to selectively observed the interface between the SEI and Li metal dendrites (Figure 2.6.2 c).[209] These experiments were performed at room temperature and showed extreme sensitivity to the interface, suggesting at the possibility of future *in situ* DNP experiments.

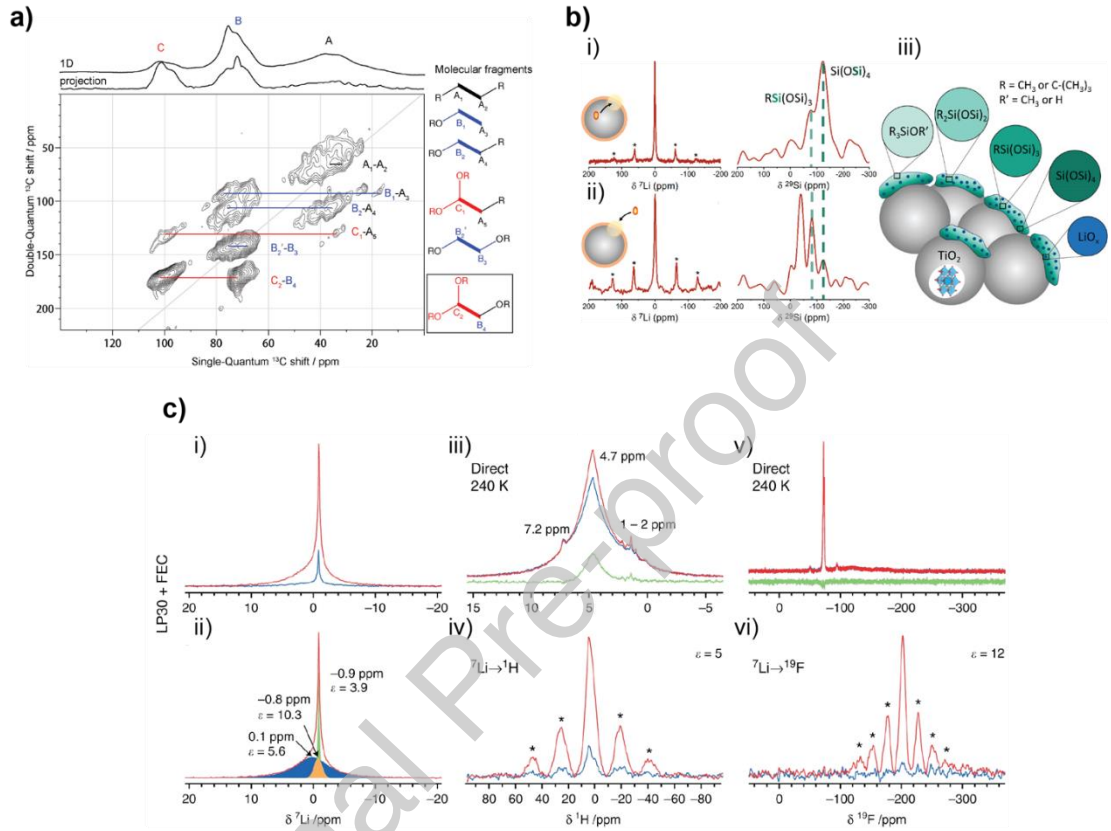

Figure 2.6.2: a) DNP-enhanced 2D SQ/DQ ^{13}C-^{13}C POST-C7 dipolar correlation spectrum of Si anode cycled for 100 cycles with FEC. The molecular fragments of the polymeric species in the SEI, as determined from the correlations in the spectrum, are also shown; b) i) endogenous and ii) exogenous DNP-enhanced ^{7}Li and ^{19}F SSNMR spectra of $Li_xSi_yO_z$ coated Fe-doped TiO_2 anode materials. iii) Representation of the structure model for the $Li_xSi_yO_z$ coating layer showing the various silicon environments as different shades of green; LiO_x is shown in blue and is uniformly distributed in the coating; c) Microwave on (red traces), microwave off (blue traces) and difference (green traces) SSNMR spectra for Li metal dendrites formed using a LP30 electrolyte with an FEC additive; i) ^{7}Li and ii) deconvolution of the microwave-on ^{7}Li spectrum, iii) direct ^{1}H and iv) ^{7}Li-^{1}H cross polarisation (CP) spectra, v) direct ^{19}F and vi) ^{7}Li-^{19}F CP spectra. The large enhancement in the ^{7}Li-^{19}F CP spectrum shows that there is LiF present in the SEI and that it is very close to the Li metal dendrite surface. Part a) was reproduced from Ref [206,207] with permission. Part b) was reproduced from Ref [210] with permission. Part c) was adapted from Ref [211] with permission.

While the application of *in situ* SSNMR to study battery materials is already well-established,[212-214] several considerations must be taken to develop *in situ* DNP-enhanced SSNMR experiments. If an exogenous DNP (i.e., adding a radical solution to the

cell) approach is to be used, the radical must be electrochemically stable throughout the cycling process. The transfer of polarization from the unpaired electrons to the nuclei of interest requires microwave irradiation; therefore, any *in situ* DNP SSNMR cell must be designed in such a way that microwaves can penetrate without significant attenuation and reach the active materials. Many of the DNP mechanisms must be performed at low temperature (100 K), thereby precluding *operando* experiments unless the Overhauser mechanism is used, but *in situ* experiments may be possible if the cell can withstand multiple freeze/thaw cycles. The benefits of being able to selectively observe the formation of interphases in a non-destructive way make the development of *in situ/operando* DNP-enhanced SSNMR an attractive research direction.

2.7. SCANNING TRANSMISSION ELECTRON MICROSCOPY & SPECTROSCOPIES

Scanning transmission electron microscopy (STEM) is a versatile technique that has become ubiquitous in the field of analytical transmission electron microscopy of battery materials. STEM uses a focused electron beam scanned on a thin specimen as a raster, with controlled probe size and current, and can be combined with various spectroscopic techniques, such as, for the most common ones, energy-dispersive X-ray spectroscopy (EDXS) and electron energy-loss spectroscopy (EELS). The current availability of aberration-corrected electron probes with high-brightness electron guns makes STEM a well-adapted and efficient approach to probe battery materials down to the atomic-scale [215-218] which is of major interest for functional interfaces where physico-chemical phenomena occur. In this section, the usefulness, and limitations of STEM, EDXS and EELS are presented in the context of interfacial investigations in battery materials.

2.7.1. SCANNING TRANSMISSION ELECTRON MICROSCOPY

Annular dark field (ADF) imaging at high resolution in the scanning transmission electron microscope provides an atomic-scale chemical contrast, or Z-contrast [219-222]. When combined with an aberration-corrected probe, sub-Angström spatial resolution can be achieved [223,224]. This incoherent imaging mode is widely used for its intrinsic versatility, providing both structural and chemical information at the scale of individual atomic columns or single atoms, of interest to understand the structural modifications occurring at surfaces and interfaces in battery materials upon electrochemical cycles.

Structural changes have been evidenced at grain surfaces following electrochemical cycling, spinel structure in Li- and Mn-rich NMC [225-227], rock-salt structure in NMC and Ni-rich NMC [228,229], or both spinel and rock-salt structures [230], as illustrated in Figure 2.7.1 I, II. Structural rearrangements have also been evidenced in TiO_2-coated $LiNi_{0.5}Mn_{1.5}O_4$ [231], $Li_{1.2}Ni_{0.2}Mn_{0.6}O_2$ [232], or $Li[Ni_{1/5}Li_{1/5}Mn_{3/5}]O_2$ [233]. One of the intrinsic limitations of ADF imaging, however, is that it is only weakly sensitive to light elements like O, especially when they are near much heavier atoms, and insensitive to Li. While Z-contrast imaging of heavy elements is typically achieved with electrons collected at high scattering angle (high angle ADF – HAADF) to minimize coherent diffraction contributions, visualizing light atoms in STEM can be obtained by collecting electrons from an annular region of the bright field disk, *i. e.*, with a lower collection angle of the detector in so-called annular bright field (ABF) imaging conditions [234,235].

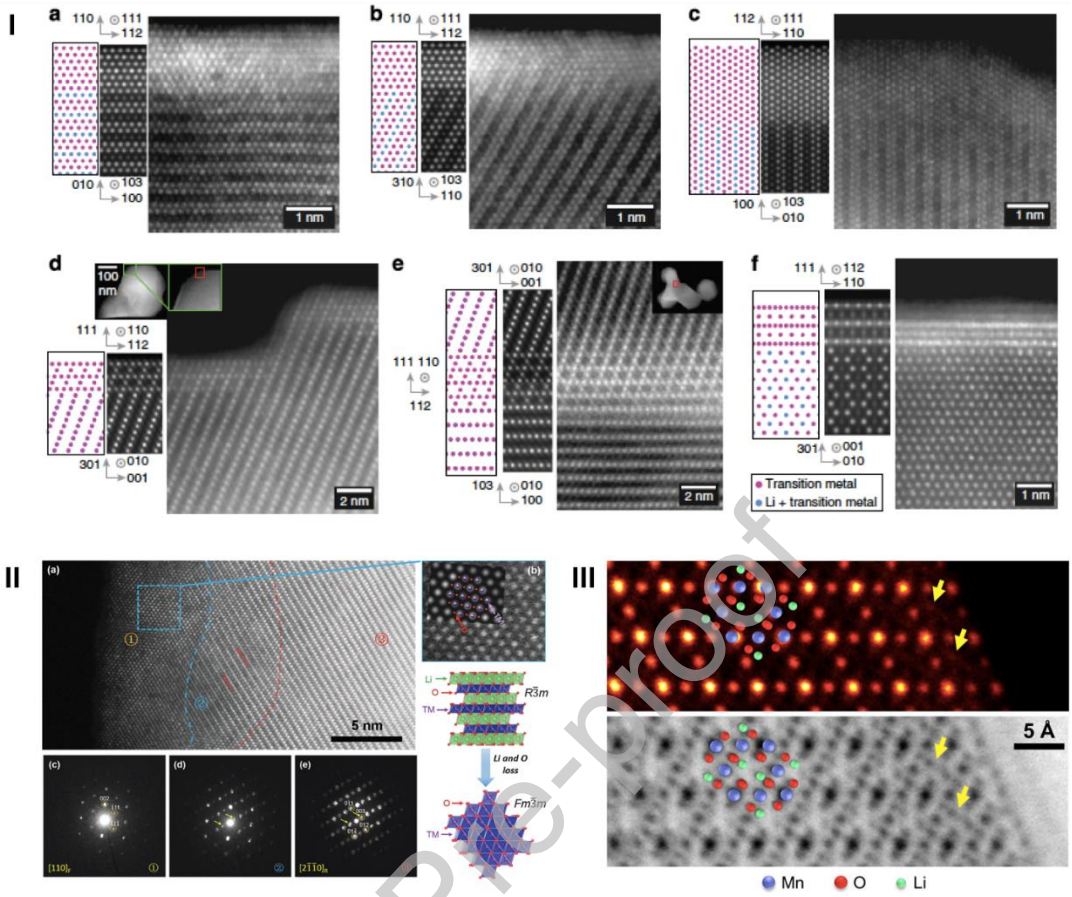

Figure 2.7.1. Aberration-corrected HAADF and ABF imaging at surfaces of Li-battery materials. I) (a-f) Experimental and simulated HAADF images of lithium- and nickel-rich $Li_{1.2}(Ni_{0.13}Mn_{0.54}Co_{0.13})O_2$ for several zone axes, highlighting the spinel structure of the surface layer and the monoclinic structure of the bulk. The interface is $(010)_M$. Adapted from [225]. II) Structural evolution of $Li_xNi_{1/3}Mn_{1/3}Co_{1/3}O_2$ after 50 cycles. (a, b) Atomic-resolution HAADF-STEM, with the corresponding simulated HAADF image in inset of (b). (c–e) Nano-beam electron diffraction patterns from the surface (1) to the bulk (2, 3) of the particle. Fm-3m and R-3m structures are indicated as subscripts F and R, respectively. Adapted from [228]; III) HAADF (top) and ABF (bottom) STEM images of $LiMn_2O_4$ surface. Yellow arrows indicate columns for which the contrast is stronger at the surface than in the bulk. These columns would contain exclusively lithium in pristine $Li(Mn,Ni)_2O_4$, but the contrast at the surface suggests manganese/nickel migration to these atomic sites. Adapted from [236].

This approach can be used to determine the position of light elements in a crystal, such as O atoms and most importantly Li [236-247]. STEM imaging at intermediate collection angles, such as medium angle ADF (MAADF) and low angle ADF (LAADF) imaging, also provide relevant chemical and strain contrast information. Combined with HAADF, ABF imaging of the surface of $LiMn_2O_4$ provides evidence of manganese/nickel migration to Li atomic sites at the very surface of grains [236], as shown in 2.7.1 III. ABF imaging brought a significant contribution to determine the structure of stacking faults in $LiMn_2O_4$ epitaxial thin films, highlighting the Li deintercalation, local oxygen loss, and the occupancy of

previously unoccupied sites by Mn upon chemical cycling as key factors contributing to capacity fading and performance degradation of $LiMn_2O_4$ as a cathode [244]. Examples of the ABF capabilities to resolve the atomic sites occupied by Li, and therefore to estimate the migration of atomic species in various structures like the solid-state electrolyte $La_{0.62}Li_{0.16}TiO_3$ [242], cathode materials $LiFePO_4$ [238], $Li_4Ti_5O_{12}$ [246,248], $LiNi_{0.5}Mn_{1.5}O_{4-x}F_x$ [240], $LiMn_2O_4$ [239,247,249,250], or $Li_{1.2}Mn_{0.567}Ni_{0.166}Co_{0.067}O_2$ [245].

Using a segmented detector, differential phase contrast (DPC) is an additional STEM imaging mode, which is sensitive to the atomic electric field, and thus enables the reconstruction of atomic-scale maps of the projected atomic potential, the electric field direction and the charge-density [251-257]. At the nanoscale, this approach has proven useful to investigate the effect of Li-ion transport at cathode/electrolyte interfaces in all solid-state Li-batteries [258,259]. One of the main advantages of DPC-STEM is its sensitivity to both light and heavy elements at atomic resolution, which provides an interesting alternative to combining HAADF and ABF. DPC-STEM was used for instance to study the mechanisms supporting the migration of Mn in $Li_{1-x}Mn_2O_4$ spinel structure [260]. With the advent of pixelated detectors for four-dimensional(4D)-STEM, the capabilities of DPC-derived approaches such as centre of mass (COM)-STEM have been explored and also provide a versatile and reliable approach to image Li, O and heavier elements at the atomic scale [261].

2.7.2. ENERGY DISPERSIVE X-RAY SPECTROSCOPY & ELECTRON ENERGY-LOSS SPECTROSCOPY

One of the main reasons for combining spectroscopies with the spatial resolution accessible in the aberration-corrected scanning transmission electron microscope is to provide evidence of where elements are located in the material from the nanometer down to the atomic-scale. EDXS is a very accessible and widely available spectroscopy that is sensitive to most elements for Z>6, with the possibility of quantitative elemental compositions. The major improvements in detector efficiency and geometry (large solid-angle, multiple detectors) since the 2000s allow extremely high throughput detection. The latest generation of EDXS detectors have fostered the capabilities of elemental mapping [262], even for light elements like O, reaching atomic-resolution [263], which was previously limited to EELS. EDXS is widely used for battery materials characterization at the nanoscale, since it provides an accurate tool to analyze the chemistry of interfaces in Li- and Na-battery materials [264-266].

EELS is also an efficient technique to detect or map most elements in battery materials at the sub-nm scale, including early transition metal elements and light elements like Li and O. This spectroscopy is particularly well-adapted to detect the L_{23} absorption edges of first-row transition metals as well as the O-K edge at ~530 eV. The Li-K edge is positioned at ~50-60 eV and offers in principle a direct spectroscopic probe of lithium in the structure [267-269]. However, the processing and interpretation of this edge is often complex as it overlaps with the M-edges of some TM elements, and it is often positioned on the tail of the bulk plasmon peak. It is possible, however, to exploit the distinct responses in the low energy-loss part of the spectrum of Li-containing compounds. This approach allows phase mapping, with the advantage of lower electron doses than core-loss EELS, which is of interest to avoid the degradation of very beam-sensitive specimens.

The morphological and chemical evolution of SEI components made of Li_xSi alloys in Si nanoparticle-based negative electrodes was mapped at high spatial resolution (5 nm) using a fitting approach of the plasmon region [270,271]. Following a similar approach, the LiF distribution was separated from other Li-Si alloys and mapped [272]. Other low-energy excitations like interband transitions have been identified as a signature of delithiation in $LiFePO_4$ [273] and have been used to track the delithation process and map the localization of delithiated areas in $LiFePO_4$ upon cycling during *in situ* EELS experiments [274]. While elemental mapping at atomic resolution using EELS and EDXS is not always possible nor meaningful in the case of, *e. g.*, interfaces that have been strongly modified during discharge-charge cycling, combining nanoscale resolution EELS or EDXS maps with atomic-scale HAADF/ABF imaging is routinely possible on most modern aberration-corrected (S)TEM instruments, and prone to provide relevant information on the nature and localization of structural and chemical changes at surfaces and interfaces.

The advent of electron-beam monochromation in the transmission electron microscope in the early 2000s has provided a significant step towards a better definition of core-loss fine structures probed using EELS. From this technological improvement, the energy resolution is close to that of X-ray absorption on most synchrotrons [275,276], however with the benefit of higher spatial resolution intrinsic to TEM. While the initial development of monochromators was strongly limiting the beam current to maintain atomic-resolution in STEM, the recent technological breakthrough of (S)TEM monochromators, linked to ever more stable aberration-correctors, allow the daily combination of ~1 Å probe and <100 meV resolution for a wide range of accelerating voltages (30-300 kV) [277,278]. As a result, the factor limiting the definition of near-edge fine structures (energy-loss near edge structures – ELNES) of absorption edges is not the instrumental energy resolution, but the intrinsic finite core-hole lifetime of the excitation. Furthermore, providing that the thickness of the TEM lamella is appropriate, the noise level linked to the quantity of matter probed with a sub-Å electron beam contributes also to limiting the definition of core-loss fine structures.

The energy-resolution provided by monochromated EELS instruments, but also the intrinsic energy spread from cold-field emission guns (C-FEG, ~0.3 eV), is often appropriate to determine subtle fine-structure changes of K edges of light elements (O, Li, Na, F, etc.) and L_{23} edges of first row transition metal (TM) elements, which are constitutive of most battery materials. The ELNES of TM-L_{23} edges provide information on the valence and local crystallographic environment of TM atoms. While a qualitative fingerprint analysis is often possible from the wealth of spectral data available in the literature, atomistic calculations considering multi-electronic effects can provide in-depth understanding of local electronic structure modifications. Hence, the variations of the Ni-L_{23} fine at different points of the discharge-charge cycle in the NMC structure demonstrates that nickel is the sole ionic species undergoing oxidation state variations upon delithiation [228]. This is further illustrated in Figure 2.7.2. Other examples involve the lithium deinsertion/insertion process in $LiFePO_4$ [279], or the study of the surface rearrangement in $Li_{1.2}Ni_{0.2}Mn_{0.6}O_2$ [232], and $Li[Li_{0.2}Mn_{0.6}Ni_{0.2}]O_2$ [280]. The K edges of light elements present in batteries, such as O, Li, F, etc., are in a well-adapted energy range for EELS detection and also contain relevant chemical-bonding information at the local scale. The fine-structure variations of K edges are typically interpreted in terms of site-

and momentum-projected density of states. Similar to the TM-L_{23} edges, a fingerprint analysis is often possible to interpret fine structure variations upon, *e.g.,* material cycling. However, a thorough analysis using atomistic calculations, *e.g.* density functional theory or multiple scattering, can be appropriate for further interpretation. The fine structures of the O-K edge are complementary to the TM-L_{23} edge and reflect the evolution of the chemical bonding of O atoms in the crystal as local structural rearrangement occurs upon cycling. Hence, fine structure analysis of core-loss eels is a commonly-used tool to interpret the structural changes occurring at surfaces of cathode or electrolyte materials, *e. g.*, in $Li_{1.2}Ni_{0.2}Mn_{0.6}O_2$ [232], $Li[Ni_{1/5}Li_{1/5}Mn_{3/5}]O_2$ [233], TiO_2-coated $LiNi_{0.5}Mn_{1.5}O_4$ [231], Ni-rich NMC [131], $LiNbO_3$-coated $Li(Ni_{1/3}Mn_{1/3}Ni_{1/3})O_2$ [281], $LiMn_{1-x}Mg_xPO_4$ [282], $LiNi_xMn_xCo_{1-2x}O_2$[230], and at interfacial layers in all solid-state battery systems, *e. g.*, between $LiCoO_2$ and LiPON [283,284], or between $Li_{1.3}Al_{0.3}Ti_{1.7}(PO_4)_3$ and $LiCoO_2$ [285,286]. As mentioned above, the Li-K edge often overlaps with other edges, furthermore its intensity is usually low above background, which is detrimental to acquire data with a high signal-to-noise ratio. Nevertheless, the Li-K edge typically displays structured ELNES, which are extremely-rich in information to identify phases and electronic structure variations [268,269,287-289] and to interpret subtle electronic structure changes using, *e.g.* first principle atomistic calculations [268,290].

The need for studying energy storage or conversion systems in their working environment has contributed to the development of *in situ* and *operando* conditions in dedicated sample holders (high temperature, biasing, liquid, etc.) adapted to these challenges for, *e.g.*, battery materials [261-262] and solid oxide fuel cells [291-293]. Tracking the evolution of battery materials during the electrochemical cycling in a liquid electrolyte poses major difficulties to EELS signal detection and interpretation from the additional signal of the liquid and membrane windows, and the increased thickness. While atomic-scale STEM imaging is possible and EDX maps reach nanoscale resolution in optimized conditions, EELS is intrinsically affected by the additional thickness of the liquid and membrane.

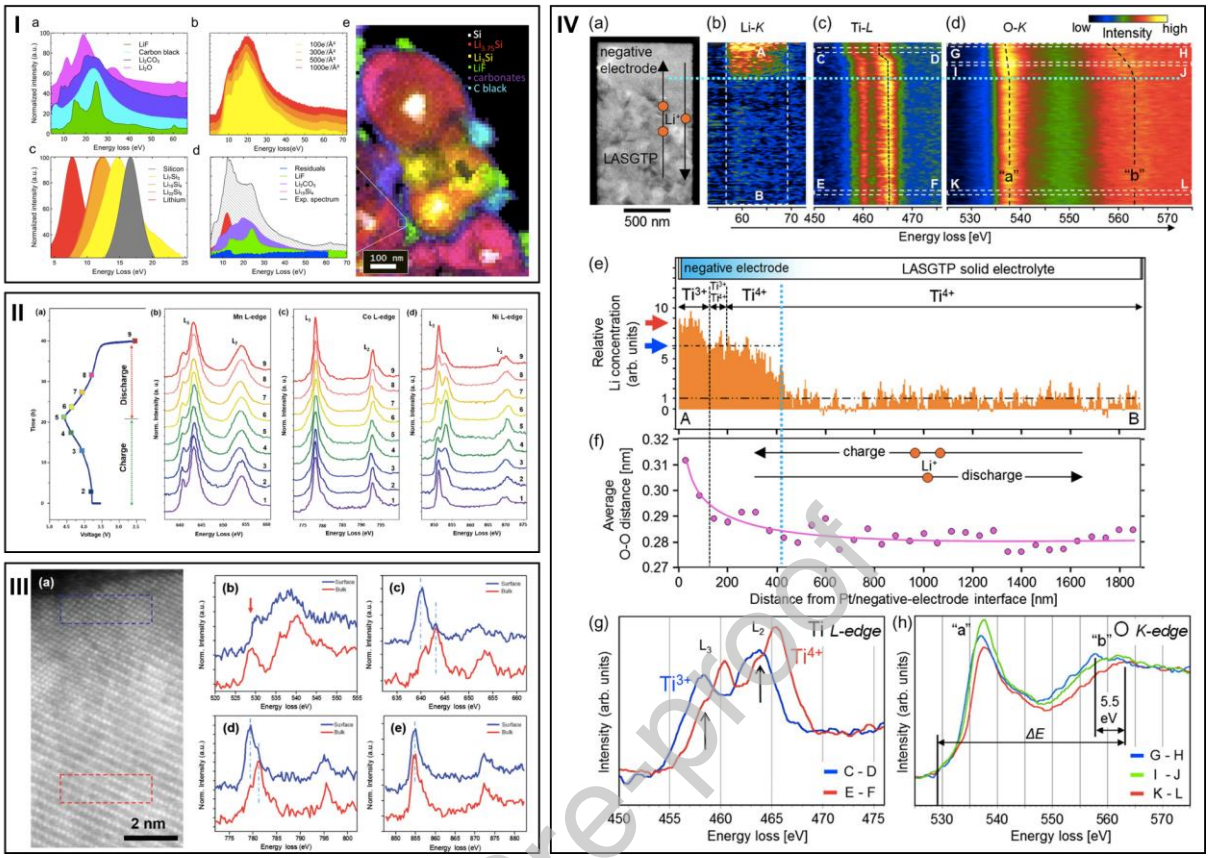

Figure 2.7.2. EELS analyses at surfaces and interfaces in Li-battery materials. I) (a) Plasmon spectra (references): LiF, C black, Li_2CO_3, and Li_2O. (b) Effect of electron doses on the plasmon spectra of Li_2CO_3. (c) Plasmon spectra (references) of Li_xSi alloys. (d) MLLS fitting of an experimental spectrum obtained after integration over four pixels in (e). (e) MLLS fitting of a spectrum image acquired in a region of an electrode charged to 3000 mAh.g^{-1}, containing multiple phases: LiF (green), Li_2CO_3 (purple), carbon black (teal), Li_7Si_3 (yellow), $Li_{15}Si_4$ (red), and Si (white). Scale bar: 100 nm. Adapted from [270] ; II) Evolution of the voltage (a), and normalized (b) Mn-$L_{2,3}$, (c) Co-$L_{2,3}$ and (d) Ni $L_{2,3}$ edges of the NMC cathode at various states of charge during the first cycle. Adapted from [228]; III) Spatially-resolved ELNES extracted from the regions indicated in (a) the high-resolution HAADF-STEM image of the NMC cathode after 20 cycles: (b) O-K edge, (c) Mn-$L_{2,3}$, (d) Co-$L_{2,3}$ and (e) Ni-$L_{2,3}$ edges from the surface layer (blue spectra) and the bulk (red spectra). Adapted from [228] IV) Spatially-resolved EELS analyses of Li-K, Ti-L_{23}, and O-K edges around *in situ*-formed-negative-electrode/solid-electrolyte interface. (a) TEM image of the region selected for EELS analysis. (b-d) Spatial distribution of (b) Li-K edge, (c) Ti-L_{23}, and (d) O-K edges. (e) Profile of the Li concentration along the vertical 'A'–'B' direction indicated in (b), and corresponding Ti^{4+} and Ti^{3+} regions obtained from (c) and (g). (f) Profile of the average O–O distance along the vertical direction in (d), as measured from the shift of peak 'b' in (d) and (h). (g) Ti-L_{23} edges integrated in regions 'C'–'D' and 'E'–'F' in (c). (h) O-K edges integrated in rregions 'G'–'H', 'I'–'J' and 'K'–'L' in (d). Adapted from [294]).

Spectral features in the low-energy loss part of the spectrum, like interband transitions, can prove useful to track and map phases at the nanoscale during *in situ* electrochemical

cycling, such as the delithiation process in $LiFePO_4$ [274], but the nature of the spectral signatures remain material-specific and this approach cannot be easily applied to other systems. Low-loss and core-loss data have been acquired successfully in $LiMn_2O_4$ and $Li_4Ti_5O_{12}$ battery electrodes within the TEM liquid cell holder [295]. Recent work on all solid-state batteries have been performed by *in situ* biasing in the TEM to probe electrolyte-electrode interfacial phenomena in $LiCoO_2$/LiPON/Si thin film battery [296]. Discrepancies between *ex situ* and *in situ* Li-K, O-K and Co-L_{23} fine structures highlight the relevance of this *in situ* approach to determine the mechanisms of interfacial impedance, which were proved to be caused by chemical changes rather than space charge effects. A similar experimental approach was employed to investigate the interfacial resistance of Li-ion transfer during cycling in $LiCoO_2$/Li_2O-Al_2O_3-TiO_2-P_2O_5 -based solid electrolyte interfaces [297]. The Li distribution as well as the variations in Co electronic state are tracked using EELS and subsequent hyperspectral image analysis during charge and discharge reactions.

2.7.3. FUTURE PERSPECTIVES

Monochromated EELS in the low energy-loss regime has recently entered a new era with sub-30 meV intrinsic energy resolution [277,278,298], allowing the unambiguous detection of phonon peaks in the spectrum while keeping high spatial resolution with a ~1Å probe [277,299]. The capabilities of vibrational EELS in STEM have been fostered over the past ~10 years, leading to the detection of individual vibrational modes with nanoscale resolution [300,301], down to individual defects and interfaces in crystals [302,303], reaching atomic-resolution sensitivity [304,305], down to single atom dopants [306], phonon polaritons [307-309], and to the distinction between carbon isotopes [310,311]. Given the abundance of light elements like Li or Na in battery materials, vibrational EELS may appear as a newly accessible technique of interest, complementary to core-level EELS, to correlate the concentration of Li or Na and the atomic structure of interfaces, and to evaluate interfacial ion conduction mechanisms as shown in the work of Venkatraman *et al.*[312]. More details can be found in the recent review of Zachman et al. [313].

With the development of direct electron detectors for EELS [314,315], which are a major technological advancement in improving the quality of collected spectral data, the high-energy range of the absorption spectrum detectable in EELS has been further extended. For instance, probing the K-edges of some TM elements [316-318] also emerges as an additional possibility to collect both near-edge and extended fine structures at the nanoscale with sufficient signal/noise ratio, providing complementary information about the local atomic environment and nearest neighbour distances.

While the majority of battery materials are investigated at RT with various approaches to minimise electron beam-induced damage, cooling the TEM lamella down to liquid nitrogen temperature can be unavoidable to ensure imaging and EELS spectroscopic characterization with minimised damage [319-321]. Cryo-EELS with high-stability stages has allowed nanoscale EELS mapping of dendrites and interfacial layers [289], revealing stunning details. Cooling down the specimen without compromising the spatial resolution will surely be of interest for the study of battery interfaces.

2.8. 4D SCANNING TRANSMISSION ELECTRON MICROSCOPY

Four-dimensional scanning transmission electron microscopy (4D-STEM) [322] is a technique where an electron microscope scans a sample in a grid pattern while collecting electron diffraction patterns at each point, creating a high-dimensional dataset that reveals detailed structural and chemical information about the material. 4D-STEM has emerged as a powerful tool in materials characterization, offering unique capabilities for studying the structural and dynamical properties of materials at the nanoscale. Several characterization techniques have been developed by leveraging the post-processing of electron diffraction patterns, which are acquired through advanced detectors under various beam convergence and precession conditions. These techniques utilize a diverse array of approaches, including pattern matching, Bragg spot displacement, center of mass analysis, phase retrieval and ptychography. Integrating controlled precession of the beam with these techniques helps mitigate dynamical effects in diffraction patterns. By precessing a tilted electron beam around the microscope's central axis, a Precession Electron Diffraction (PED) [323] pattern emerges from aggregating a variety of diffraction conditions. This results in a quasi-kinematical diffraction pattern, which serves as a more appropriate input for direct methods algorithms for elucidating the crystal structure of the sample.

The automated crystalline orientation mapping (ACOM) [324] technique uses the diffraction mode to record diffraction patterns (DP) for several probe positions. The resulting diffraction images are compared with templates calculated from known structures (CIF) to map crystalline phases and orientations through a process named pattern-matching. A quasi-parallel beam and precession are used to record diffraction patterns (DP) with a notable reduction of dynamic effects, which improves the quality of pattern-matching thanks to better proximity of the intensity values of experimental and calculated reflections due to precession use [325].

Several types of virtual detectors can be applied to this type of data to isolate certain parts of the signal. For example, the center of the diffraction figure of the non-diffuse transmitted beam is kept constructing a virtual bright field image whose intensity is weakened by the interaction of the beam with the sample. Zones of high Z (atomic number) and crystalline zones then appear darker. Isolating other parts of the image makes it possible to build dark fields, for example by keeping only certain crystalline reflections. This type of dark field provides information on crystal defects, stacking faults, dislocations, and particle/grain size. A ring-shaped filter can detect and map nanocrystalline domains or an amorphous phase. Finally, the outer part of the image corresponding to the electrons scattering at larger angles makes it possible to construct a virtual HAADF providing information mainly on the Z-contrast (with contrast approximately proportional to Z^2) and providing information on the density and thickness of the sample. Figure 2.8.

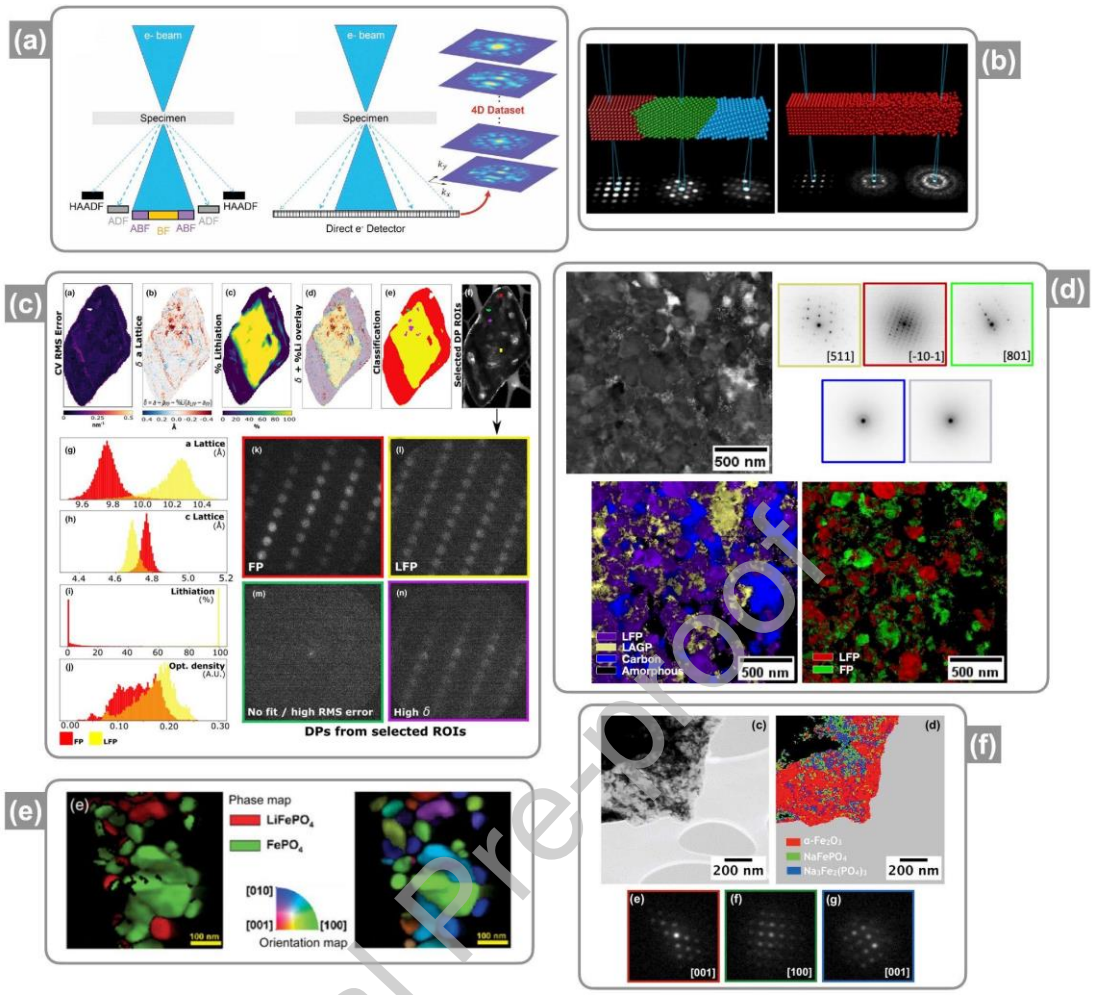

Figure 2.8. 4D-STEM techniques: orientation, phase, and strain mappings. a) Schematics of electron beam interactions with the sample and principles of multiple detection with comparison between HAADF/ADF/ABF/BF STEM detection modes and single detector using direct electron detection for the 4D-STEM approach; b) Schematics of the 4D-STEM scan on different oriented crystals and on highly crystalline and amorphous areas [322]; c) Mapping analysis of 4D-STEM strains of $LiFePO_4$ after partial delithiation, for which lattice parameter distributions were extracted based on analysis of diffraction spot displacements in each local pattern [326]; d) 4D-STEM analysis after *in situ* electrochemical cycling of FIB lamella of all solid-state battery, composed of LAGP solid electrolyte, carbon black, and LFP, in which the LFP and FP phases can be distinguished thanks to ACOM pattern matching treatment based on CIF files [327]; e) First example, from Edgar Rauch's team, on the ability of 4D-STEM ACOM to analyze $LiFePO_4$ and $FePO_4$ phases with different orientation indicating the occurrence of a cascading domino process during delithiation [328]; f) Identification of different crystalline phases inside a crystal such as alpha-Fe_2O_3, $NaFePO_4$, $Na_3Fe_2(PO_4)_3$ using 4D-STEM ACOM analysis [329].

Strain mapping works with a sufficiently convergent beam to allow nano-beam electron diffraction (NBED) disc recognition without the discs overlapping in the diffraction pattern. Indexing the reflections and quantifying their displacement according to the position in the diffraction figure and the probe position makes it possible to quantify the changes of mesh parameters and thus to map the strain. The latter are present within the

crystalline domains but also at their interfaces. Furthermore, when the probe has a similar size to the length scale of the variations of a sample's electric field, the shifts of the NBED disc may be used to map and quantify electric field intensity using the method of center of mass - differential phase contrast (COM-DPC).

To characterize "soft" battery materials with electron diffraction, it is necessary to quantify the effects of the electron beam beforehand [330]. Indeed, depending on the material, it is assumed that the damage suffered may come from the flow of electrons (in e $Å^{-2}$ s^{-1}) [331] or else from the total dose of electrons received [332]. Nevertheless, those effects of the beam have been greatly reduced with the emergence of more sensitive detectors allowing the usage of lower dose rates [333]. Another countermeasure against beam damage is to use a beam blanker to block the direct beam and thus avoid most of the beam-induced damage. Finally, it is also possible to use cryo-microscopy to preserve the morphology and the structure of the samples by limiting the diffusion of radicals in the structure as reported by Liu *et al.* [23].

A difficult limitation to define is the representativeness of the observed phenomena by 4D-STEM according to the conditions of the characterization compared to the real operating conditions of the batteries [93]. There is a question here of the influence of a scale factor and of thermodynamic and environmental conditions on the dynamics and kinetics observed around the interfaces and in the bulk of the materials.

Some cathode materials exhibit phase transitions that alternate between different regimes, such as solid solution and biphasic transitions. Even if the template matching of ACOM distinguishes relatively well different phases and crystalline orientations, it sometimes does not distinguish very close phases or orientations. For example, when a material whose structure does not change but whose lattice parameters evolve subtly according to the state of charge in a solid solution regime. Strain mapping can then be used to evaluate a relative mesh parameter change from one end of the transition to the other. The current pace of development of new detectors and analysis techniques promises the emergence of faster cameras and more comprehensive data analysis pipelines in the near future, thus making 4D-STEM techniques ever more powerful and accessible.

The investigation of the structural stability, dynamic properties, and morphological evolution using 4D-STEM techniques helps to conclude on structure evolution, solid-electrolyte interphase (SEI) formation, side reactions, and Li-ion transport properties. By mapping and/or quantifying various properties of the phases involved in cathode and anode materials, and in electrolytes, these techniques in the field of 4D-STEM thus provide essential information for the characterization of different types of interfaces present in batteries. For instance, Gallegos-Moncayo et al. [334] in their study utilized 4D-STEM ACOM to analyse the Cathode-Electrolyte Interface (CEI) in NMC 811 coin cells, identifying the presence of a LiF layer in the CEI that forms under different voltage conditions, suggesting its potential protective role against battery degradation despite variations in effectiveness. The 4D-STEM technique has been also used by Bhatia et al. [335] to study all-solid-state battery with LNMO cathode materials. In their study of pristine LMNO layers for battery materials, 4D-STEM ACOM analysis reveals that while the overall particle orientation appears random, each particle within the layers exhibits a specific

crystallographic orientation, as demonstrated by the orientation map with a spatial resolution of 2 nm. Further 4D-STEM analysis indicates a predominant alignment around the [001] orientation, highlighting both well-defined grain boundaries and the presence of unconnected grains which may be inactive during electrochemical reactions.

2.8.1. FUTURE PERSPECTIVES

In recent years, electron ptychography has emerged as a powerful technique for studying energy materials with unprecedented spatial resolution and sensitivity. 4D-STEM ptychography combines the principles of 4D-STEM, which enables the acquisition of 2D diffraction patterns at each point of the beam scan, with ptychography, which is a computational imaging technique that reconstructs the phase and amplitude of a complex-valued exit wavefront. This synergy allows for the extraction of detailed structural and chemical information from battery materials.

The unique advantage of 4D-STEM ptychography [336] lies in its ability to overcome limitations associated with traditional electron microscopy techniques, such as the trade-off between spatial resolution and field of view. By scanning a finely focused electron beam over a sample and collecting a series of diffraction patterns, high-resolution images of energy materials can be obtained after post- processing with the appropriate algorithms, revealing the atomic arrangements, crystal defects, and chemical composition.

In addition to imaging capabilities, 4D-STEM ptychography enables the quantitative analysis of energy materials. By employing advanced algorithms and computational models, it is possible to extract valuable information, including local strain fields, lattice distortions, elemental distributions, and electronic structures. This quantitative analysis provides insights into the fundamental properties that govern the performance of battery materials, such as charge transfer processes, interfacial phenomena, and ion diffusion kinetics. Recently, Yoon et al. [337] used 4D-STEM ptychography on pristine lithium nickel manganese cobalt oxide (NMC-111) cathode material, researchers successfully visualized variations in local structures and lithium distribution, capturing both light elements like lithium and oxygen, and heavier transition metals simultaneously, a contrast to their invisibility in conventional high-angle annular dark-field (HAADF) imaging. This technique uniquely identified lithium vacancies and surface phase changes in a single scan, outperforming traditional STEM modes by disentangling multiple scatterings within the sample, thus proving ideal for characterizing battery materials.

3. LIQUID PHASE CHARACTERIZATION

3.1. INTRODUCTION

Studying the chemical and physical changes to liquid electrolytes is critical for understanding interfacial reactions of electrolytes at the anode and cathode surfaces. The soluble reaction products from the interfacial reactions will reside in the electrolyte until they either react further with other species in the electrolyte or migrate to the other electrode where they can react further (electrode crosstalk). The soluble products from chemical and electrochemical reactions include organic and inorganic degradation

products from oxidation and reduction of the electrolyte at the electrodes, dissolved constituent ions from the electrodes and current collectors as well as any gasses generated during these reactions.

Once the degradation products are solubilized in the electrolyte, there is the opportunity to chemically identify them using a suite of spectroscopic techniques. Solution nuclear magnetic resonance spectroscopy (NMR)[338, 339] and liquid[340] (LS-MS) and gas[341] phase (GC-MS) mass spectroscopy are particularly suited to identifying organic degradation products. Infrared and Raman spectroscopy also are often used to identify organic species as well as to understand changes to ion coordination[342] between electrolyte salts and solvent. Ion-coupled plasma (ICP)[343] and X-ray fluorescence[344] spectroscopies can be used to quantify heavier elements such as dissolved transition metals, while X-ray absorption spectroscopy[345] and EPR[345] can be used to understand the oxidation states and coordination environment of the metal ions. Finally optical techniques including UV-Vis absorption and fluorescence[346] spectroscopies have also been used to quantify both transition metal and lithium ion concentrations[347] in electrolytes.

Despite the comprehensive set of spectroscopies available, their application often requires extracting the electrolyte from electrochemical cells using solvents or physical techniques, such as centrifugation. In either case, the volume of electrolyte extracted from commercially representative cell formats is typically limited, posing challenges in achieving adequate measurement sensitivity. This limitation may even impede the execution of some techniques that would otherwise be suitable. To obtain analytes in sufficient quantities and concentrations, cells are often made with “excess” of electrolyte leading to compromises in how representative the measurements are to commercial cells. However, flow batteries present a unique case where the large electrolyte volume allows for convenient in *operando* probing by either pumping the electrolyte through a spectrometer or simply periodically sampling it *ex situ*. Nonetheless, in general, the experimental considerations of measuring electrolytes *ex situ* must be carefully weighted for each spectroscopic technique. This is crucial for understanding the complex set of chemical reactions occurring at the electrolyte/electrode interfaces.

3.2. NUCLEAR MAGNETIC RESONANCE SPECTROSCOPY

3.2.1. EXPERIMENTAL APPROACH

The basic principles of solution-state NMR are the same as those discussed above for SSNMR. However, in contrast to SSNMR, rapid re-orientation caused by molecular tumbling results in an averaging of the abovementioned NMR interactions to either zero (dipolar coupling, quadrupolar interaction, and dipolar paramagnetic) or an isotropic value (chemical shift, *J*-coupling, and Fermi contact). By consequence, signals in solution-state NMR are often sharp and well resolved with minimal overlap. Samples for solution NMR are prepared by dissolving the material in a suitable deuterated NMR solvent. The solution is then syringed into borosilicate glass NMR tubes (typically 5 mm in outer diameter). The tube is placed in a sample holder and either manually placed in the top of the magnet or in an automatic sample changer, where it is then lowered into the coil of the NMR probe using carefully controlled streams of air. Since the sample loading occurs

through the top of the probe which is not removed from the magnet, a birdcage RF coil is used in place of a solenoid coil to apply radiofrequency irradiation perpendicular to the large external magnetic field.

3.2.2. BATTERY INTERFACIAL PHENOMENA STUDIED BY NMR

In the battery field, the high chemical specificity afforded by solution-state NMR has resulted in its routine application for the identification of electrolyte degradation products and the elucidation of the mechanisms of SEI formation. Initial studies focussed on the products of thermal degradation of $LiPF_6$ in various solvents, upon heating of electrolytes solutions in sealed glass NMR tubes. ^{19}F and ^{31}P NMR spectroscopies provide a useful to measure the degradation of the PF_6^- as both ^{19}F and ^{31}P have I =1/2, high gyromagnetic ratio, and are 100% naturally abundant. Ravdel et al. found that the major decomposition products observed in the ^{19}F and ^{31}P NMR spectra were OPF_2OR and $OPF(OR)_2$ (R = alkyl); other decomposition products (including those in the ^{1}H NMR spectra) were however not identified [348].

Shortly after and using a similar approach, Campion et al. proposed an autocatalytic decomposition pathway of $LiPF_6$ (Figure 3.2.1 a) [349]. Despite no PF_5 being directly observed in the NMR experiments, it was postulated to be a major degradation product that reacts with protic species in solution, forming POF_3. This marks the initiation of an autocatalytic reaction with carbonates, resulting in the formation of POF_2OR and $POF(OR)_2$. They demonstrated the importance of protic species in the autocatalytic process through the addition of increasing amounts of EtOH, which saw the increase in the concentration of OPF_2OEt. The addition of Lewis bases inhibited the autocatalytic reaction by forming complexes with PF_5 (observed in ^{19}F and ^{31}P NMR spectra) whereas $LiCoO_2$, $LiCo_xNi_{1-x}O_2$, and lithiated graphite added to the electrolyte solutions resulted in no formation of POF_3. Note that the mechanism of this inhibition was not explored. In a follow up study, Campion et al. used 1D and 2D (^{1}H-^{1}H COSY and ^{1}H-^{13}C HETCOR) experiments to identify the degradation products of organic carbonates and demonstrated that transesterification is an important degradation mechanism (Figure 3.2.1 b).[350] Both studies by Campion et al. illustrated the importance of protic impurities in electrolyte degradation processes and this was further verified byPlakhotnyk et al.[351] who observed that degradation could be initiated through the addition of water without the needing to heat the sample. Studies in the following years continued the approach of identifying and quantifying degradation products in aged samples (it was found that the reaction of HF with the glass NMR tubes resulted in production of water leading to further degradation) and how the inclusion of different battery materials affected $LiPF_6$ degradation.[352-354] While these studies represent an important step forward in understanding electrolyte degradation, the conditions are not fully representative of the processes occurring in a operating battery.

In 2020, Rinkel et al. published a comprehensive study to elucidate the electrolyte oxidation pathways that occur in a battery.[338] $LiCoO_2$/Li cells were assembled with a piece of Li-ion conducting ceramic (Ohara glass) to eliminate the effects of electrode cross talk and thereby determine the reactions occurring at each electrode separately. Cells were charged to various voltages, opened in an inert atmosphere, and the separators on either side of the Ohara glass were soaked in deuterated DMSO to extract the degradation

products (the deuterated solvent is also necessary for fielding locking in the NMR experiment). Using this approach, several degradation products in very low concentrations resulting from electrolyte reduction at the Li metal electrode and oxidation at the $LiCoO_2$ positive electrode were observed (Figure 3.2.1 c). The authors postulated that electrolyte degradation is the result of non-redox reactions, faradaic (i.e., electrochemical), and chemical redox reactions, the latter being responsible for most of the degradation seen on the cathode side of the cells and is driven by oxygen loss from the cathode. These results provide a detailed picture of electrolyte degradation in a real battery system (Figure 3.2.1 d).

Later studies by Dose et al. used solution-state NMR, in combination with a variety of other characterization techniques, to determine the reactivity of individual electrolyte solvents [355] and the decomposition onset potential[356] in cells with high-Ni content cathodes, namely $LiNi_xMn_yCo_{1-x}O_2$ (NMCs). In a second comprehensive study by Rinkel et al., two electrolyte degradation pathways were described for a series of NMC cathode materials, each occurring at different onset potentials [339]. At relatively low potentials and, therefore, lower states-of-charge (SOC < 80%), ethylene carbonate is dehydrogenated to form vinylene carbonate. At high potentials (SOC > 80%), a much more destructive process occurs in which singlet oxygen ($^1O_2$) is released from the NMCs and chemically oxidizes electrolyte solvents to produce H_2O, CO_2, and CO. This pathway was confirmed by reaction electrolyte solvents with ^{17}O-labelled $^1O_2$, which showed the same products as the electrolyte solutions extracted from cells at high SOC. The water generated by chemical oxidation at high SOCs then hydrolyzes the electrolyte solution, leading to further degradation reactions. Interestingly, in cells which used graphite as an anode, fewer degradation products were observed in the electrolyte solutions and this was attributed to reduction of H_2O at the anode, a reaction which consumes available Li inventory and may contribute to capacity fade when cells are cycled at higher voltages. While the studies mentioned here focused predominantly on Li-ion electrolytes and cells using transition-metal oxide and graphite electrodes, similar approaches have been used to investigate electrolyte degradation in other battery chemistries, such as: silicon anodes,[357] sodium-ion batteries,[358-360] redox flow batteries (RFBs),[361] and lithium air batteries.[362]

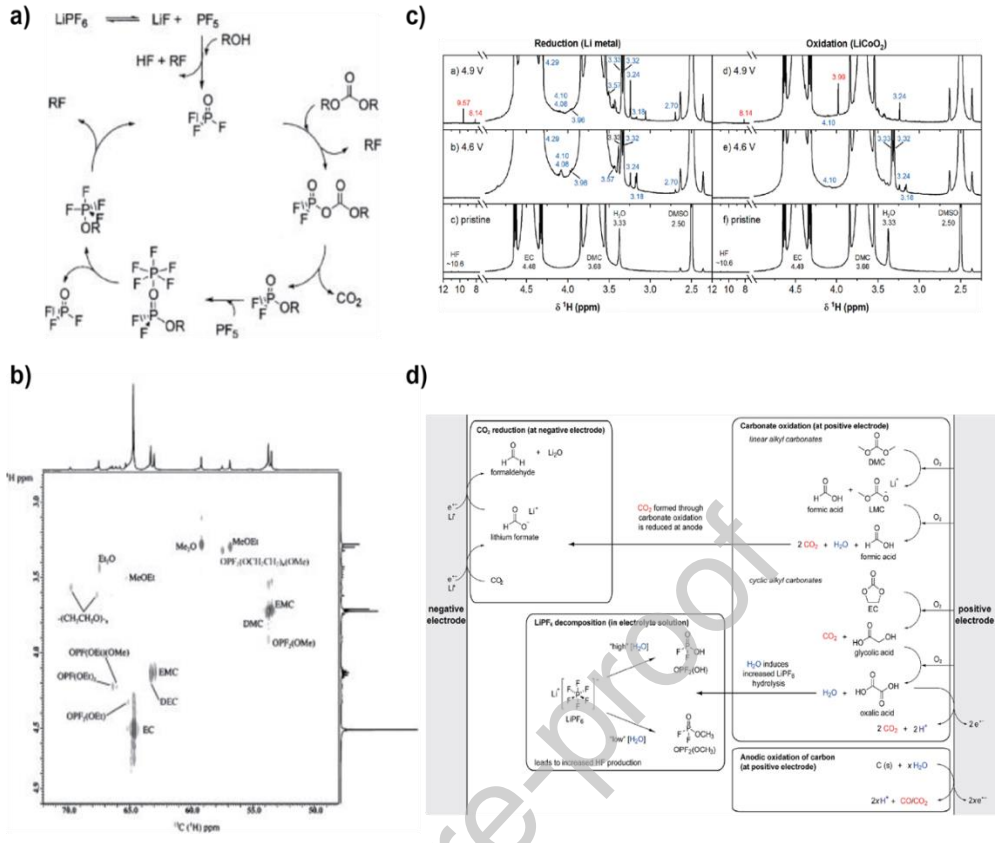

Figure 3.2.1: a) Schematic of the proposed autocatalytic thermal decomposition of $LiPF_6$ salts in Li-ion battery electrolyte. PF_5 reacts with protic impurities in the solution, which starts the autocatalytic process. b) ^{1}H-^{13}C HETCOR NMR spectrum of an aged electrolyte solution containing 1 M $LiPF_6$ in EC:DEC:DMC. Signals corresponding to EMC indicate that a transesterification reaction occurs during electrolyte decomposition. c) Representative ^{1}H NMR spectra collected from a Li metal/$LiCoO_2$ cell on either side of the Ohara glass separator. d) Schematic diagram of the various electrolyte degradation reactions occurring in a functioning cell at the positive and negative electrodes. Parts a) and b) were reproduced from Ref [363] with permission. Parts c) and d) were reproduced from Ref [364] with permission.

3.2.3. FUTURE PERSPECTIVE

The experiments described above have been so far applied *ex situ*. Early studies investigated the decomposition pathways that occur when electrolytes were heated or when large amounts of impurities were added; none of these scenarios are representative of the conditions that occur in an operating cell. Later studies used electrolytes extracted from cycled cells after disassembly, using a suitable deuterated NMR solvent. The use of multiple separators and/or of Li^+ ion selective membranes/glasses permitted the investigation of degradation processes occurring at each of the electrodes separately by eliminating cross-contamination effects, the so-called "cross-talk".

Despite the invaluable information provided by this approach, several limitations persist, namely: 1) the time required for sample preparation which may prevent the observation of some degradation products/intermediates, 2) the disassembly of the cell which may

introduce additional degradation processes, 3) the extraction of the cycled electrolyte using a deuterated NMR solvent which may not dissolve all the species of interest, and which is inherently destructive. The development of *in situ* or *operando* NMR measurements, although challenging, is therefore desirable. One possible approach consists in placing the electrochemical cell inside the NMR probe. This, however, introduces additional constraints and limitations. The coils used in typical solution NMR probes are usually 5 mm in diameter, greatly limiting cell design. Moreover, the metallic/conductive components of the cells result in a bulk magnetic susceptibility effect which broadens the peaks and greatly reduces resolution. This is particularly disadvantageous when attempting to observe signals corresponding to low-concentration degradation products.

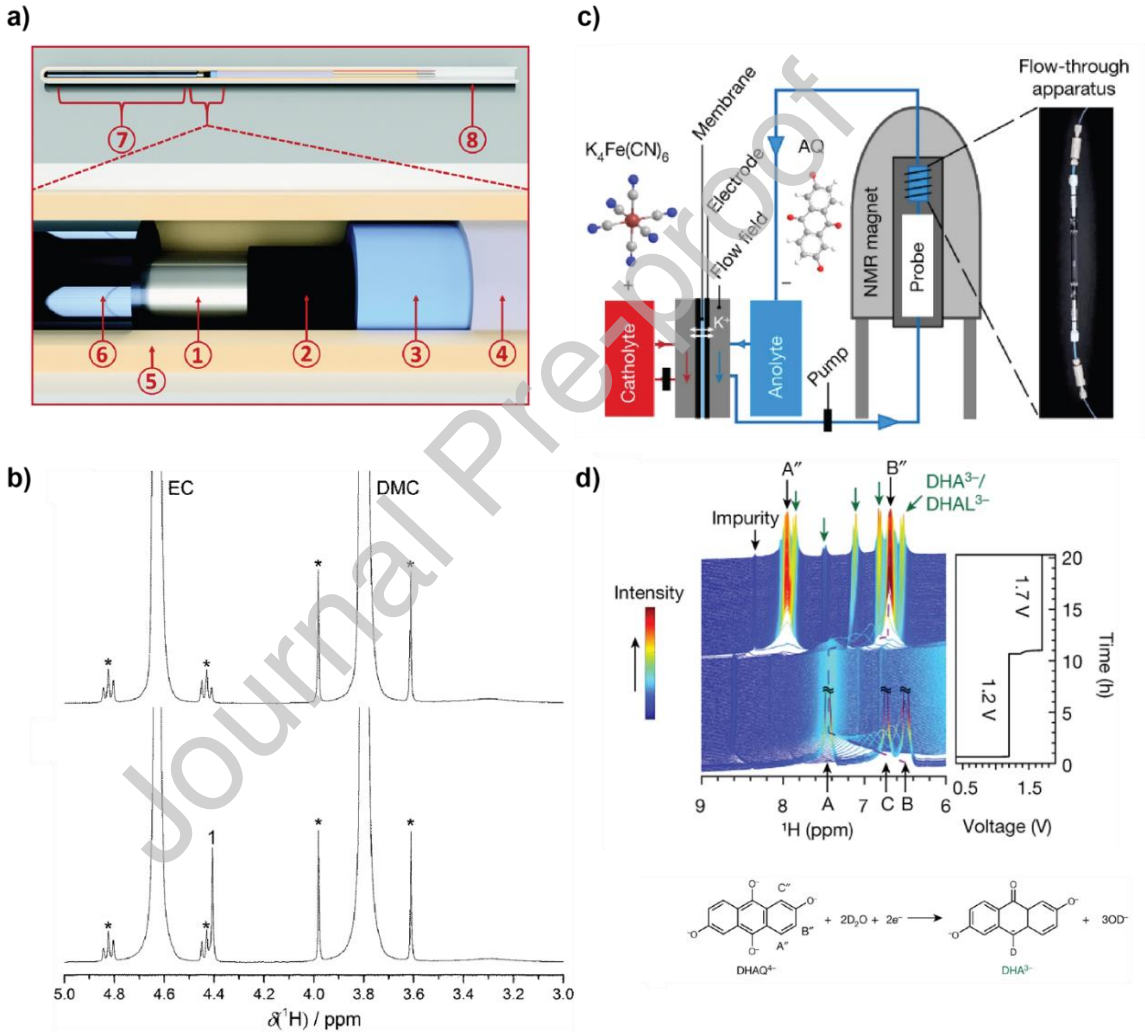

Figure 3.2.2: a) Schematic diagram of an *in situ* battery cell that fits inside a standard 5 mm outer diameter glass NMR tube showing (1) cathode current collector; (2) cathode; (3) separator; (4) Li metal coated on current collector foil; (5) polymer tube; (6) electrolyte; (7) NMR measurement area; (8) glass NMR tube. b) ^{1}H NMR spectra of a LP30 electrolyte from the *in situ* cell before cycling (top) and after the first charging step (bottom). Signals marked with * correspond to ^{13}C satellites from EC and DMC, the peak marked with 1 corresponds to a DMDOHC degradation product. c) Schematic diagram of

the on-line *in situ* NMR setup for RFBs. The cell components are external to the NMR probe/magnet and the electrolyte is flowed through the cell into the NMR probe. d) Representative *in situ* NMR data obtained for the on-line flow setup. NMR data is shown on the left and electrochemical cycling data on the right. The redox reaction being monitored is shown at the bottom. Parts a) and b) were reproduced from Ref [365] with permission. Parts c) and d) were adapted from Ref [366] with permission.

A few *operando* experiments have been successfully carried out to observe electrolytes using magnetic resonance imaging.[367-371] The cells for these experiments were small enough to fit inside the coil in the NMR probe, but contained a large amount of electrolyte so that the electrodes were outside of the detection region (i.e., the NMR coil), thereby limiting the effect of bulk magnetic susceptibility broadening. While these experiments were useful in imaging dissolved transition metals or lithium-ion concentration gradients, they lacked the chemical specificity to observe and identify degradation products. In 2017, Wiemers-Meyer et al. introduced an NMR cell which fits inside a standard 5 mm outer diameter glass NMR tube (Figure 3.2.2 a).[372] The entire cell was enclosed inside a polymer tube to prevent reactions between the glass NMR tube and the electrolyte solutions. An excess of electrolyte was used with the majority sitting beneath the electrodes, and this excess electrolyte volume was placed within the NMR detection region. The resulting spectra obtained of the pristine electrolyte from this setup showed sharp, well-resolved peaks indicating that a high level of magnetic field homogeneity was achieved. After a first charging step, a signal corresponding to dimethyl-2,5-dioxahexane dicarboxylate (DMDOHC) is clearly visible in the spectrum (Figure 3.2.2 b).

Despite the high resolution afforded by this cell design, it has very limited applications for *operando* experiments. The degradation products, which are produced at the electrode surfaces or in the space between them, must diffuse through the entire electrolyte volume and into the detection area, greatly limiting the time resolution. An alternative solution is to place the main cell components outside of the NMR magnet and to pump the electrolyte from the cell through the NMR probe and back into the cell. The advantages of this device are that there are no restrictions on the materials used to fabricate the cell (i.e., magnetic materials may be used) and that the electrode sizes can be tailored so that the electrode mass to electrolyte ratio is representative of that found in a practical cell.

Such NMR-flow setups have already been applied to the study of redox processes in RFBs [373,374] (Figure 3.2.2 c-d), only a slight modification of the electrochemical cell design is then required to study the electrolyte degradation products in LIBs. There is also the added advantage that other, non-destructive characterization techniques (e.g., EPR and UV/Vis spectroscopy) can be added in-line, allowing the observation of species that may be undetectable using NMR.

3.3. LIQUID CELL TRANSMISSION ELECTRON MICROSCOPY

Advanced characterization techniques usable in transmission electron microscopy (TEM), with which structural and chemical properties can be studied at different scales, are of great interest to provide better insight into the evolution of interfaces in battery materials. In recent years, *in situ* liquid electrochemical TEM [375] has gained wide interest for understanding the changes in active materials during the evolution of their

electrochemical performance. The (de)lithiation and degradation mechanisms can be monitored by real time imaging, with high spatial resolution and high-speed recording.

Over the last decade, the use of two types of electrochemical devices, sealed liquid cells and open solid-state cells has paved the way for challenging *in situ* and *operando* experiments, allowing direct observation of physicochemical transformations of battery materials. Based on the specific design of both *in situ* cell types, the limitations and requirements are drastically different. Sealed cells allow environmental TEM studies under ambient conditions, using conventional liquid electrolytes, while open cells permit cycling solid materials in a specific zone of interest. A large variety of *in situ* TEM studies in high vacuum condition have been reported, in which a TEM holder equipped with metallic tips [376,377] capable of piezo-actuated motion is used to contact a lithium metal source (with a LiO_2 layer as an electrolyte) to active materials prepared either as a focused ion beam (FIB) lamella or deposed on a TEM grid.

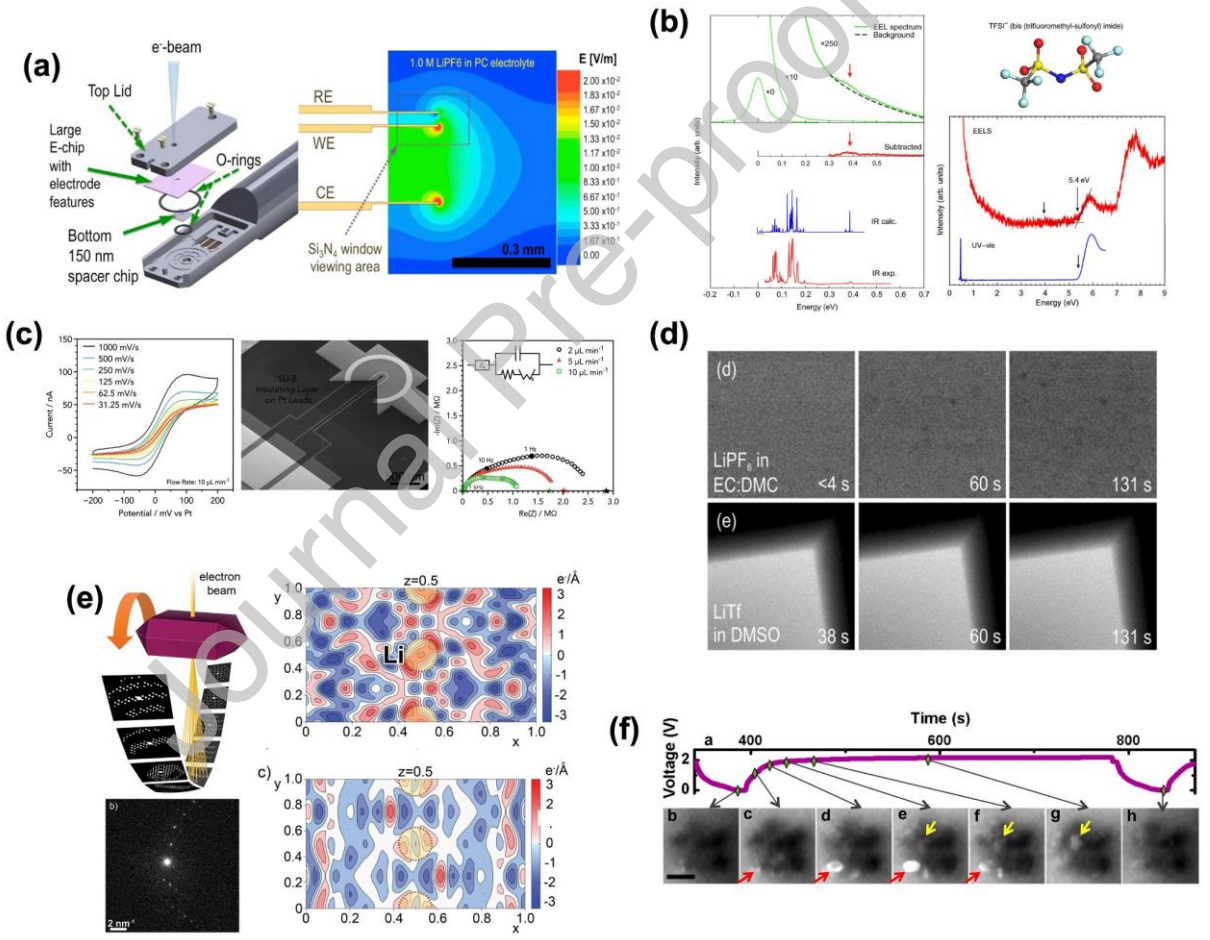

Figure 3.3.1. Electrochemical Liquid TEM for Li-ion battery materials investigation. (a) Schematic of liquid and electrochemical TEM holder with a simulation of electric field distribution using 3 Pt straight electrodes of microchips [378]; (b) First example of EELS spectroscopy (high energy resolution, 7 meV) analysis, using ionic liquid drop placed on a carbon mesh grid, in low loss region corresponding to IR and UV-visible region allowing to characterise molecules, here $TFSI^-$, inside liquid medium [299]; (c) SEM image of electrochemical micro-chip composed of 3 electrodes. Voltammetry cyclic and PEIS spectroscopy carried out inside an electrochemical liquid TEM holder proving the ability

of such devices to acquire high quality electrochemical measurements [379]; (d) Electron beam damage tests on different types of liquid electrolyte as a function of electron doses and imaging modes [380]; (e) First example of electron diffraction tomography (3DED) using electrochemical liquid TEM holder before and after delithiation of $LiFePO_4$ single crystals, with which the proof of concept was demonstrated using different Fourier map based on 3D refinement [381]; (f) Monitoring of electrochemical delithiation process in $LiFePO_4$ individual particles using EFTEM imaging at 5 eV [274].

Yamamoto *et al.* [382] first reported, using electron holography, the in situ observation of electric potential distribution at the $LiCoO_2$ solid electrolyte interface during electrochemical cycling. In another recent work, Wang *et al.* [383] used the STEM–EELS mapping technique to reveal the formation of Li_2O/Li_2O_2 as oxygen evolution reaction products in a $LiCoO_2$ electrode, which causes the rapid capacity decay during the operation of all-solid state TFB. Unocic *et al.* [384] have recently reported the use of *in situ* STEM in high-resolution mode to provide unique insights into dynamically evolving electrochemical reactions at the electrode/electrolyte interface in their native electrolyte environment. Huang *et al.* [385] developed *in situ* TEM implemented with a micro-electromechanical system (MEMS) heating device to study the precipitation and decomposition of Li_2S at high temperatures in an all-solid-state Li–S batteries. *in situ* electrochemical TEM is a powerful multimodal tool, with high spatiotemporal resolution, for fundamental investigations of electro-chemo-mechanical phenomena linked to the reactions and degradations occurring in the electrode, the solid electrolyte and various interfaces.

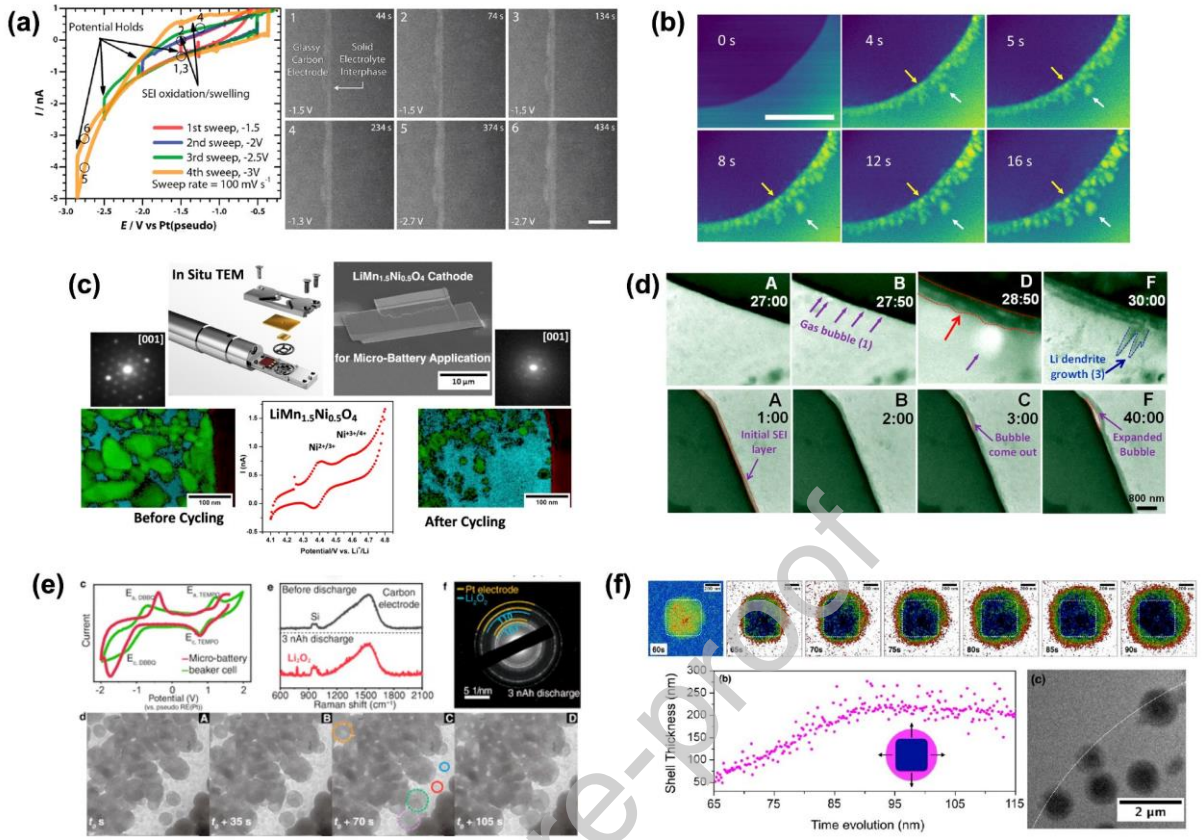

Figure 3.3.2. Electrochemical Liquid TEM for monitoring electrochemical processes inside Li-on battery. (a) Voltammetry cyclic and TEM image in liquid electrolyte during the formation of solid electrolyte interphase on glassy carbon electrode [384]; (b) TEM-sequential STEM image showing the growth of Li_2O_2 on glassy carbon electrode in a micro-battery of LiO_2 system with liquid electrolyte saturated with oxygen [386]; (c) *In situ* voltammetry cyclic and structural modifications of LMNO FIB lamella after in situ electrochemical cycling in liquid electrolyte [335]; (d) TEM electrochemical reaction monitoring showing different process steps during the SEI formation, with gas bubble and Li dendrite formation [379]; (e) TEM dynamical observation of Li_2O_2 growing during electrochemical process with voltammetry cyclic and electron diffraction pattern [387]; (f) Analysis of SEI growth process using fast TEM imaging with layer thickness quantification as a function of time evolution on a single Li_2O_2 nanocube [388].

Since the mid-2000s, in addition to the emergence of environmental TEM, the development of *in situ* TEM object holders has enabled scientists in the field of Li-ion batteries to imagine and carry out experiments in which dynamic phenomena could be observed and analysed in real time. Via these numerous devices, materials can be subjected to different stimuli, individually or in combination, such as temperature (cryo and high temperature), contact with a liquid or gas (water, electrolyte or O_2), contact with a metallic tip (indentation or electric measurement) and electric current (in solid/solid or liquid/solid contact). These *in situ* TEM slides fall into two families, those with open cells in which the sample is in the vacuum of the column and those with closed cells which isolate the sample from the vacuum. Open cells have fewer constraints, for instance, they do not have a transparent Si_3N_4 type window and are therefore more stable over time and

allow high resolution TEM analyses and EELS spectroscopy with optimal quality (without absorption/diffusion additional parasite). For these reasons, the first age of *in situ* TEM experiments based its development on the use of open cells with many new studies, but under thermodynamic and environmental conditions far from the actual operating conditions of battery materials.

In recent years, the emergence of TEM cells for electrochemistry based on the coupling of microfluidic and micro/nano-lithography technologies (for the design of specific micro-chips) has opened the way to experiments that approach actual battery operating conditions and thereby reduce experimental biases. To date, several *in situ* studies have been performed on Li-ion battery materials from the recently developed liquid/electrochemical TEM sample holders. Muller *et al.*) are the first to have shown the feasibility of using EFTEM filtered imaging (energy filtering at 5 eV) to follow the (de)lithiation within grains of a $LiFePO_4$ active material cycled in an "anode-free" cell [274]. N.D. Browning et al. observed and quantified the formation of lithium dendrites on a platinum electrode from an aqueous electrolyte [378]. A study of the kinetics of SEI (Solid Electrolyte Interphase) formation on a "glassy carbon" electrode was carried out by R.R. Unocic et al. [384]. H. Zheng et al. observed and analyzed the electrode/electrolyte interface in a 1 M $LiPF_6$ electrolyte in EC/DEC (1:1) with SEI formation and found evidence of SEI detachment induced by the formation of gas bubbles [389]. This field of investigation is in full expansion with three companies that have carried out significant developments in recent years to improve and make more sophisticated devices: Protochips, Hummingbird and DENS solutions. However, manufacturers still must carry out further optimizations to increase both stability (of Si_3N_4 windows, liquid flow, electrochemistry) and the ability to fine-tune cell parameters such as cell thickness and the arrangement of the electrodes.

The methodologies in the development of *in situ* TEM measurements allow quantitative electrochemical measurements to be made by observing, in real time, the specific dynamic reactions with high spatial and temporal resolution. For instance, the device developed by Protochips, makes it possible to perform high-quality electrochemical analyses, as shown in Figure 3.3.2 c in cyclic voltammetry, in complex impedance spectroscopy and in galvanostatics. These measurements are performed using a very low current potentiostat down to 10 pA. In practice, the measurement current is between 1 nA and 1 µA.

This multi-diffusion band strongly limits the use of EELS spectroscopy in a liquid medium, between 25 and 350 eV in the case of the LP30 electrolyte. Muller et al. [274] showed in their study with H_2O the evolution of this band with the thickness of the liquid. They believe that broadband has dominant loss mechanisms of “plasmonic” origin. Indeed, the simple unipolar plasmon model is equivalent in the case to assuming that the fluid electrons behave like free electrons. Several studies have demonstrated the possibility of carrying out EELS measurements in a liquid medium in the region close to the zero-loss peak such as Miyata et al. [299] who measured the vibration modes of the liquid TFSI molecule in the equivalent UV/vis (1-5 eV) and infrared (0.1-1.0 eV) regions. Unocic et al. [390] measured in the core-loss region the L3/L2 Mn thresholds (640-651 eV) of a 40 nm layer of LiMn2O4 with a 100 nm thickness of DMC. These EELS spectroscopic experiments in a liquid medium open new avenue of investigation in the analysis of materials (liquid/solid interfaces) but require both high energy resolutions of 5 to 20 meV

(specifically dedicated TEM) to be interesting and a better adjustment of the thickness of the analysed liquid.

Different electron diffraction techniques, such as 3DED (3D electron Diffraction), 4D-STEM, dark field and SAED (Selected Area Electron Diffraction), turned out to be perfect tools to monitor structural transformation in electrochemical liquid TEM during delithiation processes. Indeed, O. Karakulina et al. [381] in their work demonstrated that electron diffraction tomography (3DED) data can be successfully collected under in situ conditions in a liquid electrolyte electrochemical cell, mimicking the Li-ion battery (see Figure 3.3.1 e). The quality of the diffraction data was sufficient to detect structural changes occurring in the LFP positive electrode material upon charging, including variations in unit cell parameters and changes in occupancy of Li positions and interatomic distances. This opens many possibilities for the structural solution and refinement of a wide range of nanoscale particles from *in situ* transmission electron microscopy experiments, ranging from battery materials to electrocatalysts, as well as all nanoscale particles that undergo modifications or crystallisation in a liquid environment.

Furthermore, L. Lutz *et al.* [388] have reported that fast imagining TEM and HAADF-STEM, using electrochemical liquid TEM devices, are powerful analytical tools to understand the mechanism pertaining to the charge/discharge processes in DME-based Na−O_2 batteries (see Figure 3.3.2 f). They visualised the solution-mediated growth of NaO_2 in real-time and identified that the 3D growth process is governed by the equilibrium between $NaO_{2(solv)} \leftrightarrow NaO_{2(solid)}$ and the mass transport of soluble product. By imaging the charge process, they provide fundamental insights into the parasitic reactions occurring during cycling of a Na−O_2 battery where time-resolved visualisation revealed the chemical reactivity of NaO_2 at the interface with the electrolyte.

In liquid TEM, the electron dose required to perform imaging in a liquid must not exceed the threshold for the decomposition of this liquid. The microfluidic system of the *in situ* cell makes it possible to induce a flow of the electrolyte which eliminates the products of irradiation and to renew the electrolyte. However, the degradation effects of the liquid electrolyte must be carefully assessed to be able to limit them as much as possible. The observation after a significant time (from 3 to 5 minutes) of irradiation of the liquid electrolyte in STEM scanning mode (without microfluidic flow), the formation of aggregates was found [380]. The electron dose provided by the beam depends on the magnification, the size of the exposed area and the electron-conducting capacity of the irradiated materials. Damage or changes induced by the electron beam can be minimised by adjusting the accelerating voltage, condenser diaphragm, spot size and magnification. When high-energy electrons (200 kV) irradiate the solution, primary and secondary diffusions occur, generating radicals and so-called “solvated” electrons, see figure 3.3.2 The electron beam can then act as a reducing agent, where the radicals created, such as solvated electrons, induce the reduction of chemical species in solution such as ethylene carbonate (EC) and dimethyl (DMC) carbonate giving rise to reaction products (C_2H_4, CH_4 and C_2H_6) [380].

3.3.1. FUTURE PERSPECTIVES

The forthcoming advancements in TEM liquid cells, equipped with electrochemical capabilities, must address several inherent limitations that currently impede the real-time monitoring of electrochemical reactions. A pivotal aspect of this enhancement involves the reduction of liquid thickness within the cell. This modification is imperative to augment the quality of data acquisition (4D-STEM, STEM, EDX or even EELS). However, it is essential to maintain a sufficient volume of liquid to facilitate the electrochemical reactions. Therefore, identifying and establishing an optimal balance between these two factors is critical for the development of the next generation of micro-chips. This balance will not only enhance observational accuracy but also significantly expand the potential for *in situ* analysis of electrochemical processes at a microscale level.

The architecture of the electrochemical micro-chip plays a pivotal role in facilitating battery cycling experiments within a liquid TEM. A prime example of this is the ability to analyse both the cathode and anode sides of a micro-battery during electrochemical reactions. This dual-sided analytical capability is advantageous for elucidating the mechanisms of degradation processes and the dynamics of SEI and CEI formation. Such insights are crucial for understanding of battery chemistry at a microscopic scale, thereby contributing significantly to the refinement of battery technology.

It is imperative for the holding company (Protochips, Hummingbird or DenSolutions) to engage in a collaborative endeavour with scientific experts to co-develop microchip designs that are specifically optimised for enhanced battery cycling efficiency. A critical aspect of this design process is the ability to deposit a substantial quantity of active materials. Such a capability is essential not only for generating robust electrochemical signals but also for significantly reducing susceptibility to noise interference. This approach ensures that the microchip design is not only functionally efficient but also robust against the myriads of electrical disturbances that can compromise the integrity and reliability of electrochemical measurements in battery systems.

3.4. OPTICAL SPECTROSCOPIES OF LIQUID ELECTROLYTES

Optical spectroscopies offer the opportunity to probe both the reaction products and compositional changes to liquid electrolyte from interfacial reactions using readily available and relatively inexpensive instrumentation. Both the electrolyte salts and solvents themselves and the interactions between the two have vibrational signatures in the UV, visible and infrared spectra. However, one of the main challenges of using optical spectroscopies to characterize electrolytes is the large number of analytes present simultaneously. Since the techniques can be either chemically non-specific or the signatures can be attributed to multiple species or interactions, distinguishing which component or components of the electrolyte are the source often requires coupling with additional analytical techniques. Nonetheless, there are increasingly frequent examples where optical spectroscopies have been used effectively to understand degradation to the electrolyte itself [391,392], analytes introduced to the electrolyte through cathode degradation [346,393], changes in lithium and anion concentrations [394-396] and to measure heat generated from interfacial reactions [397].

Battery electrolyte degradation products have both absorption [391] and emission signatures [398]. Yan et al. [391] used an *in-situ* cuvette electrochemical cell to measure

the increase in optical absorption of electrolytes during cycling using a conventional benchtop optical spectrometer to better understand electrolyte degradation at electrode interfaces and the formation of redox shuttles. By studying single solvent systems in Na-ion electrolytes, they were able to measure increased UV absorption of linear carbonates (DEC, DMC, EMC) compared to cyclic carbonates (PC, EC) electrolytes after cycling. They combined the absorption measurements with CV experiments to conclude that the increased absorption is likely due to the formation of oxidative degradation products of the linear carbonates.

The approach of adapting a bespoke cuvette cell to make *in-situ* measurements using a conventional spectrometer highlights the typical trade-off in using optical spectroscopies for studying liquid electrolytes. The experimental approach could be executed using simple laboratory instrumentation, but required a bespoke cell, consisting of cathode powder coated onto a wire, dipped into a flooded electrolyte and sealed in a glass cell. The geometry, ratios of components and materials diverge from those of commercial or even laboratory cells. Nonetheless, similar bespoke cells have proved essential for developing more complex optical techniques and have provided value insights to cell performance in their own right.

3.4.1. MICROSCTOPY BASED TECHNIQUES

Optical microscopies are well suited for collecting the optical emission from electrolytes to study their fundamental properties, changes due to electrochemical cycling *ex-situ* after extraction and *in-situ* in bespoke cells. Fluorescent emission from electrolytes can either be collected deliberately or as a broad background signal from Raman spectroscopy measurements. In the case of Raman spectroscopy, the “fluorescent” or broad background is usually seen an obstacle to overcome, overwhelming the more chemical specific Raman signal. However, the broad signal also contains valuable information, such as the strength of hydrogen bonding between the electrolyte components [399], and should not be overlooked as an avenue for study. In order to obtain more chemically specific information from fluorescent signals, fluorophores specific to a metal ion of interest [346,347,394]or other soluble species in the electrolyte can be used [393,400]. Figure 3.4.1.

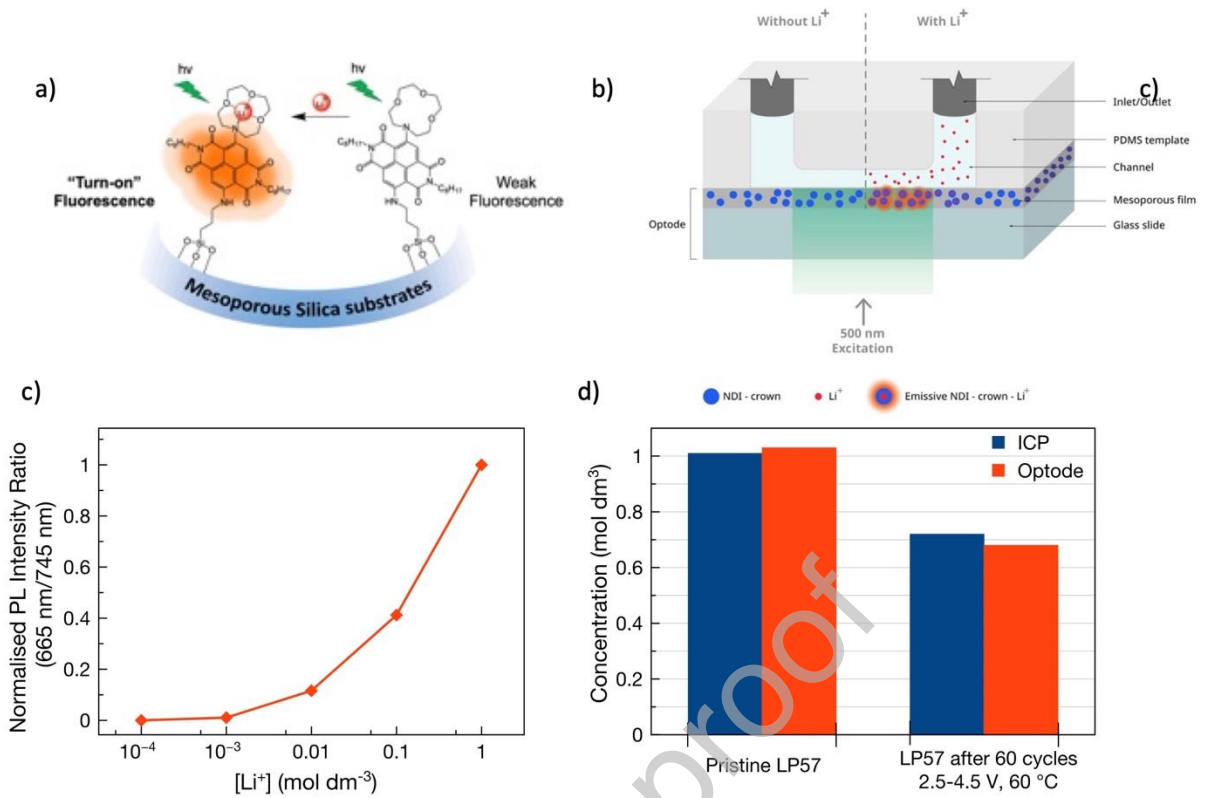

Figure 3.4.1: Scheme for functionalizing mesoporous silica substrate with lithium sensing fluorophore (a). Microfluidic channel for measuring bulk lithium concentration of electrolytes and diffusion constants of lithium salts (b). Thin film photoluminescence of the functionalized mesoporous silica substrate as a function of lithium concentration (c). Lithium concentration measurements of pristine and post-cycled electrolytes using fluorescent sensor and ICP (d).[394]

The use of dissolved fluorophores during cycling presents a number of challenges. First, the fluorophore must either be soluble or functionalize to be soluble in battery electrolytes consisting typically of highly polar aprotic solvents with a high concentrations of lithium salts. Second, fluorophores reduce at the operating potentials of the most common and commercially relevant anodes. Therefore, the fluorophores must either be isolated from the anode using a physical barrier, bonded to the separator or used with an anode operating above the fluorophore's decomposition potential.

Padilla et. al. [347] synthesized a fluorophore (2-(2-hydroxyphenyl)- naphthoxazole, HPNO) with selective "turn-on" fluorescence in the presence of lithium ions. They combined the proportional emission of the fluorophore as a functions of the electrolyte's lithium concentration with wide-field fluorescence microscopy and a microfluidic channel to measure the diffusion constant of lithium chloride (LiCl) in a propylene carbonate electrolyte. More recently, Francis et al. [394] synthesized a highly selective lithium fluorophore based on a crown either attached to a naphthalene diimide modality to operate in commercially relevant electrolytes. The fluorophore was covalently bonded to a mesoporous substrate in a microfluidic device to increase the fluorescent response of the optode (sensor). By using fluorescent microscopy to specially map changes to the lithium concentration in the optode, the self-diffusion coefficient of LiTFSI in blends of carbonate electrolytes could be measured. The optode also was used to accurately measure the depletion in the lithium concentration in a commercially important

electrolyte (LP57) extracted from multilayer pouch cells after cycling due to the consumption of lithium at the electrolyte interfaces.

Fluorescence microscopy also has the potential to be used to monitor transition metal dissolution from cathodes into electrolytes. Qiao et al. [346] took advantage of the cross-sensitivity of a commercial Ca fluorophore to quantify the rate of Mn dissolution from a LMO cathode in an acidic solution and to monitor diffusion of the dissolved ions through the electrolyte. They applied this system to study how alumina coatings can potentially suppress Mn dissolution due to reactions between the electrolyte and the cathode.

Pandya et al. [395] took advantage of the inherent optical emission from the $LiPF_6$-carbonate electrolytes and confocal fluorescence microscopy to three dimensionally map changes to lithium concentrations in commercial electrolytes during cycling in a bespoke cell. They attributed the increased fluorescence around LCO cathode particles to a local increased lithium concentrations at high SOC. Although there is still a limited understanding of origin of the fluorescence in the electrolytes [399,401], the work nonetheless shows the potential power of the combining 3D microscopy to monitor the changes in the emission of electrolytes as they are cycled without chemical labelling.

3.4.2. FIBER OPTIC BASED TECHNIQUES

The insertion of fiber optics into electrochemical cells allows for the measurement of changes to electrolytes *in-situ*, while minimizing the impact to the cell's operation. [148,392] In addition to simply acting a conduit, the fibers themselves can increase the sensitivity of the optical signal by enhancing the interaction length and the spatial overlap between the electrolyte and the optical signal. [148,392] Despite these advantages, the measurement still requires at least a small excess of electrolyte compared to commercial cells so there is free electrolyte with which the optical signal can interact and the use of highly specialized fiber optics. Figure 3.4.2

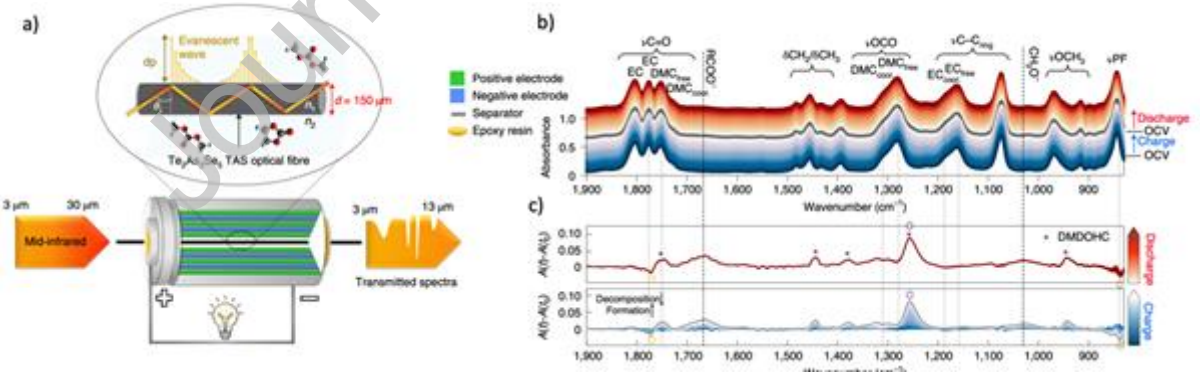

Figure 3.4.2: Scheme for using measuring Raman spectra of electrolytes *in-situ* using a hollow core fiber optic and a microfluidic pump (a). *In-situ* measurements of the electrolyte in the pouch cell showing the consumption of VC during SEI formation (b). [392]

Miele et al. [392] demonstrated that a hollow-core optical fiber could be used to measure *in-situ* changes to the electrolyte's chemical composition using Raman spectroscopy. By sealing the distal tip of a hollow fiber into a small multi-layer pouch cell, the cell's

electrolyte could be sampled using a microfluidic pump. The long interaction length of the fiber filled with electrolyte allowed for sufficient Raman signal to identify both the consumption of vinyl carbonate upon SEI formation and changes to the EC coordination environment during cycling. Figure 3.4.3

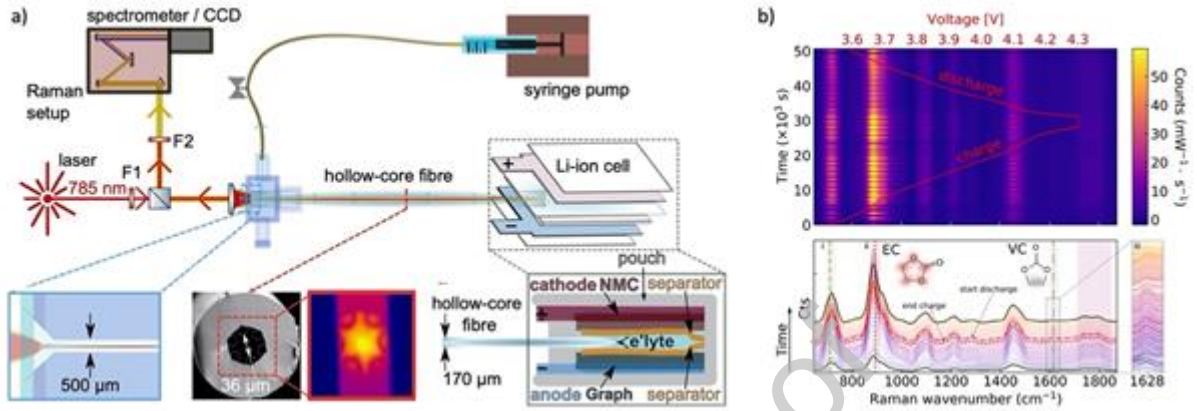

Figure 3.4.3: Scheme for using infrared fiber to measure the IR spectra of battery electrolyte *in-operando* (a). Absorption spectra as a function of state of charge (b). Changes to the relative spectra during charging and discharging showing the formation of degradation species and changes to the coordination environments in the electrolyte (c). [148]

Gervillié-Mouravieff [148] measured the complementary infrared absorption spectra of electrolytes *in-operando* in a commercial cell format also using specialty fiber optics. By inserting an unclad chalcogenide, infrared fiber into a 18650 Na-ion cell, they were able to measure changes to the IR absorption due to the overlap of the evanescent radiation as it propagated through the electrolyte. They too were able to study both changes in the coordination environment of the electrolyte and the consumption of VC during SEI formation on graphite anodes. In the same work, the group also coated the infrared fiber with a lithium iron phosphate in a bespoke half-cell. As the cell cycled, the fiber sensor was able to measure changes to the cathode's IR absorption, which they associated with the changes of the vibrational modes of the phosphate ions as in lithium concentration was modulated.

4. GAS PHASE CHARACTERIZATION

4.1. INTRODUCTION

Analogously to other phase characterization approaches, the contribution of gas analysis to the current understanding of battery interfacial evolution, is spearheaded by the li-ion battery field [402-405]. Although this approach can be, and has been to one degree or another, applied to almost any battery system from Na-ion [406] to redox-flow [407,408], metal-air batteries [409-414], etc.

Gas evolution has a profound relation to the functioning of state-of-the-art lithium-ion batteries (LIBs). The case where this is most obvious is the generation of a solid

electrolyte interface (SEI) on the surface of graphite anodes during the so-called forming protocols [403,404,415,416]. A good illustration of this fact is that in commercial battery operations, it is common practice to blead out the gas generated during forming protocols before delivery [417,418]. Furthermore, the demand for high terminal voltages and wide operational ranges (temperature, charging rates, etc.) increases the stress required of cell components, increasing electrolyte or electrode oxidation [39,403,419-422]. It is also increasingly recognised that materials contributing to the evolution of the SEI during the lifetime of LIBs may originate elsewhere and then migrate (e.g., crosstalk effect) to the anode where they react and accumulate [415,419,423,424].

The gas evolution signature of interfacial processes can be highly informative, as it can be seen in Figure 4.1.1, where several distinctive gassing events are highlighted within a single *operando* experiment (unpublished data from I. Temprano). For instance, the formation of the SEI in graphite anodes is characterized for the evolution of ethylene, carbon monoxide, and hydrogen rich gas mixtures at the beginning of the first cycle, and mostly absent in subsequent charges (Figure 4.1.1 a) [425]. However, the reduction of SEI components can still produce small amounts of hydrogen gas in subsequent cycles (Figure 4.1.1 b) [406,415]. Cathodic oxidation processes on the other hand, tend to evolve oxygen-rich species at high SoC (high cathodic potential) (Figure 4.1.1 c) [419] and can incur in the formation of a cathode electrolyte interface (CEI) or even cathode surface layers (e.g. rock-salt type, in high Ni-NMCs). Soluble products of cathodic oxidative processes can crosstalk to the anode where they can be reduced, further evolving hydrogen and other gases (Figure 4.1.1 d) [406,423]. Electrolyte salts decomposition, such as $LiPF_6$ can lead to the formation of further reactions at the SEI showing evolution of POF_x volatiles [426]. Anode slippage is associated with an increase in the impedance of the SEI and lowering of anodic potential, with the result of increased cathodic potential for a set SoC (Figure 4.1.1 f), exacerbating oxidative processes [427].

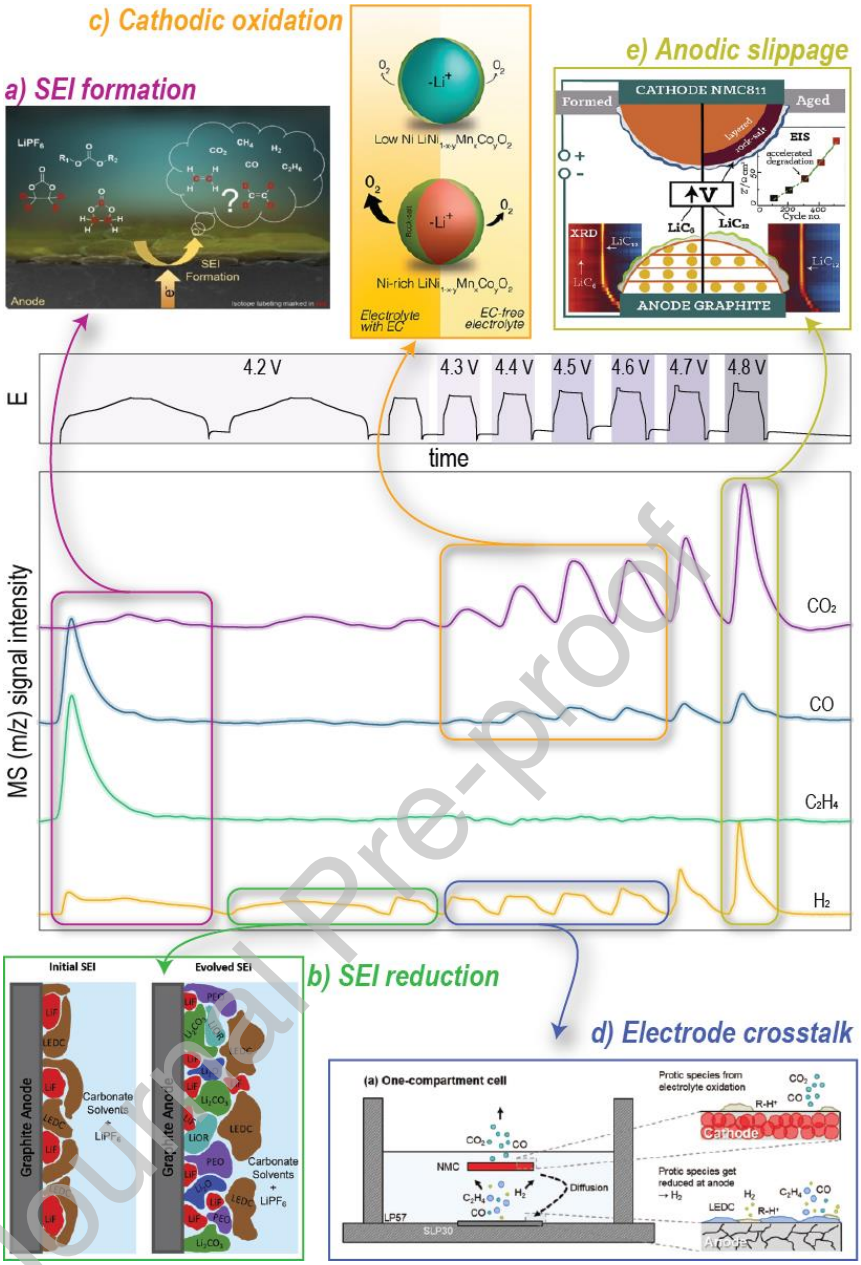

Figure 4.1.1. *Operando* gas analysis data (OEMS) showing voltage profile (top) alongside typical gas evolution profiles (bottom; m/z = 2 for H_2; m/z = 27 for C_2H_4; m/z = 28 for CO; m/z = 44 for CO_2) of electrochemical processes contributing to the formation/evolution of interfaces in LIBs. Cell composition: NMC811|LP57|G, from I. Temprano, unpublished data. Gas evolution events related to notable studies in the LIB literature: a) SEI formation during initial cycle [425]; b) Reduction of SEI components [415]; c) electrolyte oxidation leading to cathode electrolyte interface (CEI) and rock-salt surface layer formation [419]; d) crosstalk of protic species generated during electrolyte oxidation at the cathode and subsequent reduction at the anode [406,423]; e) increased cathodic voltage and accelerated electrolyte oxidation, illustrating the effects of anode slippage [427].

There are currently three general approaches for probing the gas phase in battery systems that can provide crucial information regarding the formation and evolution of interfaces: i) electrochemical mass spectrometry (EMS), in which an electrochemical cell

is connected to a mass spectrometer. This allows the identification and quantification of individual traces of gas evolved during operation with high sensitivity and (temporal/potential) resolution. EMS is currently considered the most complete tool to identify the nature and magnitude of reactions leading to the formation and evolution of battery interfaces, as these processes have very distinctive gas evolution signatures (Figure 4.1.1); ii) pressure monitoring systems (PMS), are simpler than EMS, consisting in a pressure transducer connected to an electrochemical cell. It therefore provides a more limited dataset, however, it is also more robust, easier to scale, and can test more extensively and broader conditions than EMS; and iii) gas chromatography – mass spectrometry (GC-MS), where the gas accumulated in the head-space of a battery during cycling is extracted and injected into a GC-MS system. This is a great complementary technique for post-mortem analysis, and therefore ideal for high-throughput testing. In the next section, we will look in detail at the characteristics of each technique, limitations and potential, as well as the contributions to battery interfacial formation/evolution.

4.2. ELECTROCHEMICAL MASS SPECTROMETRY

4.2.1. EXPERIMENTAL APPROACHES

Electrochemical Mass Spectrometry was first demonstrated by Gadde and Bruckenstein, using a porous electrode coated onto a non-wetting, porous PTFE membrane [428]. The volatile species in solution were driven into the MS via a pressure differential ($\sim 10^{-7}$ mbar inside the MS compared to vs $\sim 10^{+3}$ mbar in the electrochemical cell (Figure 4.2.1 a), hence known as differential electrochemical mass spectrometry (DEMS). DEMS systems showed effective in probing electrochemical reactions in various electrochemical systems, including batteries (Figure 4.2.1 b-c) [404,429]. However, the reliance on a membrane to separate the electrochemical cell from the high-vacuum required for the MS to operate imposes several limitations. For instance, DEMS systems typically use working electrodes coated onto the membrane itself, or onto a mesh in direct contact with the membrane, deviating substantially from technologically practical materials. Furthermore, differences in pumping rate through the membrane due to coating inhomogeneities, pore clogging, etc., make precise quantification challenging, as reproducibility is hard to achieve.

In recent years, DEMS systems have been largely replaced by online setups (OEMS), where an inert gas carries evolved gaseous species into the MS through a capillary (Figure 4.2.1 d-f). OEMS systems can have a variety of configurations, conferring distinctive characteristics. Early stop-go flow systems (Figure 4.2.1 f) relied on automated valves to allow the sampling of gas accumulated in the cell headspace, after a specific residence time [430-432]. This configuration provides high-sensitivity detection, as gases are allowed to accumulate, at the expense of temporal resolution (and thus of potential during galvanostatic cycling), and ought to be considered an *in situ*, rather than *operando* method. Continuous-flow OEMS systems can achieve high temporal/potential resolution [409,410,433,434], and are especially interesting for probing interlinked processes such as electrode crosstalk, crucial for understanding interfacial processes in operating batteries. OEMS systems also offer the possibility of using gas mixtures as carrier gas, flowing through the cell, which can enable experiments where the effect of atmospheric components may be relevant, such as in Li-air cells. This flexibility allows a wide range of

experimental designs, such as cathode/anode separation in dual chamber cells to avoid cross-talk (Figure 4.2.1 d) [410,419,423] isotopic labelling [410,425,435], etc., which can be very insightful in developing mechanistic understanding of interfacial reactions [402].

Various approaches to continuous-flow OEMS exist in the electrochemical literature. The most common design consists in a cell with a small headspace through which a continuous flow of carrier gas washes volatile species from the cell through a capillary into the MS (Figure 4.2.1 d) [410,436]. This setup relies on a constant pressure of the gas line and a small gas flow through the capillary, measuring rates of gas evolution, as shown in Figure 4.1.1. In order to achieve high sensitivity with this system, low gas flow through the capillary is required, however this can result in a low time resolution and long time for evolved gas to clear off the cell headspace, so a balance through careful design around the headspace/capillary section of the system is critical.

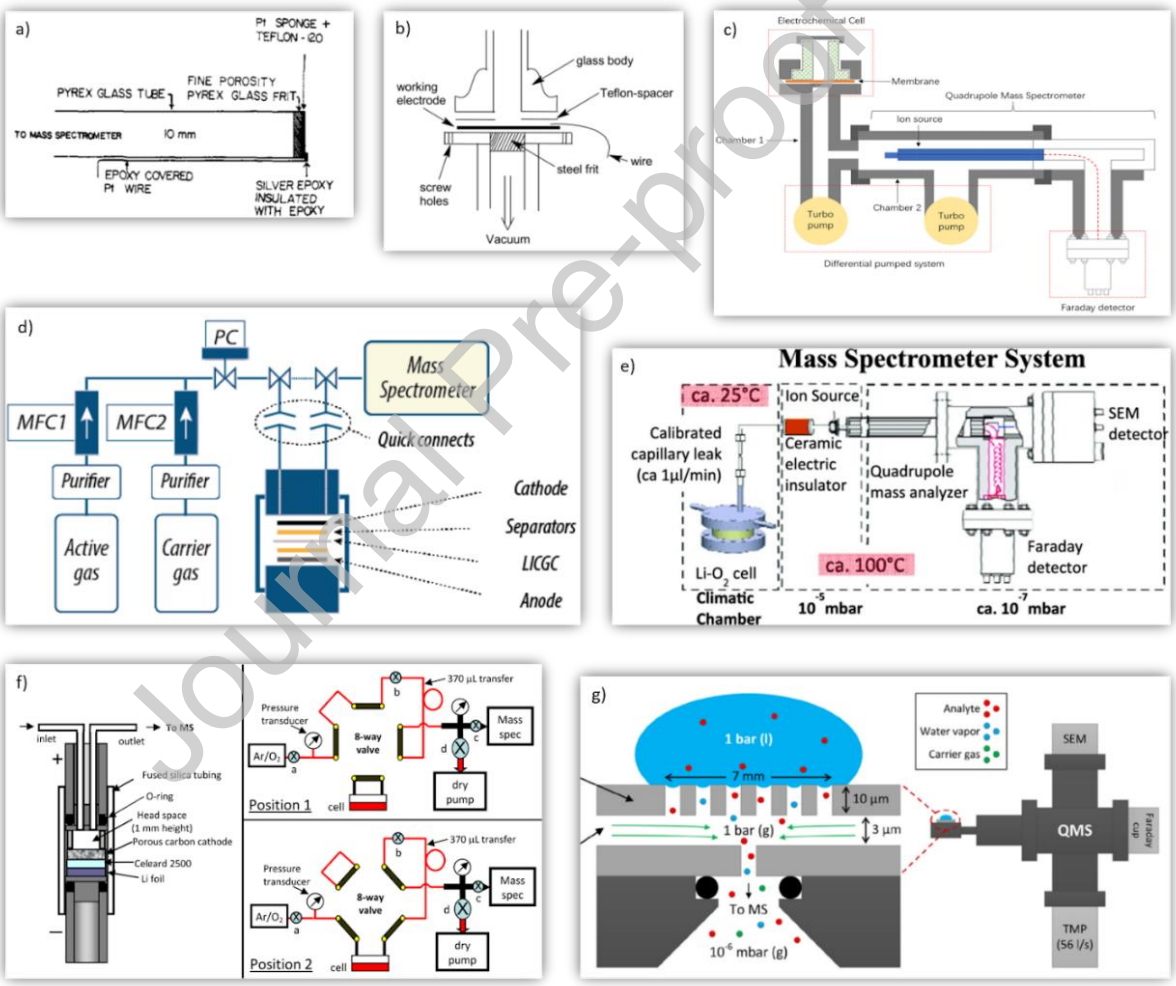

Figure 4.2.1. Schematic representations of various EMS configurations. a) Original DEMS system with a membrane mounted on a glass frit served as interface between a MS with the electrochemical cell [428]; b) Detailed representation of the component parts of a DEMS cell and c) DEMS full system [429]; d) Continuous-flow OEMS system with constant gas-line pressure [410]; e) Capillary leak OEMS with fixed gas reservoir [409]; f) Stop-Go

flow OEMS system with residence-time sampling [430]; g) On-chip OEMS with membrane and carrier gas [437].

An alternative OEMS design, developed by the Gasteiger group [409], uses a cell with a large headspace that is filled with an inert gas at the beginning of the experiment. The headspace of the cell is then connected to the MS via a capillary of very small internal diameter, allowing very low gas flow rates out of the cell (Figure 4.2.1 e). In this configuration, the pressure in the cell headspace is gradually reduced over time (by a small amount), so control of the flow rate into the MS, and experimental time limitations are important balancing considerations. The MS data acquired with this setup indicates the concentration of gases in the headspace at any given time, so when a gas evolution event occurs, the signal of the gas increases until reaching a plateau, which is then the new baseline for that particular gas (Figure 4.2.2 b). Analogously, any reduction in signal intensity for any mass/charge (m/z) channel in this setup indicates gas consumption (i.e. reduction of the concentration of a species in the gas phase) from the cell (e.g., initial CO_2 consumption as shown in Figure 4.2.2 b).

Other EMS designs have been explored, some combining advantages of different setups. An example of this involves using an electrochemical cell with a porous membrane (silicon microchip) connected to a small volume chamber, which separates it from the MS inlet. This small volume is kept at a constant pressure ($\sim 10^{+3}$ mbar) with an inert gas that serves as carrier for the volatile products generated in the cell to the MS (Figure 4.2.1 g) [437,438]. Large/commercial cell formats are also a target for this technique, as it is highly interesting for materials and cell manufacturers. Geng et al. explored the possibility of connecting a capillary embedded in a pouch cell directly to a MS, reporting high accuracy measurements [439], while the Berg group recently adapted an intermittent OEMS design for large-format PHEV2 cells [440].

4.2.2. BATTERY INTERFACIAL PHENOMENA STUDIED BY EMS

Parasitic reactions leading to electrolyte decomposition and interphase formation during LIB cycling can have very distinctive gas signatures, as shown by EMS data in Figure 4.1.1. In recent years, EMS has assisted in identifying a number of processes directly involved in the evolution of battery interfaces, and in LIBs in particular [402].

The formation of a SEI on graphite anodes is arguably the most significant, and therefore the most studied, interfacial phenomenon in commercial LIBs. Novák and collaborators showed in 2001 that the reductive decomposition of an ethylene carbonate/dimethyl carbonate (EC/DMC) electrolyte on various porous graphite composite electrodes at potentials below 1.0 V (vs Li/Li^+) [441], resulted in the evolution of gaseous products, mostly ethylene (C_2H_4) and H_2 (Figure 4.2.2 a), during the first two charges, alongside an increase in cell ohmic resistance. Sacrificial additives, such as γ-butyrolactone, were shown to supress gas evolution during SEI formation, establishing gas evolution as a useful proxy for SEI formation and stability. Similar gas mixtures were observed by the Novák & Berg groups at $Li_4Ti_5O_{12}$ (LTO) anodes during the first charge at high temperatures with EC-containing electrolytes, with CO_2 evolving only at lower anodic potentials [431].

Long-term EMS testing (> 30 cycles) on an NCM523/graphite cell by Janek and co-workers demonstrated that the formation of the SEI via EC reduction, characterised mostly by C_2H_4 evolution, is indeed almost limited to the first formation cycle (Figure 4.2.2 c) [442]. H_2, CO and CO_2 were also identified as products of anodic reactions during SEI formation using half-cells. However, in full cells the evolution of small quantities of H_2 and CO_2 was also observed in every cycle between 3.0 and 4.4 V, suggesting a link between both species involving the reduction of organic species at the graphite electrode. H_2 has also been reported to be produced from reduction of organic SEI components (Figure 4.1.1 b) such as lithium ethylene dicarbonate (LEDC) [415,423]. Gasteiger and collaborators showed that while the SEI formation in neat electrolytes results in the evolution of C_2H_4 and small amounts of H_2 from the reduction of EC, traces of H_2O yields larger amounts of H_2 and considerable amounts of CO_2 (Figure 4.2.2 b) [443]. The gas analysis also revealed that pre-cycling graphite electrodes in vinylene carbonate (VC) containing electrolyte can significantly lower H_2 evolution, thereby mitigating the influence of water. In a subsequent study, reduction of VC during charging before VC cathodic oxidation occurs above 4.3 V, sohwed to effectively passivate the anode in graphite/LNMO cells [444].

The gas signatures of cathodic degradation processes can further our understanding of interfacial phenomena at the cathode (Figure 4.1.1 c), as well as the influence of crosstalk effects on the SEI (Figure 4.1.1 d). Gasteiger and collaborators showed that protic species ($R\text{-}H^+$), formed alongside CO_2 during electrolyte oxidation, can diffuse from the cathode to the anode and be reduced, explaining the observed H_2 evolution [423]. Acidic protic species from EC oxidation were also shown to cause $LiPF_6$ decomposition into HF, PF_5, POF_3, with the latter two detected in the gaseous phase, while the reduction of HF at Li anodes emits H_2 [426]. Transition metal dissolution (Ni^{2+} and Mn^{2+}) was also identified as leading to an increase of ethylene evolution from EC reduction at the negative electrode, decomposing organic SEI components, such as LEDC, into lithium carbonate thereby reducing the protective effect of the SEI [445].

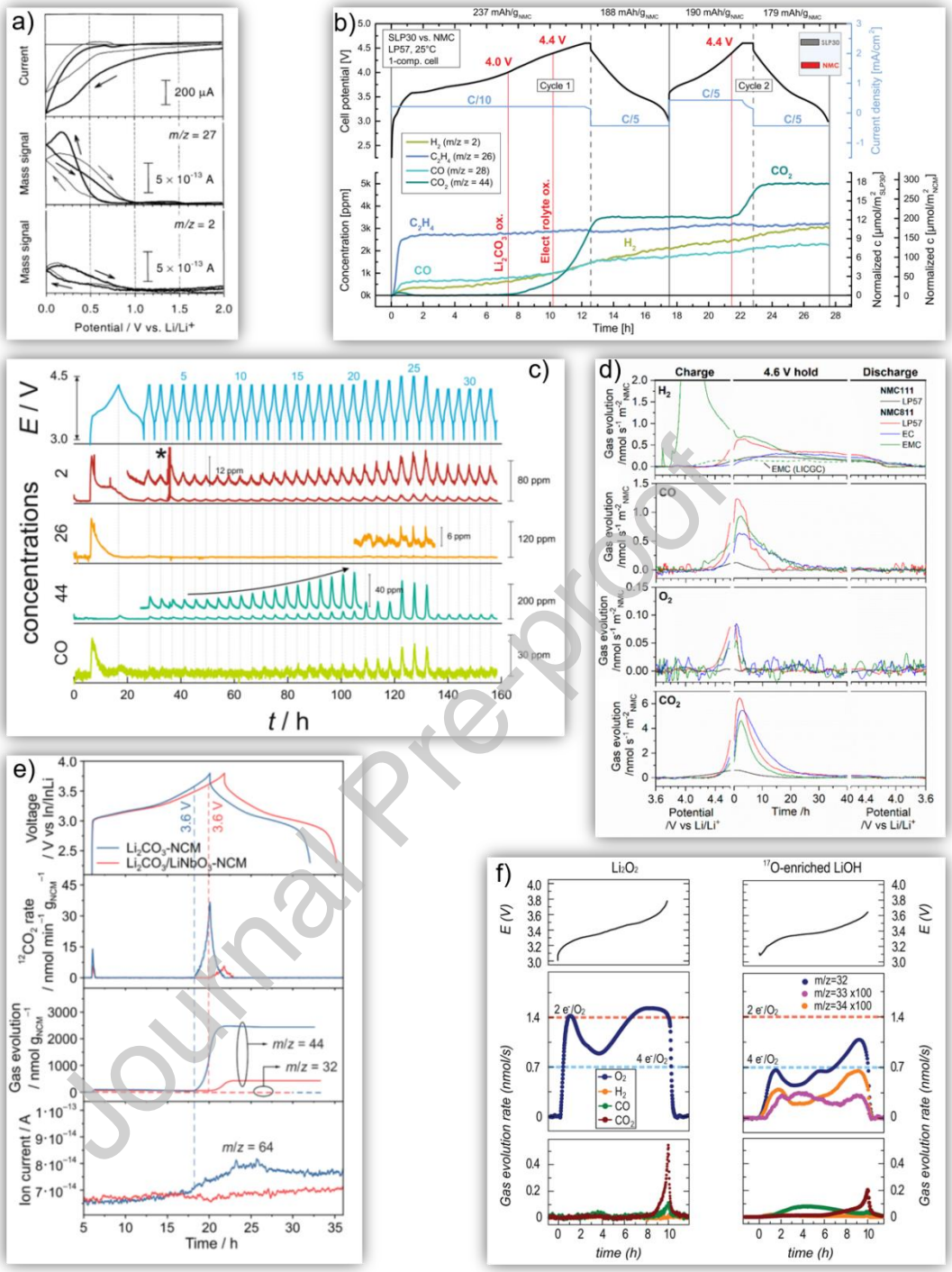

Figure 4.2.2. a) CVs and MSCVs recorded for graphite in LP30 electrolyte (1 M $LiPF_6$ in EC:DMC = 50:50 (v/v)) showing the MS channels m/z = 27 (C_2H_4, middle) and m/z = 2 (H_2, bottom) [441]; b) OEMS data during first two formation cycles of an NMC||graphite full-cell with LP57 electrolyte (1 M $LiPF_6$ in EC:EMC = 30:70 (v/v)) showing evolution of H_2 (green), CO (turquoise), C_2H_4 (blue), and CO_2 (dark green) (MS channels m/z = 2, 26, 28, and 44, respectively); c) Long-term OEMS testing (> 30 cycles) on an NCM523||graphite cell using LP57 (m/z=2 represents H_2; m/z = 26 C_2H_4, m/z = 44 CO_2) [442]; d) Electrolyte-dependent evolution of H_2 (top), CO (middle-top), O_2 (middle-

bottom), and CO_2 (bottom), (MS channels m/z = 2, 28, 32, and 44, respectively), and normalized to the NMC surface area: for NMC||Li cells during the first charge−discharge cycle between 2.5 and 4.6 V with a 40 h potentiostatic hold at 4.6 V [419]; e) First cycle voltage profile of SSB cells using Li_2CO_3-coated (blue) and Li_2CO_3/$LiNbO_3$-coated NCM622 (red) showing CO_2 signals (m/z = 44, top-middle and cumulative amounts in middle-bottom) and SO_2 evolution (m/z = 64, bottom) [403]; f) OEMS data evolution during charge of a Li-O_2 cell with electrochemically Li_2O_2 preloaded electrodes (left) and LiOH using ^{17}O-enriched H_2O as protic source (right) showing evolution of O_2 (middle, m/z = 32 $^{16}O_2$; m/z = 33 $^{16\text{-}17}O_2$; m/z = 34 $^{17}O_2$), and H_2, CO and CO_2 (bottom, MS channels m/z = 2, 28, and 44, respectively) [410].

EMS studies of cells with Ni-rich NMC cathodes illustrate the capabilities of this technique to provide a mechanistic understanding of the complex interplay of effects leading to interfacial evolution in LIBs. Comparing the gas evolution at NMC111, NMC622 and NMC811 electrodes, Gasteiger and collaborators noted for all three compositions oxygen release from the active material particles surface (Figure 4.2.2 b), with the onset occurring at lower potentials when increasing Ni-content [446] Further analysis however, revealed the O_2 evolution onset to be a function of the SoC and constant for the three materials tested, with CO_2 and CO evolution associated with oxygen loss via solvent oxidation. Grey, and collaborators later showed that larger lattice oxygen release occurred in the presence of EC-containing electrolytes (Figure 4.2.2 d), causes higher cathode interfacial impedance, a thicker oxygen-deficient surface reconstruction layer (rock-salt phase), a more pronounced electrolyte breakdown and transition metal dissolution [419,447-449]. H_2 evolution was also reported throughout potentiostatic holds at high SoC, confirming the complex interplay between oxidative and reductive processes at the positive and negative electrodes respectively (Figure 4.2.2 d – top panel) [424].

Beyond contributing to the understanding of interfacial formation and evolution in conventional LIBs, EMS has also shown effectiveness in other battery systems, and promises deeper understanding of interfacial processes in solid-state batteries (SSBs), post lithium intercalation chemistries (Na-ion in particular) and metal-air batteries. The groups of Janek and Brezesinski recently showed the formation of robust interfaces in the cathode layer, strongly suppressing CO_2 evolution (Figure 4.2.2 e) in high Ni-NMCs, indicating that high-capacity retention can be achieved in pelletized SSB cells using sulphide SEs. These results also revealed SO_2 as a particularly representative marker for interfacial instability of sulphur-based SEs [403,450]. The instability of the SEI in Na-ion batteries (NABs), mainly caused by higher solubility of SEI constituents in Na-electrolytes, is one of the applications where gas analysis can provide much needed clarity. EMS data has confirmed that electrolyte reduction gives much larger contributions to the gassing in NABs compared to LIBs, not only from direct electrolyte reduction but also from the soluble species, which migrate to the cathode, where they further oxidize [406]. EMS has been extensively used in Li-air batteries (LABs) to study the mechanism of formation and removal of electrode/discharge-product/electrolyte interfaces, emerging as one of the most important tools in the field. The formation of different discharge products (e.g. Li_2O_2, LiO_2, LiOH) can thus be evaluated by measuring the rate of O_2 consumption (Figure 4.2.2 f). Furthermore, the stability of the electrode/electrolyte interface during charge is typically assessed by measuring the production of CO_2, which is particularly relevant in

LABs due to the high overpotentials typically reached at the end of charge (Figure 4.2.2 f) [409-412].

4.2.3. FUTURE PERSPECTIVES

Although EMS is a powerful technique to investigate the mechanisms of interfacial formation and evolution in battery systems, there are some inherent limitations. A fundamental challenge for any EMS setup design is the sampling of not only gaseous species from relevant processes, but also of any volatile species present in the electrolyte. This is an issue for most battery chemistries with liquid electrolytes, as commonly used solvents have relatively high vapour pressures. As a result, electrolyte levels, salt concentration, solvent ratios, etc., change during testing, in long experiments in particular. The application of EMS is thus currently limited to mostly short cycling protocols (10-100 hours) to investigate processes over a few charge-discharge cycles.

Novel EMS systems should be therefore designed with careful consideration of the gas flow through (or pumping speed from) the cell into the MS. This should also be carefully taken into account when designing experiments, with stricter limitations on testing time and temperature required in setups with higher gas flows. On the other hand, very low sampling flows increase response time, which is problematic especially in the study of interlinked processes such as crosstalk, so a balance must be carefully considered for each setup. The development of EMS systems that can investigate gas evolution trends during extended cycling therefore highly desirable. Stop-go systems can be adapted to allow long-term cycling EMS testing, by using bypass valves that allow operando gas sampling at specified cycles. This would enable the integration of EMS in long-term cycling investigations without compromising the electrolyte integrity.

Widespread EMS implementation ought to involve the standardisation of electrode configuration, in order to provide more meaningful comparison with commercially relevant materials. This is particularly challenging for DEMS setups, where the use of a porous membrane directly in contact with the working electrode limits the options. For that reason, the use of electrodes coated onto foils using standard production procedures and treatments (e.g., calendaring) ought to be a priority in EMS studies. These considerations could also push EMS towards integration in multimodal characterization setups, which could be considered the ultimate goal for battery characterization systems. A step in that direction has been made by Janek and collaborators, developing a dual gas analysis system capable of simultaneous acquisition of mass spectrometry and infrared spectroscopy data in a continuous-flow setup [451]. More efforts on the integration of EMS systems with other solid/liquid-probing electrochemical testing methods in multimodal characterization rigs would be highly desirable in future.

4.3. PRESSURE MONITORING SYSTEMS

Pressure monitoring systems (PMS) have also been extensively deployed in the academic literature to prove the gassing caused by parasitic reactions in electrochemical cells.

4.3.1. EXPERIMENTAL APPROACHES

Comparatively to EMS, PMS provides more limited information, relying exclusively on the total pressure of the cell rather than the partial pressures of individual components of gaseous mixtures. This is not necessarily a limitation in cases where the process under investigation relies on gas absorption, such as Li-O_2 cell discharge (Figure 4.3.1 a) [452,453], but it is for most battery interface-related processes. Nevertheless, careful experimental designs can enable the quantification of interfacial processes in half-cells by pairing the electrode of interest with counter electrodes of predictable gassing behaviour, or even using two-compartment cell configurations, which can be used to evaluate the extent of crosstalk effects. PMS offers, on the other hand, complementary attributes in relation to EMS, as it can be used on a wider range of cycling conditions, including extended and high temperature cycling, calendar life testing, and combinations thereof. This stems from the fact that PMS are closed systems, and therefore electrolyte evaporation is not an issue. PMS are ideal to track and quantify particular processes, such as SEI evolution, over extended cycling protocols, once the processes at play have been identified using complementary techniques (e.g., EMS, GCMS, XRD).

4.3.2. BATTERY INTERFACIAL PHENOMENA STUDIED BY PMS

PMS data has been often reported in the academic literature related to mechanistic studies of battery interfacial phenomena alongside EMS (and other *operando* methods), for its complementarity [454,455].

The use of PMS in the LIB field is also widespread, in particular to probe the stability of the SEI formed with different electrode/electrolyte combinations and cycling protocols. Most studies of interfacial formation and evolution in LIBs involving PMS do so in combination with multiple complementary characterization methods. Using this approach, Janek and collaborators probed the gassing associated with the formation of dead lithium in LTO half cells, with EMS providing complementary data [456]. In the same study, the increased thermal decomposition of $LiPF_6$ at higher temperatures in NMC622 full cells was also reported using the PMS/EMS combination. Volume expansion during Li intercalation at the anode is one of the physical processes affecting the integrity of the SEI to greater extents. The graphite lattice expansion upon lithiation was also explored using a combination of PMS and *operando* XRD by Janek and collaborators (Figure 4.3.1 c) [455]. A total volume expansion of 13.2% was identified during lithiation, with ~ 5.9% occurring in the early dilute stages, and ~ 7.3% due to transition from stage 2 to stage 1 (Figure 4.3.1 c). This work highlights the potential of PMS to prove reversible and irreversible processes during interfacial evolution.

Grey and collaborators used PMS in combination with solution NMR to study electrolyte degradation pathways and onsets in LCO half cells with LP30 electrolyte [364]. This experimental combination allowed the mapping of parasitic processes occurring at the interfaces of either electrode via the identification of soluble products in the electrolyte and correlation to gas onset potentials. High-throughput studies of degradation processes in batteries under realistic conditions were demonstrated by Janek and collaborators, who developed a multichannel PMS system (Figure 4.3.1 b) [454]. This setup included a liquid-cooling system to minimise heat generated in parasitic processes causing thermal expansion, affecting the accuracy of the pressure measurements. Such systems can be

widely adopted by battery R&D units at reasonably low cost for the development of cell chemistries with stable interfaces.

Pressure monitoring systems have also been deployed to track volume expansion/compression, detecting irreversible interfacial processes in all-solid-state batteries [450]. Although, strictly speaking, this is not a gas evolution detection system, the principle of operation and setup are analogous. PMS has been particularly used in the Li-O_2 battery field to evaluate the nature of the discharge product being formed during the oxygen reduction reaction (ORR) in discharge processes. The differentiating gas phase stoichiometry of the ORR leading to different discharge products, and therefore new interfaces with different morphologies, properties and stabilities, has been extensively probed using PMS [435,453,456,457]. A clear example of the use of this technique to assess the formation/removal of these interfacial species in Li-O_2 batteries is shown in Figure 4.3.1 d. In this study, Grey and collaborators report the CoO_3-catalysed formation of LiOH during the ORR, characterized by a $4e^-/O_2$ process during discharge. However, the PMS shows that this is not reversible during the charge, as two processes with different stoichiometries (7.8 and 2 e^-/gas respectively) are observed, indicating interfacial instability rather than oxygen evolution reaction [435].

4.3.3. FUTURE PERSPECTIVES

Pressure monitoring systems are simpler than electrochemical mass spectrometry, as they do not require complex gas flow/control systems and pressure transducers are single channel devices. They also do not require special electrode preparation, since gas transfer is not required for detection as DEMS systems do. As a result, PMS cost a fraction of EMS, are easier to develop, operate and maintain, and are more reliable. These factors make this technique far more affordable and scalable, and as such, they are common battery testing equipment in commercial R&D settings, for high-throughput (multichannel) *in situ* gas quantification under realistic operative conditions. PMS simplicity and close system configuration makes it also very easily coupled with other characterization methods, providing an extra dimension in multimodal characterization systems.

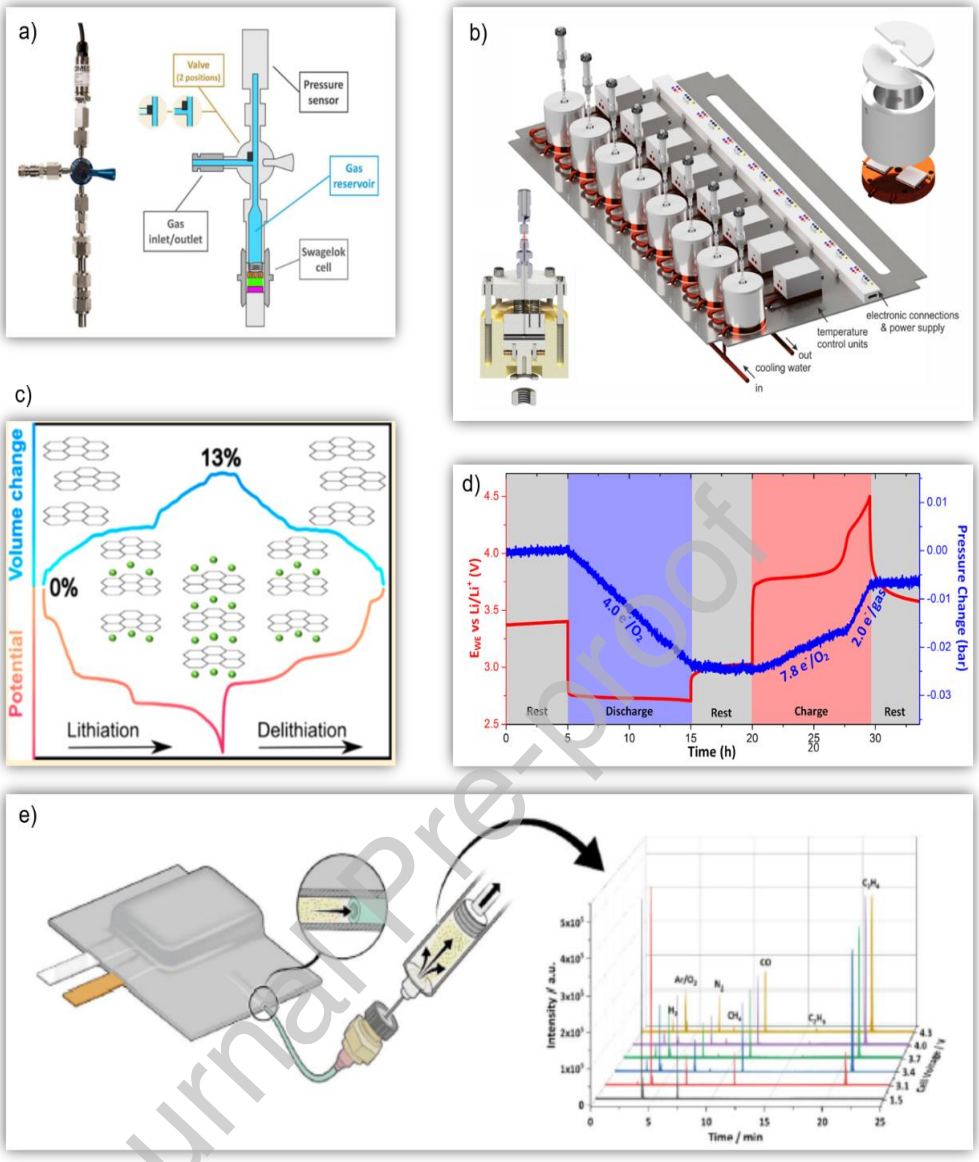

Figure 4.3.1. Schematic representations of experimental setups and data of PMS and GC-MS systems. a) PMS for Li-O_2 battery testing with relatively large gas reservoir [456]; b) multichannel PMS system for degradation studies of LIBs [454]; c) PMS data of volume changes during lithiation of graphite anode [455]; d) PMS data measuring the stoichiometry of the discharge and charge processes of a Li-O_2 cell [435] e) Potential dependent *in situ* GC-MS schematic and data [458].

4.4. GAS CHROMATOGRAPHY – MASS SPECTROMETRY

Gas chromatography mass spectrometry (GC-MS) is a routine technique in academic and industrial battery testing, both for the analysis of the liquid and gaseous species, with many scientific instrument manufacturers offering solutions specifically for this application.

4.4.1. EXPERIMENTAL APPROACHES

GC-MS is a versatile and high-throughput post-mortem characterization technique that evaluates the nature and extent of gas produced in batteries due to cell component degradation. The gas accumulated in cells of almost any configuration can be sampled before cell tear down, providing an extra dimension to post-mortem analysis.

4.4.2. BATTERY INTERFACIAL PHENOMENA STUDIED BY GC-MS

The identification and quantification of gas phase degradation products provides extra information on the mechanism and severity of the reactions leading to degradation and capacity fading, as well as interfacial formation and evolution, and it can be applied to both cycling and calendar testing. An area of battery R&D where GC-MS is particularly useful is to assess the SEI formation process in combinations of electrode/electrolyte formulations and formation protocols in commercial settings. This involves high-throughput testing and post-mortem analysis of batteries with assembly protocols and materials very close from commercial production lines after the formation protocol, as well as after ageing (cycling or calendar). The information provided by the GC-MS is highly informative in relation to the nature and extent of electrolyte degradation incurred in the formation of the SEI, as well as the level of protection to subsequent degradation that this interface provides.

A clear illustration of the capabilities of this technique was provided by Sascha Nowak and collaborators, who recently used GC-MS to identify the origin of gaseous decomposition products evolved during SEI formation in LIBs. Isotopically labelled electrolytes were used to evaluate the SEM formation of NMC622 full cells using GC-MS [425]. The use of $^{13}C_3$-EC and D_4-EC were used to assign formation gas products to the individual constituents of the electrolyte mixture. The effect of common linear carbonates in combination with EC, as well as the effect of VC as film forming additive was also identified using GC-MS.

4.4.3. FUTURE PERSPECTIVES

Novel approaches to perform *in situ* GC-MS battery testing have been made recently [403,439,458]. The principle of this approach is to fit a capillary tube heat-sealed into the inner layer of a pouch cell with which gas produced can be directly sampled by the GC-MS system (Figure 4.3.1 e). A related *in situ* GC-MS system, proposed by Schmiegel et al., consists in connecting the capillary to a rubber seal that can be used to syringe out the gas accumulated during a certain time interval [458]. This concept could be automated by connecting the capillary directly to a pneumatic valve that would allow intermittent sampling of trapped gas inside of the pouch cell, analogous to the proposed automated stop-go EMS system.

5. COMPUTATIONAL MODELLING & SIMULATION

5.1. INTRODUCTION

To understand battery interfaces at the atomic level one first needs to identify probable interface structures and chemical reactions as well as potential energy surfaces for Li-ion migration across the interface. In solid-liquid interfaces, the distribution of mobile cations

and anions in the liquid forms an electric double layer (EDL) [459]. The EDL is responsible for the surface charge screening on the solid as well as the interfacial potential change. The ionic distributions in the EDL can be modelled using the Gouy-Chapman theory, which, developed in the early 20th century, provides a foundational framework for calculating the potential distribution and ion concentration profiles within the EDL, assuming ideal conditions such as point charges and a continuous potential distribution. Modern approaches beyond the Gouy-Chapman theory incorporate the finite size of ions, ion-ion correlations, and surface heterogeneities, offering more accurate descriptions of the EDL. Techniques such as modified Poisson-Boltzmann equations, molecular dynamics simulations, and Monte Carlo methods provide refined models that account for these complex factors [460].

In contrast to EDLs in solid-liquid interfaces, solid-solid interfaces often contain only mobile cations and they can be analyzed using band theory, where Fermi energy alignment on both sides of the interface leads to the formation of a so-called ionic space charge layer (ISCL) [461]. Moreover, electrodes might induce reduction or oxidation processes in electrolytes [462], affecting the electrical conductivity of the interface as well as inducing undesired interfacial reactions. Therefore, from a theoretical viewpoint, the accurate characterization of the electronic and atomic structure of battery interfaces of technological interest is not an easy task and often requires efficient and robust first-principles theory. A proper description of the ISCL typically requires quantum mechanics to accurately obtain electronic states and Fermi energies [463,464].

In addition, it is important to keep in mind that a characteristic feature of both solid-liquid and solid-solid battery interfaces is their highly disordered and defective atomic structure, which is a consequence of the cationic migration across them during charge and discharge cycles. It is important to account for such atomic structure complexity in the simulations [465] because it can significantly modify the underlying interfacial electronic structure, which in turn governs the stability and ionic transport properties of the interface.

Over the last decades, density functional theory (DFT) has been the standard quantum mechanical method for the atomistic modelling of condensed matter [466], giving an insight into the functional properties of a breath of applied materials [467]. Yet, this physical-based method is generally computationally intensive, with limited access to complex, low-symmetry structures, such as interfaces. This is because the evaluation of atomic dynamics, including reactivity and ion migration processes, in complex systems requires exhaustive explorations of tortuous potential energy landscapes, which is a computationally expensive task for current Petascale computer resources. The imminent advent of an Exascale era could mitigate this issue, but the expected high-power consumption associated with compute-intensive workloads will probably make the approach unsustainable for scaling [468]. This therefore limits the use of DFT-based calculations to examine, for example, complex interfacial structures as a function of charge carrier concentration. And less computationally intensive alternatives to DFT-based computations [469] often come at the expense of structural detail, quantitative predictability, and transferability.

In this section we discuss a diverse selection of successful case studies where DFT-based approaches have yielded significant results over recent years. We focus on emerging new physicochemical understandings and general concepts that atomistic modelling and simulation is capable of providing, which is clearly invaluable insight for experimental interface characterization. Given the mentioned drawbacks of current DFT-based approaches to cope with more and more complex interface systems, we also provide an account of recent pioneering works that are trying to tackle these limitations head on. In this direction, we discuss some examples of recent implementations of reactive force fields (ReaxFF) and show how some techniques borrowed from network science (NS) and machine learning (ML) hold great potential to effectively examine battery interfaces. Essentially, these approaches aim at moving beyond the length and time scales accessible at DFT level , while retaining high accuracy at relatively low computational cost (Figure 5.1.1).

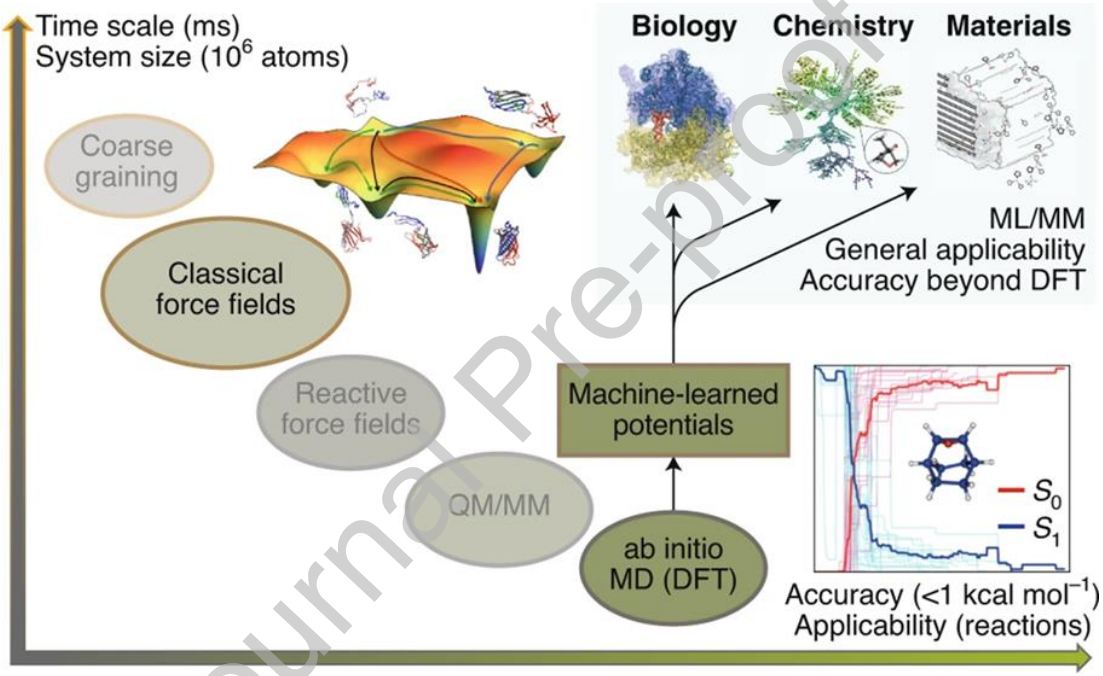

Figure 5.1.1. Interplay between system scale and simulation precision for different methodologies. While ReaxFF and other approaches provide access to length and time scales inaccessible to DFT-based simulations, their accuracy and degree of applicability gradually diminishes. In contrast, MLIPs can maintain high accuracies while simulations increase in time and system size [470].

5.2. DENSITY FUNCTIONAL THEORY

Computational modeling can be a useful complementary tool to guide the synthesis of new materials and design improved battery interfaces. For example, the possibility of intermixing of atomic species at electrode-electrolyte interfaces during synthetic procedures is often a difficult process to understand by stand-alone experimental insight. By combining thin-film X-ray spectroscopy with DFT calculations, Howard *et al.* [471] showed that Ti and Mn species intermix at the interface between $LiMn_2O_4$ and $Li_{3x}La_{2/3-x}TiO_3$ at synthesis temperature; and the theoretical insight revealed that this effect is not

thermodynamic but kinetic, providing new avenues for synthesis optimization. Moreover, when implemented in high-throughput materials discovery schemes, DFT-based calculations can also be applied to effectively examine the electrochemical and chemical thermodynamic stability of large numbers of solid-solid contacts at the electrode-electrolyte interface [471-473]. This strategy has indeed shown good applicability in the search of crystalline compounds as coatings for many cathode materials in contact with solid electrolytes [474-482]. Similarly, the approach can be used to screen a diverse range of systems such as anode-electrolyte interfaces [482-484], amorphous coatings [485], and double-layer coating designs [486].

The characterization of the structure of SEI layers is another important area where atomistic simulations can provide valuable insights to complement experiments. In this context, DFT calculations are particularly useful to unveil the chemical composition of the SEI that forms on graphite in electrolyte solutions, aiding to interpret the results of Raman, XPS, XAS, and other experimental probes [487-490]. Similarly, the approach has also been applied to simulate SEI on other anode materials such as silicon [63,491] or different metals (Li, Ca, Al, Mg, etc.) [492-495] as well as better understand the evolution of key SEI components such as LiF [496] and cathode electrolyte interface (CEI) formation [497]. These approaches could be further enhanced in the future when combined with NS [498], as recently demonstrated by Blau *et al.* [499] to identify reaction pathways towards the formation of lithium ethylene dicarbonate at the SEI of Li-ion batteries. In this study around 6.000 different chemical species and over 4.5 million reactions were taken into account to deduce a complete reaction network on a laptop in less than a day. Xie *et al.* [500] considered a similar approach to examine the formation of lithium ethylene monocarbonate and dicarbonate at the SEI, finding that the presence of water in the reaction pathway limits the formation of lithium ethylene monocarbonate. This insight opens the possibility of controlling the ratio of lithium ethylene monocarbonate and dicarbonate at the interface, and is clearly invaluable for guiding experimental characterization efforts.

It is also worth noting that current innovations in battery materials require the sampling of increasingly large and complex configuration spaces, including disordered and metastable structures, to identify those with superior multi-functional properties [501]. This complexity raises fundamental scientific questions about how substitutional (dis)order affects material properties, particularly in the evaluation of equilibrium phase diagrams. Addressing these questions is crucial, but a comprehensive high-throughput exploration of configurations, such as those found in high-entropy alloys and ceramics, is impractical due to the immense computational costs associated with the required DFT calculations. To overcome these challenges, accurate approximations and the development of methods that avoid performing vast amounts of DFT calculations are necessary. One effective way to reduce computational costs is by employing the cluster expansion (CE) technique [502]. When combined with Monte Carlo methods, CE allows for the efficient evaluation of thousands or even millions of atomic arrangements with sufficient accuracy to determine the ground state configuration for a given composition. In this statistical mechanics approach, a probability distribution is determined, enabling the evaluation of the partition function and the average thermodynamic properties of the ensemble [503]. For a thorough review of this and related approaches, interested readers are referred to Ref. [504]. The success of the CE method has been demonstrated in

numerous battery material studies, notably in investigating phase stability and evaluating open-circuit voltage profiles across the composition range of alkali-ion electrode materials (see, e.g., [505,506]). Enhanced sampling methods based on molecular dynamics also hold significant potential for addressing the sampling problem. These methods aim to accelerate the dynamics of complex systems in simulations by modifying the potential energy surface through the addition of bias potentials to the Hamiltonian, thereby lowering energy barriers to increase the sampling of transition regions [507].

Interestingly, the use of CE and Monte Carlo simulations extends beyond sampling configuration spaces to allow the evaluation of equilibrium phase diagrams. Combining these methods within kinetic Monte Carlo (kMC) simulations provides a comprehensive framework for assessing, for example, ionic diffusivities as a function of alkali content [508]. The kMC method is particularly useful for translating microscopic processes, such as individual ion hops, into macroscopic information about material behavior over longer timescales. Ion hop energy barriers, which are crucial for understanding ionic conductivity, depend significantly on the local environment of alkali ions at the transition state. This local environment is defined by specific alkali-vacancy orderings, whose stability can be accurately assessed using CE. And the migration barriers for these ion hops can be obtained through accurate DFT calculations, within the framework of transition state theory. This detailed information is then fed into kMC simulations to model the temporal evolution of ion diffusion across the material [509]. The power of kMC lies in its ability to simulate the stochastic processes that occur at the atomic scale and to predict the resultant macroscopic properties. Specifically, by statistically sampling the sequences of ion hops and their associated energy barriers, kMC can provide insights into diffusion coefficients, ionic conductivities, and other transport properties under various conditions. Consequently, this approach bridges the gap between the atomic-scale mechanisms and the macroscopic performance of battery materials, allowing for the prediction of how changes in composition, temperature, or structural order will affect the overall behavior of the material.

It is also important to explicitly understand how electrochemical interfaces evolve in space and time during battery operation, including access to metastable short-lived intermediate reaction products, which is also of high fundamental and practical relevance. For example, non-aqueous electrolytes inevitably decompose forming a SEI on the anode materials because the operating voltage is often lower than their electrochemical stability window. Similar processes occur on cathode surfaces leading to the formation of CEI layers. Away from equilibrium conditions, these processes might be largely controlled by mass transport and reaction kinetics, and, therefore, unravelling the underlying degradation mechanisms is essential to understand and predict overall battery performance. In this context, DFT-based simulations can be employed to probe interfacial reconstruction, space charge effects, and reactivity, in general. To this end, in addition to finding the lowest energy geometries of initial and final interface structures, computational workflows to gain insight into kinetic properties (i.e., ion diffusivity and reaction rates) also involve considering all plausible minimum energy paths that connect these initial and final states and calculate their corresponding transition states. Such approaches often imply considering multi-step diffusion and reaction mechanisms by taking into account metastable states. Current DFT-based workflows can provide accurate predictions for relatively simple systems [510,511]. The two most successful techniques

for this task are ab initio molecular dynamics (AIMD) simulations [see, e.g., [512-514] and nudged elastic band methods [515,516]]. These two techniques are particularly powerful when synergistically combined with *in situ* and *operando* experiments to probe buried interfaces, which is a significant challenge. In the following, we provide a breath of representative examples that show how these DFT-based methods are helping better understand battery interfaces and enhance their advanced characterization when employed with some of the experimental techniques introduced in previous sections.

DFT-based simulations are finding increasing applicability in the emerging area of solid-state batteries to unveil charge transfer processes and decomposition reactions at different solid-solid interfaces. Typical interfaces of interest are cathode materials or Li metal anode in contact with inorganic solid electrolytes and tentative protecting coatings. For example, Lu *et al.* used a range of complementary experimental probes (XPS, FIB-SEM and solid-state NMR) together with DFT calculations to examine the impact of cathodic Li content in the capacity fading of Li_xCoO_2/$Li_{10}GeP_2S_{12}$-based solid-state batteries [517]. Interestingly, the study revealed that the interplay between ISCL effects and interfacial side reactions is ultimately responsible for the observed changes in cycling stability and capacity retention. In another work, Warburton *et al.* [518] combined X-ray reflectivity measurements with AIMD simulations to track the reduction of Ti^{4+} ions at the $Li/Li_{1/2}La_{1/2}TiO_3$ interface. Furthermore, using band edge alignment analysis, La_2O_3 was identified as a suitable protective coating to prevent electrolyte reduction. Similar approaches have also been used to better understand interfacial reactivity of sulfide-based electrolytes at Li metal surfaces and help characterize decomposition products (*e.g.*, Li_3P, Li_2S, LiCl, and LiP) and underlying reaction mechanisms (*e.g.*, stepwise breaking of P−S bonds and P−P bond recombination to ultimately form reduced P_2 and S^{2-} species). [519-522]. Such molecular-level insights are essential to rationally design strategies that can mitigate electrolyte decomposition (Figure 5.2.1), while ensuring low ionic interface resistance. In this regard, the combination of AIMD simulations with computational schemes capable of efficiently assessing interfacial solid-state ionics [523,524] and electronic conductivity [525] holds great potential to identify high-performance protective coatings that can simultaneously prevent electrolyte decomposition and guarantee high ionic diffusion through the interface [521,526].

Finally, it is important to point out that DFT-based simulations under applied voltage add a layer of sophistication, providing insights into the dynamic behaviour of interfaces in practical scenarios. Despite this, simulating systems under applied potentials with DFT has been challenging, even though experiments are routinely performed under constant potential conditions. A typical approach for simulating applied electrode potentials is the grand-canonical ensemble DFT (GCE-DFT) [28,527,528]. GCE-DFT works with a single electrode and fixes the single-electrode potential, providing an exact framework for systems at constant electrochemical potential. This method is commonly used for modeling electrochemical thermodynamics [529-531] and kinetics [532,533]. However, while GCE-DFT offers a robust framework for electrochemical simulations, it requires finite-size corrections in small simulation cells and its main limitation is not properly fixing the bath chemical potential, the relevant experimental parameter. This oversight can lead to less accurate simulations of electrochemical interfaces, highlighting the need for improved approaches. The recently proposed constant inner potential DFT method

[534], which explicitly controls the bath chemical potential, promises more accurate and reliable results for a wide variety of electrochemical systems.

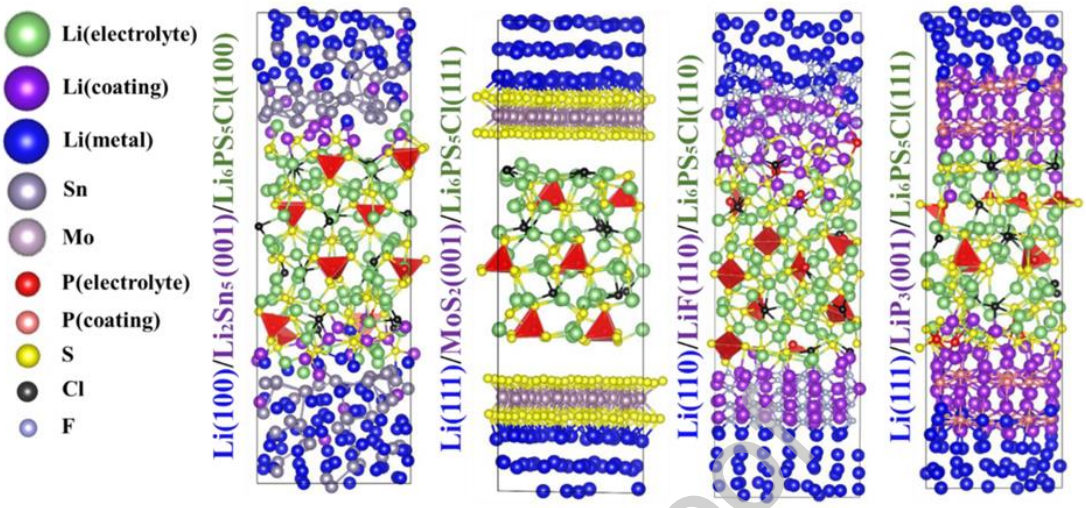

Figure 5.2.1. DFT-based molecular dynamics simulations of sandwich-like Li/coating/Li6PS5Cl interface models after 100 ps. Four different protective coating layers are considered: Li_2Sn_5, MoS_2, LiF, and LiP_3. The simulations predict that MoS_2 might effectively prevent the reduction of Li_6PS_5Cl by Li metal. In contrast, the other three coatings show partial electrolyte decomposition [521].

5.3. REACTIVE FORCE FIELDS

Force fields (FFs) are parametric functions that express the potential energy of a system as a function of the atomic positions (empirical interatomic potentials). The evaluation of such FFs is much less computationally intensive than DFT calculations and, therefore, can boost the accessible length and time scales of the simulations. There are many different analytical forms available to represent the interatomic interactions of a diverse range of compounds [535], but the main qualitative limitation of the approach is its inadequacy to account for chemical reactivity. Essentially, conventional FFs can approximate well electrostatics, dispersion, bond-stretching and bond-bending potentials; yet accurate descriptions of bond breaking and bond formation are beyond their reach. FF-based simulations are therefore suitable to model, for example, charge distributions in the EDL [459,536,537], but fail to describe reactive and charge transfer processes at interfaces. The ReaxFF method aims at bridging this gap [538]. This method implements a general bond-order-dependent potential, where the underlying electronic interactions of chemical bonding are treated implicitly to yield accurate descriptions of changes in atom connectivity. The ReaxFF method can deliver the accuracy of DFT, whilst retaining a computational cost only slightly higher than simple FFs. This allows ReaxFF to model complex systems, such as complex battery interfaces, handling the length scale of typical SEI films (*ca.* 10 nm), identifying trapped gas molecules, inorganic salts, and organic salts in good agreement with experiment [539]. However, ReaxFF also comes with its own set of challenges, particularly in terms of parameterization, which involves fitting many parameters to experimental or high-level quantum mechanical data. These parameters govern the behavior of atoms and molecules in the system and need to accurately capture

the energetics and kinetics of various chemical reactions. This process can be highly complex and time-consuming, requiring extensive computational resources and expertise in both theoretical chemistry and computer science. A key challenge in ReaxFF parameterization is achieving a balance between accuracy and computational efficiency. While adding more parameters may improve the accuracy of the potential, it also increases the computational cost of simulations. Therefore, parameterization often involves a trade-off between model complexity and computational tractability.

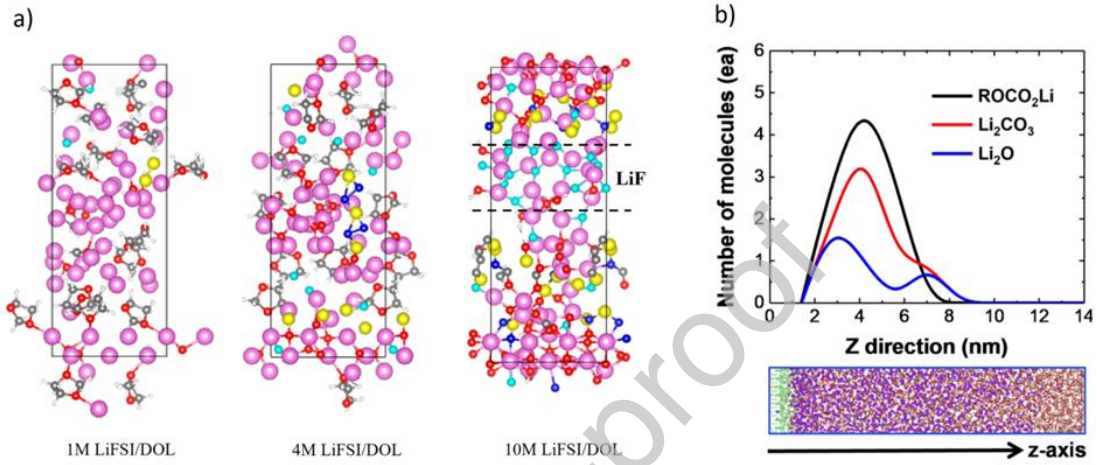

Figure 5.3.1. ReaxFF-based molecular dynamics simulations of SEI formation. In (a) it is shown the concentration effect of lithium bis(fluorosulfonyl)-imide (LiFSI, $F_2LiNO_4S_2$) in dioxalane (DOL) at concentrations of 1 M, 4 M, and 10 M after 1 ns. Purple, red, grey, cyan, yellow, blue and white balls stand for Li, O, C, F, S, N and H atoms, respectively. At 1 M and 4 M concentrations the SEI is heterogeneous, with the presence of clusters and voids; in contrast, at 10 M, the simulations reveal the formation of a rather homogeneous LiF-based SEI layer [540]; In (b) it is shown the predicted spatial distributions of different SEI products ($ROCO_2Li$, Li_2CO_3, and Li_2O, with R = CH_3 or C_2H_5) thatform at the interface between a SiO_x anode and a mixture of ethylene carbonate and ethyl methyl carbonate electrolyte [541].

ReaxFF simulations are becoming particularly useful to explore the decomposition of liquid electrolytes on Li metal anode, unveiling the formation and evolution of the SEI over simulation times generally inaccessible to DFT (nanoseconds) [540,542,543]. Interestingly, such studies allow for examining the performance of different salts (*e.g.*, $LiPF_6$ and $LiCF_3SO_3$, $F_2LiNO_4S_2$) solvents (*e.g.*, ethers, carbonates and mixtures of them) and additives with unprecedented computational detail (Figure 5.3.1 a), including the identification of hotspots during cycling for Li dendrite growth [544] and polymerization reactions with release of CO and CO_2 gases in good agreement with experiment [545]. The approach is not limited to the study of Li metal anodes but can be extended to other electrodes too; for example, Yun *et al.* [541] were able to follow the evolution of a range of SEI components such as gases (CO, CO_2, and C_xH_y) as well as inorganic (Li_2CO_3, Li_2O, and LiF) and organic (C_xH_yOLi and $C_xH_yOCO_2Li$) products that form on Si and SiO_x anodes as a function of carbonate solvent and additive composition (Figure 5.3.1 b).

5.4. MACHINE LEARNING INTERATOMIC POTENTIALS

From the viewpoint of modelling complex systems with many interacting particles, such as battery interfaces, an emerging alternative to physical-based approaches such as DFT- and ReaxFF-based simulations are data-driven methods [546-549]. These methods are designed to augment conventional approaches by applying ML techniques, with the aim of largely accelerating the simulations while keeping high accuracies. In the context of battery interfaces, a particularly relevant approach is the use of MLIPs, which, similarly to classical FFs, allow for the computation of the potential energy of a system. MLIPs are essentially empirical FFs constructed with more versatile interatomic potentials than those based on simple fixed functional forms. The construction of accurate and transferable MLIPs usually requires first-principles data (generally obtained from DFT calculations) to train the underlying ML model [550]. This training procedure is indeed the main computational bottleneck of the whole approach because normally large datasets are necessary. But once an accurate MLIP potential has been trained, it enables drastically accelerated simulations, often achieving speeds one or two orders of magnitude faster [470]. MLIPs have started to be used to simulate battery material recently and are under continuous development [550-552].

Comparing MLIPs with ReaxFF offers an interesting perspective on the challenges and advantages of each approach. MLIPs utilize ML algorithms to approximate the potential energy surface based on a set of training data. Unlike ReaxFF, MLIPs do not require explicit parameterization by hand. Instead, they learn the underlying potential energy function from data, potentially reducing the human effort involved in model development. However, MLIPs also have their own limitations and challenges. Training MLIPs requires a large and diverse dataset of atomic configurations and corresponding energies, which may be difficult to obtain, particularly for systems involving rare or complex chemical reactions. Additionally, the computational cost of training MLIPs can be significant, especially for large datasets or complex models. In terms of computational efficiency, ReaxFF is often more advantageous for systems with well-defined chemical reactions or when specific chemical insights are desired. Its explicit treatment of bond breaking and formation makes it particularly suitable for studying reaction mechanisms and kinetics. On the other hand, MLIPs may offer advantages in terms of generality and scalability, especially for systems where the underlying chemistry is less well-understood or when exploring a wide range of chemical environments.

The most popular ML methods employed to construct MLIPs so far include neural networks [553,554] as well as kernel [555-557] and linear [558] regressions. These approaches have mainly been applied to study ion insertion [559,560] and diffusion [478,561-563] in bulk materials. Yet, MLIPs for modelling explicit battery interfaces are still scarce due to their much larger complexity. Deng et al. used an electrostatic spectral neighbor analysis potential (linear regression model) to study concerted Li-ion motion and grain boundary diffusion in α-Li_3N [564]. This MLIP gave access to long-time and large-scale simulations, usually beyond the reach of DFT-based molecular dynamics, revealing that twist grain boundaries might enhance 2D Li-ion diffusion by a factor of three at room temperature with respect to diffusion in the bulk. Regarding heterogeneous interfaces, Lai *et al.* [565] implemented a neural network MLIP that successfully described the structure and Li-ion adsorption on a Cu foil current collector. And very recently, M. L. H. Chandrappa *et al.* [566] generated an accurate moment tensor potential (linear regression model) to study the S_8/β-Li_3PS_4 interphase growth in a Li-S battery. The

simulations unveiled that S_8 species rapidly decompose in contact with β-Li_3PS_4 and the initial morphology (i.e., surface terminations of the two contacted phases) determines the final thickness of the interface (Figure 5.4.1); this, in turn, impacts on the interfacial Li-ion diffusion pathways and energy barriers.

While further application of MLIPs in the field is expected to keep gaining momentum, the next generation of potentials will need to bring in higher levels of sophistication. The expectation for the continued momentum of MLIPs is driven by the increasing need to model complex interfaces accurately, advancements in machine learning techniques, and the success of MLIPs in current applications. The demand for higher sophistication in the next generation of MLIPs arises from the need for improved representations of electrified interfaces and mitigate the lack of universality, which makes the applicability of current MLIPs challenging to model complex degradation processes. Enhancing the synergy between ML models and quantum mechanics calculations is a promising strategy towards this goal [567,568].

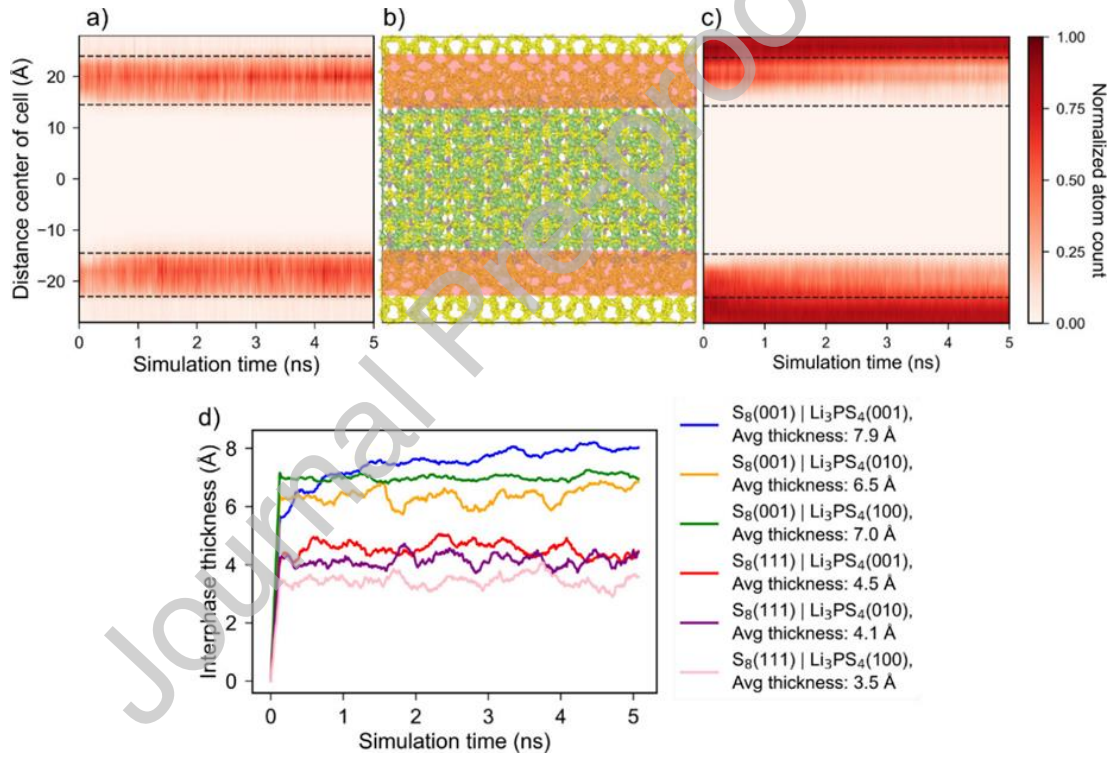

Figure 5.4.1. MLIP-based molecular dynamics simulation of a S_8/β-Li_3PS_4 interface showing the spatial distribution of $S_{x\neq8}$ (a) and S_8 (c) species along the S_8(001)/Li_3PS_4(001) interface structure shown in (b). Notice how the simulations predict that all the interphases grow very rapidly (within the first 100 ps), but they reach different steady state thicknesses (ranging from 3.5 Å to 7.9 Å) depending on the initial considered interface morphology (d). In (b), green, purple, and yellow balls stand for Li, P, and S atoms, respectively [566].

5.5. FUTURE PERSPECTIVES

The combination of high-performance computing and DFT methods has made the modelling and simulation of battery interfaces at the molecular level an almost routine

process. Typical insights provided by this approach include, for example, the screening of thermodynamically stable heterogeneous interfaces, identification of intermediate reaction products, and the assessment of interfacial ionic and electronic resistance. Yet, caveats remain, DFT-based computations of increasingly complex dynamical and reactive interfaces involve long simulation times as well as the consideration of large length scales. These two requirements invariably lead to a large increase in computational costs that makes the approach unfeasible. The development of new approaches to mitigate these deficiencies is an active field of research. In particular, the use of ReaxFF- and MLIP-based simulations might help circumvent the challenge of accurately and efficiently describing complex solid-solid and solid-liquid interfaces in battery materials beyond traditional methods. We can see how the complexity of the investigated interfaces increases year after year; yet, the construction of accurate interatomic potentials still demands the generation of high-fidelity datasets and exhaustive validations, which is time consuming, particularly in the case of MLIPs. If these barriers can be overtaken, ReaxFF- and MLIPs-based simulations hold the promise of enabling a new paradigm in the modelling of battery interfaces and effectively assist experimental characterization.

6. CONCLUSIONS

This topical and prospective review evaluates key strategies for a comprehensive understanding of interface formation and evolution in modern batteries. The in-depth characterization of complex battery interfaces remains one of the most important challenges, as these interfaces play a pivotal role on both battery performance and safety. Batteries are inherently dynamic systems, where active materials and interfaces exist in a state of non-equilibrium throughout device operation. The performance of these devices is intimately tied to the scope and nature of interfacial reactions, which stem from inherent instability at these critical junctions. The looming challenge to increase battery performance and lifespan will require a full description (and then control) of interfacial processes across multiple length and time scales, including their initial formation, and evolution over the entire battery lifetime.

This review comprehensively examines both established and emerging experimental and theoretical methodologies for characterizing interfacial phenomena in battery systems. By elucidating the critical requirements for these approaches, it underscores their pivotal role in advancing the understanding and optimization of interfacial dynamics, thereby contributing to the development of higher-performance batteries. Studying the formation and evolution of interfaces in batteries is a complex task. Given the multifaceted nature of battery interface characterization, a broad dimensional range should be considered. A comprehensive understanding of battery interfaces necessitates meticulous control over their chemical composition, physical properties, and inherent heterogeneities, as well as their spatial distribution and structural/chemical stability under varying electrochemical conditions. For instance, the SEI layer, formed on the anode, and the CEI layer, formed on the cathode, act as passivation layers that protect the electrodes from continuous degradation by the electrolyte, yet their formation and evolution are complex and multifaceted, influenced by numerous factors such as electrolyte composition, electrode materials, and cycling conditions. Additionally, probing the dynamic processes governing

the formation and evolution of these interfaces is essential for elucidating the complex interfacial phenomena that dictate battery performance and longevity. Such insights are pivotal in advancing the development of next-generation energy storage systems.

Addressing this challenge in a holistic way appears very promising to carefully study all phases present or appearing inside the battery cell. We provide a synthetic description of particularly relevant approaches for investigating the evolution of the interfacial structure and chemistry in battery systems, giving our perspectives on their forthcoming development towards the investigation of battery interfaces. We emphasize the recent advances in characterization techniques (in situ and operando), which have significantly improved our ability to probe these interfacial regions with higher spatial and temporal resolution, providing deeper insights into the chemical, structural, and morphological changes occurring at these interfaces. Techniques such as X-ray spectroscopy, nuclear magnetic resonance (NMR), and various microscopy methods have become invaluable tools in this regard. Each of these techniques offers unique advantages, from providing detailed chemical information to high-resolution imaging of morphological changes. Furthermore, the integration of multimodal characterization techniques, capable of simultaneously probing multiple parameters within a single measurement, is imperative for advancing the comprehensive understanding of battery interfaces. By combining different methods, researchers can gain complementary insights, minimizing the effects of variables and providing a more holistic view of interfacial processes. This holistic approach not only enhances the precision of parameter control but also enables a more nuanced exploration of the complex interfacial phenomena, which is essential for the development of next-generation energy storage technologies. However, these methods also come with inherent limitations, such as the need for sophisticated sample preparation, complex electrochemical cell devices or the challenge of interpreting data from non-equilibrium systems.

The widely adopted postmortem evaluation approach in battery research has consisted of measuring devices ex situ following disassembly. While this approach is of interest to gain knowledge into the structural and chemical evolution of the different battery components at specific steps of the cycling process, at the same time it is insufficient to deliver the insights into interfacial processes required to develop the next generation of battery materials. Ex situ measurements tend to be unreliable, as battery interfaces are highly reactive and liable to change during disassembly, transfer, and preparation for analysis. Such investigations often provide a picture that is remote from reality as they cannot capture the interface in its operating state, where the interfacial chemistry may be radically different than after the electrochemical processes have taken place. In order to continue progressing in the development of modern batteries, the scientific community would benefit from systematically deploying multimodal and operando characterization techniques that can test industrial-grade materials in relevant cell configurations and using realistic protocols, coupled with physics-based and data-driven models. This approach, supported by recent technological developments allowing for (near) operando experiments with better analytical performances, will allow the identification and quantification of highly complex and interrelated processes that influence the formation, evolution and properties of battery interfaces.

In addition, the development of standardized protocols for battery assembly and testing is critical for ensuring the reproducibility and reliability of characterization studies. The large variability in cell formats, electrode configurations, and cycling conditions can lead to significant differences in interfacial behavior, making it difficult to compare results across different studies. Standardization, coupled with the use of advanced characterization techniques, will enable more consistent and comparable data, facilitating the development of better-performing batteries.

Achieving better performances of batteries will rely on a better understanding of interface evolution, which suggests its total characterization by investigating the mechanisms of all chemical processes involved. To achieve a comprehensive understanding of interface formation and evolution across the relevant length and time scales, major collaborative initiatives, such as ALISTORE-ERI European network, Battery 2030+ project and the Faraday Institution, gathering complementary strengths and skills will be fundamental. While significant progress has been made in characterizing battery interfaces, there is still much work to be done. The ongoing development of advanced characterization methods, combined with the integration of multimodal approaches and computational modelling, holds great promise for deepening our understanding of interfacial processes in batteries. This, in turn, will enable the design of more efficient, durable, and safer batteries, meeting the growing demands of modern society for energy storage solutions. We hope that this review will stimulate the interest and inspiration of scientists and technologists to further improve the existing characterization techniques currently available, and better understand the role of interfaces in battery materials.

ACKNOWLEDGMENTS

I.T. acknowledges support from a Beatriz Galindo senior fellowship (BG22/00148) from the Spanish Ministry of Science and Innovation. I.L. acknowledges the European Union's Horizon Europe research and innovation program (OPINCHARGE project, grant agreement ID:101104032), Battery 2030+ and French Agence Nationale de la Recherche ANR (ZORG project, grant ID: ANR-22-CE50-0005). M. B., J. X., N. F., and A. D. acknowledge funding from the French ANR (DESTINa_ion_Operando, grant ID: ANR-19-CE42-0014) and support from Battery 2030+. R.S.W. acknowledges a CAMS-UK Fellowship through the Analytical Chemistry Trust Fund, a UKRI Future Leaders Fellowship (MR/V024558/1), and the European Research Council (ERC) under the European Union's Horizon 2020 research and innovation programme (EXISTAR, grant agreement No. 950598). This publication is part of the R&D project PID2022-143003OB-I00 funded by MCIN/AEI/10.13039/501100011033 and by EDRF "A way of making Europe".

REFERENCES

1. Palacín, M.R., *Understanding ageing in Li-ion batteries: a chemical issue.* Chemical Society Reviews, 2018. **47**(13): p. 4924-4933.

2. Usiskin, R. and J. Maier, *Interfacial Effects in Lithium and Sodium Batteries.* Advanced Energy Materials, 2021. **11**(2): p. 2001455.

3. Adenusi, H., et al., *Lithium Batteries and the Solid Electrolyte Interphase (SEI)—Progress and Outlook.* Advanced Energy Materials, 2023. **13**(10): p. 2203307.

4. Xu, K., *Interfaces and interphases in batteries.* Journal of Power Sources, 2023. **559**: p. 232652.

5. Gauthier, M., et al., *Electrode–Electrolyte Interface in Li-Ion Batteries: Current Understanding and New Insights.* The Journal of Physical Chemistry Letters, 2015. **6**(22): p. 4653-4672.

6. Grey, C.P. and D.S. Hall, *Prospects for lithium-ion batteries and beyond—a 2030 vision.* Nature Communications, 2020. **11**(1): p. 6279.

7. Xu, K., *Electrolytes and interphases in Li-ion batteries and beyond.* Chemical reviews, 2014. **114**(23): p. 11503-11618.

8. Gao, Y., et al., *Unraveling the mechanical origin of stable solid electrolyte interphase.* Joule, 2021. **5**(7): p. 1860-1872.

9. Fichtner, M., et al., *Rechargeable batteries of the future—the state of the art from a BATTERY 2030+ perspective.* Advanced Energy Materials, 2022. **12**(17): p. 2102904.

10. Tarascon, J.-M., *Key challenges in future Li-battery research.* Philosophical Transactions of the Royal Society A: Mathematical, Physical and Engineering Sciences, 2010. **368**(1923): p. 3227-3241.

11. Zhao, D. and S. Li, *Regulating the Performance of Lithium-Ion Battery Focus on the Electrode-Electrolyte Interface.* Frontiers in Chemistry, 2020. **8**.

12. Zheng, J., et al., *Understanding thermodynamic and kinetic contributions in expanding the stability window of aqueous electrolytes.* Chem, 2018. **4**(12): p. 2872-2882.

13. Chen, M., et al., *Progress on predicting the electrochemical stability window of electrolytes.* Current Opinion in Electrochemistry, 2022. **34**: p. 101030.

14. Xu, K., S.P. Ding, and T.R. Jow, *Toward reliable values of electrochemical stability limits for electrolytes.* Journal of The Electrochemical Society, 1999. **146**(11): p. 4172.

15. Fan, X. and C. Wang, *High-voltage liquid electrolytes for Li batteries: progress and perspectives.* Chemical Society Reviews, 2021. **50**(18): p. 10486-10566.

16. Chen, S., et al., *Historical development and novel concepts on electrolytes for aqueous rechargeable batteries.* Energy & Environmental Science, 2022. **15**(5): p. 1805-1839.

17. Peled, E. and S. Menkin, *SEI: past, present and future.* Journal of The Electrochemical Society, 2017. **164**(7): p. A1703.

18. An, S.J., et al., *The state of understanding of the lithium-ion-battery graphite solid electrolyte interphase (SEI) and its relationship to formation cycling.* Carbon, 2016. **105**: p. 52-76.

19. Atkins, D., et al., *Understanding battery interfaces by combined characterization and simulation approaches: challenges and perspectives.* Advanced Energy Materials, 2022. **12**(17): p. 2102687.

20. Yang, Z., et al., *Quantitative analysis of origin of lithium inventory loss and interface evolution over extended fast charge aging in Li ion batteries.* ACS Applied Materials & Interfaces, 2023. **15**(31): p. 37410-37421.

21. Heidrich, B., et al., *Determining the Origin of Lithium Inventory Loss in NMC622|| Graphite Lithium Ion Cells Using an LiPF6-Based Electrolyte.* Journal of The Electrochemical Society, 2023. **170**(1): p. 010530.

22. Xu, H., et al., *Quantification of lithium dendrite and solid electrolyte interphase (SEI) in lithium-ion batteries.* Journal of Power Sources, 2022. **529**: p. 231219.

23. Liu, D., et al., *Review of Recent Development of In Situ/Operando Characterization Techniques for Lithium Battery Research.* Advanced Materials, 2019. **31**(28): p. 1806620.

24. Villevieille, C., *Interfaces and Interphases in Batteries: How to Identify and Monitor Them Properly Using Surface Sensitive Characterization Techniques.* Advanced Materials Interfaces, 2022. **9**(8): p. 2101865.

25. Tripathi, A.M., W.-N. Su, and B.J. Hwang, *In situ analytical techniques for battery interface analysis.* Chemical Society Reviews, 2018. **47**(3): p. 736-851.

26. Wang, H. and F. Wang, *In situ, operando measurements of rechargeable batteries.* Current Opinion in Chemical Engineering, 2016. **13**: p. 170-178.

27. Källquist, I., et al., *Advances in studying interfacial reactions in rechargeable batteries by photoelectron spectroscopy.* Journal of Materials Chemistry A, 2022. **10**(37): p. 19466-19505.

28. Sakaushi, K., et al., *Advances and challenges for experiment and theory for multi-electron multi-proton transfer at electrified solid–liquid interfaces.* Physical Chemistry Chemical Physics, 2020. **22**(35): p. 19401-19442.

29. Li, Y., et al., *Advanced characterization techniques for interface in all-solid-state batteries.* Small Methods, 2020. **4**(9): p. 2000111.

30. Lombardo, T., et al., *Artificial intelligence applied to battery research: hype or reality?* Chemical reviews, 2021. **122**(12): p. 10899-10969.

31. Kasnatscheew, J., et al., *Interfaces and Materials in Lithium Ion Batteries: Challenges for Theoretical Electrochemistry*, in *Modeling Electrochemical Energy Storage at the Atomic Scale*, M. Korth, Editor. 2018, Springer International Publishing: Cham. p. 23-51.

32. Schellenberger, M., et al., *Accessing the solid electrolyte interphase on silicon anodes for lithium-ion batteries in-situ through transmission soft X-ray absorption spectroscopy.* Materials Today Advances, 2022. **14**: p. 100215.

33. Schwager, P., et al., *Review of Local In Situ Probing Techniques for the Interfaces of Lithium-Ion and Lithium–Oxygen Batteries.* Energy Technology, 2016. **4**(12): p. 1472-1485.

34. Minato, T. and T. Abe, *Surface and interface sciences of Li-ion batteries: -Research progress in electrode–electrolyte interface.* Progress in Surface Science, 2017. **92**(4): p. 240-280.

35. Henke, B.L., E.M. Gullikson, and J.C. Davis, *X-Ray Interactions: Photoabsorption, Scattering, Transmission, and Reflection at E = 50-30,000 eV, Z = 1-92.* Atomic Data and Nuclear Data Tables, 1993. **54**(2): p. 181-342.

36. Tanuma, S., C.J. Powell, and D.R. Penn, *Calculations of electron inelastic mean free paths. IX. Data for 41 elemental solids over the 50 eV to 30 keV range.* Surface and Interface Analysis, 2011. **43**(3): p. 689-713.

37. Seidler, G.T., et al., *A laboratory-based hard x-ray monochromator for high-resolution x-ray emission spectroscopy and x-ray absorption near edge structure measurements.* Review of Scientific Instruments, 2014. **85**(11): p. 113906.

38. Holburg, J., et al., *High-Resolution Table-Top NEXAFS Spectroscopy.* Analytical Chemistry, 2022. **94**(8): p. 3510-3516.

39. Björklund, E., et al., *Cycle-Induced Interfacial Degradation and Transition-Metal Cross-Over in LiNi0.8Mn0.1Co0.1O2–Graphite Cells.* Chemistry of Materials, 2022. **34**(5): p. 2034-2048.

40. Somerville, L., et al., *The Effect of Pre-Analysis Washing on the Surface Film of Graphite Electrodes.* Electrochimica Acta, 2016. **206**: p. 70-76.

41. Liu, X., et al., *Distinct charge dynamics in battery electrodes revealed by in situ and operando soft X-ray spectroscopy.* Nature Communications, 2013. **4**(1): p. 2568.

42. Endo, R., et al., *Electrochemical Lithiation and Delithiation in Amorphous Si Thin Film Electrodes Studied by Operando X-ray Photoelectron Spectroscopy.* The Journal of Physical Chemistry Letters, 2022. **13**(31): p. 7363-7370.

43. Wenzel, S., et al., *Interphase formation on lithium solid electrolytes—An in situ approach to study interfacial reactions by photoelectron spectroscopy.* Solid State Ionics, 2015. **278**: p. 98-105.

44. Wood, K.N., et al., *Operando X-ray photoelectron spectroscopy of solid electrolyte interphase formation and evolution in Li2S-P2S5 solid-state electrolytes.* Nature Communications, 2018. **9**(1): p. 2490.

45. Yu, Y., et al., *Instability at the Electrode/Electrolyte Interface Induced by Hard Cation Chelation and Nucleophilic Attack.* Chemistry of Materials, 2017. **29**(19): p. 8504-8512.

46. Falling, L.J., et al., *Graphene-Capped Liquid Thin Films for Electrochemical Operando X-ray Spectroscopy and Scanning Electron Microscopy.* ACS Applied Materials & Interfaces, 2020. **12**(33): p. 37680-37692.

47. Wu, X., et al., *Monitoring the chemical and electronic properties of electrolyte–electrode interfaces in all-solid-state batteries using operando X-ray photoelectron spectroscopy.* Physical Chemistry Chemical Physics, 2018. **20**(16): p. 11123-11129.

48. Gibson, J.S., et al., *Gently does it!: in situ preparation of alkali metal–solid electrolyte interfaces for photoelectron spectroscopy.* Faraday Discussions, 2022. **236**(0): p. 267-287.

49. Narayanan, S., et al., *Effect of current density on the solid electrolyte interphase formation at the lithium/Li6PS5Cl interface.* Nature Communications, 2022. **13**(1): p. 7237.

50. Quérel, E., et al., *Operando Characterization and Theoretical Modeling of Metal| Electrolyte Interphase Growth Kinetics in Solid-State Batteries. Part I: Experiments.* Chemistry of Materials, 2023. **35**(3): p. 853-862.

51. Weingarth, D., et al., *In situ electrochemical XPS study of the Pt/[EMIM][BF4] system.* Electrochemistry Communications, 2011. **13**(6): p. 619-622.

52. Benayad, A., et al., *Operando XPS: A Novel Approach for Probing the Lithium/Electrolyte Interphase Dynamic Evolution.* The Journal of Physical Chemistry A, 2021. **125**(4): p. 1069-1081.

53. Wang, H., et al., *X-ray-Induced Fragmentation of Imidazolium-Based Ionic Liquids Studied by Soft X-ray Absorption Spectroscopy.* The Journal of Physical Chemistry Letters, 2018. **9**(4): p. 785-790.

54. Ogletree, D.F., et al., *A differentially pumped electrostatic lens system for photoemission studies in the millibar range.* Review of Scientific Instruments, 2002. **73**(11): p. 3872-3877.

55. Axnanda, S., et al., *Using "Tender" X-ray Ambient Pressure X-Ray Photoelectron Spectroscopy as A Direct Probe of Solid-Liquid Interface.* Scientific Reports, 2015. **5**(1): p. 9788.

56. Källquist, I., et al., *Potentials in Li-Ion Batteries Probed by Operando Ambient Pressure Photoelectron Spectroscopy.* ACS Applied Materials & Interfaces, 2022. **14**(5): p. 6465-6475.

57. Maibach, J., et al., *Probing a battery electrolyte drop with ambient pressure photoelectron spectroscopy.* Nature Communications, 2019. **10**(1): p. 3080.

58. Booth, S.G., et al., *The offset droplet: a new methodology for studying the solid/water interface using x-ray photoelectron spectroscopy.* Journal of Physics: Condensed Matter, 2017. **29**(45): p. 454001.

59. Jones, E.S., J.E.N. Swallow, and R.S. Weatherup, *Enclosed Cells for Extending Soft X-ray Spectroscopies to Atmospheric Pressures and Above*, in *Ambient Pressure Spectroscopy in Complex Chemical Environments*. 2021, American Chemical Society. p. 175-218.

60. Arthur, T.S., et al., *Mg deposition observed by in situ electrochemical Mg K-edge X-ray absorption spectroscopy.* Electrochemistry Communications, 2012. **24**: p. 43-46.

61. Yang, F., et al., *In Situ/Operando (Soft) X-ray Spectroscopy Study of Beyond Lithium-ion Batteries.* ENERGY & ENVIRONMENTAL MATERIALS, 2021. **4**(2): p. 139-157.

62. Velasco-Velez, J.-J., et al., *The structure of interfacial water on gold electrodes studied by x-ray absorption spectroscopy.* Science, 2014. **346**(6211): p. 831-834.

63. Swallow, J.E.N., et al., *Revealing solid electrolyte interphase formation through interface-sensitive Operando X-ray absorption spectroscopy.* Nature Communications, 2022. **13**(1): p. 6070.

64. Masuda, T., et al., *In situ x-ray photoelectron spectroscopy for electrochemical reactions in ordinary solvents.* Applied Physics Letters, 2013. **103**(11): p. 111605.

65. Wu, C.H., R.S. Weatherup, and M.B. Salmeron, *Probing electrode/electrolyte interfaces in situ by X-ray spectroscopies: old methods, new tricks.* Physical Chemistry Chemical Physics, 2015. **17**(45): p. 30229-30239.

66. Velasco-Velez, J.J., et al., *Photoelectron Spectroscopy at the Graphene–Liquid Interface Reveals the Electronic Structure of an Electrodeposited Cobalt/Graphene Electrocatalyst.* Angewandte Chemie International Edition, 2015. **54**(48): p. 14554-14558.

67. Weatherup, R.S., *2D Material Membranes for Operando Atmospheric Pressure Photoelectron Spectroscopy.* Topics in Catalysis, 2018. **61**(20): p. 2085-2102.

68. Kolmakov, A., et al., *Graphene oxide windows for in situ environmental cell photoelectron spectroscopy.* Nature Nanotechnology, 2011. **6**(10): p. 651-657.

69. Weatherup, R.S., et al., *Graphene Membranes for Atmospheric Pressure Photoelectron Spectroscopy.* The Journal of Physical Chemistry Letters, 2016. **7**(9): p. 1622-1627.

70. Nemšák, S., et al., *Interfacial Electrochemistry in Liquids Probed with Photoemission Electron Microscopy.* Journal of the American Chemical Society, 2017. **139**(50): p. 18138-18141.

71. Hitchcock, A., et al., *Handbook of Nanoscopy*. 2012, KGaA Weinheim, Germany. p. 745-791.

72. Wang, J., *Advanced X-ray Imaging of Electrochemical Energy Materials and Devices*. 2021: Springer.

73. Zhou, J. and J. Wang, *Applications of Soft X-ray Spectromicroscopy in Energy Research from Materials to Batteries*, in *Advanced X-ray Imaging of Electrochemical Energy Materials and Devices*, J. Wang, Editor. 2021, Springer Singapore: Singapore. p. 141-178.

74. Kaznatcheev, K.V., et al., *Soft X-ray spectromicroscopy beamline at the CLS: Commissioning results.* Nuclear Instruments and Methods in Physics Research Section A: Accelerators, Spectrometers, Detectors and Associated Equipment, 2007. **582**(1): p. 96-99.

75. Kilcoyne, A.L.D., et al., *Interferometer-controlled scanning transmission X-ray microscopes at the Advanced Light Source.* Journal of Synchrotron Radiation, 2003. **10**(2): p. 125-136.

76. Bluhm, H., et al., *Soft X-ray microscopy and spectroscopy at the molecular environmental science beamline at the Advanced Light Source.* Journal of Electron Spectroscopy and Related Phenomena, 2006. **150**(2): p. 86-104.

77. Ade, H. and A.P. Hitchcock, *NEXAFS microscopy and resonant scattering: Composition and orientation probed in real and reciprocal space.* Polymer, 2008. **49**(3): p. 643-675.

78. Hitchcock, A.P., *Soft X-Ray Imaging and Spectromicroscopy*, in *Handbook of Nanoscopy*. 2012, Wiley-VCH Verlag & Co. KGaA: Weinheim, Germany.

79. Hitchcock, A.P., *Soft X-ray spectromicroscopy and ptychography.* Journal of Electron Spectroscopy and Related Phenomena, 2015. **200**: p. 49-63.

80. Stuckey, J.W., et al., *Advances in Scanning Transmission X-Ray Microscopy for Elucidating Soil Biogeochemical Processes at the Submicron Scale.* Journal of Environmental Quality, 2017. **46**(6): p. 1166-1174.

81. Li, Y., et al., *Fluid-enhanced surface diffusion controls intraparticle phase transformations.* Nature Materials, 2018. **17**(10): p. 915-922.

82. Lu, M., et al., *Unexpected phase separation in Li1–xNi0.5Mn1.5O4 within a porous composite electrode.* Chemical Communications, 2018. **54**(33): p. 4152-4155.

83. Wang, M.J., et al., *Co-regulating the surface and bulk structure of Li-rich layered oxides by a phosphor doping strategy for high-energy Li-ion batteries.* Journal of Materials Chemistry A, 2019. **7**(14): p. 8302-8314.

84. Park, J., et al., *Fictitious phase separation in Li layered oxides driven by electro-autocatalysis.* Nature Materials, 2021. **20**(7): p. 991-999.

85. Csernica, P.M., et al., *Persistent and partially mobile oxygen vacancies in Li-rich layered oxides.* Nature Energy, 2021. **6**(6): p. 642-652.

86. Xu, S., et al., *In Situ Synthesis of Graphene-Coated Silicon Monoxide Anodes from Coal-Derived Humic Acid for High-Performance Lithium-Ion Batteries.* Advanced Functional Materials, 2021. **31**(32): p. 2101645.

87. Yan, S., et al., *Revealing the Role of Liquid Electrolytes in Cycling of Garnet-Based Solid-State Lithium-Metal Batteries.* Journal of Physical Chemistry C, 2022. **126**(33): p. 14027-14035.

88. Yan, S., et al., *Elucidating the Origins of Rapid Capacity Fade in Hybrid Garnet-Based Solid-State Lithium Metal Batteries.* The Journal of Physical Chemistry C, 2023. **127**(51): p. 24641-24650.

89. Zhou, J., et al., *Imaging the surface morphology, chemistry and conductivity of LiNi1/3Fe1/3Mn4/3O4 crystalline facets using scanning transmission X-ray microscopy.* Physical Chemistry Chemical Physics, 2016. **18**(33): p. 22789-22793.

90. Zhu, Q., et al., *Imaging the space-resolved chemical heterogeneity of degraded graphite anode through scanning transmission X-ray microscope.* Journal of Power Sources, 2024. **591**: p. 233882.

91. Sun, T., et al., *Soft X-ray Ptychography Chemical Imaging of Degradation in a Composite Surface-Reconstructed Li-Rich Cathode.* ACS Nano, 2021. **15**(1): p. 1475-1485.

92. Han, L., et al., *Chemically coupling SnO2 quantum dots and MXene for efficient CO2 electroreduction to formate and Zn–CO2 battery.* Proceedings of the National Academy of Sciences, 2022. **119**(42): p. e2207326119.

93. Hughes, L.A., et al., *Correlative analysis of structure and chemistry of LixFePO4 platelets using 4D-STEM and X-ray ptychography.* Materials Today, 2022. **52**: p. 102-111.

94. Kazemian, M., et al., *X-ray imaging and micro-spectroscopy unravel the role of zincate and zinc oxide in the cycling of zinc anodes in mildly acidic aqueous electrolytes.* Journal of Power Sources, 2022. **524**.

95. Wang, J., *Applications of Soft X-ray Spectromicroscopies to Lithium Ion Battery Analysis.* Microscopy and Microanalysis, 2018. **24**(S2): p. 416-419.

96. Li, Y., et al., *Dichotomy in the Lithiation Pathway of Ellipsoidal and Platelet LiFePO4 Particles Revealed through Nanoscale Operando State-of-Charge Imaging.* Advanced Functional Materials, 2015. **25**(24): p. 3677-3687.

97. Prabu, V., et al., *Instrumentation for in situ flow electrochemical Scanning Transmission X-ray Microscopy (STXM).* Review of Scientific Instruments, 2018. **89**(6): p. 063702.

98. Eraky, H., J.J. Dynes, and A. Hitchcock, *Mn 2p and O 1s X-Ray Absorption Spectroscopy of Manganese Oxides.* Available at SSRN 4663721.

99. Lim, J., et al., *Origin and hysteresis of lithium compositional spatiodynamics within battery primary particles.* Science, 2016. **353**(6299): p. 566-571.

100. Wu, Y.A., et al., *In-situ Multimodal Imaging and Spectroscopy of Mg Electrodeposition at Electrode-Electrolyte Interfaces.* Scientific Reports, 2017. **7**(1): p. 42527.

101. Kim, M., et al., *In-Situ High-Temperature Heating Setup for Spectronanoscopy at Pohang Light Source.* Applied Science and Convergence Technology, 2022. **31**(1): p. 9-11.

102. Shin, H.J., et al., *Ni, Co, and Mn L-3-edge X-ray absorption micro-spectroscopic study on LixNi0.88Co0.08Mn0.04O2 primary particles upon annealing from room temperature to 800 degrees C.* Journal of Industrial and Engineering Chemistry, 2022. **111**: p. 447-453.

103. Shin, H.J., et al., *Spectro-nanoscopic investigation of oxidation-state changes of Ni, Co, and Mn ions in LixNi0.88Co0.08Mn0.04O2 primary particles by annealing.* Journal of Physics and Chemistry of Solids, 2021. **153**.

104. Wang, J., et al., *Nanoscale chemical imaging of the additive effects on the interfaces of high-voltage LiCoO2 composite electrodes.* Chemical Communications, 2017. **53**(61): p. 8581-8584.

105. Lu, M., et al., *Correlative imaging of ionic transport and electronic structure in nano Li0.5FePO4 electrodes.* Chemical Communications, 2020. **56**(6): p. 984-987.

106. Sun, G., et al., *Surface chemical heterogeneous distribution in over-lithiated Li1+xCoO2 electrodes.* Nature Communications, 2022. **13**(1): p. 6464.

107. Lu, M., et al., *Surface heterogeneity in Li0.5CoO2 within a porous composite electrode.* Chemical Communications, 2018. **54**(60): p. 8320-8323.

108. Li, Q., et al., *Identification of the Solid Electrolyte Interface on the Si/C Composite Anode with FEC as the Additive.* ACS Applied Materials & Interfaces, 2019. **11**(15): p. 14066-14075.

109. Holler, M., et al., *High-resolution non-destructive three-dimensional imaging of integrated circuits.* Nature, 2017. **543**(7645): p. 402-406.

110. Su, Z., et al., *Towards a Local In situ X-ray Nano Computed Tomography under Realistic Cycling Conditions for Battery Research.* Chemistry–Methods, 2022. **2**(5): p. e202100051.

111. Lu, X., et al., *3D microstructure design of lithium-ion battery electrodes assisted by X-ray nano-computed tomography and modelling.* Nature Communications, 2020. **11**(1): p. 2079.

112. Shearing, P.R., J. Gelb, and N.P. Brandon, *X-ray nano computerised tomography of SOFC electrodes using a focused ion beam sample-preparation technique.* Journal of the European Ceramic Society, 2010. **30**(8): p. 1809-1814.

113. Shearing, P.R., et al., *Characterization of the 3-dimensional microstructure of a graphite negative electrode from a Li-ion battery.* Electrochemistry Communications, 2010. **12**(3): p. 374-377.

114. Ebner, M., et al., *Electrodes: Tortuosity Anisotropy in Lithium-Ion Battery Electrodes (Adv. Energy Mater. 5/2014).* Advanced Energy Materials, 2014. **4**(5).

115. Müller, S., et al., *Quantifying Inhomogeneity of Lithium Ion Battery Electrodes and Its Influence on Electrochemical Performance.* Journal of The Electrochemical Society, 2018. **165**(2): p. A339.

116. Robinson, J.B., et al., *Non-uniform temperature distribution in Li-ion batteries during discharge – A combined thermal imaging, X-ray micro-tomography and electrochemical impedance approach.* Journal of Power Sources, 2014. **252**: p. 51-57.

117. Malik, R., et al., *Synthesis of layered silicon-graphene hetero-structures by wet jet milling for high capacity anodes in Li-ion batteries.* 2D Materials, 2021. **8**(1): p. 015012.

118. Kashkooli, A.G., et al., *Multiscale modeling of lithium-ion battery electrodes based on nano-scale X-ray computed tomography.* Journal of Power Sources, 2016. **307**: p. 496-509.

119. Liu, Z., et al., *Three-dimensional morphological measurements of LiCoO2 and LiCoO2/Li(Ni1/3Mn1/3Co1/3)O2 lithium-ion battery cathodes.* Journal of Power Sources, 2013. **227**: p. 267-274.

120. Nelson, G.J., et al., *Comparison of SOFC cathode microstructure quantified using X-ray nanotomography and focused ion beam–scanning electron microscopy.* Electrochemistry Communications, 2011. **13**(6): p. 586-589.

121. Shearing, P.R., et al., *Exploring microstructural changes associated with oxidation in Ni–YSZ SOFC electrodes using high resolution X-ray computed tomography.* Solid State Ionics, 2012. **216**: p. 69-72.

122. Satjaritanun, P., et al., *Micro-Scale Analysis of Liquid Water Breakthrough inside Gas Diffusion Layer for PEMFC Using X-ray Computed Tomography and Lattice Boltzmann Method.* Journal of The Electrochemical Society, 2017. **164**(11): p. E3359.

123. Xiao, L., et al., *Pore-Scale Characterization and Simulation of Porous Electrode Material for Vanadium Redox Flow Battery: Effects of Compression on Transport Properties.* Journal of The Electrochemical Society, 2020. **167**(11): p. 110545.

124. Fathiannasab, H., et al., *Three-dimensional modeling of all-solid-state lithium-ion batteries using synchrotron transmission X-ray microscopy tomography.* Journal of The Electrochemical Society, 2020. **167**(10): p. 100558.

125. Hao, S., et al., *3D imaging of lithium protrusions in solid-state lithium batteries using X-ray computed tomography.* Advanced Functional Materials, 2021. **31**(10): p. 2007564.

126. Nguyen, T.-T., et al., *3D Quantification of Microstructural Properties of LiNi0.5Mn0.3Co0.2O2 High-Energy Density Electrodes by X-Ray Holographic Nano-Tomography.* Advanced Energy Materials, 2021. **11**(8): p. 2003529.

127. Shearing, P.R., et al., *Using Synchrotron X-Ray Nano-CT to Characterize SOFC Electrode Microstructures in Three-Dimensions at Operating Temperature.* Electrochemical and Solid-State Letters, 2011. **14**(10): p. B117.

128. Lewis, J.A., et al., *Linking void and interphase evolution to electrochemistry in solid-state batteries using operando X-ray tomography.* Nature Materials, 2021. **20**(4): p. 503-510.

129. Lu, X., et al., *Microstructural Evolution of Battery Electrodes During Calendering.* Joule, 2020. **4**(12): p. 2746-2768.

130. Boyce, A.M., et al., *Cracking predictions of lithium-ion battery electrodes by X-ray computed tomography and modelling.* Journal of Power Sources, 2022. **526**: p. 231119.

131. Li, T., et al., *Characterization of dynamic morphological changes of tin anode electrode during (de)lithiation processes using in operando synchrotron transmission X-ray microscopy.* Electrochimica Acta, 2019. **314**: p. 212-218.

132. Sun, F., et al., *Morphological Evolution of Electrochemically Plated/Stripped Lithium Microstructures Investigated by Synchrotron X-ray Phase Contrast Tomography.* ACS Nano, 2016. **10**(8): p. 7990-7997.

133. Michael, H., et al., *A Dilatometric Study of Graphite Electrodes during Cycling with X-ray Computed Tomography.* Journal of The Electrochemical Society, 2021. **168**(1): p. 010507.

134. Ebner, M., et al., *Visualization and Quantification of Electrochemical and Mechanical Degradation in Li Ion Batteries.* Science, 2013. **342**(6159): p. 716-720.

135. Frisco, S., et al., *Understanding Li-ion battery anode degradation and pore morphological changes through nano-resolution X-ray computed tomography.* Journal of The Electrochemical Society, 2016. **163**(13): p. A2636.

136. Choi, P., et al., *Operando particle-scale characterization of silicon anode degradation during cycling by ultrahigh-resolution X-ray microscopy and computed tomography.* ACS Applied Energy Materials, 2021. **4**(2): p. 1657-1665.

137. Ge, R., D.J. Cumming, and R.M. Smith, *Discrete element method (DEM) analysis of lithium ion battery electrode structures from X-ray tomography-the effect of calendering conditions.* Powder Technology, 2022. **403**: p. 117366.

138. Xu, J., et al., *Lithium ion battery electrode manufacturing model accounting for 3D realistic shapes of active material particles.* Journal of Power Sources, 2023. **554**: p. 232294.

139. Shodiev, A., et al., *Insight on electrolyte infiltration of lithium ion battery electrodes by means of a new three-dimensional-resolved lattice Boltzmann model.* Energy Storage Materials, 2021. **38**: p. 80-92.

140. Yan, B., et al., *Three dimensional simulation of galvanostatic discharge of LiCoO2 cathode based on X-ray nano-CT images.* Journal of The Electrochemical Society, 2012. **159**(10): p. A1604.

141. Su, Z., et al., *X-ray nanocomputed tomography in Zernike phase contrast for studying 3D morphology of Li–O2 battery electrode.* ACS Applied Energy Materials, 2020. **3**(5): p. 4093-4102.

142. Zielke, L., et al., *A combination of x-ray tomography and carbon binder modeling: reconstructing the three phases of LiCoO2 Li-ion battery cathodes.* Advanced Energy Materials, 2014. **4**(8): p. 1301617.

143. Su, Z., et al., *Artificial neural network approach for multiphase segmentation of battery electrode nano-CT images.* npj Computational Materials, 2022. **8**(1): p. 30.

144. Daemi, S.R., et al., *Computer-Vision-Based Approach to Classify and Quantify Flaws in Li-Ion Electrodes.* Small Methods, 2022. **6**(10): p. 2200887.

145. Jiang, Z., et al., *Machine-learning-revealed statistics of the particle-carbon/binder detachment in lithium-ion battery cathodes.* Nature communications, 2020. **11**(1): p. 2310.

146. Dixit, M.B., et al., *Synchrotron imaging of pore formation in Li metal solid-state batteries aided by machine learning.* ACS Applied Energy Materials, 2020. **3**(10): p. 9534-9542.

147. Cowan, A.J. and L.J. Hardwick, *Advanced Spectroelectrochemical Techniques to Study Electrode Interfaces Within Lithium-Ion and Lithium-Oxygen Batteries.* Annual Review of Analytical Chemistry, 2019. **12**(1): p. 323-346.

148. Gervillié-Mouravieff, C., et al., *Unlocking cell chemistry evolution with operando fibre optic infrared spectroscopy in commercial Na(Li)-ion batteries.* Nature Energy, 2022. **7**(12): p. 1157-1169.

149. Weiling, M., F. Pfeiffer, and M. Baghernejad, *Vibrational Spectroscopy Insight into the Electrode|electrolyte Interface/Interphase in Lithium Batteries.* Advanced Energy Materials, 2022. **12**(46): p. 2202504.

150. Raman, C.V. and K.S. Krishnan, *A New Type of Secondary Radiation.* Nature, 1928. **121**(3048): p. 501-502.

151. Baddour-Hadjean, R. and J.P. Pereira-Ramos, *Raman microspectrometry applied to the study of electrode materials for lithium batteries.* Chem Rev, 2010. **110**(3): p. 1278-319.

152. Fleischmann, M., P.J. Hendra, and A.J. McQuillan, *Raman spectra of pyridine adsorbed at a silver electrode.* Chemical Physics Letters, 1974. **26**(2): p. 163-166.

153. Schmitz, R., et al., *SEI investigations on copper electrodes after lithium plating with Raman spectroscopy and mass spectrometry.* Journal of Power Sources, 2013. **233**: p. 110-114.

154. Tang, S., et al., *An electrochemical surface-enhanced Raman spectroscopic study on nanorod-structured lithium prepared by electrodeposition.* Journal of Raman Spectroscopy, 2016. **47**(9): p. 1017-1023.

155. Peng, Z., et al., *Oxygen reactions in a non-aqueous Li+ electrolyte.* Angew Chem Int Ed Engl, 2011. **50**(28): p. 6351-5.

156. Liu, K., et al., *A universal surface enhanced Raman spectroscopy (SERS)-active graphene cathode for lithium–air batteries.* RSC Advances, 2016. **6**(104): p. 102272-102279.

157. Galloway, T.A., et al., *Shell isolated nanoparticles for enhanced Raman spectroscopy studies in lithium–oxygen cells.* Faraday Discussions, 2017. **205**(0): p. 469-490.

158. Mayer, K.M. and J.H. Hafner, *Localized Surface Plasmon Resonance Sensors.* Chemical Reviews, 2011. **111**(6): p. 3828-3857.

159. Nehl, C.L. and J.H. Hafner, *Shape-dependent plasmon resonances of gold nanoparticles.* Journal of Materials Chemistry, 2008. **18**(21): p. 2415-2419.

160. Julien, C., *Fluorescence and Surface Enhanced Raman Scattering (SERS) of single molecules*. 2004, Université Paris Sud - Paris XI.

161. Jensen, T.R., et al., *Nanosphere Lithography: Effect of the External Dielectric Medium on the Surface Plasmon Resonance Spectrum of a Periodic Array of Silver Nanoparticles.* The Journal of Physical Chemistry B, 1999. **103**(45): p. 9846-9853.

162. Kim, K., et al., *Surface-Enhanced Raman Scattering Characteristics of 4-Aminobenzenethiol Derivatives Adsorbed on Silver.* The Journal of Physical Chemistry C, 2011. **115**(50): p. 24960-24966.

163. Ou, W., et al., *Thermal and Nonthermal Effects in Plasmon-Mediated Electrochemistry at Nanostructured Ag Electrodes.* Angewandte Chemie International Edition, 2020. **59**(17): p. 6790-6793.

164. Li, G., et al., *Further identification to the SEI film on Ag electrode in lithium batteries by surface enhanced Raman scattering (SERS).* Journal of Power Sources, 2002. **104**(2): p. 190-194.

165. Li, H., et al., *Surface-Enhanced Raman Scattering Study on Passivating Films of Ag Electrodes in Lithium Batteries.* The Journal of Physical Chemistry B, 2000. **104**(35): p. 8477-8480.

166. Mozhzhukhina, N., et al., *Direct Operando Observation of Double Layer Charging and Early Solid Electrolyte Interphase Formation in Li-Ion Battery Electrolytes.* J Phys Chem Lett, 2020. **11**(10): p. 4119-4123.

167. Gogoi, N., T. Melin, and E.J. Berg, *Elucidating the Step-Wise Solid Electrolyte Interphase Formation in Lithium-Ion Batteries with Operando Raman Spectroscopy.* Advanced Materials Interfaces, 2022. **9**(22): p. 2200945.

168. Chen, D., et al., *Operando Investigation into Dynamic Evolution of Cathode–Electrolyte Interfaces in a Li-Ion Battery.* Nano Letters, 2019. **19**(3): p. 2037-2043.

169. Piernas-Muñoz, M.J., et al., *Surface-enhanced Raman spectroscopy (SERS): a powerful technique to study the SEI layer in batteries.* Chemical Communications, 2021. **57**(18): p. 2253-2256.

170. Ha, Y., et al., *Probing the Evolution of Surface Chemistry at the Silicon–Electrolyte Interphase via In Situ Surface-Enhanced Raman Spectroscopy.* The Journal of Physical Chemistry Letters, 2020. **11**(1): p. 286-291.

171. Dinda, S., et al., *Capturing Nano-Scale Inhomogeneity of the Electrode Electrolyte Interface in Sodium-Ion Batteries Through Tip-Enhanced Raman Spectroscopy.* Advanced Energy Materials, 2023. **13**(42): p. 2302176.

172. Nanda, J., et al., *Unraveling the nanoscale heterogeneity of solid electrolyte interphase using tip-enhanced Raman spectroscopy.* Joule, 2019. **3**(8): p. 2001-2019.

173. Keilmann, F. and R. Hillenbrand, *Near-field microscopy by elastic light scattering from a tip.* Philos Trans A Math Phys Eng Sci, 2004. **362**(1817): p. 787-805.

174. Dazzi, A. and C.B. Prater, *AFM-IR: Technology and Applications in Nanoscale Infrared Spectroscopy and Chemical Imaging.* Chemical Reviews, 2017. **117**(7): p. 5146-5173.

175. Lucas, I.T., et al., *IR Near-Field Spectroscopy and Imaging of Single LixFePO4 Microcrystals.* Nano Letters, 2015. **15**(1): p. 1-7.

176. Ayache, M., et al., *Near-Field IR Nanoscale Imaging of the Solid Electrolyte Interphase on a HOPG Electrode.* Journal of The Electrochemical Society, 2015. **162**(13): p. A7078-A7082.

177. Ayache, M., S.F. Lux, and R. Kostecki, *IR Near-Field Study of the Solid Electrolyte Interphase on a Tin Electrode.* The Journal of Physical Chemistry Letters, 2015. **6**(7): p. 1126-1129.

178. Li, J.F., et al., *Shell-isolated nanoparticle-enhanced Raman spectroscopy.* Nature, 2010. **464**(7287): p. 392-395.

179. Hy, S., et al., *In situ surface enhanced Raman spectroscopic studies of solid electrolyte interphase formation in lithium ion battery electrodes.* Journal of Power Sources, 2014. **256**: p. 324-328.

180. Gajan, A., et al., *Solid Electrolyte Interphase Instability in Operating Lithium-Ion Batteries Unraveled by Enhanced-Raman Spectroscopy.* ACS Energy Letters, 2021. **6**(5): p. 1757-1763.

181. Cabo-Fernandez, L., et al., *In-Situ Electrochemical SHINERS Investigation of SEI Composition on Carbon-Coated Zn0.9Fe0.1O Anode for Lithium-Ion Batteries.* Batteries & Supercaps, 2019. **2**(2): p. 168-177.

182. Hy, S., et al., *Direct In situ Observation of Li2O Evolution on Li-Rich High-Capacity Cathode Material, Li[NixLi(1–2x)/3Mn(2–x)/3]O2 (0 ≤ x ≤0.5).* Journal of the American Chemical Society, 2014. **136**(3): p. 999-1007.

183. Li, C.-Y., et al., *Surface Changes of LiNixMnyCo1–x–yO2 in Li-Ion Batteries Using in Situ Surface-Enhanced Raman Spectroscopy.* The Journal of Physical Chemistry C, 2020. **124**(7): p. 4024-4031.

184. Pfeiffer, F., et al., *Study of a High-Voltage NMC Interphase in the Presence of a Thiophene Additive Realized by Operando SHINERS.* ACS Applied Materials & Interfaces, 2023. **15**(5): p. 6676-6686.

185. Pfeiffer, F., et al., *Quadrupled Cycle Life of High-Voltage Nickel-Rich Cathodes: Understanding the Effective Thiophene-Boronic Acid-Based CEI via Operando SHINERS.* Advanced Energy Materials, 2023: p. 2300827.

186. Gajan, A., *Study of interfacial processes in lithium-ion technology by operando analysis*. 2022, Sorbonne Université.

187. Morino, Y. and K.-I. Fukui, *Interface Behavior of Electrolyte/Quinone Organic Active Material in Battery Operation by Operando Surface-Enhanced Raman Spectroscopy.* Langmuir, 2022. **38**(12): p. 3951-3958.

188. Xue, L., et al., *In Situ/Operando Raman Techniques in Lithium–Sulfur Batteries.* Small Structures, 2022. **3**(3): p. 2100170.

189. Wang, C., et al., *In-situ SHINERS Study of the Size and Composition Effect of Pt-based Nanocatalysts in Catalytic Hydrogenation.* ChemCatChem, 2020. **12**(1): p. 75-79.

190. Dong, J.-C., et al., *In situ Raman spectroscopic evidence for oxygen reduction reaction intermediates at platinum single-crystal surfaces.* Nature Energy, 2019. **4**(1): p. 60-67.

191. Nie, M., et al., *Silicon Solid Electrolyte Interphase (SEI) of Lithium Ion Battery Characterized by Microscopy and Spectroscopy.* The Journal of Physical Chemistry C, 2013. **117**(26): p. 13403-13412.

192. Gu, Y., et al., *Resolving nanostructure and chemistry of solid-electrolyte interphase on lithium anodes by depth-sensitive plasmon-enhanced Raman spectroscopy.* Nature Communications, 2023. **14**(1): p. 3536.

193. Martin-Yerga, D., et al., *Dynamics of Solid-Electrolyte Interphase Formation on Silicon Electrodes Revealed by Combinatorial Electrochemical Screening.* Angew Chem Int Ed Engl, 2022. **61**(34): p. e202207184.

194. Mehring, M., *Principles of High Resolution NMR in Solids*. 1983, Berlin Heidelberg: Springer-Verlag.

195. Duer, M.J., *Solid-state NMR: Principles and applications.pdf*. Blackwell. 2002, Oxford, UK.

196. Duer, M.J., *Introduction to Solid-State NMR*. 2004, Oxford, UK: Blackwell.

197. Levitt, M.H., *Spin Dynamics*. 2006, Chichester: John Wiley & Sons.

198. Keeler, J., *Understanding NMR Spectroscopy*. 2010, Chichester, UK: John Wiley & Sons.

199. Leskes, M., et al., *Surface-Sensitive NMR Detection of the Solid Electrolyte Interphase Layer on Reduced Graphene Oxide.* J Phys Chem Lett, 2017. **8**(5): p. 1078-1085.

200. Michan, A.L., et al., *Solid Electrolyte Interphase Growth and Capacity Loss in Silicon Electrodes.* J Am Chem Soc, 2016. **138**(25): p. 7918-31.

201. Michan, A.L., M. Leskes, and C.P. Grey, *Voltage Dependent Solid Electrolyte Interphase Formation in Silicon Electrodes: Monitoring the Formation of Organic Decomposition Products.* Chemistry of Materials, 2015. **28**(1): p. 385-398.

202. Michan, A.L., et al., *Fluoroethylene Carbonate and Vinylene Carbonate Reduction: Understanding Lithium-Ion Battery Electrolyte Additives and Solid Electrolyte Interphase Formation.* Chemistry of Materials, 2016. **28**(22): p. 8149-8159.

203. Michan, A.L., et al., *Solid electrolyte interphase growth and capacity loss in silicon electrodes.* Journal of the American Chemical Society, 2016. **138**(25): p. 7918-7931.

204. Castaing, R., et al., *NMR quantitative analysis of solid electrolyte interphase on aged Li-ion battery electrodes.* Electrochimica Acta, 2015. **155**: p. 391-395.

205. Hestenes, J.C., et al., *Resolving Chemical and Spatial Heterogeneities at Complex Electrochemical Interfaces in Li-Ion Batteries.* Chemistry of Materials, 2021. **34**(1): p. 232-243.

206. Jin, Y., et al., *Identifying the Structural Basis for the Increased Stability of the Solid Electrolyte Interphase Formed on Silicon with the Additive Fluoroethylene Carbonate.* J Am Chem Soc, 2017. **139**(42): p. 14992-15004.

207. Jin, Y., et al., *Understanding Fluoroethylene Carbonate and Vinylene Carbonate Based Electrolytes for Si Anodes in Lithium Ion Batteries with NMR Spectroscopy.* J Am Chem Soc, 2018. **140**(31): p. 9854-9867.

208. Haber, S., et al., *Structure and Functionality of an Alkylated Li(x)Si(y)O(z) Interphase for High-Energy Cathodes from DNP-ssNMR Spectroscopy.* J Am Chem Soc, 2021. **143**(12): p. 4694-4704.

209. Hope, M.A., et al., *Selective NMR observation of the SEI-metal interface by dynamic nuclear polarisation from lithium metal.* Nat Commun, 2020. **11**(1): p. 2224.

210. Haber, S., et al., *Structure and functionality of an alkylated Li x Si y O z interphase for high-energy cathodes from DNP-ssNMR spectroscopy.* Journal of the American Chemical Society, 2021. **143**(12): p. 4694-4704.

211. Hope, M.A., et al., *Selective NMR observation of the SEI–metal interface by dynamic nuclear polarisation from lithium metal.* Nature communications, 2020. **11**(1): p. 2224.

212. Pecher, O., et al., *Automatic Tuning Matching Cycler (ATMC) in situ NMR spectroscopy as a novel approach for real-time investigations of Li- and Na-ion batteries.* J Magn Reson, 2016. **265**: p. 200-9.

213. Pecher, O., et al., *Materials' Methods: NMR in Battery Research.* Chemistry of Materials, 2016. **29**(1): p. 213-242.

214. Stratford, J.M., et al., *Mechanistic insights into sodium storage in hard carbon anodes using local structure probes.* Chem Commun (Camb), 2016. **52**(84): p. 12430-12433.

215. Qian, D., et al., *Advanced analytical electron microscopy for lithium-ion batteries.* NPG Asia materials, 2015. **7**(6): p. e193-e193.

216. Wang, Z. and Y.S. Meng, *Analytical Electron Microscopy—Study of All Solid-State Batteries*, in *Handbook of Solid State Batteries*. 2016, World Scientific. p. 109-131.

217. Yu, L., et al., *(S) TEM-EELS as an advanced characterization technique for lithium-ion batteries.* Materials Chemistry Frontiers, 2021. **5**(14): p. 5186-5193.

218. Zhang, C., et al., *Electrochemical and Structural Analysis in All-Solid-State Lithium Batteries by Analytical Electron Microscopy: Progress and Perspectives.* Advanced Materials, 2020. **32**(27): p. 1903747.

219. Howie, A., *Image contrast and localized signal selection techniques.* Journal of Microscopy, 1979. **117**(1): p. 11-23.

220. Pennycook, S. and D. Jesson, *High-resolution incoherent imaging of crystals.* Physical review letters, 1990. **64**(8): p. 938.

221. Nellist, P. and S. Pennycook, *Incoherent imaging using dynamically scattered coherent electrons.* Ultramicroscopy, 1999. **78**(1-4): p. 111-124.

222. Shin, D., E. Kirkland, and J. Silcox, *Annular dark field electron microscope images with better than 2 Å resolution at 100 kV.* Applied physics letters, 1989. **55**(23): p. 2456-2458.

223. Batson, P.E., N. Dellby, and O.L. Krivanek, *Sub-ångstrom resolution using aberration corrected electron optics.* Nature, 2002. **418**(6898): p. 617-620.

224. Nellist, P.D., et al., *Direct sub-angstrom imaging of a crystal lattice.* science, 2004. **305**(5691): p. 1741-1741.

225. Shukla, A.K., et al., *Unravelling structural ambiguities in lithium-and manganese-rich transition metal oxides.* Nature communications, 2015. **6**(1): p. 8711.

226. Shukla, A.K., et al., *Effect of composition on the structure of lithium-and manganese-rich transition metal oxides.* Energy & Environmental Science, 2018. **11**(4): p. 830-840.

227. Liu, H., et al., *Unraveling the rapid performance decay of layered high-energy cathodes: from nanoscale degradation to drastic bulk evolution.* ACS nano, 2018. **12**(3): p. 2708-2718.

228. Liu, H., et al., *Spatially resolved surface valence gradient and structural transformation of lithium transition metal oxides in lithium-ion batteries.* Physical Chemistry Chemical Physics, 2016. **18**(42): p. 29064-29075.

229. Li, X., et al., *Unravelling the chemistry and microstructure evolution of a cathodic interface in sulfide-based all-solid-state Li-ion batteries.* ACS Energy Letters, 2019. **4**(10): p. 2480-2488.

230. Lin, F., et al., *Surface reconstruction and chemical evolution of stoichiometric layered cathode materials for lithium-ion batteries.* Nature communications, 2014. **5**(1): p. 3529.

231. Xiao, B., et al., *Nanoscale Manipulation of Spinel Lithium Nickel Manganese Oxide Surface by Multisite Ti Occupation as High-Performance Cathode.* Advanced materials, 2017. **29**(47): p. 1703764.

232. Carroll, K.J., et al., *Probing the electrode/electrolyte interface in the lithium excess layered oxide $Li_{1.2}Ni_{0.2}Mn_{0.6}O_2$.* Physical Chemistry Chemical Physics, 2013. **15**(26): p. 11128-11138.

233. Xu, B., et al., *Identifying surface structural changes in layered Li-excess nickel manganese oxides in high voltage lithium ion batteries: A joint experimental and theoretical study.* Energy & Environmental Science, 2011. **4**(6): p. 2223-2233.

234. Okunishi, E., et al., *Visualization of light elements at ultrahigh resolution by STEM annular bright field microscopy.* Microscopy and Microanalysis, 2009. **15**(S2): p. 164-165.

235. Findlay, S., et al., *Robust atomic resolution imaging of light elements using scanning transmission electron microscopy.* Applied Physics Letters, 2009. **95**(19): p. 191913.

236. Findlay, S.D., et al., *Direct visualization of lithium via annular bright field scanning transmission electron microscopy: a review.* Microscopy, 2017. **66**(1): p. 3-14.

237. Wen, Y., T. Shang, and L. Gu, *Analytical ABF-STEM imaging of Li ions in rechargeable batteries.* Microscopy, 2017. **66**(1): p. 25-38.

238. Gu, L., et al., *Direct observation of lithium staging in partially delithiated LiFePO4 at atomic resolution.* Journal of the American Chemical Society, 2011. **133**(13): p. 4661-4663.

239. Tang, D., et al., *Surface structure evolution of LiMn2O4 cathode material upon charge/discharge.* Chemistry of Materials, 2014. **26**(11): p. 3535-3543.

240. Kim, D.-w., et al., *Full picture discovery for mixed-fluorine anion effects on high-voltage spinel lithium nickel manganese oxide cathodes.* NPG Asia Materials, 2017. **9**(7): p. e398-e398.

241. Huang, R. and Y. Ikuhara, *STEM characterization for lithium-ion battery cathode materials.* Current Opinion in Solid State and Materials Science, 2012. **16**(1): p. 31-38.

242. Gao, X., et al., *Lithium atom and A-site vacancy distributions in lanthanum lithium titanate.* Chemistry of Materials, 2013. **25**(9): p. 1607-1614.

243. Gu, L., et al., *Atomic-Scale Structure Evolution in a Quasi-Equilibrated Electrochemical Process of Electrode Materials for Rechargeable Batteries.* Advanced Materials, 2015. **27**(13): p. 2134-2149.

244. Ikuhara, Y.H., et al., *Atomic-Level Changes during Electrochemical Cycling of Oriented LiMn2O4 Cathodic Thin Films.* ACS Applied Materials & Interfaces, 2022. **14**(5): p. 6507-6517.

245. Yu, H., et al., *Direct atomic-resolution observation of two phases in the Li1. 2Mn0. 567Ni0. 166Co0. 067O2 cathode material for lithium-ion batteries.* Angewandte Chemie International Edition, 2013. **52**(23): p. 5969-5973.

246. Lu, X., et al., *Lithium storage in Li4Ti5O12 spinel: the full static picture from electron microscopy.* Advanced Materials, 2012. **24**(24): p. 3233-3238.

247. Gao, X., et al., *Structural distortion and compositional gradients adjacent to epitaxial LiMn2O4 thin film interfaces.* Advanced Materials Interfaces, 2014. **1**(8): p. 1400143.

248. Wang, Y.-Q., et al., *Rutile-TiO2 nanocoating for a high-rate Li4Ti5O12 anode of a lithium-ion battery.* Journal of the American Chemical Society, 2012. **134**(18): p. 7874-7879.

249. Huang, R., et al., *Oxygen-vacancy ordering at surfaces of lithium manganese (III, IV) oxide spinel nanoparticles.* Angewandte Chemie-International Edition, 2011. **50**(13): p. 3053-3057.

250. Tang, D., et al., *Electrochemical behavior and surface structural change of $LiMn_2O_4$ charged to 5.1 V.* Journal of Materials Chemistry A, 2014. **2**(35): p. 14519-14527.

251. Lazić, I., E.G. Bosch, and S. Lazar, *Phase contrast STEM for thin samples: Integrated differential phase contrast.* Ultramicroscopy, 2016. **160**: p. 265-280.

252. Müller, K., et al., *Atomic electric fields revealed by a quantum mechanical approach to electron picodiffraction.* Nature communications, 2014. **5**(1): p. 5653.

253. Müller-Caspary, K., et al., *Measurement of atomic electric fields and charge densities from average momentum transfers using scanning transmission electron microscopy.* Ultramicroscopy, 2017. **178**: p. 62-80.

254. Shibata, N., et al., *Differential phase-contrast microscopy at atomic resolution.* Nature Physics, 2012. **8**(8): p. 611-615.

255. Shibata, N., et al., *Electric field imaging of single atoms.* Nature communications, 2017. **8**(1): p. 15631.

256. Cao, M.C., et al., *Theory and practice of electron diffraction from single atoms and extended objects using an EMPAD.* Microscopy, 2018. **67**(suppl_1): p. i150-i161.

257. Hachtel, J.A., J.C. Idrobo, and M. Chi, *Sub-Ångstrom electric field measurements on a universal detector in a scanning transmission electron microscope.* Advanced structural and chemical imaging, 2018. **4**: p. 1-10.

258. Wang, L., et al., *In-situ visualization of the space-charge-layer effect on interfacial lithium-ion transport in all-solid-state batteries.* Nature Communications, 2020. **11**(1): p. 5889.

259. He, W., et al., *Microscopic Segregation Dominated Nano-Interlayer Boosts 4.5 V Cyclability and Rate Performance for Sulfide-Based All-Solid-State Lithium Batteries.* Advanced Energy Materials, 2023. **13**(3): p. 2203703.

260. Ribeiro, R. and P. Ferreira, *Manganese migration in Li1-xMn2O4 cathode materials.* Ultramicroscopy, 2021. **225**: p. 113285.

261. Zachman, M.J., et al., *Robust Atomic-Resolution Imaging of Lithium in Battery Materials by Center-of-Mass Scanning Transmission Electron Microscopy.* ACS nano, 2022. **16**(1): p. 1358-1367.

262. Zaluzec, N.J., *Quantitative assessment and measurement of X-ray detector performance and solid angle in the analytical electron microscope.* Microscopy and Microanalysis, 2022. **28**(1): p. 83-95.

263. Kothleitner, G., et al., *Quantitative elemental mapping at atomic resolution using X-ray spectroscopy.* Physical Review Letters, 2014. **112**(8): p. 085501.

264. Wang, K., et al., *Preparation of intergrown P/O-type biphasic layered oxides as high-performance cathodes for sodium ion batteries.* Journal of Materials Chemistry A, 2021. **9**(22): p. 13151-13160.

265. Nishio, K., et al., *Immense Reduction in Interfacial Resistance between Sulfide Electrolyte and Positive Electrode.* ACS Applied Materials & Interfaces, 2022. **14**(30): p. 34620-34626.

266. Laurita, A., et al., *Pristine Surface of Ni-Rich Layered Transition Metal Oxides as a Premise of Surface Reactivity.* ACS Applied Materials & Interfaces, 2022. **14**(37): p. 41945-41956.

267. Santhanagopalan, D., et al., *Interface limited lithium transport in solid-state batteries.* The journal of physical chemistry letters, 2014. **5**(2): p. 298-303.

268. Mauchamp, V., et al., *Ab initio simulation of the electron energy-loss near-edge structures at the Li K edge in Li, Li 2 O, and Li Mn 2 O 4.* Physical Review B, 2006. **74**(11): p. 115106.

269. Wang, F., et al., *Chemical distribution and bonding of lithium in intercalated graphite: Identification with optimized electron energy loss spectroscopy.* ACS nano, 2011. **5**(2): p. 1190-1197.

270. Boniface, M., et al., *Nanoscale chemical evolution of silicon negative electrodes characterized by low-loss STEM-EELS.* Nano letters, 2016. **16**(12): p. 7381-7388.

271. Dupré, N., et al., *Carbonate and ionic liquid mixes as electrolytes to modify interphases and improve cell safety in silicon-based li-ion batteries.* Chemistry of Materials, 2017. **29**(19): p. 8132-8146.

272. Chen, J., et al., *Electrolyte design for LiF-rich solid–electrolyte interfaces to enable high-performance microsized alloy anodes for batteries.* Nature Energy, 2020. **5**(5): p. 386-397.

273. Moreau, P., et al., *Fast determination of phases in Li_xFePO_4 using low losses in electron energy-loss spectroscopy.* Applied Physics Letters, 2009. **94**(12): p. 123111.

274. Holtz, M.E., et al., *Nanoscale imaging of lithium ion distribution during in situ operation of battery electrode and electrolyte.* Nano letters, 2014. **14**(3): p. 1453-1459.

275. Lazar, S., et al., *Materials science applications of HREELS in near edge structure analysis and low-energy loss spectroscopy.* Ultramicroscopy, 2003. **96**(3-4): p. 535-546.

276. Terauchi, M., et al., *Development of a high energy resolution electron energy-loss spectroscopy microscope.* Journal of microscopy, 1999. **194**(1): p. 203-209.

277. Krivanek, O.L., et al., *High-energy-resolution monochromator for aberration-corrected scanning transmission electron microscopy/electron energy-loss*

spectroscopy. Philosophical Transactions of the Royal Society A: Mathematical, Physical and Engineering Sciences, 2009. **367**(1903): p. 3683-3697.

278. Mukai, M., et al., *Development of a monochromator for aberration-corrected scanning transmission electron microscopy.* Microscopy, 2015. **64**(3): p. 151-158.

279. Laffont, L., et al., *Study of the $LiFePO_4/FePO_4$ two-phase system by high-resolution electron energy loss spectroscopy.* Chemistry of materials, 2006. **18**(23): p. 5520-5529.

280. Jarvis, K., et al., *Surface reconstruction in Li-rich layered oxides of Li-ion batteries.* Chemistry of Materials, 2017. **29**(18): p. 7668-7674.

281. Kobayashi, S., et al., *Atomic-Scale Observations of Oxygen Release Degradation in Sulfide-Based All-Solid-State Batteries with Layered Oxide Cathodes.* ACS Applied Materials & Interfaces, 2022. **14**(34): p. 39459-39466.

282. Lu, Q., et al., *Nanostructured flexible Mg-modified LiMnPO 4 matrix as high-rate cathode materials for Li-ion batteries.* Journal of Materials Chemistry A, 2014. **2**(18): p. 6368-6373.

283. Yang, L., et al., *Direct View on the Origin of High Li+ Transfer Impedance in All-Solid-State Battery.* Advanced Functional Materials, 2021. **31**(35): p. 2103971.

284. Wang, Z., et al., *Effects of cathode electrolyte interfacial (CEI) layer on long term cycling of all-solid-state thin-film batteries.* Journal of Power Sources, 2016. **324**: p. 342-348.

285. Yamamoto, Y., Y. Iriyama, and S. Muto, *STEM-EELS analysis of the interface structures of composite ASS-LIB electrodes fabricated via aerosol deposition.* Journal of the American Ceramic Society, 2020. **103**(2): p. 1454-1462.

286. Muto, S., et al., *STEM-EELS spectrum imaging of an aerosol-deposited NASICON-type LATP solid electrolyte and LCO cathode interface.* ACS Applied Energy Materials, 2021. **5**(1): p. 98-107.

287. Mauchamp, V., et al., *Determination of Lithium Insertion Sites in Li x TiP4 (x= 2–11) by Electron Energy-Loss Spectroscopy.* The Journal of Physical Chemistry C, 2007. **111**(10): p. 3996-4002.

288. Muto, S., et al., *Mapping of heterogeneous chemical states of lithium in a LiNiO2-based active material by electron energy-loss spectroscopy.* Electrochemical and Solid-State Letters, 2010. **13**(8): p. A115.

289. Zachman, M.J., et al., *Cryo-STEM mapping of solid–liquid interfaces and dendrites in lithium-metal batteries.* Nature, 2018. **560**(7718): p. 345-349.

290. Mauchamp, V., et al., *Local field effects at Li K edges in electron energy-loss spectra of Li, Li 2 O and LiF.* Physical Review B, 2008. **77**(4): p. 045117.

291. Yamamoto, K., Y. Iriyama, and T. Hirayama, *Operando observations of solid-state electrochemical reactions in Li-ion batteries by spatially resolved TEM EELS and electron holography.* Microscopy, 2017. **66**(1): p. 50-61.

292. Sun, Z., et al., *In situ transmission electron microscopy for understanding materials and interfaces challenges in all-solid-state lithium batteries.* eTransportation, 2022. **14**: p. 100203.

293. Jeangros, Q., et al., *Operando analysis of a solid oxide fuel cell by environmental transmission electron microscopy.* arXiv preprint arXiv:2302.12514, 2023.

294. Yamamoto, K., et al., *Nano-scale simultaneous observation of Li-concentration profile and Ti-, O electronic structure changes in an all-solid-state Li-ion battery by spatially-resolved electron energy-loss spectroscopy.* Journal of Power Sources, 2014. **266**: p. 414-421.

295. Unocic, R.R., et al., *Probing battery chemistry with liquid cell electron energy loss spectroscopy.* Chemical Communications, 2015. **51**(91): p. 16377-16380.

296. Wang, Z., et al., *In situ STEM-EELS observation of nanoscale interfacial phenomena in all-solid-state batteries.* Nano letters, 2016. **16**(6): p. 3760-3767.

297. Nomura, Y., et al., *Quantitative operando visualization of electrochemical reactions and Li ions in all-solid-state batteries by STEM-EELS with hyperspectral image analyses.* Nano letters, 2018. **18**(9): p. 5892-5898.

298. Kapetanovic, V., et al., *Tunable Infrared Plasmon Response of Lithographic Sn-doped Indium Oxide Nanostructures.* Advanced Optical Materials, 2020. **8**(22): p. 2001024.

299. Miyata, T., et al., *Measurement of vibrational spectrum of liquid using monochromated scanning transmission electron microscopy–electron energy loss spectroscopy.* Journal of Electron Microscopy, 2014. **63**(5): p. 377-382.

300. Krivanek, O.L., et al., *Vibrational spectroscopy in the electron microscope.* Nature, 2014. **514**(7521): p. 209-212.

301. Rez, P., et al., *Damage-free vibrational spectroscopy of biological materials in the electron microscope.* Nature communications, 2016. **7**(1): p. 10945.

302. Yan, X., et al., *Single-defect phonons imaged by electron microscopy.* Nature, 2021. **589**(7840): p. 65-69.

303. Gadre, C.A., et al., *Nanoscale imaging of phonon dynamics by electron microscopy.* Nature, 2022. **606**(7913): p. 292-297.

304. Venkatraman, K., et al., *Vibrational spectroscopy at atomic resolution with electron impact scattering.* Nature Physics, 2019. **15**(12): p. 1237-1241.

305. Hage, F., et al., *Phonon spectroscopy at atomic resolution.* Physical review letters, 2019. **122**(1): p. 016103.

306. Hage, F., et al., *Single-atom vibrational spectroscopy in the scanning transmission electron microscope.* Science, 2020. **367**(6482): p. 1124-1127.

307. Lagos, M.J., et al., *Mapping vibrational surface and bulk modes in a single nanocube.* Nature, 2017. **543**(7646): p. 529-532.

308. Li, X., et al., *Three-dimensional vectorial imaging of surface phonon polaritons.* Science, 2021. **371**(6536): p. 1364-1367.

309. Li, N., et al., *Direct observation of highly confined phonon polaritons in suspended monolayer hexagonal boron nitride.* Nature Materials, 2021. **20**(1): p. 43-48.

310. Hachtel, J.A., et al., *Identification of site-specific isotopic labels by vibrational spectroscopy in the electron microscope.* Science, 2019. **363**(6426): p. 525-528.

311. Senga, R., et al., *Imaging of isotope diffusion using atomic-scale vibrational spectroscopy.* Nature, 2022. **603**(7899): p. 68-72.

312. Venkatraman, K., et al., *Probing Lithium Ion Transport at Individual Interfaces.* arXiv preprint arXiv:2312.06041, 2023.

313. Zachman, M.J., et al., *Emerging electron microscopy techniques for probing functional interfaces in energy materials.* Angewandte Chemie International Edition, 2020. **59**(4): p. 1384-1396.

314. Plotkin-Swing, B., et al., *Hybrid pixel direct detector for electron energy loss spectroscopy.* Ultramicroscopy, 2020. **217**: p. 113067.

315. Cheng, S., et al., *The performance evaluation of direct detection electron energy-loss spectroscopy at 200 kV and 80 kV accelerating voltages.* Ultramicroscopy, 2020. **212**: p. 112942.

316. Craven, A.J., et al., *Getting the most out of a post-column EELS spectrometer on a TEM/STEM by optimising the optical coupling.* Ultramicroscopy, 2017. **180**: p. 66-80.

317. MacLaren, I., et al., *EELS at very high energy losses.* Microscopy, 2018. **67**(suppl_1): p. i78-i85.

318. Hart, J.L., et al., *A synchrotron in the TEM: spatially resolved fine structure spectra at high energies.* arXiv preprint arXiv:1909.06323, 2019.

319. Dai, Q., et al., *Cryo-EM Studies of Atomic-Scale Structures of Interfaces in Garnet-Type Electrolyte Based Solid-State Batteries.* Advanced Functional Materials, 2022: p. 2208682.

320. Shimizu, R., et al., *Unraveling the Stable Cathode Electrolyte Interface in all Solid-State Thin-Film Battery Operating at 5 V.* Advanced Energy Materials, 2022. **12**(31): p. 2201119.

321. Yousaf, M., et al., *Visualization of battery materials and their interfaces/interphases using cryogenic electron microscopy.* Materials Today, 2022.

322. Ophus, C., *Four-dimensional scanning transmission electron microscopy (4D-STEM): From scanning nanodiffraction to ptychography and beyond.* Microscopy and Microanalysis, 2019. **25**(3): p. 563-582.

323. Midgley, P.A. and A.S. Eggeman, *Precession electron diffraction–a topical review.* IUCrJ, 2015. **2**(1): p. 126-136.

324. Rauch, E. and M. Véron, *Automated crystal orientation and phase mapping in TEM.* Materials Characterization, 2014. **98**: p. 1-9.

325. Folastre, N., et al., *Adaptative Diffraction Image Registration for 4D-STEM to optimize ACOM Pattern Matching.* arXiv preprint arXiv:2305.02124, 2023.

326. Hughes, L., et al., *Correlative analysis of structure and chemistry of LixFePO4 platelets using 4D-STEM and X-ray ptychography.* Materials Today, 2022. **52**: p. 102-111.

327. Cretu, S., et al., *The Impact of Inter-grain Phases on the Ionic Conductivity of LAGP Solid Electrolyte Prepared by Spark Plasma Sintering.* arXiv preprint arXiv:2211.06129, 2022.

328. Brunetti, G., et al., *Confirmation of the domino-cascade model by LiFePO4/FePO4 precession electron diffraction.* Chemistry of Materials, 2011. **23**(20): p. 4515-4524.

329. Brunet, F., et al., *Oxidative decomposition products of synthetic NaFePO4 marićite: nano-textural and electrochemical characterization.* European Journal of Mineralogy, 2019. **31**(4): p. 837-842.

330. Chen, Q., et al., *Imaging Beam-Sensitive Materials by Electron Microscopy.* Advanced Materials, 2020. **32**(16): p. 1907619.

331. Jiang, N. and J.C.H. Spence, *On the dose-rate threshold of beam damage in TEM.* Ultramicroscopy, 2012. **113**: p. 77-82.

332. Egerton, R.F., *Radiation damage to organic and inorganic specimens in the TEM.* Micron, 2019. **119**: p. 72-87.

333. Li, X., et al., *Influence of electron dose rate on electron counting images recorded with the K2 camera.* Journal of Structural Biology, 2013. **184**(2): p. 251-260.

334. Gallegos-Moncayo, K., et al., *Investigating Cathode Electrolyte Interphase Formation in NMC 811 Primary Particles Through Advanced 4D-STEM ACOM Analysis.* arXiv preprint arXiv:2312.13174, 2023.

335. Bhatia, A., et al., *In Situ Liquid Electrochemical TEM Investigation of LiMn1. 5Ni0. 5O4 Thin Film Cathode for Micro-Battery Applications.* Small Methods, 2022. **6**(2): p. 2100891.

336. Humphry, M., et al., *Ptychographic electron microscopy using high-angle dark-field scattering for sub-nanometre resolution imaging.* Nature communications, 2012. **3**(1): p. 730.

337. Yoon, D., et al., *Imaging Li Vacancies in a Li-Ion Battery Cathode Material by Depth Sectioning Multi-slice Electron Ptychographic Reconstructions*. 2023, Oxford University Press US.

338. Rinkel, B.L., et al., *Electrolyte oxidation pathways in lithium-ion batteries.* Journal of the American Chemical Society, 2020. **142**(35): p. 15058-15074.

339. Rinkel, B.L., et al., *Two electrolyte decomposition pathways at nickel-rich cathode surfaces in lithium-ion batteries.* Energy & environmental science, 2022. **15**(8): p. 3416-3438.

340. Sahore, R., F. Dogan, and I.D. Bloom, *Identification of Electrolyte-Soluble Organic Cross-Talk Species in a Lithium-Ion Battery via a Two-Compartment Cell.* Chemistry of Materials, 2019. **31**(8): p. 2884-2891.

341. Petibon, R., et al., *Study of electrolyte components in Li ion cells using liquid-liquid extraction and gas chromatography coupled with mass spectrometry.* Journal of The Electrochemical Society, 2014. **161**(6): p. A1167.

342. Kondo, K., et al., *Conductivity and Solvation of Li+ Ions of LiPF6 in Propylene Carbonate Solutions.* The Journal of Physical Chemistry B, 2000. **104**(20): p. 5040-5044.

343. Ruff, Z., C. Xu, and C. Grey, *Transition Metal Dissolution and Degradation in NMC811-Graphite Electrochemical Cells.* Journal of The Electrochemical Society, 2021.

344. Twining, B.S., et al., *Quantifying trace elements in individual aquatic protist cells with a synchrotron X-ray fluorescence microprobe.* Analytical chemistry, 2003. **75**(15): p. 3806-3816.

345. Banerjee, A., et al., *On the Oxidation State of Manganese Ions in Li-Ion Battery Electrolyte Solutions.* Journal of the American Chemical Society, 2017. **139**(5): p. 1738-1741.

346. Qiao, Y., et al., *Visualizing ion diffusion in battery systems by fluorescence microscopy: a case study on the dissolution of LiMn2O4.* Nano Energy, 2018. **45**: p. 68-74.

347. Padilla, N.A., et al., *Tracking Lithium Ions via Widefield Fluorescence Microscopy for Battery Diagnostics.* ACS Sensors, 2017. **2**(7): p. 903-908.

348. Ravdel, B., et al., *Thermal stability of lithium-ion battery electrolytes.* Journal of Power Sources, 2003. **119-121**: p. 805-810.

349. Campion, C.L., et al., *Suppression of Toxic Compounds Produced in the Decomposition of Lithium-Ion Battery Electrolytes.* Electrochemical and Solid-State Letters, 2004. **7**(7).

350. Campion, C.L., W. Li, and B.L. Lucht, *Thermal Decomposition of LiPF[sub 6]-Based Electrolytes for Lithium-Ion Batteries.* Journal of The Electrochemical Society, 2005. **152**(12).

351. Plakhotnyk, A.V., L. Ernst, and R. Schmutzler, *Hydrolysis in the system LiPF6—propylene carbonate—dimethyl carbonate—H2O.* Journal of Fluorine Chemistry, 2005. **126**(1): p. 27-31.

352. Wilken, S., et al., *Initial stages of thermal decomposition of LiPF6-based lithium ion battery electrolytes by detailed Raman and NMR spectroscopy.* RSC Advances, 2013. **3**(37).

353. Wiemers-Meyer, S., et al., *Influence of Battery Cell Components and Water on the Thermal and Chemical Stability of LiPF6 Based Lithium Ion Battery Electrolytes.* Electrochimica Acta, 2016. **222**: p. 1267-1271.

354. Wiemers-Meyer, S., M. Winter, and S. Nowak, *Mechanistic insights into lithium ion battery electrolyte degradation - a quantitative NMR study.* Phys Chem Chem Phys, 2016. **18**(38): p. 26595-26601.

355. Dose, W.M., et al., *Electrolyte Reactivity at the Charged Ni-Rich Cathode Interface and Degradation in Li-Ion Batteries.* ACS Appl Mater Interfaces, 2022. **14**(11): p. 13206-13222.

356. Dose, W.M., et al., *Onset Potential for Electrolyte Oxidation and Ni-Rich Cathode Degradation in Lithium-Ion Batteries.* ACS Energy Lett, 2022. **7**(10): p. 3524-3530.

357. Jin, Y., N.H. Kneusels, and C.P. Grey, *NMR Study of the Degradation Products of Ethylene Carbonate in Silicon-Lithium Ion Batteries.* J Phys Chem Lett, 2019. **10**(20): p. 6345-6350.

358. Ould, D.M.C., et al., *New Route to Battery Grade NaPF(6) for Na-Ion Batteries: Expanding the Accessible Concentration.* Angew Chem Int Ed Engl, 2021. **60**(47): p. 24882-24887.

359. Ould, D.M.C., et al., *Sodium Borates: Expanding the Electrolyte Selection for Sodium-Ion Batteries.* Angew Chem Int Ed Engl, 2022. **61**(32): p. e202202133.

360. Barnes, P., et al., *A non-aqueous sodium hexafluorophosphate-based electrolyte degradation study: Formation and mitigation of hydrofluoric acid.* Journal of Power Sources, 2020. **447**.

361. Jing, Y., et al., *In situ electrochemical recomposition of decomposed redox-active species in aqueous organic flow batteries.* Nat Chem, 2022. **14**(10): p. 1103-1109.

362. Wang, E., E.W. Zhao, and C.P. Grey, *New Magnetic Resonance and Computational Methods to Study Crossover Reactions in Li-Air and Redox Flow Batteries Using TEMPO.* The Journal of Physical Chemistry C, 2021. **125**(50): p. 27520-27533.

363. Campion, C.L., W. Li, and B.L. Lucht, *Thermal decomposition of LiPF6-based electrolytes for lithium-ion batteries.* Journal of The Electrochemical Society, 2005. **152**(12): p. A2327.

364. Rinkel, B.L.D., et al., *Electrolyte Oxidation Pathways in Lithium-Ion Batteries.* Journal of the American Chemical Society, 2020. **142**(35): p. 15058-15074.

365. Wiemers-Meyer, S., M. Winter, and S. Nowak, *A battery cell for in situ NMR measurements of liquid electrolytes.* Physical Chemistry Chemical Physics, 2017. **19**(7): p. 4962-4966.

366. Zhao, E.W., et al., *In situ NMR metrology reveals reaction mechanisms in redox flow batteries.* Nature, 2020. **579**(7798): p. 224-228.

367. Klett, M., et al., *Quantifying Mass Transport during Polarization in a Li Ion Battery Electrolyte by in Situ 7Li NMR Imaging.* Journal of the American Chemical Society, 2012. **134**(36): p. 14654-14657.

368. Bray, J.M., et al., *Quantitative, In Situ Visualization of Metal-Ion Dissolution and Transport Using (1) H Magnetic Resonance Imaging.* Angew Chem Int Ed Engl, 2016. **55**(32): p. 9394-7.

369. Britton, M.M., *Magnetic resonance imaging of electrochemical cells containing bulk metal.* Chemphyschem, 2014. **15**(9): p. 1731-6.

370. Klamor, S., et al., *(7)Li in situ 1D NMR imaging of a lithium ion battery.* Phys Chem Chem Phys, 2015. **17**(6): p. 4458-65.

371. Wang, A.A., et al., *Potentiometric MRI of a Superconcentrated Lithium Electrolyte: Testing the Irreversible Thermodynamics Approach.* ACS Energy Lett, 2021. **6**(9): p. 3086-3095.

372. Wiemers-Meyer, S., M. Winter, and S. Nowak, *A battery cell for in situ NMR measurements of liquid electrolytes.* Phys Chem Chem Phys, 2017. **19**(7): p. 4962-4966.

373. Zhao, E.W., et al., *Coupled In Situ NMR and EPR Studies Reveal the Electron Transfer Rate and Electrolyte Decomposition in Redox Flow Batteries.* J Am Chem Soc, 2021. **143**(4): p. 1885-1895.

374. Zhao, E.W., et al., *In situ NMR metrology reveals reaction mechanisms in redox flow batteries.* Nature, 2020. **579**(7798): p. 224-228.

375. Hodnik, N., G. Dehm, and K.J. Mayrhofer, *Importance and challenges of electrochemical in situ liquid cell electron microscopy for energy conversion research.* Accounts of chemical research, 2016. **49**(9): p. 2015-2022.

376. Huang, J.Y., et al., *In situ observation of the electrochemical lithiation of a single SnO2 nanowire electrode.* Science, 2010. **330**(6010): p. 1515-1520.

377. McDowell, M.T., et al., *The effect of metallic coatings and crystallinity on the volume expansion of silicon during electrochemical lithiation/delithiation.* Nano Energy, 2012. **1**(3): p. 401-410.

378. Mehdi, B.L., et al., *Observation and quantification of nanoscale processes in lithium batteries by operando electrochemical (S) TEM.* Nano letters, 2015. **15**(3): p. 2168-2173.

379. Unocic, R.R., et al., *Quantitative electrochemical measurements using in situ ec-S/TEM devices.* Microscopy and Microanalysis, 2014. **20**(2): p. 452-461.

380. Abellan, P., et al., *Probing the degradation mechanisms in electrolyte solutions for Li-ion batteries by in situ transmission electron microscopy.* Nano letters, 2014. **14**(3): p. 1293-1299.

381. Karakulina, O.M., et al., *In situ electron diffraction tomography using a liquid-electrochemical transmission electron microscopy cell for crystal structure determination of cathode materials for Li-ion batteries.* Nano letters, 2018. **18**(10): p. 6286-6291.

382. Yamamoto, K., Y. Iriyama, and T. Hirayama, *Visualization of electrochemical reactions in all-solid-state Li-ion batteries by spatially resolved electron energy-loss spectroscopy and electron holography.* Materials transactions, 2015. **56**(5): p. 617-624.

383. Wang, F., et al., *Tracking lithium transport and electrochemical reactions in nanoparticles.* Nature communications, 2012. **3**(1): p. 1201.

384. Sacci, R.L., et al., *Nanoscale imaging of fundamental Li battery chemistry: solid-electrolyte interphase formation and preferential growth of lithium metal nanoclusters.* Nano letters, 2015. **15**(3): p. 2011-2018.

385. Liu, X.H. and J.Y. Huang, *In situ TEM electrochemistry of anode materials in lithium ion batteries.* Energy & Environmental Science, 2011. **4**(10): p. 3844-3860.

386. He, K., et al., *Operando liquid cell electron microscopy of discharge and charge kinetics in lithium-oxygen batteries.* Nano Energy, 2018. **49**: p. 338-345.

387. Lee, D., et al., *Direct observation of redox mediator-assisted solution-phase discharging of Li–O2 battery by liquid-phase transmission electron microscopy.* Journal of the American Chemical Society, 2019. **141**(20): p. 8047-8052.

388. Lutz, L., et al., *Operando monitoring of the solution-mediated discharge and charge processes in a Na–O2 battery using liquid-electrochemical transmission electron microscopy.* Nano letters, 2018. **18**(2): p. 1280-1289.

389. Zeng, Z., et al., *Visualization of electrode–electrolyte interfaces in LiPF6/EC/DEC electrolyte for lithium ion batteries via in situ TEM.* Nano letters, 2014. **14**(4): p. 1745-1750.

390. Unocic, R.R., et al., *In situ Nanoscale Imaging and Spectroscopy of Energy Storage Materials.* Microscopy and Microanalysis, 2017. **23**(S1): p. 1964-1965.

391. Yan, G., et al., *Assessment of the electrochemical stability of carbonate-based electrolytes in Na-ion batteries.* Journal of the Electrochemical Society, 2018. **165**(7): p. A1222.

392. Miele, E., et al., *Hollow-core optical fibre sensors for operando Raman spectroscopy investigation of Li-ion battery liquid electrolytes.* Nature Communications, 2022. **13**(1): p. 1651.

393. Córdoba, D., H.n.B. Rodríguez, and E.J. Calvo, *Operando Fluorescence Detection of Singlet Oxygen inside High-Performance Li–O2 Batteries.* The Journal of Physical Chemistry C, 2022. **127**(1): p. 78-84.

394. Francis et al., i.p.

395. Pandya, R., et al., *Three-dimensional operando optical imaging of particle and electrolyte heterogeneities inside Li-ion batteries.* Nature Nanotechnology, 2023. **18**(10): p. 1185-1194.

396. Cheng, Q., et al., *Operando and three-dimensional visualization of anion depletion and lithium growth by stimulated Raman scattering microscopy.* Nature communications, 2018. **9**(1): p. 2942.

397. Huang, J., et al., *Operando decoding of chemical and thermal events in commercial Na (Li)-ion cells via optical sensors.* Nature energy, 2020. **5**(9): p. 674-683.

398. Jarry, A., et al., *The Formation Mechanism of Fluorescent Metal Complexes at the LixNi0.5Mn1.5O4−δ/Carbonate Ester Electrolyte Interface.* Journal of the American Chemical Society, 2015. **137**(10): p. 3533-3539.

399. Schroder, K.W., et al., *Effects of Solute–Solvent Hydrogen Bonding on Nonaqueous Electrolyte Structure.* The Journal of Physical Chemistry Letters, 2015. **6**(15): p. 2888-2891.

400. Ren, X., et al., *Direct monitoring of trace water in Li-ion batteries using operando fluorescence spectroscopy.* Chemical Science, 2018. **9**(1): p. 231-237.

401. Cabo-Fernandez, L., et al., *Kerr gated Raman spectroscopy of LiPF 6 salt and LiPF 6-based organic carbonate electrolyte for Li-ion batteries.* Physical Chemistry Chemical Physics, 2019. **21**(43): p. 23833-23842.

402. Kim, S., et al., *In Situ Gas Analysis by Differential Electrochemical Mass Spectrometry for Advanced Rechargeable Batteries: A Review.* Advanced Energy Materials, 2023. **13**(39): p. 2301983.

403. Dreyer, S.L., et al., *In situ analysis of gas evolution in liquid- and solid-electrolyte-based batteries with current and next-generation cathode materials.* Journal of Materials Research, 2022. **37**(19): p. 3146-3168.

404. Shi, B., et al., *Differential electrochemical mass spectrometry (DEMS) for batteries*, in *Batteries*. 2021, IOP Publishing. p. 5-1-5-45.

405. Strauss, F., et al., *Gas Evolution in Lithium-Ion Batteries: Solid versus Liquid Electrolyte.* ACS Applied Materials & Interfaces, 2020. **12**(18): p. 20462-20468.

406. Zhang, L., et al., *Unraveling gas evolution in sodium batteries by online electrochemical mass spectrometry.* Energy Storage Materials, 2021. **42**: p. 12-21.

407. Zhao, E.W., et al., *In situ NMR metrology reveals reaction mechanisms in redox flow batteries.* Nature, 2020. **579**(7798): p. 224-228.

408. Carrington, M.E., et al., *Associative pyridinium electrolytes for air-tolerant redox flow batteries.* Nature, 2023. **623**(7989): p. 949-955.

409. Tsiouvaras, N., et al., *A Novel On-Line Mass Spectrometer Design for the Study of Multiple Charging Cycles of a Li-O2Battery.* Journal of The Electrochemical Society, 2013. **160**(3): p. A471-A477.

410. Temprano, I., et al., *Toward Reversible and Moisture-Tolerant Aprotic Lithium-Air Batteries.* Joule, 2020. **4**: p. 1-20.

411. Qiao, Y., et al., *Unraveling the Complex Role of Iodide Additives in Li-O_2 Batteries.* ACS Energy Letters, 2017. **2**(8): p. 1869-1878.

412. Temprano, I., et al., *Recent Progress in Developing a LiOH-based Reversible Nonaqueous Lithium-Air Battery.* Advanced Materials, 2023. **35**: p. 2201384.

413. Su, Z., et al., *Binder-Free Cnt Cathodes for Li-O2 Batteries with More Than One Life.* Small Methods, 2024. **8**(1): p. 2300452.

414. Archer, L.A., et al., *Towards practical metal–oxygen batteries: general discussion.* Faraday Discussions, 2024.

415. Heiskanen, S.K., J. Kim, and B.L. Lucht, *Generation and Evolution of the Solid Electrolyte Interphase of Lithium-Ion Batteries.* Joule, 2019. **3**(10): p. 2322-2333.

416. Müller, V., et al., *Introduction and application of formation methods based on serial-connected lithium-ion battery cells.* Journal of Energy Storage, 2017. **14**: p. 56-61.

417. Wood, D.L., J. Li, and S.J. An, *Formation Challenges of Lithium-Ion Battery Manufacturing.* Joule, 2019. **3**(12): p. 2884-2888.

418. Liu, Y., et al., *Current and future lithium-ion battery manufacturing.* iScience, 2021. **24**(4): p. 102332.

419. Dose, W.M., et al., *Electrolyte Reactivity at the Charged Ni-Rich Cathode Interface and Degradation in Li-Ion Batteries.* ACS Applied Materials & Interfaces, 2022. **14**(11): p. 13206-13222.

420. Hausbrand, R., et al., *Fundamental degradation mechanisms of layered oxide Li-ion battery cathode materials: Methodology, insights and novel approaches.* Materials Science and Engineering: B, 2015. **192**: p. 3-25.

421. Li, T., et al., *Degradation Mechanisms and Mitigation Strategies of Nickel-Rich NMC-Based Lithium-Ion Batteries.* Electrochemical Energy Reviews, 2019. **3**(1): p. 43-80.

422. Teichert, P., et al., *Degradation and Aging Routes of Ni-Rich Cathode Based Li-Ion Batteries.* Batteries, 2020. **6**(1): p. 8.

423. Metzger, M., et al., *Origin of H2 Evolution in LIBs: H2O Reduction vs. Electrolyte Oxidation.* Journal of The Electrochemical Society, 2016. **163**(5): p. A798.

424. Páez Fajardo, G.J., et al., *Synergistic Degradation Mechanism in Single Crystal Ni-Rich NMC//Graphite Cells.* ACS Energy Letters, 2023: p. 5025-5031.

425. Leißing, M., et al., *The Origin of Gaseous Decomposition Products Formed During SEI Formation Analyzed by Isotope Labeling in Lithium-Ion Battery Electrolytes.* Batteries & Supercaps, 2021. **4**(11): p. 1731-1738.

426. Solchenbach, S., et al., *Quantification of PF5 and POF3 from Side Reactions of LiPF6 in Li-Ion Batteries.* Journal of The Electrochemical Society, 2018. **165**(13): p. A3022-A3028.

427. Dose, W.M., et al., *Effect of Anode Slippage on Cathode Cutoff Potential and Degradation Mechanisms in Ni-Rich Li-Ion Batteries.* Cell Reports Physical Science, 2020. **1**(11): p. 100253.

428. Bruckenstein, S. and R.R. Gadde, *Use of a porous electrode for in situ mass spectrometric determination of volatile electrode reaction products.* Journal of the American Chemical Society, 1971. **93**(3): p. 793-794.

429. Baltruschat, H., *Differential electrochemical mass spectrometry.* Journal of the American Society for Mass Spectrometry, 2004. **15**(12): p. 1693-1706.

430. McCloskey, B.D., et al., *Solvent's Critical Role in Nonaqueous Lithium-Oxygen Battery Electrochemistry.* The Journal of Physical Chemistry Letters, 2011. **2**(10): p. 1161-1166.

431. He, M., et al., *In situ gas analysis of Li4Ti5O12 based electrodes at elevated temperatures.* Journal of The Electrochemical Society, 2015. **162**(6): p. A870.

432. Castel, E., et al., *Differential Electrochemical Mass Spectrometry Study of the Interface of xLi2MnO3·(1–x)LiMO2 (M = Ni, Co, and Mn) Material as a Positive Electrode in Li-Ion Batteries.* Chemistry of Materials, 2014. **26**(17): p. 5051-5057.

433. Berkes, B.B., et al., *Online Continuous Flow Differential Electrochemical Mass Spectrometry with a Realistic Battery Setup for High-Precision, Long-Term Cycling Tests.* Analytical Chemistry, 2015. **87**(12): p. 5878-5883.

434. Berkes, B.B., et al., *In Situ Characterization of Gassing Processes in Lithium-Ion Batteries By Dems-Deirs.* ECS Meeting Abstracts, 2016. **MA2016-02**(2): p. 221.

435. Lu, J., et al., *Co3O4-Catalyzed LiOH Chemistry in Li–O2 Batteries.* ACS Energy Letters, 2020. **5**(12): p. 3681-3691.

436. Lebens-Higgins, Z., et al., *Electrochemical Utilization of Iron IV in the Li1.3Fe0.4Nb0.3O2 Disordered Rocksalt Cathode.* Batteries & Supercaps, 2021. **4**(5): p. 771-777.

437. Trimarco, D.B., et al., *Enabling real-time detection of electrochemical desorption phenomena with sub-monolayer sensitivity.* Electrochimica Acta, 2018. **268**: p. 520-530.

438. Thornton, D.B., et al., *Probing Degradation in Lithium Ion Batteries with On-Chip Electrochemistry Mass Spectrometry.* Angewandte Chemie, 2024. **136**(6): p. e202315357.

439. Geng, L., et al., *High accuracy in-situ direct gas analysis of Li-ion batteries.* Journal of Power Sources, 2020. **466**: p. 228211.

440. Misiewicz, C., et al., *Online electrochemical mass spectrometry on large-format Li-ion cells.* Journal of Power Sources, 2023. **554**: p. 232318.

441. Lanz, M. and P. Novák, *DEMS study of gas evolution at thick graphite electrodes for lithium-ion batteries: the effect of γ-butyrolactone.* Journal of Power Sources, 2001. **102**(1): p. 277-282.

442. Berkes, B.B., et al., *On the gassing behavior of lithium-ion batteries with NCM523 cathodes.* Journal of Solid State Electrochemistry, 2016. **20**(11): p. 2961-2967.

443. Bernhard, R., M. Metzger, and H.A. Gasteiger, *Gas Evolution at Graphite Anodes Depending on Electrolyte Water Content and SEI Quality Studied by On-Line Electrochemical Mass Spectrometry.* Journal of The Electrochemical Society, 2015. **162**(10): p. A1984.

444. Pritzl, D., et al., *Analysis of Vinylene Carbonate (VC) as Additive in Graphite/LiNi0.5Mn1.5O4 Cells.* Journal of The Electrochemical Society, 2017. **164**(12): p. A2625.

445. Solchenbach, S., et al., *Electrolyte and SEI Decomposition Reactions of Transition Metal Ions Investigated by On-Line Electrochemical Mass Spectrometry.* Journal of The Electrochemical Society, 2018. **165**(14): p. A3304.

446. Jung, R., et al., *Oxygen Release and Its Effect on the Cycling Stability of LiNixMnyCozO2(NMC) Cathode Materials for Li-Ion Batteries.* Journal of The Electrochemical Society, 2017. **164**(7): p. A1361-A1377.

447. Dose, W.M., et al., *Onset Potential for Electrolyte Oxidation and Ni-Rich Cathode Degradation in Lithium-Ion Batteries.* ACS Energy Letters, 2022. **7**(10): p. 3524-3530.

448. Wang, R., et al., *Influence of Carbonate Electrolyte Solvents on Voltage and Capacity Degradation in Li-Rich Cathodes for Li-ion Batteries.* Advanced Energy Materials. **n/a**(n/a): p. 2401097.

449. Ogley, M.J.W., et al., *Metal–Ligand Redox in Layered Oxide Cathodes for Li-ion Batteries.* 2024.

450. Strauss, F., et al., *Operando Characterization Techniques for All-Solid-State Lithium-Ion Batteries.* Advanced Energy and Sustainability Research, 2021. **2**(6): p. 2100004.

451. Berkes, B.B., et al., *Simultaneous acquisition of differential electrochemical mass spectrometry and infrared spectroscopy data for in situ characterization of gas evolution reactions in lithium-ion batteries.* Electrochemistry Communications, 2015. **60**: p. 64-69.

452. Lepoivre, F., et al., *Long-Time and Reliable Gas Monitoring in Li-O_2 Batteries via a Swagelok Derived Electrochemical Cell.* Journal of The Electrochemical Society, 2016. **163**(6): p. A923-A929.

453. Liu, T., et al., *Understanding LiOH Formation in a Li-O_2 Battery with LiI and H_2O Additives.* ACS Catalysis, 2018. **9**: p. 66-77.

454. Schiele, A., et al., *High-Throughput in Situ Pressure Analysis of Lithium-Ion Batteries.* Analytical Chemistry, 2017. **89**(15): p. 8122-8128.

455. Schweidler, S., et al., *Volume Changes of Graphite Anodes Revisited: A Combined Operando X-ray Diffraction and In Situ Pressure Analysis Study.* The Journal of Physical Chemistry C, 2018. **122**(16): p. 8829-8835.

456. Lepoivre, F., et al., *Long-Time and Reliable Gas Monitoring in Li-O2 Batteries via a Swagelok Derived Electrochemical Cell.* Journal of The Electrochemical Society, 2016. **163**(6): p. A923.

457. Burke, C.M., et al., *Implications of 4 e^- Oxygen Reduction via Iodide Redox Mediation in Li-O_2 Batteries.* ACS Energy Letters, 2016. **1**(4): p. 747-756.

458. Schmiegel, J.-P., et al., *Novel In Situ Gas Formation Analysis Technique Using a Multilayer Pouch Bag Lithium Ion Cell Equipped with Gas Sampling Port.* Journal of The Electrochemical Society, 2020. **167**(6): p. 060516.

459. Wu, J., *Understanding the Electric Double-Layer Structure, Capacitance, and Charging Dynamics.* Chemical Reviews, 2022. **122**(12): p. 10821-10859.

460. Becker, M., et al., *Multiscale Modeling of Aqueous Electric Double Layers.* Chemical Reviews, 2024. **124**(1): p. 1-26.

461. Tateyama, Y., et al., *Theoretical picture of positive electrode–solid electrolyte interface in all-solid-state battery from electrochemistry and semiconductor physics viewpoints.* Current Opinion in Electrochemistry, 2019. **17**: p. 149-157.

462. Park, H., S. Yu, and D.J. Siegel, *Predicting Charge Transfer Stability between Sulfide Solid Electrolytes and Li Metal Anodes.* ACS Energy Letters, 2021. **6**(1): p. 150-157.

463. Leung, K., *DFT modelling of explicit solid–solid interfaces in batteries: methods and challenges.* Physical Chemistry Chemical Physics, 2020. **22**(19): p. 10412-10425.

464. Cherkashinin, G., et al., *Energy Level Alignment at the Cobalt Phosphate/Electrolyte Interface: Intrinsic Stability vs Interfacial Chemical Reactions in 5 V Lithium Ion Batteries.* ACS Applied Materials & Interfaces, 2022. **14**(1): p. 543-556.

465. Gao, B., et al., *Interface structure prediction via CALYPSO method.* Science Bulletin, 2019. **64**(5): p. 301-309.

466. Verma, P. and D.G. Truhlar, *Status and Challenges of Density Functional Theory.* Trends in Chemistry, 2020. **2**(4): p. 302-318.

467. Hasnip, P.J., et al., *Density functional theory in the solid state.* Philosophical Transactions of the Royal Society A: Mathematical, Physical and Engineering Sciences, 2014. **372**(2011): p. 20130270.

468. Almeida, F., et al., *Energy monitoring as an essential building block towards sustainable ultrascale systems.* Sustainable Computing: Informatics and Systems, 2018. **17**: p. 27-42.

469. Muy, S., et al., *Lithium Conductivity and Meyer-Neldel Rule in Li3PO4–Li3VO4–Li4GeO4 Lithium Superionic Conductors.* Chemistry of Materials, 2018. **30**(16): p. 5573-5582.

470. Friederich, P., et al., *Machine-learned potentials for next-generation matter simulations.* Nature Materials, 2021. **20**(6): p. 750-761.

471. Howard, J.D., et al., *Understanding the Solid-State Electrode–Electrolyte Interface of a Model System Using First-Principles Statistical Mechanics and Thin-Film X-ray Characterization.* ACS Applied Materials & Interfaces, 2022. **14**(5): p. 7428-7439.

472. Lin, C.-a. and S.-k. Lin, *Issues, Developments, and Computation Analyses of Interfacial Stability in All-Solid-State Li Batteries.* JOM, 2022. **74**(12): p. 4654-4663.

473. Yu, S., H. Park, and D.J. Siegel, *Thermodynamic Assessment of Coating Materials for Solid-State Li, Na, and K Batteries.* ACS Applied Materials & Interfaces, 2019. **11**(40): p. 36607-36615.

474. Xiao, Y., et al., *Computational Screening of Cathode Coatings for Solid-State Batteries.* Joule, 2019. **3**(5): p. 1252-1275.

475. Liu, B., et al., *Insights into LiMXO4F (M–X = Al–P and Mg–S) as Cathode Coatings for High-Performance Lithium-Ion Batteries.* ACS Applied Materials & Interfaces, 2022. **14**(39): p. 44859-44868.

476. Wu, Y.-T. and P.-C. Tsai, *Ab initio Interfacial Chemical Stability of Argyrodite Sulfide Electrolytes and Layered-Structure Cathodes in Solid-State Lithium Batteries.* JOM, 2022. **74**(12): p. 4664-4671.

477. Nolan, A.M., E.D. Wachsman, and Y. Mo, *Computation-guided discovery of coating materials to stabilize the interface between lithium garnet solid electrolyte and high-energy cathodes for all-solid-state lithium batteries.* Energy Storage Materials, 2021. **41**: p. 571-580.

478. Wang, C., et al., *Ionic Conduction through Reaction Products at the Electrolyte–Electrode Interface in All-Solid-State Li+ Batteries.* ACS Applied Materials & Interfaces, 2020. **12**(49): p. 55510-55519.

479. Park, D., et al., *Theoretical Design of Lithium Chloride Superionic Conductors for All-Solid-State High-Voltage Lithium-Ion Batteries.* ACS Applied Materials & Interfaces, 2020. **12**(31): p. 34806-34814.

480. Zhang, Y.-Q., et al., *Direct Visualization of the Interfacial Degradation of Cathode Coatings in Solid State Batteries: A Combined Experimental and Computational Study.* Advanced Energy Materials, 2020. **10**(27): p. 1903778.

481. Liu, B., et al., *High-Throughput Computational Screening of Li-Containing Fluorides for Battery Cathode Coatings.* ACS Sustainable Chemistry & Engineering, 2020. **8**(2): p. 948-957.

482. Chun, G.H., J.H. Shim, and S. Yu, *Computational Investigation of the Interfacial Stability of Lithium Chloride Solid Electrolytes in All-Solid-State Lithium Batteries.* ACS Applied Materials & Interfaces, 2022. **14**(1): p. 1241-1248.

483. Li, S., et al., *High-throughput screening of protective layers to stabilize the electrolyte-anode interface in solid-state Li-metal batteries.* Nano Energy, 2022. **102**: p. 107640.

484. Liu, C., et al., *Computational Screening of Anode Coatings for Garnet-Type Solid-State Batteries.* Batteries & Supercaps, 2022. **5**(4): p. e202100357.

485. Cheng, J., K.D. Fong, and K.A. Persson, *Materials design principles of amorphous cathode coatings for lithium-ion battery applications.* Journal of Materials Chemistry A, 2022. **10**(41): p. 22245-22256.

486. Wang, C., K. Aoyagi, and T. Mueller, *Computational design of double-layer cathode coatings in all-solid-state batteries.* Journal of Materials Chemistry A, 2021. **9**(40): p. 23206-23213.

487. Xing, L., et al., *Deciphering the Ethylene Carbonate–Propylene Carbonate Mystery in Li-Ion Batteries.* Accounts of Chemical Research, 2018. **51**(2): p. 282-289.

488. Shi, P.C., et al., *Effect of propylene carbonate-Li+ solvation structures on graphite exfoliation and its application in Li-ion batteries.* Electrochimica Acta, 2017. **247**: p. 12-18.

489. Ming, J., et al., *Molecular-Scale Interfacial Model for Predicting Electrode Performance in Rechargeable Batteries.* ACS Energy Letters, 2019. **4**(7): p. 1584-1593.

490. Ohba, N., S. Ogata, and R. Asahi, *Hybrid Quantum-Classical Simulation of Li Ion Dynamics and the Decomposition Reaction of Electrolyte Liquid at a Negative-Electrode/Electrolyte Interface.* The Journal of Physical Chemistry C, 2019. **123**(15): p. 9673-9679.

491. Leung, K., et al., *Modeling Electrochemical Decomposition of Fluoroethylene Carbonate on Silicon Anode Surfaces in Lithium Ion Batteries.* Journal of The Electrochemical Society, 2014. **161**(3): p. A213.

492. Wu, L.-T., et al., *Prediction of SEI Formation in All-Solid-State Batteries: Computational Insights from PCL-based Polymer Electrolyte Decomposition on Lithium-Metal.* Batteries & Supercaps, 2022. **5**(9): p. e202200088.

493. Young, J., et al., *Comparative Study of Ethylene Carbonate-Based Electrolyte Decomposition at Li, Ca, and Al Anode Interfaces.* ACS Applied Energy Materials, 2019. **2**(3): p. 1676-1684.

494. Sitapure, N., et al., *A computational approach to characterize formation of a passivation layer in lithium metal anodes.* AIChE Journal, 2021. **67**(1): p. e17073.

495. Prabhakaran, V., et al., *Coordination-Dependent Chemical Reactivity of TFSI Anions at a Mg Metal Interface.* ACS Applied Materials & Interfaces, 2023. **15**(5): p. 7518-7528.

496. Cao, C., et al., *Toward Unraveling the Origin of Lithium Fluoride in the Solid Electrolyte Interphase.* Chemistry of Materials, 2021. **33**(18): p. 7315-7336.

497. Wu, S., et al., *Fluorinated Carbonate Electrolyte with Superior Oxidative Stability Enables Long-Term Cycle Stability of Na2/3Ni1/3Mn2/3O2 Cathodes in Sodium-Ion Batteries.* Advanced Energy Materials, 2021. **11**(9): p. 2002737.

498. Aziz, A. and J. Carrasco, *Towards Predictive Synthesis of Inorganic Materials Using Network Science.* Frontiers in Chemistry, 2021. **9**.

499. Blau, S.M., et al., *A chemically consistent graph architecture for massive reaction networks applied to solid-electrolyte interphase formation.* Chemical Science, 2021. **12**(13): p. 4931-4939.

500. Xie, X., et al., *Data-Driven Prediction of Formation Mechanisms of Lithium Ethylene Monocarbonate with an Automated Reaction Network.* Journal of the American Chemical Society, 2021. **143**(33): p. 13245-13258.

501. Liu, B., et al., *Application of high-throughput first-principles calculations in ceramic innovation.* Journal of Materials Science & Technology, 2021. **88**: p. 143-157.

502. Sanchez, J.M., F. Ducastelle, and D. Gratias, *Generalized cluster description of multicomponent systems.* Physica A: Statistical Mechanics and its Applications, 1984. **128**(1): p. 334-350.

503. Metropolis, N., et al., *Equation of State Calculations by Fast Computing Machines.* The Journal of Chemical Physics, 1953. **21**(6): p. 1087-1092.

504. *Computational Design of Battery Materials*. Topics in Applied Physics, ed. D.A.H. Hanaor. Springer Cham.

505. Van der Ven, A., et al., *First-principles investigation of phase stability in ${\mathrm{Li}}_{x}{\mathrm{CoO}}_{2}$.* Physical Review B, 1998. **58**(6): p. 2975-2987.

506. Wolverton, C. and A. Zunger, *First-Principles Prediction of Vacancy Order-Disorder and Intercalation Battery Voltages in ${\mathrm{Li}}_{\mathit{x}}{\mathrm{CoO}}_{2}$.* Physical Review Letters, 1998. **81**(3): p. 606-609.

507. Yang, Y.I., et al., *Enhanced sampling in molecular dynamics.* The Journal of Chemical Physics, 2019. **151**(7).

508. Canepa, P., *Pushing Forward Simulation Techniques of Ion Transport in Ion Conductors for Energy Materials.* ACS Materials Au, 2023. **3**(2): p. 75-82.

509. Deng, Z., et al., *kMCpy: A python package to simulate transport properties in solids with kinetic Monte Carlo.* Computational Materials Science, 2023. **229**: p. 112394.

510. Van der Ven, A., et al., *Rechargeable Alkali-Ion Battery Materials: Theory and Computation.* Chemical Reviews, 2020. **120**(14): p. 6977-7019.

511. Franco, A.A., et al., *Boosting Rechargeable Batteries R&D by Multiscale Modeling: Myth or Reality?* Chemical Reviews, 2019. **119**(7): p. 4569-4627.

512. Wang, Y., et al., *Design principles for solid-state lithium superionic conductors.* Nature Materials, 2015. **14**(10): p. 1026-1031.

513. Kahle, L., A. Marcolongo, and N. Marzari, *High-throughput computational screening for solid-state Li-ion conductors.* Energy & Environmental Science, 2020. **13**(3): p. 928-948.

514. He, X., et al., *Statistical variances of diffusional properties from ab initio molecular dynamics simulations.* npj Computational Materials, 2018. **4**(1): p. 18.

515. Liu, M., et al., *Spinel compounds as multivalent battery cathodes: a systematic evaluation based on ab initio calculations.* Energy & Environmental Science, 2015. **8**(3): p. 964-974.

516. Carrasco, J., *Role of van der Waals Forces in Thermodynamics and Kinetics of Layered Transition Metal Oxide Electrodes: Alkali and Alkaline-Earth Ion Insertion into V2O5.* The Journal of Physical Chemistry C, 2014. **118**(34): p. 19599-19607.

517. Lu, G., et al., *Distinguishing the Effects of the Space-Charge Layer and Interfacial Side Reactions on Li10GeP2S12-Based All-Solid-State Batteries with Stoichiometric-Controlled LiCoO2.* ACS Applied Materials & Interfaces, 2022. **14**(22): p. 25556-25565.

518. Warburton, R.E., et al., *Tailoring Interfaces in Solid-State Batteries Using Interfacial Thermochemistry and Band Alignment.* Chemistry of Materials, 2021. **33**(21): p. 8447-8459.

519. Cheng, T., et al., *Quantum Mechanics Reactive Dynamics Study of Solid Li-Electrode/Li6PS5Cl-Electrolyte Interface.* ACS Energy Letters, 2017. **2**(6): p. 1454-1459.

520. Camacho-Forero, L.E. and P.B. Balbuena, *Exploring interfacial stability of solid-state electrolytes at the lithium-metal anode surface.* Journal of Power Sources, 2018. **396**: p. 782-790.

521. Golov, A. and J. Carrasco, *Molecular-Level Insight into the Interfacial Reactivity and Ionic Conductivity of a Li-Argyrodite Li6PS5Cl Solid Electrolyte at Bare and Coated Li-Metal Anodes.* ACS Applied Materials & Interfaces, 2021. **13**(36): p. 43734-43745.

522. Arnold, W., et al., *Synthesis of Fluorine-Doped Lithium Argyrodite Solid Electrolytes for Solid-State Lithium Metal Batteries.* ACS Applied Materials & Interfaces, 2022. **14**(9): p. 11483-11492.

523. Golov, A. and J. Carrasco, *Enhancing first-principles simulations of complex solid-state ion conductors using topological analysis of procrystal electron density.* npj Computational Materials, 2022. **8**(1): p. 187.

524. Gao, B., et al., *Li+ Transport Mechanism at the Heterogeneous Cathode/Solid Electrolyte Interface in an All-Solid-State Battery via the First-Principles Structure Prediction Scheme.* Chemistry of Materials, 2020. **32**(1): p. 85-96.

525. Tian, H.-K., et al., *Electron and Ion Transfer across Interfaces of the NASICON-Type LATP Solid Electrolyte with Electrodes in All-Solid-State Batteries: A Density Functional Theory Study via an Explicit Interface Model.* ACS Applied Materials & Interfaces, 2020. **12**(49): p. 54752-54762.

526. Gao, B., R. Jalem, and Y. Tateyama, *First-Principles Study of Microscopic Electrochemistry at the LiCoO2 Cathode/LiNbO3 Coating/β-Li3PS4 Solid Electrolyte Interfaces in an All-Solid-State Battery.* ACS Applied Materials & Interfaces, 2021. **13**(10): p. 11765-11773.

527. Melander, M.M., et al., *Grand-canonical approach to density functional theory of electrocatalytic systems: Thermodynamics of solid-liquid interfaces at constant ion and electrode potentials.* The Journal of Chemical Physics, 2019. **150**(4).

528. Sundararaman, R., W.A. Goddard, III, and T.A. Arias, *Grand canonical electronic density-functional theory: Algorithms and applications to electrochemistry.* The Journal of Chemical Physics, 2017. **146**(11).

529. Taylor, C.D., et al., *First principles reaction modeling of the electrochemical interface: Consideration and calculation of a tunable surface potential from atomic and electronic structure.* Physical Review B, 2006. **73**(16): p. 165402.

530. Jinnouchi, R. and A.B. Anderson, *Electronic structure calculations of liquid-solid interfaces: Combination of density functional theory and modified Poisson-Boltzmann theory.* Physical Review B, 2008. **77**(24): p. 245417.

531. Letchworth-Weaver, K. and T.A. Arias, *Joint density functional theory of the electrode-electrolyte interface: Application to fixed electrode potentials, interfacial capacitances, and potentials of zero charge.* Physical Review B, 2012. **86**(7): p. 075140.

532. Kastlunger, G., P. Lindgren, and A.A. Peterson, *Controlled-Potential Simulation of Elementary Electrochemical Reactions: Proton Discharge on Metal Surfaces.* The Journal of Physical Chemistry C, 2018. **122**(24): p. 12771-12781.

533. Melander, M.M., *Grand Canonical Rate Theory for Electrochemical and Electrocatalytic Systems I: General Formulation and Proton-coupled Electron Transfer Reactions.* Journal of The Electrochemical Society, 2020. **167**(11): p. 116518.

534. Melander, M.M., et al., *Constant inner potential DFT for modelling electrochemical systems under constant potential and bias.* npj Computational Materials, 2024. **10**(1): p. 5.

535. Brenner, D.W., *The Art and Science of an Analytic Potential.* physica status solidi (b), 2000. **217**(1): p. 23-40.

536. Welch, D.A., et al., *Using molecular dynamics to quantify the electrical double layer and examine the potential for its direct observation in the in-situ TEM.* Advanced Structural and Chemical Imaging, 2015. **1**(1): p. 1.

537. Bonilla, M.R., et al., *On the interfacial lithium dynamics in Li7La3Zr2O12:poly(ethylene oxide) (LiTFSI) composite polymer-ceramic solid electrolytes under strong polymer phase confinement.* Journal of Colloid and Interface Science, 2022. **623**: p. 870-882.

538. Senftle, T.P., et al., *The ReaxFF reactive force-field: development, applications and future directions.* npj Computational Materials, 2016. **2**(1): p. 15011.

539. Wang, Y., et al., *Reductive Decomposition of Solvents and Additives toward Solid-Electrolyte Interphase Formation in Lithium-Ion Battery.* The Journal of Physical Chemistry C, 2020. **124**(17): p. 9099-9108.

540. Liu, Y., et al., *Effects of High and Low Salt Concentrations in Electrolytes at Lithium–Metal Anode Surfaces Using DFT-ReaxFF Hybrid Molecular Dynamics Method.* The Journal of Physical Chemistry Letters, 2021. **12**(11): p. 2922-2929.

541. Yun, K.-S., et al., *Simulation Protocol for Prediction of a Solid-Electrolyte Interphase on the Silicon-based Anodes of a Lithium-Ion Battery: ReaxFF Reactive Force Field.* The Journal of Physical Chemistry Letters, 2017. **8**(13): p. 2812-2818.

542. Ospina-Acevedo, F., N. Guo, and P.B. Balbuena, *Lithium oxidation and electrolyte decomposition at Li-metal/liquid electrolyte interfaces.* Journal of Materials Chemistry A, 2020. **8**(33): p. 17036-17055.

543. Bertolini, S. and P.B. Balbuena, *Buildup of the Solid Electrolyte Interphase on Lithium-Metal Anodes: Reactive Molecular Dynamics Study.* The Journal of Physical Chemistry C, 2018. **122**(20): p. 10783-10791.

544. Yang, P.-Y. and C.-W. Pao, *Molecular Simulations of the Microstructure Evolution of Solid Electrolyte Interphase during Cyclic Charging/Discharging.* ACS Applied Materials & Interfaces, 2021. **13**(4): p. 5017-5027.

545. Liu, Y., et al., *Formation of Linear Oligomers in Solid Electrolyte Interphase via Two-Electron Reduction of Ethylene Carbonate.* Advanced Theory and Simulations, 2022. **5**(5): p. 2100612.

546. Agrawal, A. and A. Choudhary, *Perspective: Materials informatics and big data: Realization of the "fourth paradigm" of science in materials science.* APL Materials, 2016. **4**(5): p. 053208.

547. Jennings, P.C., et al., *Genetic algorithms for computational materials discovery accelerated by machine learning.* npj Computational Materials, 2019. **5**(1): p. 46.

548. Noh, J., et al., *Machine-enabled inverse design of inorganic solid materials: promises and challenges.* Chemical Science, 2020. **11**(19): p. 4871-4881.

549. Lombardo, T., et al., *Artificial Intelligence Applied to Battery Research: Hype or Reality?* Chemical Reviews, 2022. **122**(12): p. 10899-10969.

550. Deringer, V.L., *Modelling and understanding battery materials with machine-learning-driven atomistic simulations.* Journal of Physics: Energy, 2020. **2**(4): p. 041003.

551. Shao, Y., et al., *Modelling Bulk Electrolytes and Electrolyte Interfaces with Atomistic Machine Learning.* Batteries & Supercaps, 2021. **4**(4): p. 585-595.

552. Ko, T.W. and S.P. Ong, *Recent advances and outstanding challenges for machine learning interatomic potentials.* Nature Computational Science, 2023: p. 1-3.

553. Behler, J., *First Principles Neural Network Potentials for Reactive Simulations of Large Molecular and Condensed Systems.* Angewandte Chemie International Edition, 2017. **56**(42): p. 12828-12840.

554. Behler, J. and M. Parrinello, *Generalized Neural-Network Representation of High-Dimensional Potential-Energy Surfaces.* Physical Review Letters, 2007. **98**(14): p. 146401.

555. Bartók, A.P., et al., *Gaussian Approximation Potentials: The Accuracy of Quantum Mechanics, without the Electrons.* Physical Review Letters, 2010. **104**(13): p. 136403.

556. Glielmo, A., P. Sollich, and A. De Vita, *Accurate interatomic force fields via machine learning with covariant kernels.* Physical Review B, 2017. **95**(21): p. 214302.

557. Bartók, A.P. and G. Csányi, *Gaussian approximation potentials: A brief tutorial introduction.* International Journal of Quantum Chemistry, 2015. **115**(16): p. 1051-1057.

558. Thompson, A.P., et al., *Spectral neighbor analysis method for automated generation of quantum-accurate interatomic potentials.* Journal of Computational Physics, 2015. **285**: p. 316-330.

559. Artrith, N., A. Urban, and G. Ceder, *Constructing first-principles phase diagrams of amorphous LixSi using machine-learning-assisted sampling with an evolutionary algorithm.* The Journal of Chemical Physics, 2018. **148**(24): p. 241711.

560. Fujikake, S., et al., *Gaussian approximation potential modeling of lithium intercalation in carbon nanostructures.* The Journal of Chemical Physics, 2018. **148**(24): p. 241714.

561. Li, W., et al., *Study of Li atom diffusion in amorphous Li3PO4 with neural network potential.* The Journal of Chemical Physics, 2017. **147**(21): p. 214106.

562. Miwa, K. and R. Asahi, *Molecular dynamics simulations of lithium superionic conductor Li10GeP2S12 using a machine learning potential.* Solid State Ionics, 2021. **361**: p. 115567.

563. Shao, Y., et al., *Temperature effects on the ionic conductivity in concentrated alkaline electrolyte solutions.* Physical Chemistry Chemical Physics, 2020. **22**(19): p. 10426-10430.

564. Deng, Z., et al., *An electrostatic spectral neighbor analysis potential for lithium nitride.* npj Computational Materials, 2019. **5**(1): p. 75.

565. Lai, G., et al., *A Deep Neural Network Interface Potential for Li-Cu Systems.* Advanced Materials Interfaces, 2022. **9**(27): p. 2201346.

566. Holekevi Chandrappa, M.L., et al., *Thermodynamics and Kinetics of the Cathode–Electrolyte Interface in All-Solid-State Li–S Batteries.* Journal of the American Chemical Society, 2022. **144**(39): p. 18009-18022.

567. Schütt, K.T., et al., *Unifying machine learning and quantum chemistry with a deep neural network for molecular wavefunctions.* Nature Communications, 2019. **10**(1): p. 5024.

568. Bogojeski, M., et al., *Quantum chemical accuracy from density functional approximations via machine learning.* Nature Communications, 2020. **11**(1): p. 5223.

Declaration of interests

☒ The authors declare that they have no known competing financial interests or personal relationships that could have appeared to influence the work reported in this paper.

☐ The authors declare the following financial interests/personal relationships which may be considered as potential competing interests: